

Concept, System Design, Evaluation and Safety Requirements for a Multispectral Sensor

DISSERTATION

zur Erlangung des Grades eines Doktors
der Ingenieurwissenschaften

vorgelegt von

Oliver Schwaneberg (MSc)

eingereicht bei der Naturwissenschaftlich-Technischen Fakultät
der Universität Siegen

Siegen 2013

Gutachter der Dissertation:

1. Prof. Dr. Andreas Kolb
2. Prof. Dr.-Ing. Peter Haring Bolívar
3. Prof. Dr. Dietmar Reinert

Tag der mündlichen Prüfung: 26. September 2013

Eidesstattliche Erklärung

Die vorliegende Dissertation wurde von mir selbständig angefertigt. Die verwendeten Hilfsmittel und Quellen sind im Literaturverzeichnis vollständig aufgeführt.

Eingetragene Warenzeichen und Copyrights werden anerkannt, auch wenn sie nicht explizit gekennzeichnet sind.

Oliver Schwaneberg

Danksagung

Herzlichen Dank möchte ich Allen sagen, die mich während der letzten Jahre bei meiner Arbeit unterstützt haben. Beginnen möchte ich mit Herrn Prof. Dr. Andreas Kolb und Herrn Prof. Dr.-Ing. Peter Haring Bolívar von der Universität Siegen, sowie Herrn Prof. Dr.-Ing. Norbert Jung von der Hochschule Bonn-Rhein-Sieg, die mir in vielen Gesprächen mit Tipps und konstruktiver Kritik geholfen haben. Besonderer Dank gilt auch Herrn Prof. Dr. Dietmar Reinert vom Institut für Arbeitsschutz, dessen jahrelanges Engagement und Unterstützung diese Arbeit erst möglich gemacht haben. Des Weiteren möchte ich mich bei all meinen Kollegen und speziell bei Holger Steiner und Sebastian Sporrer bedanken, die nicht nur für eine angenehme Arbeitsatmosphäre gesorgt haben, sondern mir ebenfalls stets mit Rat und Tat zur Seite standen. Des weiteren möchte ich mich bei meiner Frau Andrea Schwaneberg und meinem Freund Martin Pelzer bedanken, die diese Arbeit auf korrekte Rechtschreibung und Grammatik überprüft haben. Bei meinen Eltern möchte ich mich für ihre Unterstützung in all den Jahren bedanken. Zusätzlich möchte ich mich bei meinen Söhnen Martin und Tim bedanken, weil sie mir Zuversicht für die Zukunft geben.

Außerdem möchte ich mich bei der Deutschen Gesetzlichen Unfallversicherung, dem regionalen Entwicklungsfond Ziel2.NRW sowie dem Wettbewerb Science-to-Business PreSeed für die finanzielle Unterstützung bedanken. Zu guter Letzt gilt mein Dank der Deutschen Forschungsgemeinschaft, welche das DFG Graduiertenkolleg 1564 „Imaging New Modalities“ an der Universität Siegen ermöglicht hat.

Zusammenfassung

Die Arbeit mit handbeschickten Maschinen (wie z.B. Kreissägen) birgt deutlich höhere Verletzungsrisiken als vergleichbare Arbeitsplätze mit hohem Risikopotential. Die weite Verbreitung solcher Maschinen führt zu schwerwiegenden Problemen für den Arbeitsschutz und hohen Kosten für medizinische Behandlungen sowie Unfallrenten.

In dieser Arbeit wird ein neues Konzept eines multispektralen Sensors vorgestellt, welcher den Bereich vor der Gefahrenzone einer Maschine überwachen soll, um Gliedmaßen des Benutzers zu erkennen. Ziel ist, rechtzeitig Schutzmaßnahmen einzuleiten, um einen drohenden Unfall zu verhindern.

Das Sensorkonzept ermöglicht eine berührungslose Materialklassifikation. Ein entsprechendes Systemdesign und spezielle Sicherheitsanforderungen unter Berücksichtigung internationaler Sicherheitsstandards wurden entwickelt. Darüber hinaus wurde ein Prototyp implementiert, welcher vier Wellenlängenbänder verwendet. Diese wurden durch eine Analyse von Reflexionsspektren ermittelt, die eigens für diesen Zweck erhoben wurden.

Der Sensor beinhaltet ein Embedded System, welches eine Materialklassifikation innerhalb weniger Millisekunden durchführt. Um dies zu erreichen, wurden mehrere Methoden zur Verarbeitung der Sensordaten erforscht und entwickelt. Die dargestellten Methoden wurden mit gemessenen und synthetisierten Sensordaten evaluiert. Ebenfalls erfolgte eine Evaluierung der Prototypen, welche die dargestellten Methoden implementieren. Die Ergebnisse zeigen, dass menschliche Haut unter verschiedensten Messbedingungen, auch unter Störeinflüssen, verlässlich erkannt wird.

Abstract

The use of manually fed machines (e.g. table saws) bares risks of injury that are clearly above the average level of other high risk workplaces. The wide use of such machines causes severe problems for occupational safety and implies high costs for medical treatments and accident annuities.

This thesis presents a new concept of a multispectral sensor to monitor an area in front of a danger zone to detect the user's limbs and trigger safeguarding measures to prevent an accident in time. The sensor concept realizes a contact-free material classification, which comprises the development of a system design and specific safety requirements with respect to international safety standards. Furthermore, a prototypical implementation using four wavebands, which were determined for skin detection through an analysis of reflectance spectra acquired specifically for this purpose, was built.

This sensor comprises an embedded system which is able to perform a material classification within a few milliseconds. To achieve this, several algorithms were researched and developed to process the raw sensor readings. An evaluation of the presented methods on both real and synthesized sensor data as well as on the prototypical implementation was performed. The evaluation yields that the prototype implementing the presented methods can detect human skin reliably within a wide range of measurement conditions, including the presence of interference sources.

Contents

Contents	xi
List of Figures	xv
List of Tables	xxi
1 Introduction	1
2 Basics	5
2.1 Problem Formulation	5
2.2 Physical Basis	7
2.3 Machine Learning Methods	8
2.3.1 Support Vector Machine (SVM)	9
2.3.2 Binary Decision Trees	14
2.3.3 Common Evaluation Criteria for Classifiers	16
2.4 Methods for Distance Measurement	18
2.4.1 Mathematical Notation	18
2.4.2 Peak Estimation	20
2.4.3 Distance Mapping	21
3 Prior Work	25

3.1	Comparison of Technical Concepts	25
3.1.1	Imaging Systems for Skin Detection	26
3.1.2	Non-Imaging Systems for Skin Detection	29
3.1.3	Summary of Prior Work on Skin Detection	31
3.1.4	Beamforming with Light Emitting Diodes	32
3.2	Summary of Prior Work to the Sensor Concept	35
4	Preliminary Study	37
4.1	Metrology	37
4.2	Data Composition	38
4.3	Data Analysis	39
4.4	Data Mapping and Additional Experiments	43
4.4.1	Multi-angle Reflectance Spectroscopy	46
4.4.2	Spectroscopy of Subsurface and Specular Scattering Components	49
5	Sensor Concept	53
5.1	Safety Requirements and Applicable Standards	54
5.1.1	Differentiation of Relevant Materials	55
5.1.2	Varying Distances of Operation	57
5.1.3	Reaction Speed	57
5.1.4	Beam Width (Detection Area)	59
5.1.5	Atmospheric Humidity	59
5.1.6	Temperature Range	63
5.1.7	Shock Resistance	64
5.1.8	Ambient Light	65
5.1.9	Eye Safety	75
5.1.10	Self Tests	76

5.2	System Design Concepts	78
5.2.1	Optics and Optoelectronics	78
5.2.2	Electronics	88
5.3	System Specifications	93
5.3.1	Functional Specifications	93
5.3.2	Technical Specifications	95
5.3.3	Delimitation of this System Specification	96
5.4	Prototypical Implementation	96
5.4.1	Implemented Concept	97
5.4.2	Primary Microcontroller	103
5.4.3	Previous Prototypes	104
6	Acquisiton, Data Processing and Classification	105
6.1	Data Acquisition	105
6.2	Low-Level Correction	111
6.3	Data Processing Concept	112
6.3.1	Distance Estimation	113
6.3.2	Data Fusion	116
6.4	Classification of Materials	120
7	Concept Validation	123
7.1	Data Processing Methods	123
7.1.1	Data Basis	124
7.1.2	Distance Estimation	129
7.1.3	Data Fusion	137
7.1.4	Material Classification	146
7.1.5	Computational Performance	153

7.2	Typical Artifacts	154
7.2.1	Measuring on Edges	154
7.2.2	Measuring Multiple Objects Simultaneously	157
7.2.3	Measuring Shiny Surfaces	160
7.3	Environmental Influences	162
7.3.1	Ambient Light	162
7.3.2	Atmospheric Humidity	165
7.3.3	Ambient Temperature	167
7.4	Cross Relations of Interference Factors	170
8	Examples of Applications	173
8.1	Woodwork Shops	173
8.2	Meat Processing	176
8.3	Construction Sites	178
9	Summary and Outlook	183
9.1	Summary	183
9.2	Outlook	186
	Bibliography	187
	Acronyms	197
	Glossary	201

List of Figures

1.1	Principle setup and signal processing of a multispectral point sensor for material classification (compare [4, Fig. 1]).	2
2.1	Reflectance of human skin with different pigmentation.	8
2.2	Different skin types after Fitzpatrick [8].	9
2.3	Linear separation of two classes by a hyperplane in a two-dimensional example [12, see Fig. 1.5].	10
2.4	Example of a not linearly separable problem: separating dots from crosses.	11
2.5	Example of a binary decision tree.	15
2.6	Examples for \mathbf{X}_{ref}^v (with $v = 2$) and \mathbf{X}_{in} , such that the subpixel peak position of \mathbf{X}_{in} can be approximated as $v + \Delta$	19
2.7	Power-function model on EGCC-results vs. true measurement distance (see [4]).	22
3.1	Absorption coefficient of water in the visual and near-infrared spectrum (Source: [27, Fig. 4]).	28
3.2	Free-form lens to combine three light emitting diodes (LEDs). Original source: [31, Fig. 3].	32

3.3	Illustration of a free-form lens. The lens is depicted in an isometric view (a), a right view (b) as well as a sectional drawing for half a lens including exemplified ray paths (c). Source: [33, Fig. 2+3].	34
3.4	The prototype of the collimator lens by Chen et al.. Source: [34, Fig. 11].	35
4.1	Reflectance of human skin and spruce wood at different humidity levels.	42
4.2	Principle Component Analysis (PCA) of skin and wood samples. . . .	43
4.3	Mapping of reflectance measurements acquired using the <i>irSys</i> [®] 1.7 spectrometer to measurements of the Skinner mark 1 sensor system. .	44
4.4	Reflectance measurement module for <i>irSys</i> [®] 1.7.	45
4.5	Measurement setup for scattering measurement comprising light source S , light detector D , angle of incidence α and the distance of measurement d [42, Fig. 4.1].	46
4.6	Reflectance of human skin at different angles of observation.	47
4.7	Measurement setup for angular dependent reflectance measurement comprising light source S , light detector D , angle of incidence α and the distance of measurement d [42, Fig. 4.2].	48
4.8	Setup to measure the subsurface components of the reflection spectrum.	49
4.9	Setup to measure to specular components of the reflection spectrum. .	50
4.10	Subsurface and specular reflectance components in comparison to measurements performed with the measurement setup used for the study, a spectroscopy setup which is similar to the Skinner sensor and data by Jacquez et al. [9].	51
5.1	Atmospheric attenuation - a comparison of irradiance at sea level and the top of the atmosphere (Source: [54]).	60
5.2	Mapping of temperature and relative humidity to absolute humidity. .	61

5.3	Relative transmission over an air path length of 0.34 m. The reference measurement was acquired at a temperature of 20 °C and 11 % relative humidity (RH).	62
5.4	Relative transmission at 1365 nm.	64
5.5	Spectral responsivity of an indium gallium arsenic (InGaAs) photodiode (Original source: [60]).	66
5.6	Two-sided multispectral light curtain configuration.	67
5.7	Single-sided multispectral barrier configuration.	68
5.8	False color image and plot of skimmed and whole milk as well as human skin. False color mapping: 1060nm \mapsto red, 1300nm \mapsto green and 1550nm \mapsto blue.	70
5.9	Illustration of a finger passing the beam at an acute angle.	73
5.10	Test rod at acute angle to transmitted beam.	74
5.11	Limits for small continuous wave sources of classes 1 and 1M. Compare [62, Fig. 130].	75
5.12	Classification of risks by ISO 13849-1 and IEC 61508 [46, Tab. 4] [47, Tab. 3].	77
5.13	Optical paths united by a beam splitter.	79
5.14	Optical paths aligned using a parabolic mirror. Distance dependent projections are illustrated.	79
5.15	Optical paths aligned using a parabolic mirror. Obstruction by additional shielding is illustrated.	80
5.16	Optical paths aligned in parallel.	80
5.17	Image of two LED chips with bond wires.	82
5.18	Overview of beamforming concepts.	83

5.19	False color images of simulated projections from three concepts at four projection distances. All units in millimeter. Note that the scale changes with projection distance.	86
5.20	Detecting dust using an additional LED.	92
5.21	Sideways illuminated protective screen showing very low and medium soil level.	93
5.22	Virtually augmented photograph of the implemented sensor. Source: [5, Fig. 3].	98
5.23	Block diagram of the Skinner sensor.	99
5.24	LEDs and photodiodes on their printed circuit boards (PCBs).	100
5.25	LED driver to generate pulses at controlled current.	100
5.26	Photocurrent readout PCB.	101
5.27	Schematic of the circuit for a single photodiode.	101
6.1	Flow diagram showing data acquisition and processing.	106
6.2	Transmission characteristic of the used $f_c = 154\text{Hz}$ high-pass filter of first order.	107
6.3	Output signal of a charge integrator during signal acquisition.	109
6.4	Simulation of high-pass filter and integrator output.	110
6.5	Sensor readings of all four photodiodes acquired at $\lambda_0 = 830\text{nm}$ ($\mathbf{X}_{in}[0][0]$ to $\mathbf{X}_{in}[3][0]$).	114
6.6	Sensor readings combined with ratios of signals from neighboring photodiodes on a logarithmic scale.	115
6.7	Exemplified data fusion $\mathbf{X}_{in} \rightarrow \vec{s}$	119
7.1	Rotation and shift of the reference tile (see [4, Fig. 8]).	125
7.2	Comparison of real (HW) and synthesized (M1) data.	126

7.3	FFT of a signal from the last photodiode.	128
7.4	Simulation of sensor (M1) showing target shifted by -50 mm at $d = 150$ mm.	133
7.5	Distance estimation from 100 mm to 800 mm on actual sensor data using EGCC and QBTM (Compare [4, Fig. 10]).	136
7.6	Influence of noise on the distance estimation.	137
7.7	Gaussian functions as noise free synthetic sensor data (T_4).	139
7.8	Relative deviations with $\rho = 8$ mm for the presented methods on set T_1	140
7.9	Relative deviations with $\rho = 8$ mm for the presented methods on set T_2	141
7.10	Relative deviations with $\rho = 8$ mm for the presented methods on set T_3	141
7.11	Relative deviations with $\rho = 8$ mm for the presented methods on set T_4	142
7.12	Raw signals within T_3 with $b = 0$	143
7.13	Maximum relative deviation δ computed from \vec{r} with $\rho = 8$ mm for the presented methods on set T_1	143
7.14	Maximum relative deviation δ computed from \vec{r} with $\rho = 8$ mm for the presented methods on set T_2	144
7.15	Maximum relative deviation δ computed from \vec{r} with $\rho = 8$ mm for the presented methods on set T_3	145
7.16	Maximum relative deviation δ computed from \vec{r} with $\rho = 8$ mm for the presented methods on set T_4	145
7.17	principle component analysis (PCA) of spectral signatures acquired from all samples of human skin and meat (compare [4, Fig. 12]).	148
7.18	Similar spectra from human skin and pork samples.	149
7.19	Signal ratio of neighboring photodiodes. Measured at full and partial beam coverage using a Skinner mark 1 sensor.	155

7.20	Maximum deviation of ratios within spectral signatures acquired at partial beam coverage to a wooden board using Skinner mark 1 and mark 2 sensors.	157
7.21	A forefinger on a wooden board as measurement target.	158
7.22	Evaluation of the experiment using the ratio of $\bar{s}[0]/\bar{s}[2]$ (see [5, Fig. 6]).	159
7.23	Signal-to-noise ratios of $\bar{s}[0]$ and $\bar{s}[2]$ from measurements of the wooden board. Acquired with and without field stop.	160
7.24	Positions of ambient light source.	162
7.25	Averaged spectral signatures with standard deviation acquired at different positions of an alternating-current (AC) powered 50 W lamp. . .	163
7.26	Averaged spectral signatures with standard deviation acquired at different positions of a direct-current (DC) powered 50 W lamp.	164
7.27	Atmospheric attenuation measured using a Skinner mark 2 sensor. . .	166
7.28	Spectral signatures acquired from 0 °C to 50 °C using a Skinner mark 2 sensor.	168
7.29	Relative standard deviation of spectral signatures acquired over a temperature range from 0 °C to 50 °C.	169
8.1	Concept image depicting an observed spot. (Source: SMART.HOOVER project)	175
8.2	Practical test of a Skinner mark 2 sensor at a bone band saw.	177
8.3	Soiled supporting timber and glove from a construction site.	179
8.4	Reflectance spectra of new and soiled nitrile gloves.	179
8.5	Reflectance spectra of new and soiled nitrile gloves, normalized to the reflectance at 1070 nm.	180
8.6	Reflectance spectra of common workpieces at construction sites.	181

List of Tables

2.1	Structure of a confusion matrix.	17
4.1	Distribution of skin types.	38
4.2	Distribution of age.	38
5.1	Applicability of current standards to active optoelectronic material classifying protective devices (AOMCPDs).	55
5.2	Absorption coefficients for 1365 nm.	63
5.3	Modified parameters for Skinner mark 1, 2 and 3.	97
7.1	Definition of the 17 orientations of the target tile (see [4, Tab. 1]).	124
7.2	Root mean square error (RMS) in millimeters of all configurations with all basic estimators. Measurements of a Skinner mark 2 sensor (HW) and virtual sensor configurations M1, M2, M3 and M4 are used as data sources (compare [4, Tab. 2]).	131
7.3	Results as averaged root mean square error (RMS) in millimeters from additional configurations.	132

7.4	Evaluation of multispectral extensions by the root mean square error (RMS) in millimeters of all configurations with all multispectral estimators. Measurements of a Skinner mark 2 sensor (HW) and virtual sensor configurations M1 and M2 are used as data sources.	134
7.5	Averaged RMS in millimeters on a selection of samples from hands, wooden boards and meat samples.	135
7.6	Maximum distance between peak positions at all wavebands.	139
7.7	Results for material classification using decision trees.	147
7.8	Results for material classification using C-Support Vector Machines (SVMs) (compare [4, Tab. 4]).	150
7.9	Analysis of the scenario <i>Skin vs. Wood</i> with artificially added white noise.	151
7.10	Maximum measured computational time.	153
7.11	Development of the relative standard deviation in relation to the position of an AC powered 50 W lamp, averaged over $\vec{s}[0]$ to $\vec{s}[3]$	163
7.12	Development of the relative standard deviation in relation to the position of a DC powered 50 W lamp, averaged over $\vec{s}[0]$ to $\vec{s}[3]$	164
7.13	Pulse current settings for the used Skinner sensor.	168
7.14	Overview of interference factors and their impact.	171

Chapter 1

Introduction

Manually fed machines are generally prone to accidents, as dangerous moving parts are within the user's reach during normal operation. In Germany, for instance, the use of circular bench saws at joineries, construction sites and woodworking shops led to about 2750 reported accidents in 2005, which resulted in 98 new accident annuities¹ [1]. Furthermore, in the United States of America, about 65000 accidents were reported which led to costs for medical treatments of 1.967 billion USD in 2001 [2, Table 1]. Despite the individual sorrow, the economic damage caused by accidents involving such machines is severe. A technical solution to allow a contact-free detection of human limbs at certain positions could dramatically increase the safety standards at many manually fed machines. However, such a technical solution must react fast and sufficiently reliable while not obstructing the user in any way. In addition to those challenging requirements, the costs for the needed hardware shall be as low as possible in order to achieve market acceptance.

This thesis presents and validates a concept of a multispectral point sensor for contact-free material classification. If such a sensor is optimized for skin detection, it

¹Accident statistics for construction sites were supplied on demand by the department "Statistics - Occupational accidents, Prevention" of the German Legal Accident Insurance (DGUV).

can only be used as long as the user does not wear gloves. The limitation to bare hands is not a problem for most applications, as the use of gloves is discouraged at many machines with rotating tools, as tear-proof gloves increase the risk of getting caught in by the moving parts of the machines [3]. The resulting injuries are often more severe than a plain cut resulting from direct contact of hand and tool. Exceptions are found in industries with special requirements to hygiene like food processing industries, which require the use of special gloves. However, the presented sensor concept can also be optimized to detect certain gloves or a sensor optimized for skin detection might even be able to distinguish a particular glove from certain workpieces.

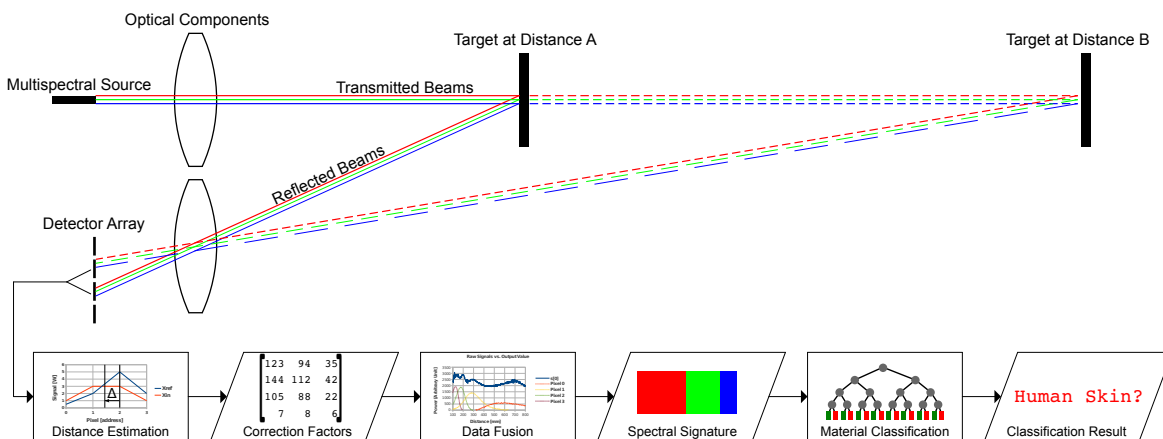


Figure 1.1: Principle setup and signal processing of a multispectral point sensor for material classification (compare [4, Fig. 1]).

As depicted in Fig. 1.1, the concept suggests a transmitter unit with LEDs of different peak-wavelengths to generate strobe pulses of spectral-selective illumination, which are formed into a homogeneous and narrow beam. A broadband receiver unit featuring an array of photodetectors is used to measure the incident radiation reflected from surfaces in front of the sensor. The receiver is synchronized to the transmitter's strobe pulses to measure the specific amplitude change per waveband. These

amplitudes can be used to judge whether the probed surface's material is human skin or not. Furthermore, the sensor is able to estimate its distance to the targeted surface by triangulation. This concept was first published in the OSA Journal of Applied Optics [5, 6]. The basic physical properties and state-of-the-art methods, which are used for distance estimation and material classification, are described in chapters 2 and 3.

In Chap. 4, the selection of appropriate wavebands to discriminate human skin from typical workpieces is made and denoted as a *spectral signature*. The main contribution of this chapter is the systematic analysis of over 1000 reflectance spectra acquired from 330 people of all ages, sex and skin color as well as from several hundred typical workpieces of wood and plastics. Intermediate results from this chapter were also published in the IOP Journal of Measurement Science and Technology [4].

In Chap. 5, the applicability of current safety standards on this new type of sensors for material classification is investigated. In this context, it is a primary objective to identify the gaps in current safety standards with respect to the proposed concept and to present recommendations on how to close these gaps. To best of my knowledge, this dissertation is the first document to address this issue. Furthermore, system design concepts are presented and discussed, which are used to derive a system specification. At the end of the chapter, a prototypical implementation, which aims for compliance with these specifications, is presented.

In Chap. 6, appropriate methods were investigated to process the signals acquired by such sensors, where the focus is on the selection of suitable state-of-the-art methods. However, a new method to estimate the measurement distance is introduced in addition to a standard method. Furthermore, an approach to extract the spectral signature from the available sensor readings is presented. Intermediate results on

these topics were also published in the IOP Journal of Measurement Science and Technology [4].

It is necessary that such a sensor operates reliable in every situation, as the health of the users depends on the efficacy of the safeguarding equipment. Therefore, Chap. 7 presents a number of experiments that have been carried out to evaluate the presented methods as well as the prototypical implementation. A part of these experiments were also published in the OSA and IOP journal articles mentioned above [5, 4]. This dissertation presents comprehensive results from these experiments as well as new experiments, e.g. on measurement artifacts caused by external factors such as ambient temperature, humidity and light.

Chapters 5, 6 and 7 yield the major contributions of this work. An outlook on possible applications is described in Chap. 8.

This thesis is devoted to the concept, implementation and evaluation of a multispectral sensor for skin detection. The thesis does not address any mechanical solutions to actively protect a machine's user from being harmed, as the necessary means must be designed individually for any application and machine. Furthermore, the development of the presented prototypical implementation should be understood as a proof of concept rather than the attempt of a product development.

Chapter 2

Basics

In this chapter, the problem and motivation for this work is described. Furthermore, relevant techniques and a mathematical notation are introduced.

2.1 Problem Formulation

Detecting human limbs within a supervised area is a challenging task. For safety applications, it is reasonable that a sensor system triggers a protective measure at the very last moment before an accident becomes inevitable to allow the user as much freedom of action as possible. For instance, a fast stopping mechanism for a saw blade should only be triggered if a finger is less than 50mm away from the saw blade to allow the handling of small workpieces. Considering a quick movement of the hand of about 2 m s^{-1} , only $50 \text{ mm} / 2 \text{ m s}^{-1} = 25 \text{ ms}$ would be available to prevent an accident. Stopping a saw blade within 25 ms is challenging, so the safety sensor must trigger the brake within a few milliseconds in order to maximize the remaining time span. On the other hand, the system must always react precisely and reliably, as it should not trigger protective means if the hands are still outside the danger zone or if

a workpiece enters the danger zone. In consequence, the spot observed by the sensor system must be sharply outlined and smaller than the width of the smallest object that must be recognized (e.g., a little finger) over the whole permissible operating distance. Having a well-defined spot (or beam), the objects within this spot must be classified with very high accuracy. As discussed in Chap. 5.1.1, requirements for the accuracy can be derived from the international safety standard IEC 61508-1, yielding that the rate of human limbs being misclassified as workpieces must be in the range from 10^{-5} to 10^{-1} (depending on the expected risk and severity of injuries). All these requirements must be met at all expectable ambient conditions, including vibrations as well as varying temperatures, humidity and external light sources. Furthermore, the system should be inexpensive, compact and mounted in a way that the users of the machine will not be hindered by it in any way.

Therefore, at least one well suited physical feature must be used for a reliable differentiation from usual workpieces. A variety of physical properties can be utilized to detect the presence of human limbs. Certain properties as shape, size, temperature and color are obvious candidates to think of, because they can be perceived with at least one of our five human senses. In practice, all of these properties are hard to exploit:

- With its 27 degrees of freedom, the *shape* of a hand is highly variable [7]. Furthermore, the information on *shape* and *size* acquired by most sensors, e.g. stereo cameras or [Photonic Mixing Devices \(PMDs\)](#), usually is incomplete and does heavily depend on the observation angle. Under these circumstances, detecting a human hand fast and reliably by shape and size is a very complex task, which is not expected to be solved by an inexpensive sensor system.
- The surface *temperature* of the human hand is influenced by the blood flow and

room temperature. Nevertheless, work pieces can warm up to body temperature during processing easily, e.g. by heat which is generated during sawing or drilling.

- The detectability of human skin must not depend on the *skin color*. Considering woodworking industries, a sensor is required to differentiate human skin from all types of wood. Both, skin and wood, show heavy variations as well as a high degree of similarity in the visual spectrum, thus making a reliable differentiation within the visual spectrum almost impossible.

Alternatively, physical properties which are independent of the human perception can be considered. The following section presents physical basics for skin detection beyond human perception.

2.2 Physical Basis

In 1955, J. A. Jacquez published one of the earliest scientific articles on the reflectance spectrum of human skin in the [near-infrared spectrum](#) [9]. Jacquez concluded his paper with the following sentence:

"Above $1.2\mu\text{(m)}$, the reflectance curves of the skin of differently pigmented persons are practically identical and show primarily the absorption spectrum of water."

His conclusion can be explained by the interaction of the incident radiation with water within the human tissue, which is possible due to the translucency of human skin. Fig. 2.1 shows the reflectance spectra of six differently pigmented persons, acquired at the back of the hand. The categorization of skin types, one (pale) to six (black), is done by a scheme which was introduced by Fitzpatrick [10]. Fig. 2.2 shows an

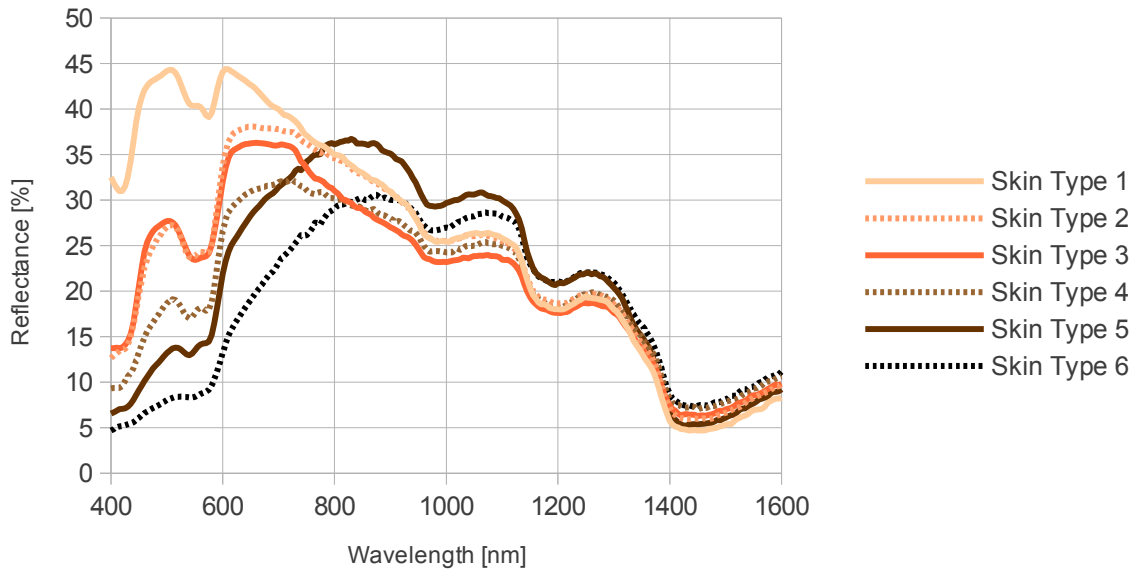


Figure 2.1: Reflectance of human skin with different pigmentation.

example for each of the six skin types. Obviously, the reflectance spectra within the visual spectrum depend strongly on the skin type, but all spectra come close to each other within the near infrared spectrum (see Fig. 2.1). In conclusion, the reflection properties of human skin within the near-infrared spectrum are a good basis for a skin detecting sensor system, as the properties are distinctive and do not depend on the skin color.

2.3 Machine Learning Methods

The presented sensor concept produces a vector of multispectral remission intensity values \vec{s} , which is denoted as *spectral signature*. These signatures form a vector space, whereby the dimensionality equals the number of available wavebands. Classifiers are needed to map a *spectral signature* to its material class. Plenty of machine learning methods are available to perform such classifications. In this work, the focus



Figure 2.2: Different skin types after Fitzpatrick [8].

is on [SVMs](#) because of their superior performance and decision trees for their simple evaluation. Both techniques are described in the following subsections.

2.3.1 Support Vector Machine (SVM)

[SVMs](#) are able to recognize patterns in n -dimensional data and can be used for classification and regression. The basic idea of using hyperplanes was introduced and denoted as *perceptron* by Rosenblatt in 1958 [11].

A (single-layer) perceptron requires a set of labeled vectors $(\vec{x}_1, y_1), \dots, (\vec{x}_m, y_m) \in X \times \{-1, 1\}$ for training, whereby X must be a dot product space, the label $y \in \{-1, 1\}$ defines the membership of each vector to one of the two classes and \vec{w} is an orthogonal

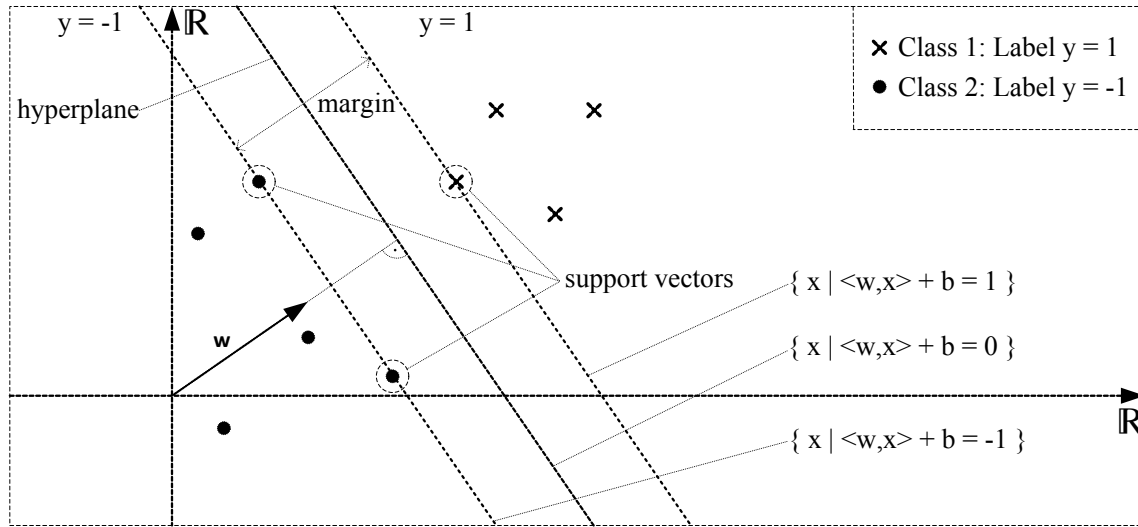


Figure 2.3: Linear separation of two classes by a hyperplane in a two-dimensional example [12, see Fig. 1.5].

vector to the hyperplane. Note that problems having more than two classes are called multi-class problems and require additional processing steps, e.g. subdivision into several two-class problems. To solve the classification problem, a hyperplane is fitted in the vector space to separate the members of the classes as depicted in Fig. 2.3. The hyperplane is positioned in a way that the margin to the nearest training vectors (which are denoted as *support vectors* for *SVMs*) is maximized. This is done to optimize the classification stability with respect to further class members, that are not available for training.

As depicted in Fig. 2.4, the training vectors are not always linearly separable by a hyperplane. During the 1970s, Vapnik and Chervonenkis enhanced the concept of perceptrons by a transformation of all vectors into a feature space \mathcal{H} of higher dimensionality, in which the separation task is linearly solvable (see [13, 12]). When back transforming into the original space, the hyperplane becomes a non-linear hypersurface.

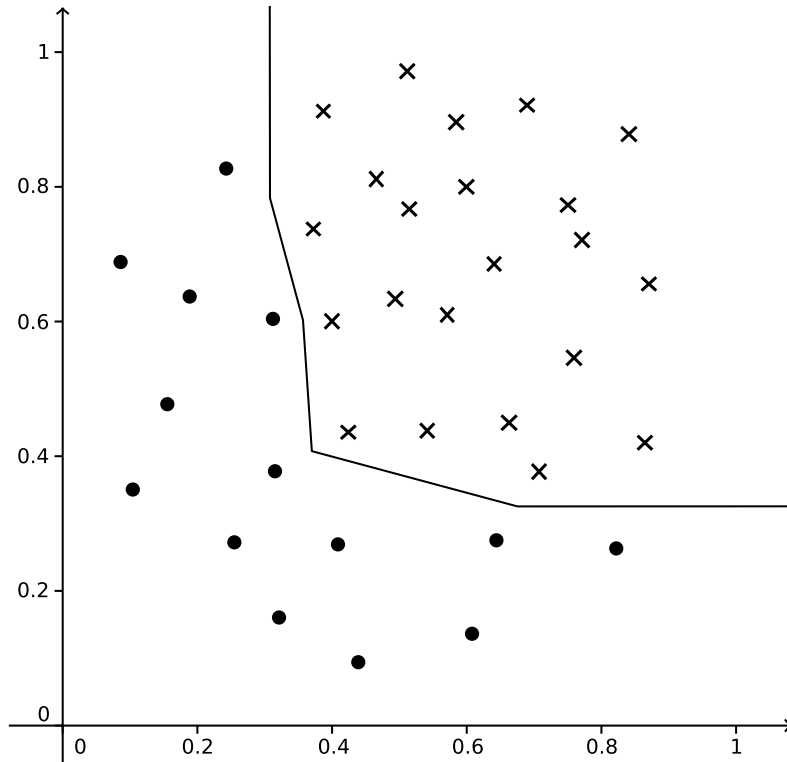


Figure 2.4: Example of a not linearly separable problem: separating dots from crosses.

However, the transformation in such a dot product space is considered to be too computationally expensive. Therefore, Vapnik and Chervonenkis used a kernel to perform an implicit transformation, which is more efficient to compute.

Mathematical Description

All possible hyperplanes in X are defined by Eq. 2.1.

$$\langle \vec{w}, \vec{x} \rangle + b = 0, \vec{w} \in X, \vec{x} \in X, b \in \mathbb{R}. \quad (2.1)$$

In this equation, $\vec{w} \in X$ is a vector orthogonal to the hyperplane and $b \in \mathbb{R}$ is a bias [12, S. 189]. A *decision function* $y_i = f(x_i) = \text{sgn}(\langle w, x_i \rangle + b)$ is required for the evaluation of a previously unseen vector \vec{x}_i . The decision function will determine the position of \vec{x}_i .

with respect to the hyperplane. As the hyperplane cuts X into two zones, the result of the decision function is either $y_i = -1$ or $y_i = 1$ to indicate the class membership of \vec{x}_i . To build a decision function with optimal margin, it is necessary to minimize the *objective function* $\tau(\vec{w}) = \frac{1}{2}\|\vec{w}\|^2$ so that the *inequality constraint* $y_i\langle\vec{x}_i, \vec{w}\rangle \geq 1 \forall i = 1, \dots, m$ is satisfied (see [12, chapter 7]). This is called the *constraint optimization problem*. To solve the problem, *Lagrange multipliers* $\alpha_i \geq 0$ are introduced. With the aid of the *Karush-Kuhn-Tucker* conditions, w is expressed as a linear combination of training vectors: $w = \sum_{i=1}^m \alpha_i y_i \vec{x}_i$, whereby all vectors having Lagrange multipliers $\alpha_i > 0$ are denoted as *support vectors*. Consequently, all vectors having $\alpha_i = 0$ have no influence on the hyperplane and are discarded from the final decision function to simplify the computation. To determine the Lagrange multipliers in practice, the so called *dual optimization problem*, in which the *primal variables* w and b are substituted, can be stated as:

$$\begin{aligned} \max_{\alpha \in \mathbb{R}^m} \quad & \sum_{i=1}^m \alpha_i - \frac{1}{2} \sum_{i=1}^m \alpha_i \alpha_j y_i y_j \langle \vec{x}_i, \vec{x}_j \rangle, \\ \text{subjected to} \quad & \alpha_i \geq 0 \quad \forall i = 1, \dots, m \text{ and } \sum_{i=1}^m \alpha_i y_i = 0 \end{aligned} \tag{2.2}$$

Thus, the decision function can be defined as:

$$f(\vec{x}) = \text{sgn}(\langle w, \vec{x} \rangle + b) = \text{sgn}\left(\sum_{i=1}^m \alpha_i y_i \langle \vec{x}, \vec{x}_i \rangle + b\right) \tag{2.3}$$

[12, S. 196ff]

As stated above, a hyperplane can only solve linearly separable problems. If a problem is non-linear, it might be mappable into a linearly separable problem by transforming the input space X into a feature space (or linearization space) \mathcal{H} of higher dimensionality. The transformation $\Phi : \vec{x}_i \in X \rightarrow \tilde{\mathbf{x}}_i \in \mathcal{H}$ is usually computational

expensive. Therefore, an implicit transformation is used to make the computation more efficient, which is occasionally referred to as the *kernel trick*. The kernel trick is an efficient transformation for all dot product based algorithms. A kernel function k can be used to substitute the transformation Φ and the vectors \vec{x}_i , if they are used in only one dot product:

$$\langle \Phi(\vec{x}), \Phi(\vec{x}_i) \rangle = k(\vec{x}, \vec{x}_i). \quad (2.4)$$

Using k , the transformation into the feature space as well as the computation of the dot product are done implicitly. Finally, a kernel based decision function can be constructed as:

$$f(\vec{x}) = \text{sgn} \left(\sum_{i=1}^m \alpha_i y_i k(\vec{x}, \vec{x}_i) + b \right). \quad (2.5)$$

[12, S. 200f]

However, the presented approach lacks an error compensation for faulty training data as every training vector might effect the resulting hyperplane. For instance, a high noise level might cause an overlap of classes, which may prevent the definition of a separating hyperplane. Hence, different advancements to suppress the influence of outliers were suggested. The C-SVM is a prominent derivative, which is used in this work and will be described in the following section.

C-SVM

The C-SVM is an error tolerant derivative of the original SVM. The C-SVM is often denoted as C-SVC for *support vector classification*. This is realized by the introduction of so-called *slack variables* $\xi_i \geq 0$ to the optimization constraints. Every violation of a constraint leads to an increment of ξ_i , so that ξ_i will be greater than zero. The sum of violations $\sum_{i=1}^m \xi_i$ is added to the optimization problem in order to prevent an exaggerated growth of ξ . Additionally, the sum is multiplied by a constant $C > 0$ to

reach a balance between the maximization of the margin and the minimization of the training error. The optimization problem of the C-SVM is formalized as:

$$\begin{aligned} \min_{\vec{w} \in X, \xi^m \in \mathbb{R}} \quad & \frac{1}{2} \|\vec{w}\|^2 + \frac{C}{m} \sum_{i=1}^m \xi_i, \\ \text{subject to} \quad & y_i (\langle \vec{x}_i, w \rangle) \geq 1 - \xi_i \\ & \text{and } \xi_i \geq 0 \quad \forall i = 1, \dots, m \end{aligned} \tag{2.6}$$

[14]

LIBSVM

LIBSVM is an open source programming library which implements a C-SVM as well as a number of kernels. In this work, LIBSVM was used for training and evaluation of SVM based classifiers. All supported kernels are listed in the following:

- Linear: $K(\vec{x}_i, \vec{x}_j) = \vec{x}_i^T \vec{x}_j$.
- Polynomial: $K(\vec{x}_i, \vec{x}_j) = (\gamma \vec{x}_i^T \vec{x}_j + r)^d, \gamma > 0$.
- Radial Basis Function (RBF): $K(\vec{x}_i, \vec{x}_j) = \exp(-\gamma \|\vec{x}_i - \vec{x}_j\|^2), \gamma > 0$.
- Sigmoid: $K(\vec{x}_i, \vec{x}_j) = \tanh(\gamma \vec{x}_i^T \vec{x}_j + r)$.

γ , r , and d are kernel parameters. Some parameters differ from common literature. These modifications were done for algorithmic optimization and do not effect the functionality [15].

2.3.2 Binary Decision Trees

Fig. 2.5 exemplifies a binary decision tree. Binary decision trees have the characteristic that every node yields a condition, which is either satisfied or not. Therefore, every

node has exactly two children. The children can be further nodes or leaves, whereby each leaf represents a target value or class. For the exemplified tree, the target values are the classes $c1$ and $c2$. Once a leaf is reached, the traversal of the tree is terminated and the target value of that leaf is accepted as output. As the traversal of binary decision trees always begins at the root node and terminates at a leaf without the possibility of back traversal, the worst case computation cost is $O(n)$, with n being the depth of the tree (which is $n = 3$ for Fig. 2.5). Binary decision trees can be computed on low power 8-Bit [microcontrollers](#) conveniently, as the operation performed for each node is only a comparison of two integer or floating point values.

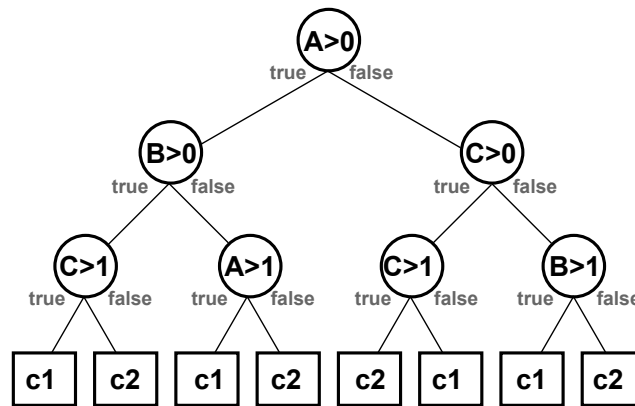


Figure 2.5: Example of a binary decision tree.

In contrast to the easy classification, the generation of an efficient binary decision tree is rather complicated. The widely accepted *C4.5* tree learning algorithm, which is based on the *ID3* algorithm, is used in this work [16].

The *C4.5* algorithm relies on a simple idea: It searches for the i -th attribute that discriminates most instances of the training set M with respect to their class membership y and stores a corresponding rule as a node, which is recursively repeated for each child node.

This is done by sorting all elements $(\vec{x}_1, y_1), \dots, (\vec{x}_{|M|}, y_{|M|})$ in a training set M by

their value $\vec{x}[i] \mid i \in [0, \dim(\vec{x}) - 1] \subset \mathbb{N}$ in ascending order. Once the elements are sorted, the C4.5 algorithm computes a mean $t_{i,n}$ between all neighboring values as $t_{i,n} = 0.5(\vec{x}_n[i] + \vec{x}_{n+1}[i]) \mid n \in [0, |M| - 2] \subset \mathbb{N}$ and splits the set M in two subsets $T_{i,n}$ and $F_{i,n}$ by using $t_{i,n}$ as a threshold, with $T_{i,n} = \{(\vec{x}, y) \in M \mid \vec{x}[i] > t_{i,n}\}$ and $F_{i,n} = \{(\vec{x}, y) \in M \mid \vec{x}[i] \leq t_{i,n}\}$. This threshold-split can be done very efficiently, as the set M is already sorted by the i -th attribute. These sets are then evaluated by computing the information gain of $T_{i,n}$ and $F_{i,n}$ compared to the original set M . The better the elements are separated with respect to their class membership y , the higher the information gain, which is calculated through the entropy of all classes in these subsets as introduced with the ID3 algorithm [17]. After the evaluation of all threshold-splits, the threshold $t_{i,v}$ that reduces the entropy the most is stored and therefore has the highest information gain for the i -th attribute.

Once this procedure is done for all available attributes $i \in [0, \dim(\vec{x}) - 1]$, attribute index ι with the highest information gain is chosen and the corresponding condition $\vec{x}[\iota] < t_{\iota,v}$ is stored in the root node.

This process is repeated recursively for both subsets $T_{\iota,v}$ as well as $F_{\iota,v}$ and new nodes are added, until the new resulting subsets only contain elements of the same class y . In that case, a leaf instead of a node will be created, storing class y as output. Furthermore, the C4.5 algorithm balances and prunes the resulting trees for performance optimization [17, 16]. However, these processes will not be explained here.

2.3.3 Common Evaluation Criteria for Classifiers

As exemplified in Tab. 2.1, the *confusion matrix*, which contains the true classes against the assigned classes, is used as a basis for the evaluation of a classifier's performance. Correct classifications of the target class and not-target class are called *true positive*

(*TP*) or *true negative (TN)*, respectively. A wrong assignment of the target class is a *false positive (FP)* or a *false negative (FN)* in the opposite case. In case of more than two classes, multiple confusion matrices are evaluated, whereby one class is the true class and all members of other classes are treated as one class of negative samples.

Table 2.1: Structure of a confusion matrix.

	actual positive	actual negative
predicted positive	<i>true positive</i>	<i>false positive</i>
predicted negative	<i>false negative</i>	<i>true negative</i>

Several evaluation measures can be derived from confusion matrices, as the *accuracy (ACC)*, *true positive rate (TPR)*, *false positive rate (FPR)* and the *precision (PREC)*. According to [18] these measure are defined as:

$$ACC = \frac{TP + TN}{TP + FP + TN + FN} \quad (2.7)$$

$$TPR = \frac{TP}{TP + FN} \quad (2.8)$$

$$FPR = \frac{FP}{FP + TN} \quad (2.9)$$

$$PREC = \frac{TP}{TP + FP} \quad (2.10)$$

One reason for using additional measures besides the accuracy is that it does not reflect a classifiers rate of misclassified positive or negative instances [19]. For instance, if 1 000 positive training samples would be available and classified correctly but only 50 negative training samples would be available and misclassified completely, the resulting accuracy would still be $\frac{1000}{1000+50} = 0.95$ while the *FPR* would become $\frac{50}{50} = 1.0$.

If not explicitly stated, all confusion matrices in this work contain median values of all individual confusion matrices from a 10-fold cross validation. Unless otherwise described, all 10-fold evaluations use 10 unique sets for training and testing, whereby

90% of all samples are used for training and 10% are used for testing within each fold.

2.4 Methods for Distance Measurement

The sensor concept involves a line of detectors (e.g. pixels or photodiodes) for the receiver, as depicted in Fig. 1.1 on page 2. A single detector would have to be unusually large to cover a wide measuring range, as the projection of the reflected radiation inside the receiver is shifted in relation to the measurement distance. This shift Δ of the projection can be used to estimate the measurement distance d by triangulation.

In prior work, two state-of-the-art time delay estimation methods were modified to be used for an estimation of the projection's peak position on the detector with subpixel resolution. Therefore, the methods were adapted from the temporal to the spatial domain. These methods, the [generalized cross-correlation \(GCC\)](#) and [average square difference function \(ASDF\)](#), are used as references in this work [20, 21]. In the next subsection, the notation used for these methods is described.

2.4.1 Mathematical Notation

In general, all estimations are marked by a hat, i.e. \hat{d} , \hat{p} and $\hat{\Delta}$, while the ground truth data is expressed without marks. The [GCC](#) and [ASDF](#) perform a comparison of a reference signal \mathbf{X}_{ref} and a previously unknown signal \mathbf{X}_{in} in the spatial domain.

In this work, all raw sensor readings from a multispectral sensor are represented as matrices $\mathbf{X} \in \mathbb{N}^{N \times B}$, where B is the amount of available spectral wavebands and N is the amount of available pixels on the detector line. Furthermore, elements of matrices or vectors are addressed by indices in square brackets (e.g. $\vec{s}[n]$ represents the n -th

element of vector \vec{s}). So, each component $\mathbf{X}[n][b], n \in [0, N - 1], b \in [0, B - 1]$ represents the strength of the incident illumination measured at pixel n during a strobe pulse emitted at waveband b . In the following section, b is always 0 to address the first column of the matrix, as the original methods do not make any use of multispectral information. Distance estimation is also discussed in a related journal article, in which a single vector \vec{x} is extracted from \mathbf{X} to discard the spectral information [4]. In this work, the spectral information is preserved to allow for corresponding extensions of the algorithms.

For distance estimation, a reference matrix \mathbf{X}_{ref} will be chosen from a set of previously obtained signals $R = \left\{ \mathbf{X}_{ref}^v \mid v \text{ holds the pixel peak index } \forall b \right\}$. In other words, each column within each $\mathbf{X}_{ref}^v \in R$ has the property that its subpixel peak position p_v equals v . As depicted in Fig. 2.6, the relation of \mathbf{X}_{ref}^v to \mathbf{X}_{in} can be expressed as $\mathbf{X}_{ref}^v[v][0] = \alpha \mathbf{X}_{in}[v + \Delta][0]$, whereby α is a scaling factor and Δ a (subpixel) signal shift.

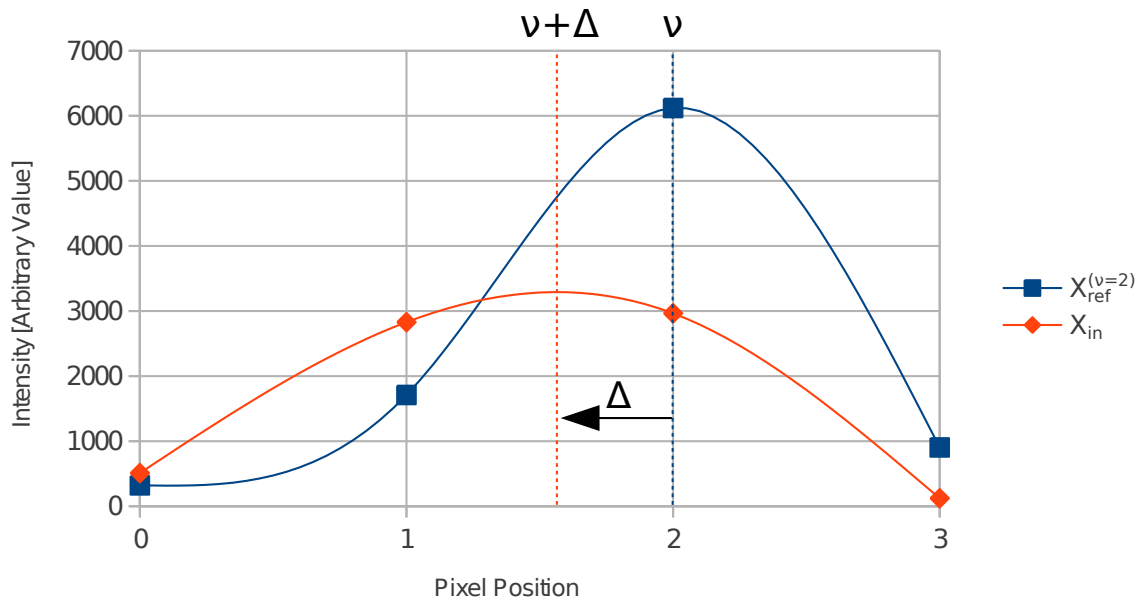


Figure 2.6: Examples for \mathbf{X}_{ref}^v (with $v = 2$) and \mathbf{X}_{in} , such that the subpixel peak position of \mathbf{X}_{in} can be approximated as $v + \Delta$.

To estimate the measurement distance of a previously unknown signal \mathbf{X}_{in} , ν must be chosen to match the index of the pixel with the maximum received energy. When expecting a Gauss-like energy distribution over the detector line, the corresponding $\mathbf{X}_{in}[\nu][0]$ will denote the pixel with the closest position to the signal's subpixel peak position p . Therefore, Δ has to be in $[\nu - 0.5, \nu + 0.5] \subset \mathbb{Q}$ instead of $[0, N - 1] \subset \mathbb{Q}$.

2.4.2 Peak Estimation

The subpixel shift $\hat{\Delta}$ can be estimated using the [GCC](#) or [ASDF](#). A discrete cross-correlation function $\tilde{R}[m]$ of \mathbf{X}_{ref}^v and \mathbf{X}_{in} is defined as:

$$\tilde{R}_{\text{GCC}}[m] = \frac{1}{N-m} \sum_{n=0}^{N-m-1} \mathbf{X}_{ref}^v[n][0] \mathbf{X}_{in}[n+m][0] \quad (2.11)$$

$$\tilde{R}_{\text{ASDF}}[m] = \frac{1}{N-m} \sum_{n=0}^{N-m-1} \left(\mathbf{X}_{ref}^v[n][0] - \mathbf{X}_{in}[n+m][0] \right)^2 \quad (2.12)$$

Whereby $m \in \mathbb{N}$ is the search window index over $M \in [3, N] \subset \mathbb{N}$ pixels. This leads to a parabola $f_{\tilde{R}}$ fitted through at least three points (e.g., $\tilde{R}[\nu - 1]$, $\tilde{R}[\nu]$, $\tilde{R}[\nu + 1]$) with vertex $(\hat{\Delta}, f_{\tilde{R}}(\hat{\Delta}))$, which provides $\hat{\Delta}$ as a shift of the peak position with respect to ν .

This definition is now expanded to allow a negative search window index $m \in [-0.5M, 0.5M]$, $m \in \mathbb{Z}$, so that the search window can be centered around ν and $\hat{\Delta}$ can therefore be negative.

To process a negative index m , an expanded index calculation using $n_-(m)$ (Eq. 2.15) and $n_+(m)$ (Eq. 2.16) was proposed by Kim et al. to introduce the [expanded generalized cross-correlation \(EGCC\)](#) (Eq. 2.13) and the [expanded average square difference function \(EASDF\)](#) (Eq. 2.14), analogously [20]. Now, the estimated peak position of \mathbf{X}_{in} is denoted as $\hat{p} = \nu + \hat{\Delta}$ [22, 23].

$$\tilde{R}_{\text{EGCC}}[m] = \frac{1}{N-|m|} \sum_{n=0}^{N-|m|-1} \mathbf{X}_{ref}^v[n_-(m)][0] \mathbf{X}_{in}[n_+(m)][0] \quad (2.13)$$

$$\tilde{R}_{\text{EASDF}}[m] = \frac{1}{N-|m|} \sum_{n=0}^{N-|m|-1} \left(\mathbf{X}_{ref}^v[n_-(m)][0] - \mathbf{X}_{in}[n_+(m)][0] \right)^2 \quad (2.14)$$

$$n_-(m) = n - \frac{m-|m|}{2} \quad (2.15)$$

$$n_+(m) = n + \frac{m+|m|}{2} \quad (2.16)$$

2.4.3 Distance Mapping

Finally, a mapping of the estimated subpixel peak position to an estimated distance $\hat{p} \rightarrow \hat{d}$ is required. This mapping is disregarded in the original work [20, 21], as a physical setup was used which shows a linear relation between \hat{p} and \hat{d} . In this work, the setup of the prototypical implementation presented in the following chapters has a parallel alignment of receiver and transmitter, resulting in a nonlinear relation of \hat{p} to \hat{d} . Furthermore, the spot projected onto a flat surface by the transmitter is round and the photodiodes are round too. When a round projection moves over a round photodiode, the signals describe a Gauss-like shape with respect to the measurement distance d (compare Fig. 6.6 on page 115). Another factor is the Gauss-like distribution of energy within the cross-section of the beam. In consequence, when the beam's reflection is projected onto the detector array, its spatial energy distribution will be captured within the sensor readings (compare reference signal $\mathbf{X}_{ref}^{v=2}$ in Fig. 2.6 on page 2.6).

As depicted in Fig. 2.7, a test set, recorded in the distance range from 100 mm to 600 mm, causes non-linear output values using the EGCC, where discontinuities occur whenever the reference index v is changed. In between these discontinuities, individual curves can be seen, where each curve has three points of inflection. These

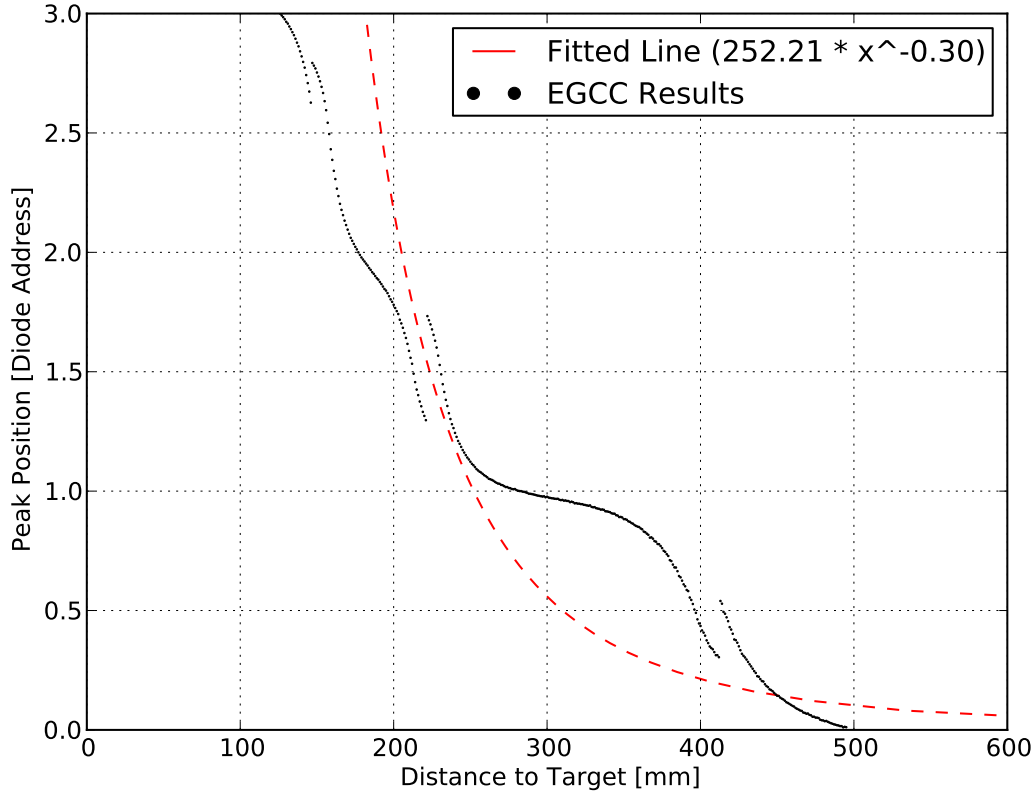


Figure 2.7: Power-function model on EGCC-results vs. true measurement distance (see [4]).

points of inflection are caused by the Gauss-like nature of the input values coming from each pixel as a function of d . However, the mapping $\hat{p} \rightarrow \hat{d}$ can be approximated coarsely by a simple function $\hat{d} = 252.21 \hat{p}^{-0.3}$. In this work, a more accurate mapping is found by an isotonic regression on tuples (\hat{p}, d) with distance classes \hat{d}_i , which results in the boundaries r_i and the maximum amount of boundaries ϱ as defined in Eq. 2.17 [24, 4]. However, this mapping is still ambiguous for the three discontinuities shown in Fig. 2.7, where some output values could be mapped to two different distances.

$$\hat{d}_{\text{step}}(\hat{p}) = \begin{cases} \hat{d}_0, & \text{if } 0 \leq \hat{p} < r_0 \\ \hat{d}_1, & \text{if } r_0 \leq \hat{p} < r_1 \\ \vdots & \\ \hat{d}_{\varrho-1}, & \text{if } r_{\varrho-1} \leq \hat{p} \leq r_{\varrho} \end{cases} \quad (2.17)$$

Chapter 3

Prior Work

In this chapter, prior and related work are summarized. Furthermore, alternative sensor concepts are discussed and compared. An overview and comparison of prior work on technical concepts for skin detection is given in Sec. 3.1, which is subdivided for imaging and non-imaging sensor concepts. Furthermore, prior work on beamforming with LEDs is discussed. In Sec. 3.2, prior publications and patents with respect to the presented sensor concept are summarized.

3.1 Comparison of Technical Concepts

A number of different technical solutions in the field of human skin detection have been investigated, which make use of the [near-infrared domain](#). In this section, a summary of this work is presented. First, the imaging systems are separated from the non-imaging systems by the two following sections. In the last section, several approaches on beamforming with LEDs are described.

3.1.1 Imaging Systems for Skin Detection

All systems presented here comprise an active illumination and a comparable spectral resolution of two to four wavebands. Generally, the objective for the presented development is to use such small sets of wavebands, whereby the individual wavebands can be relatively broad. This has the advantage that the receivable energy within a waveband increases with its width or, respectively, with its coverage of the present illumination source. Furthermore, minimizing the number of wavebands is desirable, as it helps to reduce the hardware complexity and to increase the measurement frequency, which are also important objectives for this work. Therefore, setups that aim for maximum spectral resolution, such as hyperspectral imaging systems, are not taken into account for this comparison.

Pavlidis et al. [25]

Pavlidis et al. presented a system comprising two cameras equipped with different band-pass filters, leading to a lower waveband in the range from 1 100 nm to 1 400 nm and an upper waveband in the range from 1 400 nm to 1 700 nm. A broadband illumination source is used covering the whole relevant spectrum from 1 000 nm to 2 000 nm. As the reflectance of human skin is much stronger in the lower band, every area that is much brighter in the lower waveband than in the upper one is likely to be human skin. This system was developed for automatic detection and counting of vehicle passengers at so called *HOV lanes*, which are reserved for car-pools in Minneapolis and elsewhere [25]. Further optimization, such as the fusion of the field of view of both cameras using a setup of beamsplitters and the use of advanced algorithms for classification, were described in a series of consecutive publications [26]. This approach is designed well with respect to the targeted applications, as the energy within

two broad wavebands is integrated for a fast measurement. However, integrating the spectrum over only two comparably broad wavebands eliminates much details of the spectrum.

In consequence, materials with similar reflectance spectra might not be differentiable by using only this information. To clarify the limits of this concept with respect to the requirements formulated in this thesis, an analysis of twelve samples from wood (each having a humidity of $\geq 20\%$) and twelve samples from human hands was carried out. All samples were randomly selected from the database which resulted from the preliminary study presented in Chap. 4. For each sample, a ratio R of the energy between both wavebands was calculated as defined in equation 3.1, whereby $I(\lambda)$ is the intensity of the reflectance at wavelength λ .

$$R = \frac{E_{upper}}{E_{lower}}, \text{ where } E_{upper} = \int_{1.4 \mu\text{m}}^{1.7 \mu\text{m}} I(\lambda) d\lambda \text{ and } E_{lower} = \int_{1.1 \mu\text{m}}^{1.4 \mu\text{m}} I(\lambda) d\lambda \quad (3.1)$$

For the wood samples, the calculated ratios were in the range of $0.33 \leq R_{wood} \leq 0.73$, which comprises the entire range of ratios calculated for the skin samples with $0.40 \leq R_{skin} \leq 0.51$. Furthermore, three of the twelve wood samples are within the same range as the skin samples. This proves that the selected wood and skin samples cannot be differentiated using ratio R alone. The system's accuracy can be further lowered by the unknown spectrum¹ of the daylight, which is used to perform measurements.

Iwasaki et al. [27]

Another approach was published by Iwasaki et al., where two bandpass filters on a filter wheel are used to filter the incident light for an InGaAs camera. The first filter has its transmission peak at 1060 nm and the second at 1450 nm, whereby each filter

¹The daylight spectrum depends on the solar azimuth angle and weather conditions.

has a full-width at half-maximum (FWHM) of 30 nm. Two halogen lamps were used to supply a broadband illumination. A test subject's head was fixed at a well defined position for measurement, as the setup was meant to measure the ability of facial skin to retain moisture.

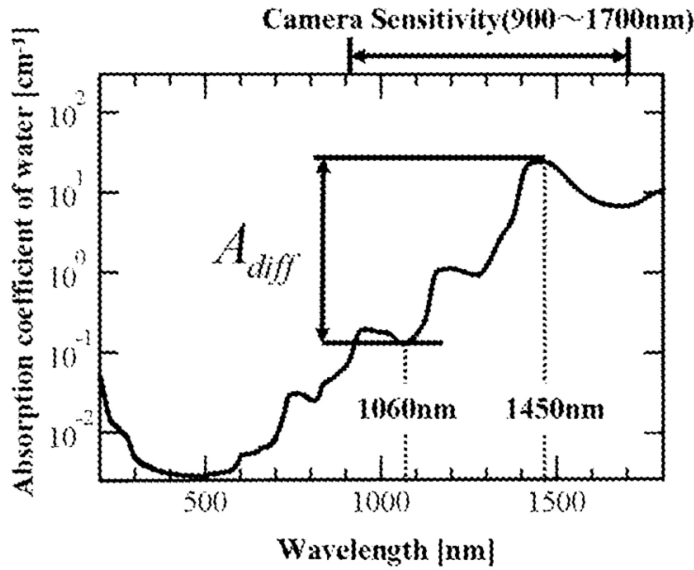


Figure 3.1: Absorption coefficient of water in the visual and near-infrared spectrum (Source: [27, Fig. 4]).

This ability was processed as a ratio of absorption rates $A_{diff} = \log_{10} \frac{I_{1060nm}}{I_{1450nm}}$ with I_{1060nm} and I_{1450nm} being intensity values measured using the corresponding filters [27]. A_{diff} is a good indicator for moisture, as the filters are chosen with respect to the absorption coefficients of water (see Fig. 3.1). It takes about 5 s for the system to perform a measurement. This is comparably slow, as only two images at the lower and upper waveband are taken [27, Sec. 2.1.]. However, the speed of acquisition is by far not as important for Iwasaki's application as it is for safety applications or counting passengers in moving cars. Using only two wavebands the presented system's capability of differentiating materials is limited, but the design generally allows the use of filter wheels with more than two filters. In conclusion, the concept

presented by Iwasaki et al. offers a variable system for multispectral imaging at rather slow acquisition speed.

Steiner et al. [28]

A derivative of the sensor concept presented in this dissertation is a setup featuring a camera with an InGaAs image sensor and a synchronized illumination unit. Hereby, the illumination unit has multiple LEDs of four distinct wavebands. Similar to the non-imaging sensors, the illumination unit transmits a sequence of strobe pulses at all available wavebands, whereby the camera grabs frames synchronously to every strobe pulse. During each sequence of multispectral strobe pulses, one frame is taken without active illumination to acquire ambient illumination on its own. This frame can then be subtracted from the frames acquired with additional, active illumination [28]. In consequence, the time for a complete acquisition is limited by $a = \frac{1}{fps_{max}}(N + 1)$, whereby fps_{max} denotes the maximum number of frames per second by the camera and N the number of wavebands. For a configuration featuring a camera with $fps_{max} = 30$ and three wavebands, a complete acquisition takes 133 ms. In conclusion, the approach by Steiner et al. offers a superior spatial resolution at a lower acquisition speed, when compared to the sensor concept presented in this work.

3.1.2 Non-Imaging Systems for Skin Detection

This section describes prior work non-imaging sensor technologies. Note that the sensor concept presented in this work also belongs to the non-imaging sensor systems for skin detection.

HacsKaylo [29]

A simple setup comprising an incandescent light, being a broadband near infrared illumination source, and three band-filters for individual detectors (1110 nm to 1330 nm, 1440 nm to 1560 nm and 1660 nm to 1780 nm) is described in a patent by HacsKaylo [29]. The system should measure signal levels which meet certain thresholds, if human skin is present. While it is not addressed in the original patent, it is necessary that the measurement is taken at a certain distance and angle to produce comparable signal levels, as the classification is performed using thresholds for the amplitude value of each waveband. These signal thresholds are given by the patent specification and yield a tolerance from $\pm 11\%$ to $\pm 20\%$, which is already in the magnitude of the variance found in human skin (see Chap. 4.3). Therefore, the system described by HacsKaylo is not suited for contact-free operation, as ambient light and signal attenuation by varying measurement distance are not compensated. However, HacsKaylo's concept could be improved by developing dedicated beamforming and an optimization of the methods used for data processing.

Determan and Wunderlin [30]

A similar setup is described in a patent by Determan and Wunderlin, which was filed 25 years after HacsKaylo's patent application. One difference to HacsKaylo's patent is that Determan and Wunderlin claim two different approaches at once:

- A broadband illumination source and two relatively wide bandpass filters for individual detectors at 800 nm to 1400 nm and 1400 nm to 2200 nm.
- Two broadband illumination sources with the same two bandpass filters and one broadband detector.

The setup is described in the context of a biometrical sensor system. Determan and Wunderlin do not take ambient light or varying measurement distances into account [30]. The wavebands proposed by Determan and Wunderlin are very similar to those used by Pavlidis et al. and share the disadvantage of a very low spectral resolution.

3.1.3 Summary of Prior Work on Skin Detection

The prior work offers a range of technical approaches for the task of human skin detection using near-infrared radiation. A unique feature of the presented work within the non-imaging sensor systems is the ability to compensate for ambient light and varying measurement distances.

Furthermore, it is one of only two approaches using LEDs for illumination. In most approaches, an incandescent lamp is used as illumination source. The filament of such lamps is usually heated up to about 3000 K for operation. Therefore, such lamps are not suited to generate short strobe pulses of ≤ 1 ms, as the heating and cooling of the filament usually takes too much time. Without the use of fast shutters, no sequence of strobe pulses can be generated within the range from 10 μ s to 1000 μ s by switching an incandescent lamp, as it is required for the presented sensor concept.

The concepts presented by Pavlidis et al., Iwasaki et al. as well as Determan and Wunderlin feature only two wavebands. Those two wavebands are always chosen with respect to the absorption characteristics of water. Generally, it depends on the desired application if the evaluation of only two wavebands is sufficient. For instance, a small number of misclassified pixels can be ignored by imaging systems for most applications, but a single misclassified spot can easily cause a false reaction of a non-imaging system, as such systems depend on only one or a few points of measurement. Increasing the spectral resolution theoretically strengthens the data

basis for a material classification and therefore reduces the risk of false alarms and dangerous failures on demand.

3.1.4 Beamforming with Light Emitting Diodes

As discussed in Sec. 5.1.8, forming a collimated and homogeneous multispectral beam using several LEDs is an important topic within this work. In this section, a selection of relevant prior work is presented as follows:

Simultaneous Multiple Surface

Researchers at *Light Prescriptions Innovators (LPI), LLC* published a number of articles on designs involving their patented *simultaneous multiple surface* design method for nonimaging optics. For instance, a free-form lens to combine the light of three high-luminance white LEDs was presented and is depicted in Fig. 3.2 [31].

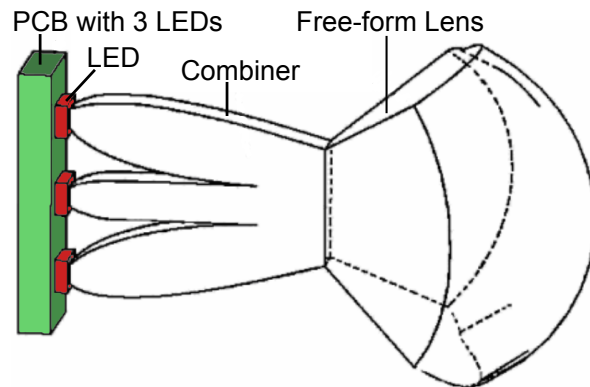


Figure 3.2: Free-form lens to combine three LEDs. Original source: [31, Fig. 3].

The authors emphasize that this nonimaging design is largely independent of illuminance variations across the LED surfaces as well as LED placing errors of up to ± 0.2 mm. Therefore, this technique improves beam homogeneity and reproducibility.

This free-form lens was meant to be used with a curved mirror to form the desired beam pattern for an automotive headlamp. According to information by Rubén Mohedano, the managing director of LPI, the simultaneous multiple surface design tool could probably be used to develop a beamforming optic which meets the requirements for this work without the use of additional mirrors. Unfortunately, the molding of such free-form lenses requires the preparation of special tools, which were beyond the budget of this work.

Sun et al. [32]

Prior work by Sun et al. is on combining the light from red, green and blue LEDs to a homogeneously illuminated beam [32]. They used a commercial surface mounted device (SMD) component comprising a red, green and blue LED underneath a common lens which was coupled into a light guide. The open end of the light guide was connected to a diffuser which was coupled to a projection lens. Note that using a light guide for homogeneous mixing was also described in prior work related to this dissertation [6].

However, the setups presented in their article formed beams with an opening angle from 22° to 84° . From the work of Sun et al., it can be concluded that a narrow opening angle and homogeneous color mixing are contrary design goals [32]. This is not surprising as most color mixers are spreading the light beam, but it clarifies how demanding the requirements for this application are, as the multispectral beam's opening angle should be as narrow as possible.

Wang et al. [33]

Another design method for nonimaging optics to form a highly collimated beam from an LED source was presented by Wang et al. [33]. Wang et al. designed a

free-form lens using their own method as depicted in Fig. 3.3. The outside of the lens acts as a parabolic mirror by internal reflection, while the inner surfaces act as transmissive beamforming structures. Their design method approximates the LED chip to be a point light source, thus simulations of the presented lens used with a LED chip having a footprint of 1 mm^2 resulted in an opening angle of 4° . However, it is expensive and complicated to manufacture such lenses. Therefore, this approach could not be adopted for this work, as the prototypical implementation of the sensor concept must be constructed of practically available parts.

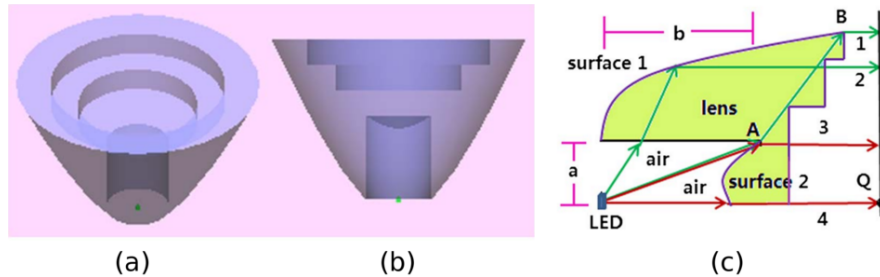


Figure 3.3: Illustration of a free-form lens. The lens is depicted in an isometric view (a), a right view (b) as well as a sectional drawing for half a lens including exemplified ray paths (c). Source: [33, Fig. 2+3].

Chen et al. [34]

An alternative method for the design of highly collimating, nonimaging optics for LEDs was published by Chen et al. [34]. Overall, the results of this work are pretty comparable to those presented by Wang et al.

The most prominent difference in the resulting shape is that the light exit side is formed as a smooth curve instead of several flat segments, as seen in Fig. 3.3. Unlike Wang et al., Chen et al. actually built a prototype of the lens depicted in Fig. 3.4, which proved to have an optical efficiency of 90.3% and an opening angle of 4.75° .

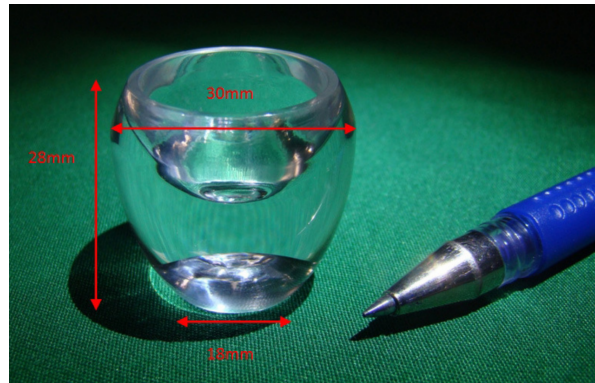


Figure 3.4: The prototype of the collimator lens by Chen et al.. Source: [34, Fig. 11].

If this technique would be used for this work, the design priorities would shift from optical efficiency towards an even narrower opening angle.

Using such advanced methods to design optimized beamformings for near-infrared LEDs is promising, but could not be done in the scope of this work. In contrast to this potential future work, the next section summarizes the prior work within the context of this work.

3.2 Summary of Prior Work to the Sensor Concept

Initially, the search for a technical solution for the problem described in Sec. 2.1 motivated a cooperation of the Institute for Occupational Safety and Health of the German Social Accident Insurance (IFA) and the Bonn-Rhein-Sieg University of Applied Sciences (BRSU). Within this cooperation, a number of approaches have been investigated, including the use of passive infrared sensors, electrical field sensors and computer vision systems. A summary of this work is described by Reinert et al. [35]. The first work on a multispectral, LED based sensor was a master thesis in 2006 [36], which led to a patent subscription [37]. While the patent was pending the research continued and formed the basis of this dissertation. Three sensors were

implemented before the prototypical sensor implementation presented in this work, which is denoted as *Skinner*. None of the previous sensors implemented the final sensor concept as described in this work. However, two articles were published in the context of this dissertation that describe and evaluate the optical design and data processing methods which are proposed to implement the final sensor concept [4, 5]. The particular contributions of these articles are the discussion of partial overlaps of the sensor's beam and arbitrary objects as a source for artifacts, the possibility of reducing the beam diameter using field stops, measures to optimize the homogeneity of the beam, the introduction of a new method for distance estimation as well as a method to isolate the spectral information from all sensor readings and a first performance evaluation of the material classification. This dissertation describes the results of both publications and presents updated and enhanced content as well as new experiments and comprehensive results. Furthermore, this work issues the applicability of international standards and proposes recommendations to enhance their content if required.

In parallel, new research fields were derived, such as a multispectral sensor for push buttons to verify the proper hand clothing before starting a machine in the context of hygiene or safety, a liveness sensor for a biometric fingerprint scanner and a multispectral camera system (see [38, 39, 28]).

This chapter summarized relevant prior and related work. In the following chapter, the reflectance spectra of several hundred people and different workpieces, which were acquired within a preliminary study, are analyzed and compared. The objective is to derive a *spectral signature* to differentiate human skin from surface materials of typical workpieces.

Chapter 4

Preliminary Study

As a preliminary study within a research project called *LBIS*¹, the visual and near-infrared reflectance spectra of the thumb, palm and back of the hand were examined on a total of 330 persons. To best of my knowledge, no comparable data is available from prior work. The data presented in this chapter were gathered to select appropriate wavebands for a multispectral sensor with respect to the application of human skin detection at manually fed machines.

4.1 Metrology

A hand-held spectrometer of the type *spectrocam* by Avantes BV was used for measurements within the *visual spectrum*. Measurements within the near-infrared spectrum were performed using an *irSys*[®]1.7 spectrometer, which was equipped with a module to block out ambient light and an internal tungsten lamp for well defined illumination through a measurement port. This measurement port is intended to perform reflectance spectroscopy and must be directly in contact with a surface of interest.

¹See glossary for project description.

For calibration of the *irSys*[®]1.7 spectrometer, a reference target of sandblasted gold with a known spectrum of reflection (REF_G) was used. The gold target was used to occlude the measurement port of the module for reflectance measurement to perform a reference measurement (REF_M). Additionally, internal stray light was measured with the measurement port being open ($STRAY_M$). Each measurement of a new subject ($SAMPLE_M$) was then corrected with the following equation to obtain a calibrated output ($SAMPLE_C$):

$$SAMPLE_{C,\lambda} = \frac{REF_{G,\lambda}}{REF_{M,\lambda} - STRAY_{M,\lambda}} (SAMPLE_{M,\lambda} - STRAY_{M,\lambda}) \mid \lambda \in \{660\text{nm}, \dots, 1730\text{nm}\}$$

The system's dark current is automatically canceled out, as it occurs in REF_M , $SAMPLE_M$ and $STRAY_M$, where $STRAY_M$ is subtracted from REF_M and $SAMPLE_M$.

4.2 Data Composition

For a systematic categorization of skin types, we use a scale of six skin types as introduced by Fitzpatrick, going from pale white (type one) to black (type six) [10].

Tab. 4.1 shows the distribution of skin types over the subjects that participated in

Table 4.1: Distribution of skin types.

Skin Type	1	2	3	4	5	6
Count	3	37	255	27	2	6

Table 4.2: Distribution of age.

Age	<18	18-25	26-33	34-41	42-49	50-57	58-65	>65
Count	6	142	82	22	41	21	11	5

the campaign. The distribution of age is shown in Tab. 4.2. A total of 67 females and

263 males participated in the study. According to the typical population composition at the locations of the study, the Bonn-Rhein-Sieg University of Applied Sciences and the Hannover Messe, the data is focused on central European males aged 18 to 33. However, all age classes and skin types are represented in the data base. The participants at the Hannover Messe included carpenters and construction workers with calluses and very thick cornea at their hands.

4.3 Data Analysis

The results of the analysis reconfirmed certain correlations of the reflectance spectra and the persons age, as described in prior work [40]. Within the spectrum from 700 nm to 1300 nm, the skin of the subject group aged ≤ 30 years reflects about 10% more radiation than that of the subjects aged ≥ 50 years. Naturally, the skin type is correlated to the reflectance as well. It is primarily given by the concentration of melanin. However, the absorption coefficient of melanin is about $\alpha = 19 \text{ mm}^{-1}$ at $\lambda = 700 \text{ nm}$ and decreases to $\alpha = 5 \text{ mm}^{-1}$ at $\lambda = 1000 \text{ nm}$ [41]. As the back of the hand is a densely pigmented region, there is a strong attenuation in correlation with the skin type at $\lambda = 700 \text{ nm}$, which is rapidly decreasing towards about $\lambda \approx 1000 \text{ nm}$. For $\lambda \geq 1200 \text{ nm}$, no significant correlation of skin type and reflectance was found, which reconfirms Jacquez's conclusion quoted in section 2.2.

In summary, although the amplitude over all acquired spectra varies about factor two from the darkest to the brightest skin sample, there are very similar local minima and maxima on all slopes in the spectral range from about 970 nm to 1730 nm, whereby 1730 nm is the upper limit of the used near-infrared spectrometer.

Considering the highly variable concentration of melanin within human skin, it is a logical conclusion to prefer the near-infrared spectrum over the visual spectrum.

Within the *near-infrared spectrum*, the absorption is dominated by the water within the tissue. The amount of water within the human skin varies with a persons age and other parameters [40]. Furthermore, the thickness of the cornea (also known as horn skin) varies and thickens at spots where the hand is often exposed to mechanical strain. Therefore, the individual variations of the reflectance spectra within the *near-infrared spectrum* need to be taken into account when choosing a set of wavebands that is well suited for skin detection. On the other hand, the selected wavebands must contain features that can be used to differentiate human skin from surface materials of typical workpieces, such as wood and plastic.

To identify a set of well-suited wavebands within the *near-infrared spectrum*, a data mining software called *AnaSpec* was developed to analyze the acquired data base. *AnaSpec* features a brute force search to find the best composition of wavelengths to differentiate two classes of samples. A brute force search evaluates $\binom{C}{B}$ sets of wavebands, where $B \subset \mathbb{N}$ is the desired number of wavebands within the resulting set and $C \subset \mathbb{N}$ is the number of wavebands considered as candidates. For instance, if a set of $C = 33$ waveband candidates $\{800\text{nm}, 825\text{nm}, 850\text{nm}, \dots, 1575\text{nm}, 1600\text{nm}\}$ is used and the targeted number of wavebands is chosen to be $B = 4$, the brute force search will evaluate $\binom{33}{4} = 40920$ sets of wavebands. For each set, a vector \vec{r} of $\binom{B}{2}$ different ratios from amplitude pairs $\hat{\lambda}_i/\hat{\lambda}_j \mid i, j \in [0, B-1] \wedge i < j$ is computed for all selected samples within the data base. The motivation to use only the ratios is to be independent of absolute amplitude values, which are altered with the angle and distance of measurement. However, the ratio of energy between different wavebands can be expected to be mostly independent of measurement angle and distance (see 4.4.1).

In the next step, the algorithm computes minimum and maximum thresholds for each ratio to enclose all members of a target set, which defines a subset of samples

within all selected samples from the database. Afterward, all selected samples are tested against all minimum and maximum thresholds. No members of the target class will be falsely classified (FN), as these thresholds were chosen to enclose the whole subset. However, samples from other material classes, which are not included in the target set, may falsely be classified as a member of the target set, if they satisfy all thresholds. Generally, the better a set of wavebands is chosen, the fewer samples will be misclassified from the resulting ratios. This ratio-based classification is a very simple, but fast approach to evaluate the suitability of a combination of wavelengths.

It is possible that several combinations of wavelengths can be used to achieve a perfect separation of a target set from all other selected samples. In that case, additional metrics can be applied to compare the ratios of all true negative and true positive samples.

Furthermore, the relative reflectance at a certain wavelength is transformed for each sample to simulate the spectral response when using a particular LED. This transformation is implemented as a convolution of a sample's reflectance spectrum with an LED's emission spectrum. For this purpose, a data base of seventeen reference LEDs was build to cover typical emission spectra for LEDs with peak-wavelengths between 360 nm and 1550 nm. If the peak-wavelength $\hat{\lambda}_c$ of a considered LED is not included in the reference data base, the emission spectrum of the reference LED with the closest peak-wavelength $\hat{\lambda}_{ref}$ is shifted by $\hat{\lambda}_c - \hat{\lambda}_{ref}$. Therefore, LEDs with arbitrary peak-wavelengths between 360 nm and 1550 nm can be simulated.

A combination of $B = 4$ wavelengths was targeted for the brute force search, as a maximum of four wavelengths is desirable with respect to the design of the multispectral source: The time required for a multispectral measurement increases with the number of acquired wavebands, as the strobe pulses are sequentially emitted. Furthermore, a number of four LED chips allows a comparably compact and sym-

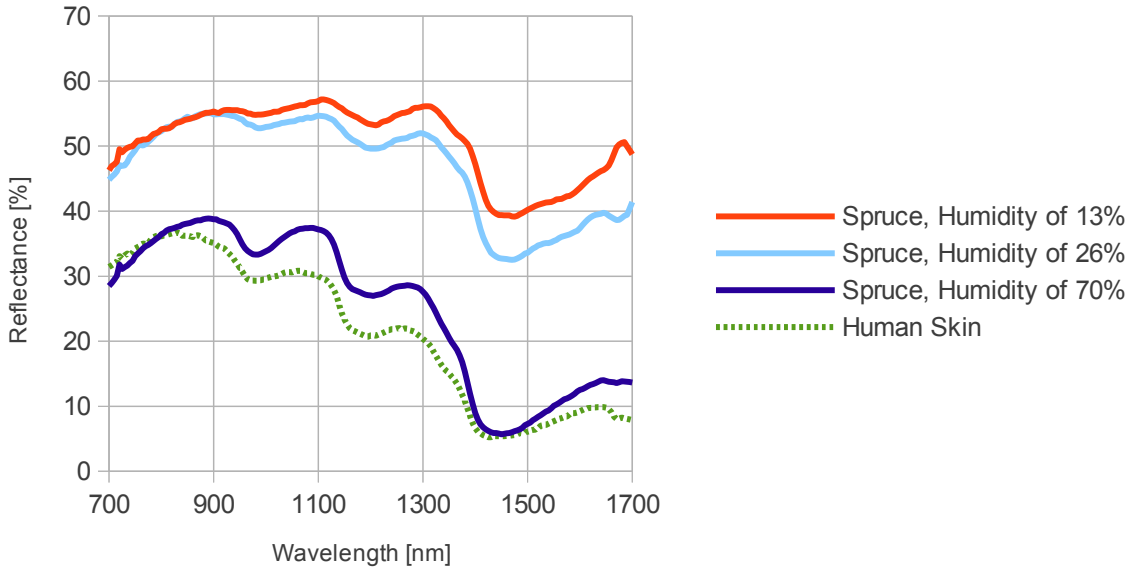


Figure 4.1: Reflectance of human skin and spruce wood at different humidity levels.

metrical arrangement within the transmitter, which helps to form a homogeneous beam (see Chap. 5.2.1). Last but not least, the costs for such a sensor system depend on the number and type of the required LEDs.

For the targeted application of manually fed machines for wood processing, a training set was created from all available skin measurements and about 330 wood samples, which include samples having a plastic laminated finish. Furthermore, at least 12 wood samples yielded a moisture of $\geq 30\%$. As shown in Fig. 4.1, the near-infrared reflectance spectra of wood are changing towards the characteristics of human skin, when increasing the humidity. However, the results of the brute force search on the training set yields that a set of four peak-wavelengths is sufficient, as the resulting threshold-based filters are able to classify 99.9% of all skin and wood samples correctly. Furthermore, a perfect separation could be achieved using an SVM. The best peak-wavelengths with respect to commercially available LEDs are

$\hat{\lambda}_0 = 830\text{nm}$, $\hat{\lambda}_1 = 1060\text{nm}$, $\hat{\lambda}_2 = 1300\text{nm}$ and $\hat{\lambda}_3 = 1550\text{nm}$. Fig. 4.2 shows the two most prominent components derived from a PCA of measurements from wood and skin samples at these four wavelengths. This two-dimensional representation already indicates a good separability of both classes.

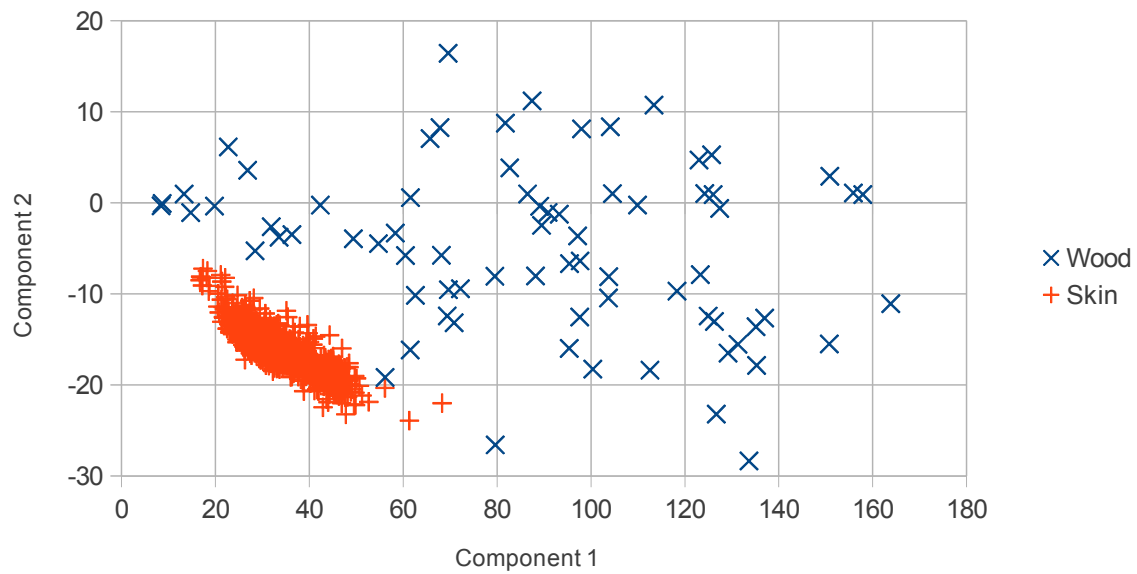


Figure 4.2: Principle Component Analysis (PCA) of skin and wood samples.

4.4 Data Mapping and Additional Experiments

To prove the validity of the concept, it is necessary to show that the data acquired from the preliminary study are mappable to the data acquired with an actual sensor system. Fig. 4.3 depicts reflection spectra of a set of samples, which have been acquired during the preliminary study. Each spectrum is normalized to a maximum of 1. For comparison, the same samples have been scanned using a Skinner mark 1 sensor system, which is described in detail in section 5.4, at a measurement distance of 200 mm. The output values for each waveband have been normalized as well.

Furthermore, the sensor readings corresponding to the wavebands $\hat{\lambda}_1$, $\hat{\lambda}_2$ and $\hat{\lambda}_3$ are scaled by factors to improve the alignment with the measured spectra. To compute these factors, an individual correction factor is calculated per sample and waveband as $f_{\hat{\lambda}} = I_{\hat{\lambda}}^{irSys} / I_{\hat{\lambda}}^{Skinner}$, with $I_{\hat{\lambda}}$ being the intensity measured at a waveband $\hat{\lambda}$ with the Skinner sensor or the *irSys*^{®1.7} spectrometer. In a following step, a median factor $f_{\hat{\lambda}}$ is computed per waveband over the individual factors of all samples. Namely, these factors are $f_{1060nm} = 1.15$, $f_{1300nm} = 1.29$ and $f_{1550nm} = 1.19$. After applying these common factors, the mapping of the sensor readings is accurate to an average mapping error of 0.028 for all depicted samples.

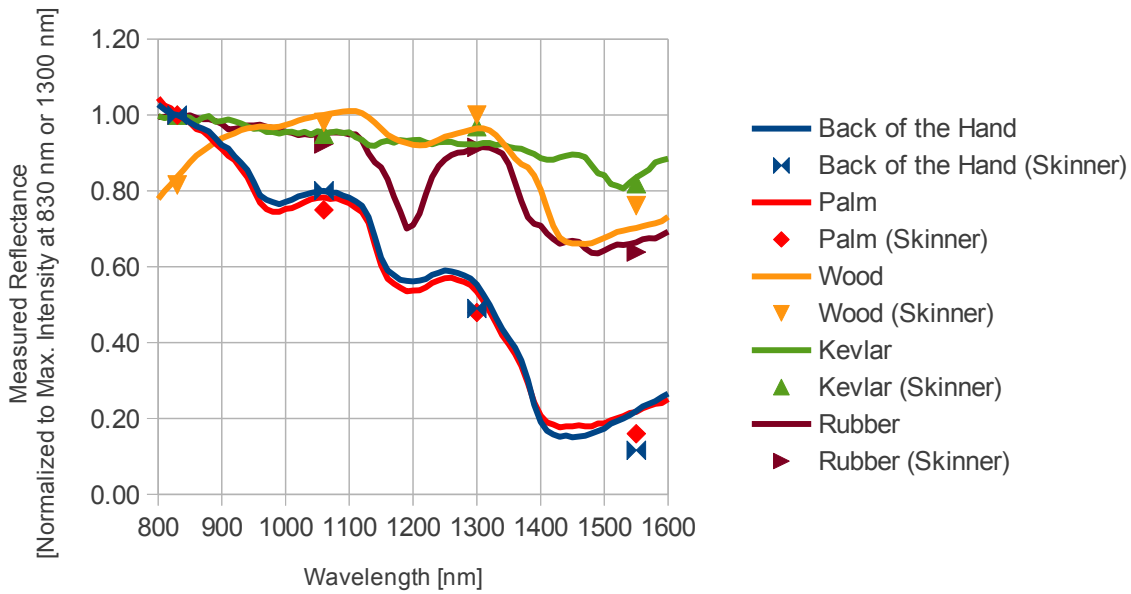


Figure 4.3: Mapping of reflectance measurements acquired using the *irSys*^{®1.7} spectrometer to measurements of the Skinner mark 1 sensor system.

The remaining mapping error is smaller than the magnitude of typical variances for these materials within the data base. Thus, there are basic differences in the used measurement methods, which are discussed in the following sections. Obviously, the spectral resolution of the spectrometer is significantly higher. The used LEDs

have a **FWHM** of 35 nm to 130 nm and a peak-stability of 20 nm to 40 nm. As a consequence, the sensor readings for each waveband represent the integral over a comparably wide and volatile spectrum. However, the bandwidth of an **LED** can be reduced using optical filters and the peak-wavelength can be stabilized by controlling the chip's temperature (see Sec. 5.2.2).

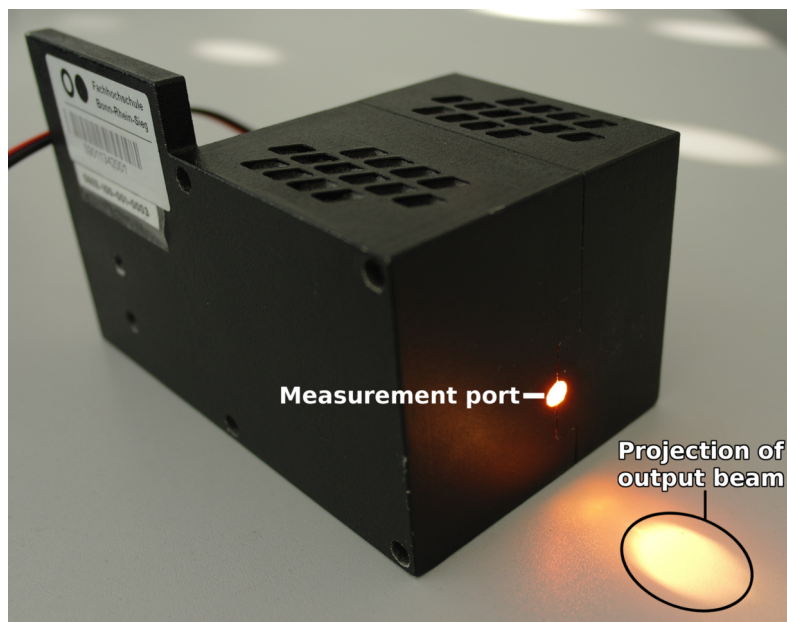


Figure 4.4: Reflectance measurement module for *irSys*[®]1.7.

Another factor is the measuring setup itself. As depicted in Fig. 4.4, the module for reflectance measurement, which is mounted to the spectrometer, illuminates a spot with a diameter of $\varnothing_i \approx 5 \text{ mm}$ at an incidence angle of $\delta_i \approx 40^\circ$. On the other hand, the actual sensor system illuminates the target surface at an incidence angle of $\delta_s = 12^\circ$ at the minimal measurement distance of $d = 100 \text{ mm}$, which decreases with an increasing measurement distance. Furthermore, the illuminated spot is not as sharply restricted as the measurement port of the spectrometer's module.

The influence of those differences in metrology was evaluated as described below.

4.4.1 Multi-angle Reflectance Spectroscopy

As part of a bachelor thesis, a measuring setup for multi-angle reflectance spectroscopy was created [42]. This setup features two stepper motor driven angular positioning arms and a measurement platform. The setup was used to measure human skin and other material samples at various incidence and observation angles. Theoretically, the setup can be used to acquire accurate *Bi-directional Spectral Reflectance Distribution Function (BSRDF)* models. All measurements in the *near-infrared spectrum* were carried out using a fiber-coupled tungsten lamp for illumination and a fiber-coupled collecting optic for the receiving side. The receiving fiber was connected to the same *irSys®1.7* spectrometer that was used for the preliminary study. Both optics were mounted at a distance of $d \approx 100$ mm above the samples. The diameter of the illuminated spot on the measured object was about $\varnothing_i \approx 40$ mm.

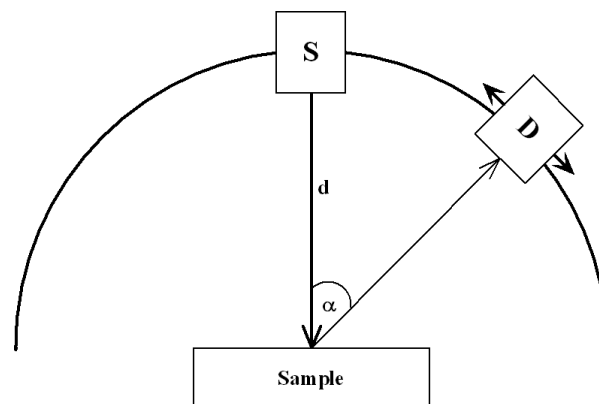


Figure 4.5: Measurement setup for scattering measurement comprising light source S , light detector D , angle of incidence α and the distance of measurement d [42, Fig. 4.1].

The setup offers different modes of operation. As depicted in Fig 4.5, the first mode is used to acquire the scattering distribution of a sample's surface.

Fig. 4.6 depicts a series of measurements of the back of a hand as well as a wooden board from different angles of observations. A diffuse white reference tile was used

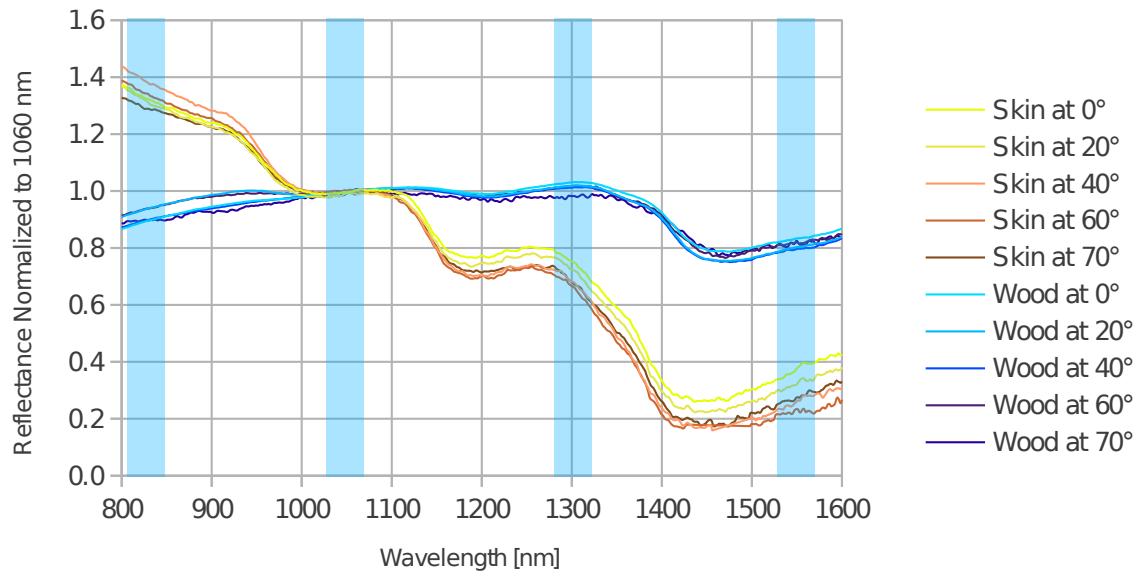


Figure 4.6: Reflectance of human skin at different angles of observation.

to calibrate the amplitudes for each individual angle, but the tile turned out to be less diffuse than human skin. Therefore, all spectra were individually normalized to their amplitude at 1060 nm, which eliminates information on the absolute amplitudes of the spectra. However, the skin spectra coarsely keep their shape and are significantly different from the wood spectra provided for comparison. Only a small decrease of reflected energy at long wavelengths of ≥ 1400 nm can be seen, which is likely related to a weaker share of specular reflection components at acute angles, as discussed in the following section. For comparison, the wood spectra do not yield significant deviations at all.

An alternative mode of operation is implemented to move the transmitter and receiver in parallel, which is depicted in Fig. 4.7. This mode offers measurement conditions which are very similar to the actual sensor system. Both systems are sampling a surface at an arbitrary angle from a certain distance d with transmitter

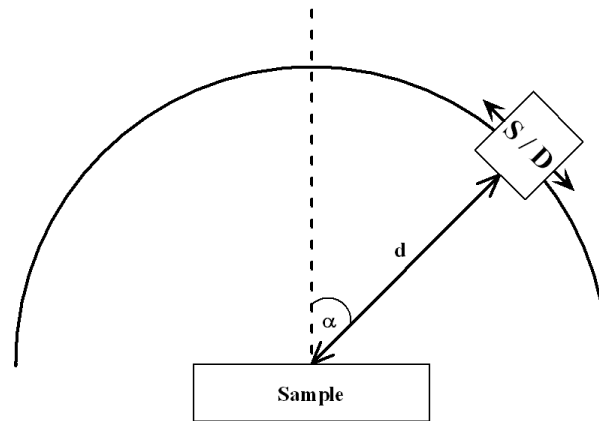


Figure 4.7: Measurement setup for angular dependent reflectance measurement comprising light source S , light detector D , angle of incidence α and the distance of measurement d [42, Fig. 4.2].

and receiver aligned in parallel. The measurement results in this mode yield no significant change of the reflection spectra as well.

In conclusion, neither the angle of illumination nor the angle of observance have a considerable influence on the near-infrared reflection spectrum of human skin.

This result, however, is extremely valuable with respect to the background of this work, as the sensor system must be able to perform a dependable detection of human skin without knowing the orientation of the measured surface. Therefore, the experiment was repeated using a [Skinner](#) mark 2 sensor, which is described in detail in section 5.4, to perform measurements at various angles. The experiment yield the same results. While the signals are attenuated with increasing angle of measurement, the ratios between the signals remain constant. In fact, the [Skinner](#) mark 2 sensor was able to detect human skin at every measurement configuration, including an extremely acute measurement angle of 85° .

4.4.2 Spectroscopy of Subsurface and Specular Scattering Components

To best of my knowledge, no data on the specular, diffuse and subsurface components of the reflectance spectrum of human skin is available in prior work for wavelengths of 1100 nm to 1600 nm. Therefore, new measurements were performed using the *irSys*[®]1.7 spectrometer.

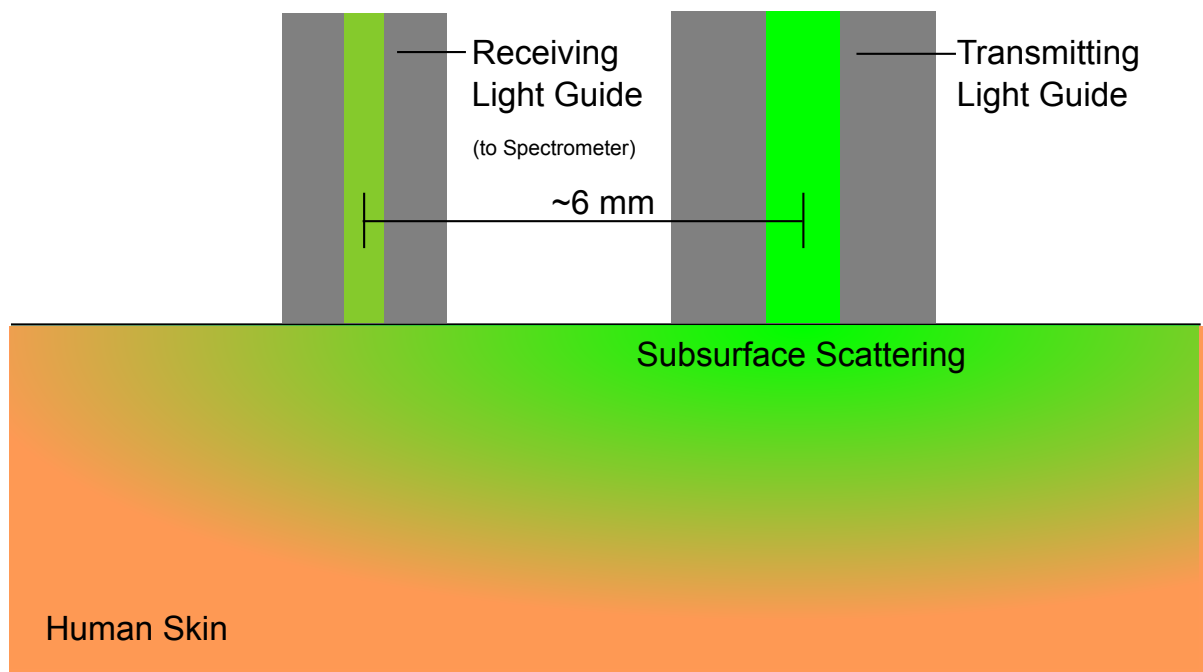


Figure 4.8: Setup to measure the subsurface components of the reflection spectrum.

Analogously to a measurement setup presented by Meglinski and Matcher, the subsurface component was measured using a setup as depicted in Fig. 4.8 [41]. A fiber coupled tungsten lamp is used for illumination, whereby the emitting side of the fiber is put directly on the surface. Another fiber is put at a nearby (≈ 6 mm) spot for measurement. This simple setup assures that all received light has traveled through the tissue underneath the surface. Consequently, the previous setup was modified and extended by a polarizer (type CODIXX colorPol[®]VISIR CW02) to isolate the

specular reflectance component as depicted in Fig. 4.9. According to CODIXX, which is the manufacturer of the polarizer, the filter has a contrast of $>10000 : 1$ in the wavelength range from 550 nm to 1500 nm. Unfortunately, the performance of the filter at 1550 nm is not specified, which is the center of the fourth waveband of the *Skinner* sensor. As only one filter was available for this measurement, both fibers were sharing a common polarizer (CODIXX). The measurement setup is based

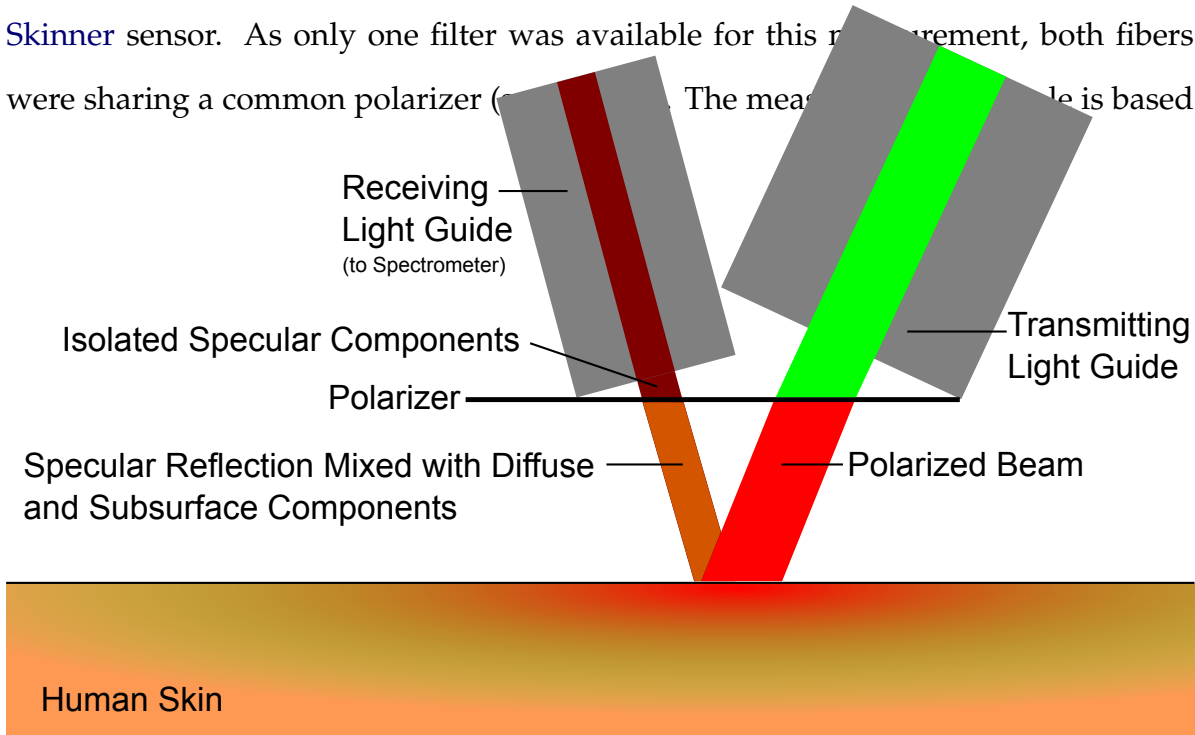


Figure 4.9: Setup to measure to specular components of the reflection spectrum.

on the assumption that polarized light will not alter its polarization when reflected at the surface, while the polarization will be altered randomly when moving through the tissue. In consequence, the majority of the light reflected with unchanged polarization comes from specular reflections. This circumstance is exploited, as the receiving light guide is placed behind the polarizer, which absorbs the majority of incoming light with changed polarization and, therefore, isolates the specular reflection component from diffuse and sub-surface components.

However, it must be taken into account that specular reflections from dielectric surfaces, such as human skin are partially polarized when measuring near the Brew-

ster angle [43]. As the incident light was polarized beforehand, the polarization of light by the measured surface was unwanted. Therefore, the measurement was taken at an acute angle of about 35° , while the Brewster angle for the first skin layer (stratum corneum) and air is about $\arctan(n_{skin} = 1.55/n_{air} \approx 1.00) \approx 57^\circ$ [44].

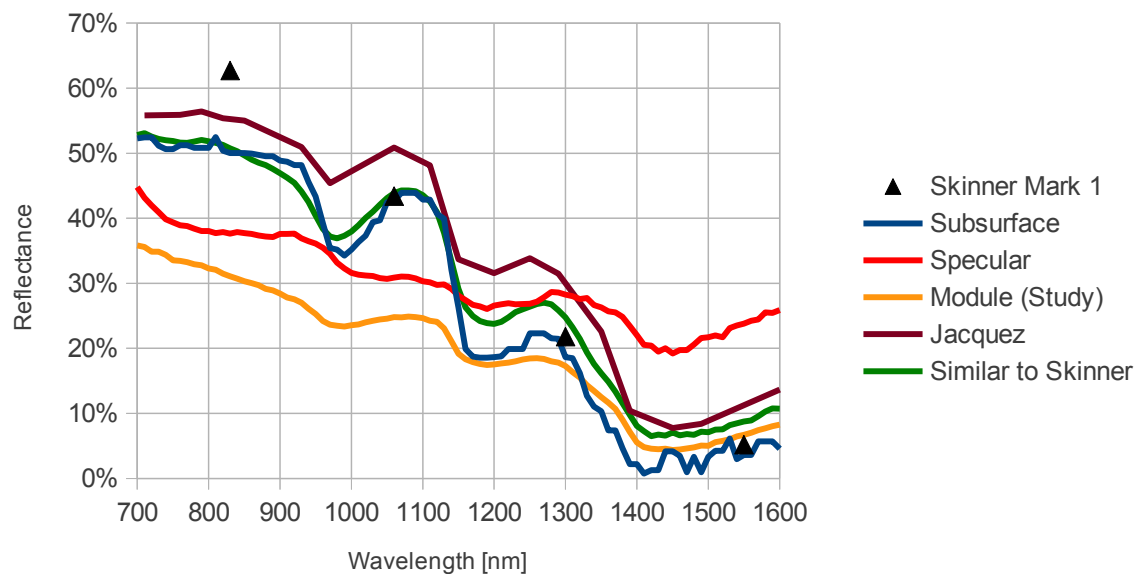


Figure 4.10: Subsurface and specular reflectance components in comparison to measurements performed with the measurement setup used for the study, a spectroscopy setup which is similar to the Skinner sensor and data by Jacquez et al. [9].

Overall, this improvised measurement setup was difficult to calibrate, as the measurement distance could not be adjusted precisely on the uneven surface of a human hand. However, the result displayed in Fig. 4.10 shows how the local minima and maxima are less distinctive compared to the subsurface scattering component. This was expected, as the specular reflected light did not pass the top skin layer and thus cannot be influenced by water within the skin.

The reflectance spectrum with the label *Module (Study)* was acquired during the preliminary study using the *irSys*[®]1.7 spectrometer with the module shown in Fig. 4.4

on page 45. When compared to the data published by Jacquez, it is noticeable that the local minima and maxima are less distinctive in the data of the study [9]. This indicates that the measurement setup used for the study measures a composition of reflectance components in which the specular component is more dominant than in the spectrum measured by Jacquez. Considering this observation, the mapping error at 1 300 nm and 1 550 nm seen in Fig. 4.3 on page 44, where the intensities measured at skin by the *Skinner* sensor are below the acquired reflectance spectra, can be explained. Finally, it is likely that the measurement port of the spectrometer cancels out a portion of subsurface remissions, which are exiting the tissue around the directly illuminated spot (see Fig. 4.4 on page 45).

In conclusion, a selection of wavebands is chosen as a result of the analysis of the data presented in this chapter. However, a concept to design such a sensor system must be developed. In the following chapter, such a design concept as well as applicable safety requirements are presented. Furthermore, system specifications are derived and a prototypical implementation is described: the *Skinner* sensor system.

Chapter 5

Sensor Concept

A concept for a new type of sensor: the [active optoelectronic material classifying protective device \(AOMCPD\)](#) is presented in this chapter. In Sec. 5.1, safety related requirements for such an [AOMCPD](#) are discussed on the basis of international safety standards. Current standards define requirements to assure the functional safety of a sensor with respect to state-of-the-art [active optoelectronic protective devices \(AOPDs\)](#) such as common light curtains and laser scanners, which are denoted as [active optoelectronic protective devices responsive to diffuse reflections \(AOPDDR\)](#)s [45]. In consequence, the applicability to the new class of [AOMCPDs](#) is limited and must be assessed. Furthermore, special requirements and test procedures are proposed, which account for new questions that arise with such devices.

In Sec. 5.2, a design concept for such sensors is determined with respect to the formulated requirements. At first, the structure of the sensor is discussed and defined. Then, design concepts for each component of the chosen structure are presented.

Based on the developed concept, specifications for a prototypical implementation are defined in Sec. 5.3. That section is subdivided for functional and technical specifications.

Finally, the presented sensor concept is realized in a prototypical implementation, which aims for full compliance with the presented specifications. The prototypical implementation is denoted as the *Skinner* sensor.

5.1 Safety Requirements and Applicable Standards

Detailed safety requirements on the sensor system must consider all aspects of the targeted application and, if necessary, even the characteristics of a particular machine. In consequence, the safety requirements presented in this section can only establish a common basis for typical safety applications. This basis is presented in the following subsections with respect to international standards, which are focusing on different aspects of functional safety. Important information such as general design rules, methods for failure analysis (e.g. Failure Mode and Effects Analysis (FMEA)), guidelines to determine the required performance of a safety function (e.g. Risk Graph) and performance measures (e.g. *safety integrity level (SIL)* or *performance level (pl)*) are provided by prominent standards like the ISO 13849-1 or IEC 61508 [46, 47]. Other standards provide expectancy values for certain velocities or measurements. For instance, the DIN 33402-2 provides 70 tables of expectancy values for body measurements. All these standards are relevant for the proposed type of sensor system and must be taken into account. Another standard, the IEC 61496-2, defines specific requirements and test procedures for common *AOPDs* (i.e., light curtains and light barriers), which react on beam interruption [48, 49]. In consequence, the requirements and test procedures provided by this standard are not always applicable to the proposed type of material classifying sensor system.

Tab. 5.1 presents an overview on the applicability of current standards with respect to the topics that are presented in detail within the following subsections. As

Table 5.1: Applicability of current standards to AOMCPDs.

	Requirements	Tests / Assessment
Material Classification	61508 (p)	N/A
Distances of Operation	N/A	N/A
Reaction Speed	13855, 33402, 61496-2 (p)	61496-2 (p)
Beam Width	33402, 61496-2 (p)	61496-2 (p)
Atmospheric Humidity	61496-1 (p)	61496-1
Temperature Range	61496-1	61496-1
Shock Resistance	61496-1	61496-1
Ambient Light	61496-2 (p)	61496-2 (p)
Eye Safety	60825	60825
Self Tests	13849, 61508	13849, 61508
(p)	Partially Applicable	N/A No Applicable Standard
13849	ISO 13849-1 [46]	13855 ISO 13855 [50]
33402	DIN 33402-2 [51]	60825 IEC 60825-1 [52]
61496-1	IEC 61496-1 [48]	61496-2 IEC 61496-2 [49]
61508	IEC 61508-1 [47]	

a key contribution of this work, new requirements and test procedures are proposed whenever existing standards are not applicable. The intention is to provide recommendations which can be used as a starting point for the standardization of AOMCPDs as a new type of safety sensor, e.g. by adding a fourth part to the international standard IEC 61496. In the end, the members of standardization organizations (e.g., International Electrotechnical Commission (IEC) or German Institute for Standardization e.V. (DIN)) will have to decide about appropriate tests and requirements, if AOMCPDs will be included in future versions of the standards.

5.1.1 Differentiation of Relevant Materials

The basic requirement is that a sensor is able to differentiate human skin sufficiently reliable from typical workpieces. Generally, the reliability of such a system would be considered to be sufficient if the risk of injury related to the work at the corresponding manually fed machine can be reduced to an average level with respect to other high

risk work. In consequence, the required reliability as well as the surface material of typical workpieces strongly depend on the application. Furthermore, many applications have the obligation to either wear or not to wear gloves. If a user of a machine wears gloves, a sensor optimized for skin detection will not be able to detect the user's hands. Therefore, the focus of this work is set on the example application of circular table saws and sliding table saws at joineries and woodwork shops. In Germany, the safety regulations do not allow the use of gloves at circular table saws, because of the risk of getting pulled in when a tear-resistant glove is caught by the saw blade (see [53, Sec. 2.5.1.4]). In consequence, the detection of bare human skin is defined as the main safety function. Surface materials for typical workpieces are assumed to be wood, different types of plastic and metal. Plastic is included to cover both plastic-coated wood and some often processed plastic types such as Polycarbonate or *Polymethylmethacrylate* (PMMA). Metal is considered for the sawing table itself and aluminum alloy, which can be processed using special blades.

Requirements for the reliability of the material classification can be derived from the IEC 61508-1 [47], which defines the safety integrity levels (SIL) 1 to 4. These levels define thresholds for the average *probability of a dangerous failure on demand* (PFD), which are in the range from 10^{-5} to 10^{-1} . For instance, the SIL 2 requires a PFD within 10^{-3} to 10^{-2} [47, Tab. 2]. For AOMCPDs, it is important to find an abstract definition of a *demand*. A demand is any event, where protective means must be triggered to prevent an accident. The probability of such events is not important in this abstract contemplation, as only the *probability* of a false classification must be taken into account. Let it be supposed that there is a worst-case scenario, where only one measurement can be performed before an accident becomes inevitable. In consequence, every single measurement can be considered as a demand - and thus every false negative classification of a skin measurement (FN) must be considered as

a dangerous failure on demand. The probability of a false negative classification, and analogously a dangerous failure on demand, is implicitly given through the TPR as $PFD = 1 - TPR$ (see Eq. 2.8 on page 17). Considering the PFD's upper threshold of 0.01 for SIL 2, the corresponding requirement would be a $TPR > 0.99$. This worst-case model will be used to evaluate the classification reliability in this work.

5.1.2 Varying Distances of Operation

The required distance range heavily depends on the application and the mount point of the sensor. For this work, the targeted operation range is chosen as 0.1 m to 1 m, because this range should sufficiently cover most applications at manually fed machines. The IEC 61496-2 does not provide a minimum requirement for the range, although the devices are categorized by the maximum allowable distance of operation.

5.1.3 Reaction Speed

Generally, the reaction time of such a sensor system should be as fast as possible. For this system, there is a minimum measurement frequency f_{min} that can be derived from dimensions and typical speeds of human hands: For finger safety, the system must be capable to detect the smallest single finger that can be expected. According to the German national standard DIN 33402-2, the minimum width of a finger can be expected to be $\varnothing_f = 11 \text{ mm}$ [51, Tab. 39]. The maximum speed of a human hand is assumed to be $K = 2 \text{ m s}^{-1}$, according to IEC EN ISO 13855 [50, Sec. 6.2.3.1]. In contrast, the IEC 61496-2 defines a procedure to test the reaction speed using a test body that passes a light barrier at a velocity of only $K = 1.6 \text{ m s}^{-1}$ [49, Sec. 5.2.1.1]. However, the higher velocity of $K = 2 \text{ m s}^{-1}$ is used for the considerations in this work.

Furthermore, a **beam width**¹ \varnothing_b must be defined for a point sensor system, which satisfies the mandatory condition $\varnothing_b < \varnothing_f$. Having this information, the minimum measurement frequency can be calculated as in equation 5.1.

$$f_{min} = \left(\frac{(\varnothing_f - \varnothing_b)}{K} \right)^{-1} \quad (5.1)$$

For instance, when assuming $\varnothing_b = 6 \text{ mm}$, this leads to a required measurement frequency of $f_{min} = ((11 \text{ mm} - 6 \text{ mm}) / 2000 \text{ mm s}^{-1})^{-1} = 400 \text{ Hz}$.

This frequency is sufficient in a way that at least one acquisition is started during a total overlap of the beam with the finger, but will the measurement be finished within this state and if not, is a total overlap really necessary? The sensor system will acquire a mixed signal of the finger and the background, if there is no total overlap of beam and finger. As the background is generally unknown, it is not possible to calculate its influence on the mixed signal. E.g., a strongly reflective surface may reflect much more radiation towards the sensor's receiver than human skin and therefore have an disproportional strong influence on the acquired signal. In consequence, a detection cannot be guaranteed without a total overlap of beam and finger. To ensure a complete measurement within a total overlap it is necessary to take the acquisition time t_a into account by extending equation 5.1 to 5.2.

$$f_{min} = \left(\frac{(\varnothing_f - \varnothing_b)}{K} - t_a \right)^{-1} \quad (5.2)$$

Assuming an acquisition time of $t_a = 0.5 \text{ ms}$, the resulting measurement frequency is $f_{min} = ((11 \text{ mm} - 6 \text{ mm}) / 2000 \text{ mm s}^{-1} - 0.5 \text{ ms})^{-1} = 500 \text{ Hz}$, which is taken as a guideline for this work.

¹In the IEC 61496-1, the *beam width* is denoted as *detection area*.

5.1.4 Beam Width (Detection Area)

The size of the smallest object that can be detected by the sensor is in direct relation to the diameter of the output beam. A total overlap of the beam and an object is possible if all dimensions of the object are greater than the diameter of the beam \varnothing_b . Therefore, the transmitted beam's diameter defines the **beam width** (or detection area) of the sensor.

To detect a single finger, the **beam width** must be smaller than the width of the smallest expected adult finger, which is $\varnothing_f = 11$ mm according to DIN 33402-2 [51, Tab. 39]. Not all applications require finger safe detectors. Therefore, a lower specification can be used if it is sufficient to detect the presence of a hand. The minimal dimensions of a palm are 70 mm in width, 92 mm in length and 21 mm in thickness. In consequence, the beam diameter must be $\varnothing_b < 21$ mm for hand detection.

Special care must be taken for finger or hand safe light curtains. IEC 61496-2 defines the *detection capacity* of conventional light curtains as $dc = P + \varnothing_b$, whereby P is the beam spacing. The limits of the *detection capacity* are defined as $dc \leq 14$ mm for finger safety and $dc \leq 30$ mm for hand safety [49, Annex E.1]. For instance, the beam spacing must be $P \leq 9$ mm for $\varnothing_b < 21$ mm to ensure $dc = 9$ mm + 21 mm = 30 mm, whereby the actual beams will overlap if the beam diameter is greater than the beam spacing. Furthermore, the beam must not exceed its specified diameter over the whole range of operation, which requires a sufficiently narrow half beam angle.

5.1.5 Atmospheric Humidity

The atmosphere of the earth has strong absorption bands within the **near-infrared domain** as depicted in Fig. 5.1. This figure shows the accumulated attenuation of the

sunlight on its path through the atmosphere down to sea level at an incidence angle of about 48.2° , which corresponds to an air mass of $AM=1.5$.

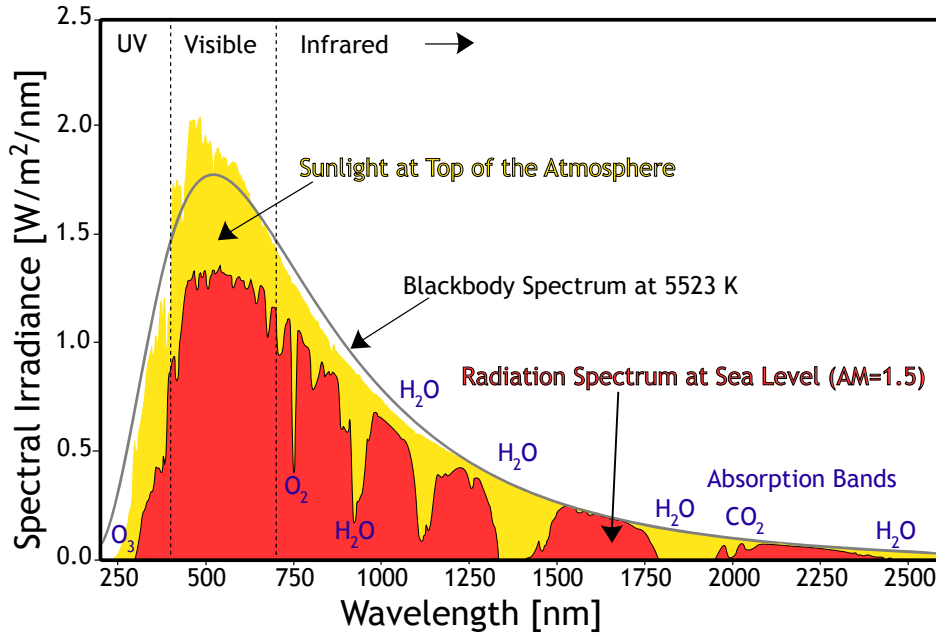


Figure 5.1: Atmospheric attenuation - a comparison of irradiance at sea level and the top of the atmosphere (Source: [54]).

Naturally, the absorption bands of water vapor at about 940 nm, 1130 nm and 1365 nm are relevant with respect to this work. In this spectral range, the attenuation of air depends on various factors such as pressure, temperature and relative humidity [55]. In consequence, the significant attenuation of ambient air at around 1365 nm would cause a distance and humidity dependent distortion of the spectral signature, if this waveband would be used by the sensor system.

However, the attenuation at short distances of a few meters is expected to be much lower than that of the entire atmosphere. Therefore, measurements in a climate chamber were carried out to evaluate the practical impact of such effects. As parameters for outdoor environments, a temperature range from -20°C to 50°C , a relative humidity RH of 4% to 95% and an air pressure of 86 kPa to 106 kPa can be

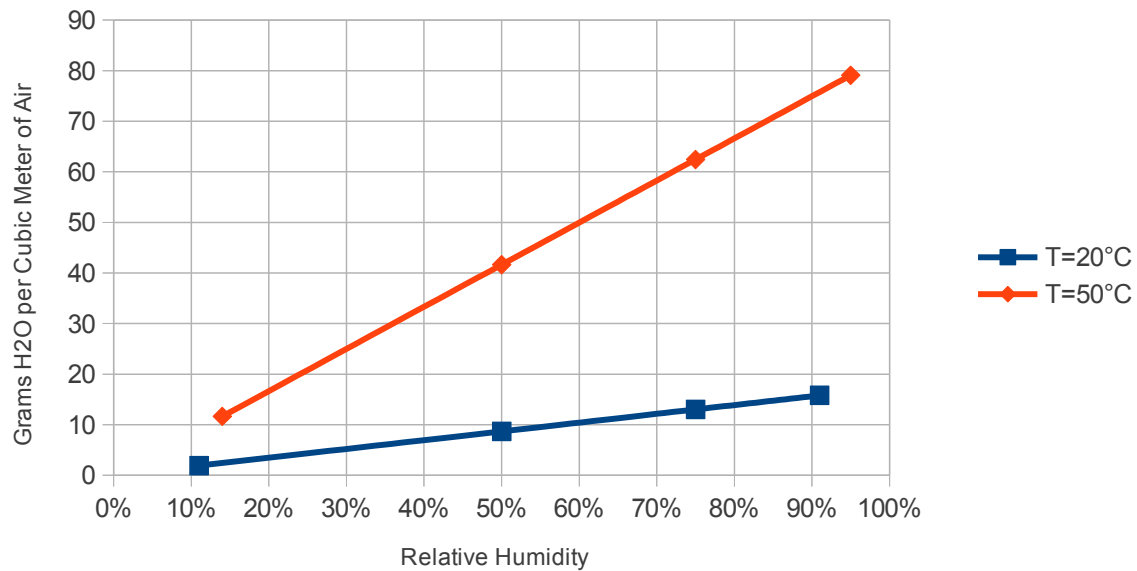


Figure 5.2: Mapping of temperature and relative humidity to absolute humidity.

assumed [56]. IEC 61496-1 defines a temperature range from 0 °C to 50 °C at $\leq 95\%$ RH as minimum requirement for AOPDs [48, Sec. 5.4.2]. In the presented experiment, the attenuation has been measured at different conditions from 20 °C to 50 °C at 11 % to 95 % RH. The measurements were carried out using an optical fiber which was coupled to the *irSys*[®]1.7 spectrometer. The open end of this optical fiber was turned towards an incandescent lamp at a distance of 0.34 m within the climate chamber. A temperature of 20 °C at 11 % RH was chosen as a dry reference atmosphere, as the used climate chamber is not able to control the relative humidity below 11 % or at lower temperatures sufficiently. Please note that the absolute humidity increases with the temperature, if the relative humidity is constant. Fig. 5.2 maps the relative humidity, used for the measurements displayed in Fig. 5.3, to the corresponding absolute humidity [57]. To compensate for drifting of the *irSys*[®]1.7 spectrometer, all transmission spectra were normalized to the window of 1000 nm to 1100 nm,

where no H₂O absorption band is located. Fig. 5.3 summarizes the measurements, which are showing a significant absorption with a relative attenuation of up to 13% at around 1365 nm. A weak absorption of 1% at around 1130 nm can be seen at 50 °C and ≥ 75% RH while no absorption can be observed at the absorption band around 940 nm. Based on these results, the absorption bands at around 940 nm and 1130 nm are not expected to have a practically relevant impact.

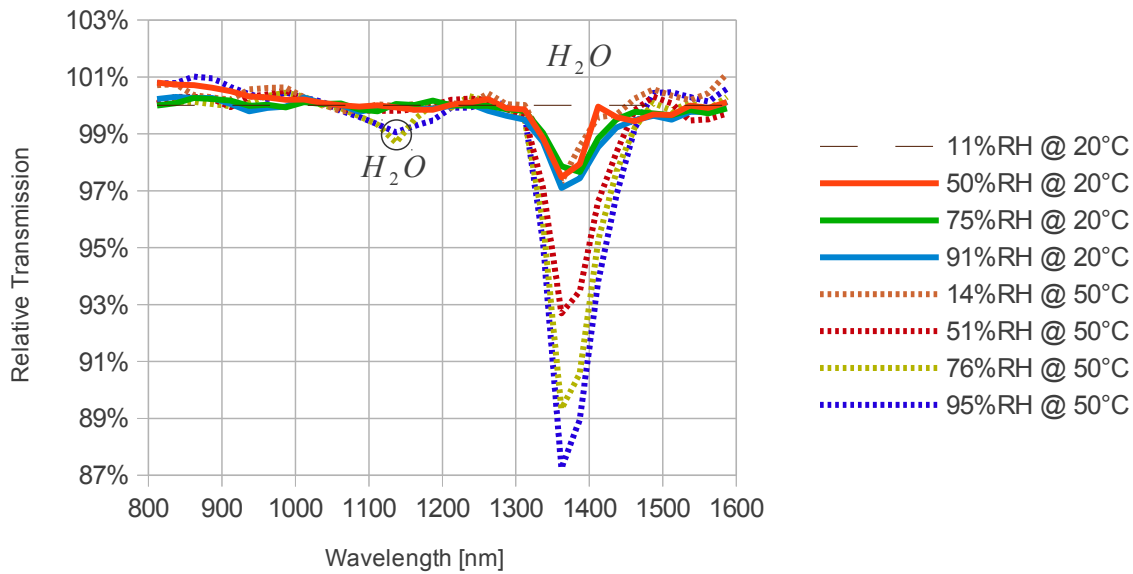


Figure 5.3: Relative transmission over an air path length of 0.34 m. The reference measurement was acquired at a temperature of 20 °C and 11% RH.

With respect to the Beer-Lambert law, the attenuation in gases can be expressed as shown in equation 5.3, whereby T denotes the transmission, I_{in} is the intensity of incident light, I_{out} the intensity of the transmitted light, α' is the absorption coefficient of a media and l is the optical path length [58].

$$T = \frac{I_{out}}{I_{in}} = e^{-\alpha' l} \quad (5.3)$$

Based on the presented experiment, the α' values were derived for the wavelength of 1365 nm and listed in Tab. 5.2 with respect to the reference conditions of 11 % RH at 20 °C.

Table 5.2: Absorption coefficients for 1365 nm.

Temperature	Relative Humidity	α'
20 °C	50 %	0.0896
20 °C	91 %	0.1592
50 °C	14 %	0.0945
50 °C	51 %	0.2614
50 °C	95 %	0.5014

Using these absorption coefficients, the attenuation at path lengths of up to 10 m is illustrated in Fig. 5.4. As a consequence of the severe attenuation even at relatively short air path lengths, the waveband of about 1340 nm to 1450 nm should be avoided in AOMCPD designs.

The housing of an AOPD must be compliant to the ingress protection rating IP54 or higher [48, Sec. 4.3.4]. When considering outdoor applications, the enclosure of the system must sufficiently prevent the intrusion of dust and humidity, and an ingress protection rating of IP67 or IP69 is recommended [59]. Furthermore, care should be taken to avoid heavy formation of condensation water on the optical components at the outside of the housing, which could be a plate of polycarbonate for mechanical protection or bare lenses. As the actual housing is not taken into account within this work, no protection class is defined as requirement.

5.1.6 Temperature Range

According to IEC 61496-1, an AOPD must withstand a temperature range from 0 °C to 50 °C [48, Sec. 4.3.1]. An extended range from –20 °C to 50 °C should be used for outdoor environments. For this work, the standard range is adopted as a requirement.

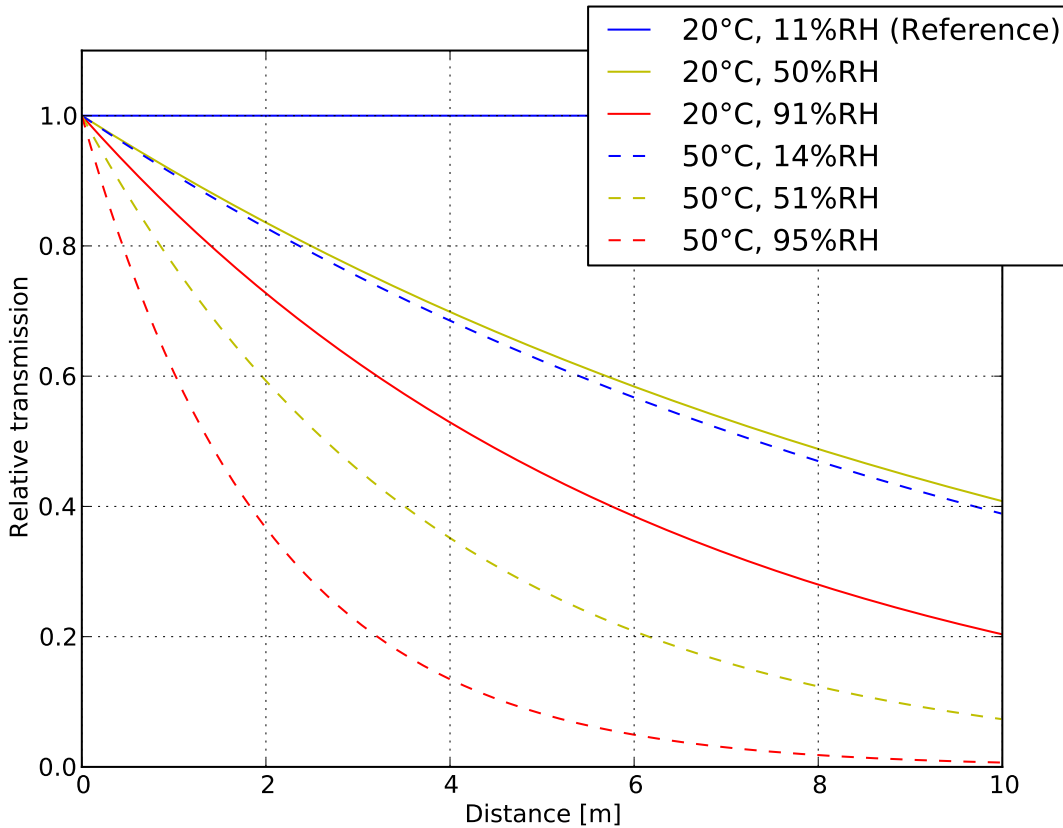


Figure 5.4: Relative transmission at 1365 nm.

5.1.7 Shock Resistance

IEC 61496-1 defines that an **AOPD** must withstand the following tests for vibrations and shocks:

- The **AOPD** must withstand vibrations from 10 Hz to 55 Hz and an amplitude of 0.35 mm while operating [48, Sec. 5.4.4.1].
- The **AOPD** must withstand 1 000 shocks per axis of 10 g with an impulse duration of 16 ms while operating [48, Sec. 5.4.4.2].

These test conditions can be adopted for the presented sensor concept without restrictions.

5.1.8 Ambient Light

Requirements for Conventional Light Curtains

The IEC 61496 standard defines general requirements and testing procedures for conventional light curtains, which are collectively referred to as AOPDs [48, 49]. Generally, this standard can be used as a guideline to define requirements and testing procedures for the presented AOMCPDs. However, the requirements and especially the testing procedures on optical interference robustness must be viewed with a critical eye, as the multispectral reflectance measurements used by AOMCPDs must operate more sensitively than common light curtains using special reflectors or performing two-sided transmission tests. According to IEC 61496-2, an AOPD must operate within its specified parameters while being exposed to either:

- A white light emitted by a tubular quartz lamp with a length within 150 mm to 250 mm and a power consumption within 500 W to 1000 W, positioned at a distance of 2 m to the receiver. The color temperature of the lamp must be within 3000 K to 3200 K and the frequency of the supply current must be within 48 Hz to 62 Hz. A diffuse parabolic reflector of high reflectivity over the whole spectrum must be mounted to the lamp [49, Sec. 5.4.6.2].
- A xenon flash light flashing at a distance of 3 m with a frequency from 0.5 Hz to 2 Hz with a flash duration from 40 μ s to 1200 μ s and a flash energy within 3 J to 5 J without using a reflector, filter or other housing [49, Sec. 5.4.6.2].
- A xenon strobe light operating at a distance of 1 m with a frequency from 5 Hz to 200 Hz with a strobe duration from 5 μ s to 30 μ s and a flash energy of 0.05 J at 200 Hz to 0.5 J at 5 Hz without using a reflector, filter or other housing [49, Sec. 5.4.6.2].

- A tubular fluorescent lamp with a length of 600 mm, a diameter of 25 mm, a power consumption within 18 W to 20 W, a color temperature within 5000 K to 6000 K and a nominal frequency within 30 kHz to 40 kHz must be used without a reflector at a distance of about 120 mm [49, Sec. 5.4.6.2].
- If a high specification is aimed (type 4), then the system must withstand the radiation emitted by a transmitter of the same kind [49, Sec. 4.3.5].

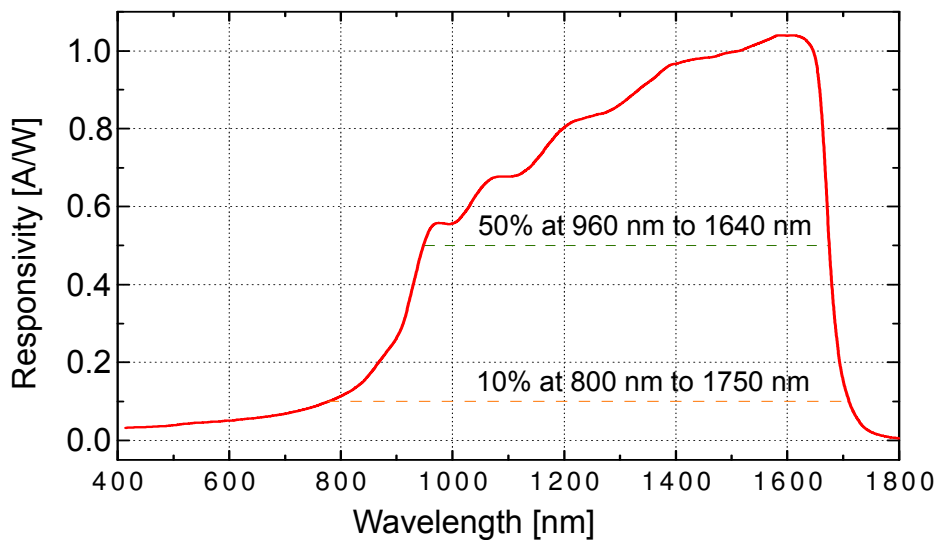


Figure 5.5: Spectral responsivity of an [InGaAs](#) photodiode (Original source: [60]).

By definition, the IEC 61496-2 does not apply if the [AOPD](#) operates outside the spectral range from 400 nm to 1500 nm, which technically excludes the [Skinner](#) sensor for its fourth waveband around 1550 nm. The standard does not provide an explanation for this restriction [49, Sec. 1]. However, the quartz and xenon lamps defined for testing emit a high share of energy beyond 1500 nm, while fluorescent lamps usually emit very little energy above 750 nm [61]. Another important aspect is the temporal domain, where quartz lamps oscillate with their supply voltage and xenon lights may generate strobe pulses of the same duration as the [AOMCPD](#) itself, such that a

frequency-based suppression of ambient light by the receiver can become inefficient. In consequence, quartz lamps, xenon flashes and xenon strobe lights are particularly relevant for the safety of AOMCPDs, if InGaAs based detectors are used (see Fig. 5.5).

Two Modes of Operation

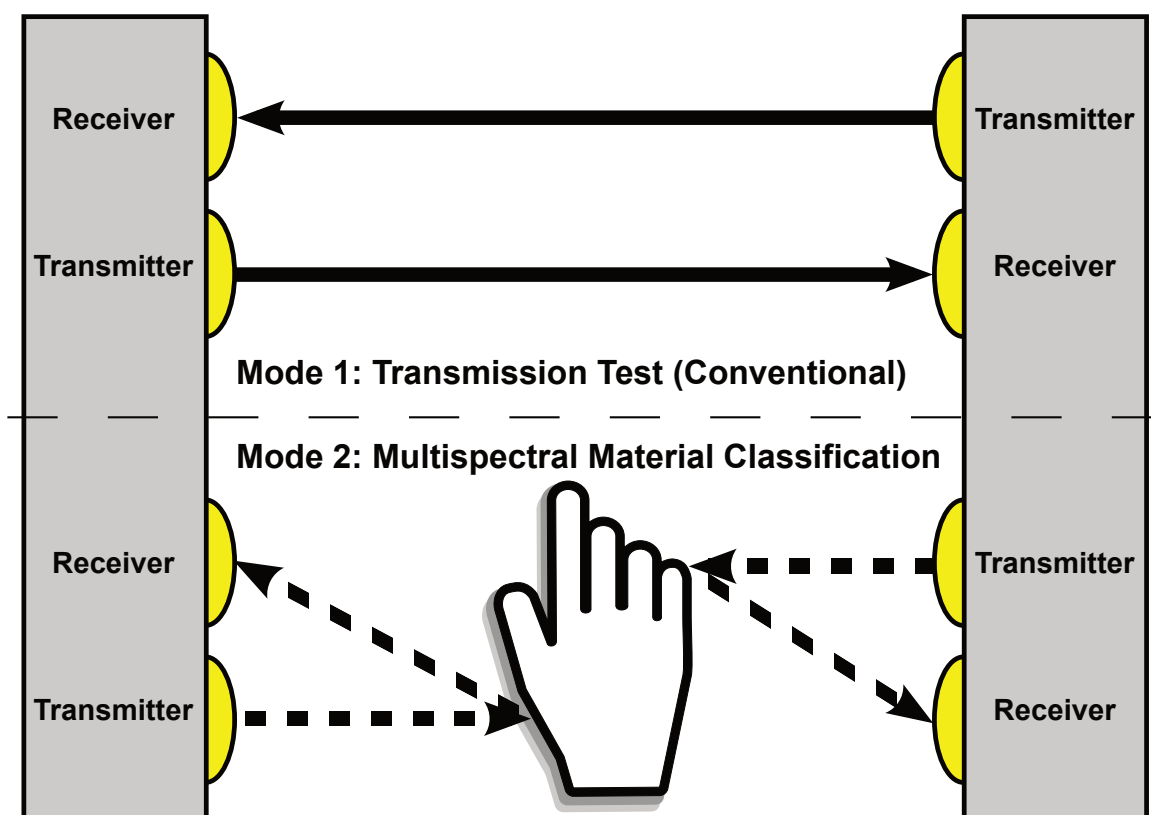


Figure 5.6: Two-sided multispectral light curtain configuration.

The standard IEC 61496-2 defines precise test configurations for the angle and position of the lamp to the AOPD. However, the defined conditions can only be applied to configurations with light curtains that are spanned between a dedicated transmitter and receiver unit or a combined transmitter/receiver unit and dedicated reflectors. As depicted in Fig. 5.6, the first configuration can also be realized with

AOMCPDs, when replacing the dedicated receiver and transmitter units by combined receiver/transmitter units at both sides.

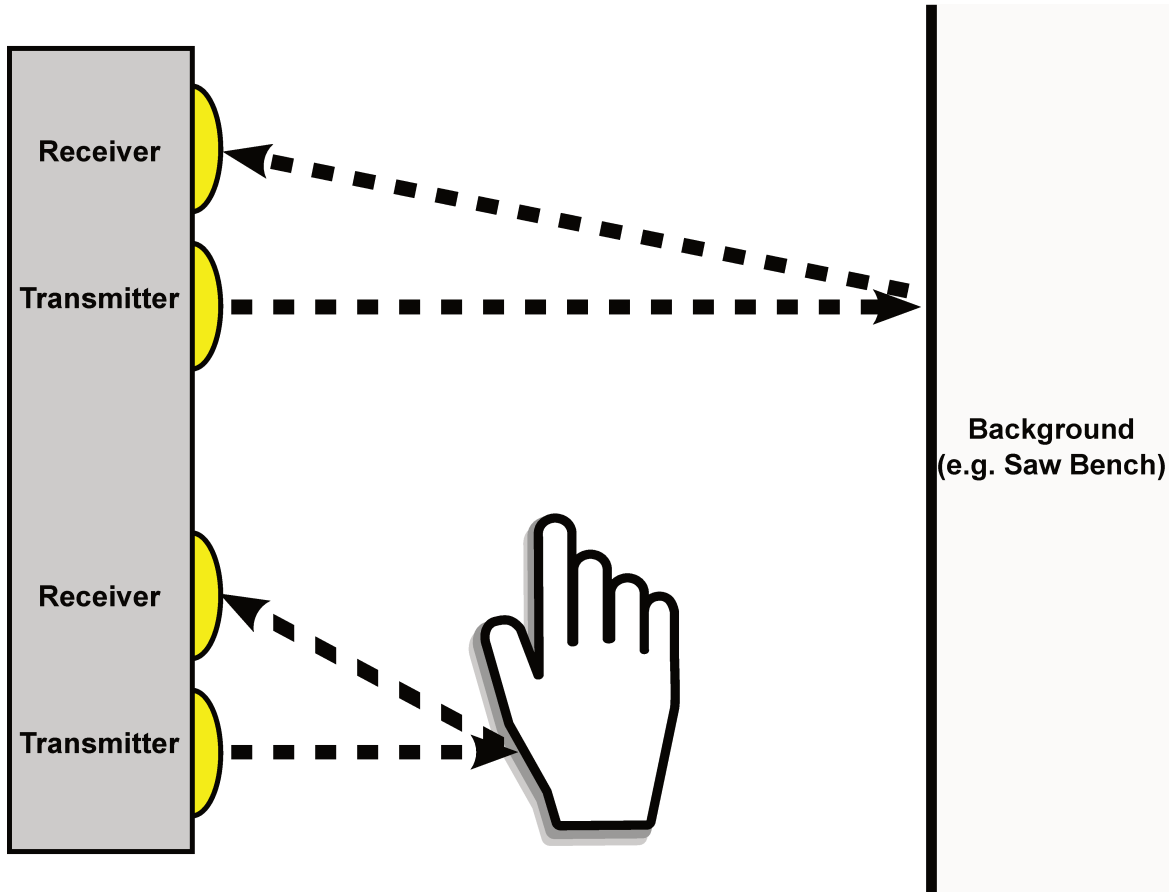


Figure 5.7: Single-sided multispectral barrier configuration.

Alternatively, a single-sided configuration can be used as depicted in Fig. 5.7 on page 68 without the necessity of a dedicated reflector at the other side. The current version of the IEC 61496-2 standard defines additional tests involving the use of an highly reflective, cylindrical test rod and other highly reflecting objects, if an AOPD uses reflectors [49, Sec. 5.2.1.3]. Obviously, these tests are based on the assumption that the system requires a highly reflective target (reflector) to terminate the light curtain. This assumption is not valid for configurations using AOMCPDs. For instance, a sensor can be mounted at a circular table saw's protective hood pointing

downwards onto the saw bench to monitor objects at the vicinity of the saw blade. In such an application, the sensor system must be capable of differentiating human skin from the saw bench, wood and other workpieces at all times, which contradicts with the requirement of a well defined reflector. Furthermore, reflectors cannot be used to enhance the range of an AOMCPD, as the reflections coming from safety critical objects (as the user's hands) must be sufficiently strong to perform a classification at maximum distance anyways. Considering the application of circular table saws, the protective hood should be positioned as low as possible above the saw bench, so that the system will operate at short distances of usually less than 0.5 m. The tests listed above, such as positioning a xenon flash at a distance of 3 m in front of the sensor, are not applicable if an AOMCPD is designed for short range operation (e.g. ≤ 0.5 m). In this case, the optical path can be extended by reflecting the test lamp using a highly reflecting surface, as a worst case substitute for a shiny background surface or workpiece, to test the interference robustness during standard operation. For instance, the lamp could be positioned at a distance of ≤ 2 m to the reference surface and the sensor could be positioned at a distance of ≤ 1 m to the same surface, such that the total optical path length from lamp to sensor (via the surface) would be ≤ 3 m. However, the highly reflective surface itself must be positioned within the operating range of the tested system.

Special Rod to Test for Dangerous Failures

When testing the system for a dangerous failure, the system must continuously detect a critical object (such as a hand) within its specified operation range during the interference by ambient light sources as listed above. Again, these light sources should be positioned behind the AOMCPD, so that the optical path lengths from the light sources to the critical test object and back to the sensor matches the distances

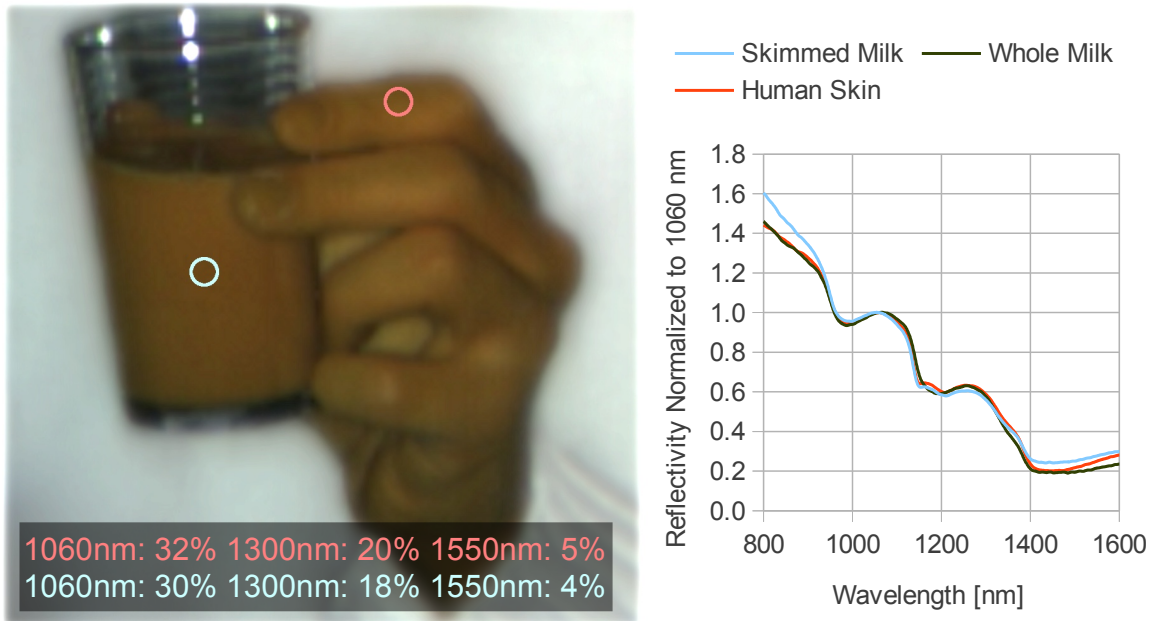


Figure 5.8: False color image and plot of skimmed and whole milk as well as human skin. False color mapping: 1060nm \mapsto red, 1300nm \mapsto green and 1550nm \mapsto blue.

specified by the previous standard, which are listed above. As human hands differ from person to person, the use of a special test rod with defined properties would be helpful to generate reproducible results. Especially the spectral properties must be reproducible and as close to human skin as possible. A tubular cuvette filled with whole milk is proposed for this purpose, as whole milk matches the spectral properties of human skin well within the spectrum from 800 nm to 1600 nm (see Fig. 5.8). Whole milk can be purchased with defined fat content and filled into a cuvette of well-defined length and diameter. Furthermore, the cuvette should be made of transparent plastic with a matte surface on the outside to minimize specular reflections.

Homogeneity Test

Conventional light curtains may not detect an interruption, if a sidelobe of the transmitter is being reflected into the receiver by a nearby mirror. This known issue is taken into account by current standards [49, Annex D.2]. AOMCPDs will introduce new issues, which must be addressed by defining new tests. A new aspect of AOMCPDs is the homogeneity of the multispectral beam. Distortion of spectral signatures may occur when measuring an object at partial overlap with the beam, if the beams of the individual wavebands do not align on the same optical path or the energy distribution within this path is inhomogeneous [5]. Therefore, an AOMCPD should either utilize measures to detect a partial overlap of an object within the beam or the beam must be as homogeneous as necessary to guarantee the acquisition of sufficiently undistorted spectral signatures under all conditions.

A spectral signature has a sufficient quality if the used material classifier is able to classify materials correctly (as specified for the desired application). This can be verified by testing the whole system at critical conditions as proposed in the following: Tubular test bodies having a diameter \varnothing_t of at least twice the beam width \varnothing_b must be used to test standard operation to cover possible sidelobes. There should be test bodies with a reflecting surface and a matte surface with a reflectivity of $\geq 95\%$ over the used spectrum with respect to an ideal Lambertian scatterer¹. Furthermore, a test body having similar scattering and subsurface scattering properties as human skin should be used when testing a skin detecting AOMCPD, whereby the test body must generally be differentiable from human skin by its spectral signature. For instance, silicone rubber which is meant to create realistic masks such as CPflesh^{®2} could be used to build such a test body. Using all test bodies, a series of measurements should

¹A Lambertian scatterer is homogeneously reflecting in every direction.

²See <http://www.cpflesh.de/> (online 2012-12-22)

be carried out from e.g. 10% to 90% partial overlap with the beam, stepping by 10 percentage points between each test. Additionally, the test bodies can be rotated around the center of the beam during measurement while the test body is aligned for a certain degree of overlap. The system should pass these tests without triggering a false alarm.

In this context, a test procedure for dangerous failures, where a system must detect a test body representing a critical object at partial beam overlap, is not necessary as the assumption formulated in Sec. 5.1.4 defines that a complete overlap of beam and surface is required for a robust detection anyways. Therefore, such tests can be considered as optional, as the probability of false alarms is not directly regarding the safety of a system. However, the rate of false alarms should be minimized to maximize the machine's availability and to achieve market acceptance of the technology.

Maximum Measurement Angle

In contrast to a conventional AOPD, an AOMCPD must perform measurements on the surface of an object entering the light curtain rather than just detecting the interruption of the optical path. Therefore, the maximum measurement angle α_m^{max} between the surface normal and the transmitted beam, in which a detection of critical materials can be done reliably, must be taken into account. As illustrated in Fig. 5.9, the significance of α_m^{max} depends on the beam width \varnothing_b , the shape and size of the critical objects (e.g. fingers) and the scattering properties of the critical material (e.g. human skin). As discussed in Sec. 4.4.1, human skin has very diffuse scattering characteristics and behaves well at measuring angles of at least $\alpha_m = 70^\circ$. Furthermore, practical experiments with an actual sensor yielded a detectability of human skin at every possible angle. However, a statement about α_m^{max} should be made for every critical surface material, which must be detected reliably by the AOMCPD.

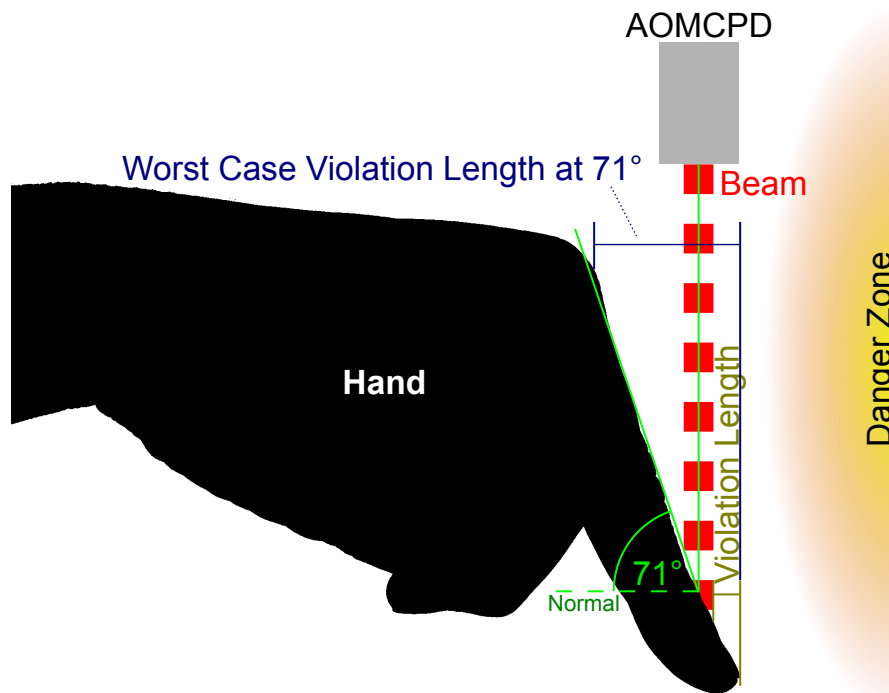


Figure 5.9: Illustration of a finger passing the beam at an acute angle.

The assumption that $\alpha_m^{max} = 70^\circ$ is set for the following discussion. For a safety assessment, the *worst case violation length* must be specified, which denotes the maximum depth about which an object can pass the beam at an illegally acute angle before any surface of the object will face the sensor at a legal angle. Thinking about a narrow danger zone at the vicinity of a circular saw blade, a finger coming in by its fingernail first at an acute angle is the worst case scenario, because the finger nail ends at a relatively sharp edge so no surface will face the sensor at a flat angle. Fig. 5.9 depicts an example of a straightened finger coming in at $\alpha_m = 71^\circ$ to the beam's normal, which is the smallest illegal value for α_m in this example. The worst case violation length l_w can then be calculated using equation 5.4, if simplifying the surface in question to be flat.

$$l_w = \sqrt{c^2 - (c \cdot \cos(90^\circ - \alpha_m))^2} \quad (5.4)$$

According to DIN 33402, the length of a long male middle finger is about $c = 94$ mm

[51, Tab. 48]. In consequence, when setting $c = 94\text{ mm}$ and $\alpha_m = 71^\circ$, the worst case violation length would be $l_w = 31\text{ mm}$, which then can be taken into account as a safety margin when positioning the sensor.

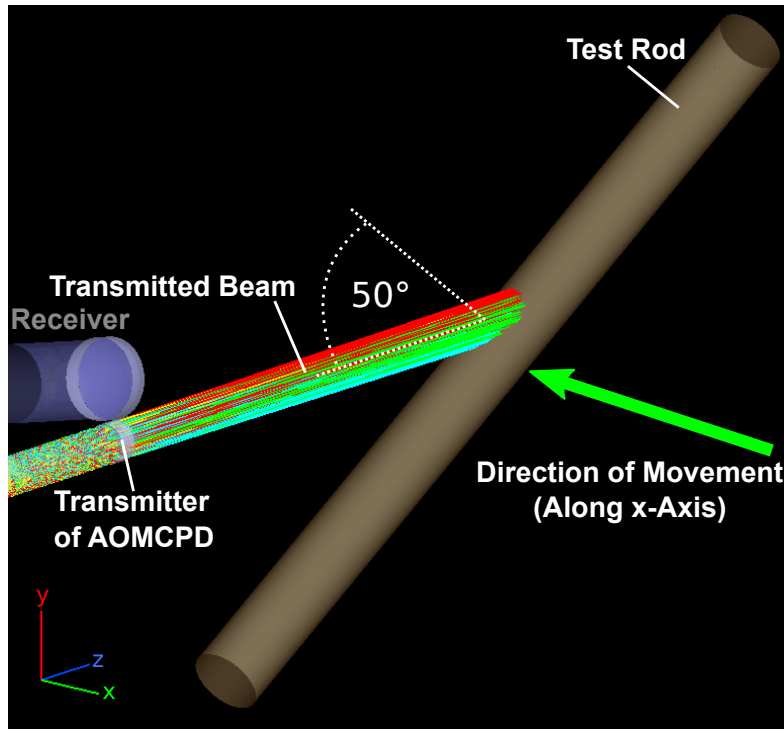


Figure 5.10: Test rod at acute angle to transmitted beam.

However, this model can only be used for relatively coarse estimations. Therefore, a simple test procedure to provide a general acceptance criteria should be defined. A simple approach would be to use cylindrical test rods with diameters matching the minimum specified detectable diameter, e.g. $\varnothing_f = 11\text{ mm}$. The surface materials of these rods must substitute all critical surface materials specified for a certain **AOMCPD**. These test rods must be moved into the beam, at all specified detection distances, with an acute measurement angle to the side of the rod of e.g. $\alpha_m = 50^\circ$. Under these conditions, the **AOMCPD** must trigger an alarm even if the rod is passing the beam at the specified maximum velocity (e.g. 2 m s^{-1}) and being oriented as depicted in Fig. 5.10. Using a cylindrical test rod of minimum detectable diameter

leads to a very unfavorable, but practically oriented measurement condition: The curved surface will face the beam at an infinite number of different angles, whereby all angles will be at least as sharp as the defined α_m . Furthermore, a cylindrical test rod roughly approximates the shape of a finger, which is naturally the most filigreed part of a hand.

5.1.9 Eye Safety

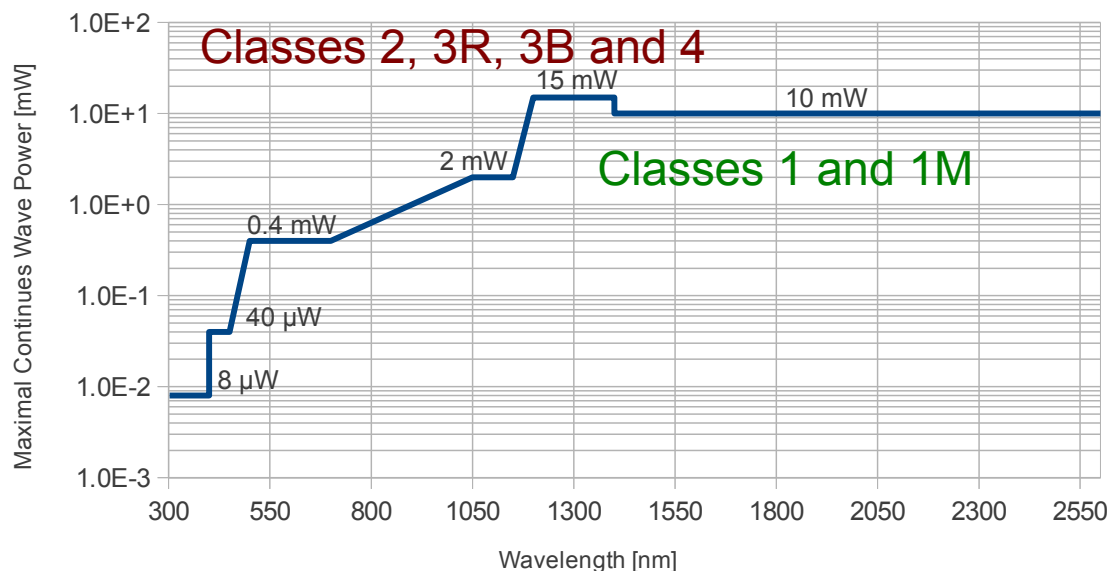


Figure 5.11: Limits for small continuous wave sources of classes 1 and 1M. Compare [62, Fig. 130].

The system must be compliant to laser class 1M as defined in IEC 60825-1 [52, Tab. 1] [49, Sec. 4.2.15]. Class 1 and 1M both define requirements for non-hazardous systems, which do not require the use of protective equipment such as laser protection glasses. Both classes have the same limits for radiation that can be received by a human eye. The difference is that the total amount of radiation emitted by a class 1

system must not exceed an eye-safe level, while a class 1M system is allowed to emit hazardous levels of radiation, if the radiation is spatially distributed sufficiently to assure that a human eye cannot receive a critical share of radiation. In consequence, class 1 systems cannot harm a human eye even if external optics are used to focus the emitted radiation, while a class 1M system might become hazardous in combination with external focusing optics. Fig. 5.11 illustrates the limits that apply for continuously radiating sources, which are small enough to couple all emitted radiation into a human eye. These are worst case limits, as it is expected that the eye might be permanently exposed to the total optical power. The actual limits that apply for a system depend on additional factors such as beam diameter and beam divergence as well as pulse duration and duty cycle for pulsed sources [52, p. 28ff]. Due to the comparably low thermal hazard and no photochemical hazard to the human eye that may be caused by near-infrared radiation, the allowable limits rise for wavelengths above 700 nm towards a maximum of 15 mW at 1200 nm to 1400 nm.

5.1.10 Self Tests

The system must implement self testing measures as specified in ISO 13849-1 or IEC 61508. The standards define different requirement levels, which are known as **performance level (pl)** or **safety integrity level (SIL)** and can partially be used interchangeably as illustrated in Fig. 5.12. The appropriate pl or SIL must be determined by a risk assessment of the targeted application. The higher the rated risk, the lower must be the probability of a *dangerous undetected failure*, which is expressed as the **probability of a dangerous failure per hour (PFH)** or **probability of a dangerous failure on demand (PFD)**, alternatively. A dangerous undetected failure is defined as a dangerous operating status of a machine, which is caused by at least one faulty

component of the system, whereby the fault cannot be detected by the system's self testing measures [46].

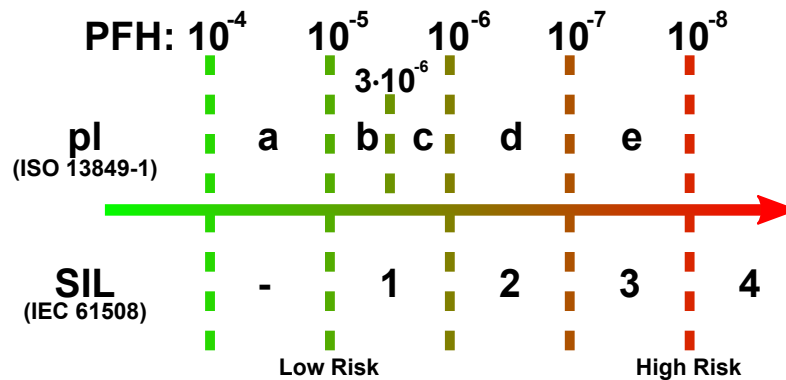


Figure 5.12: Classification of risks by ISO 13849-1 and IEC 61508 [46, Tab. 4] [47, Tab. 3].

ISO 13849 defines how a system can be designed to fulfill the requirements of a certain pl. These definitions affect especially the required degree of redundancy and the general approaches that should be used for self testing. It is important to note that ISO 13849 rates complete systems or machines rather than single components such as a sensor. In consequence, the **probability of a dangerous failure per hour (PFH)** of protective means, which are triggered by an **AOMCPD**, must be taken into account as well. So, if an **AOMCPD** is integrated into a circular table saw, the whole machine must be assessed with respect to the appropriate requirements. Therefore, it is not possible to formulate general requirements covering all **AOMCPDs**.

At this point, the discussion of safety requirements and applicable standards is concluded. The results of this section are used as a basis to define an optimized design concept.

5.2 System Design Concepts

System design concepts for LED based AOMCPDs with respect to the derived safety requirements are discussed in this section. In a first step, the optical design is discussed by comparison of fundamentally different structures. Afterward, matching concepts for electronic circuitry are presented.

5.2.1 Optics and Optoelectronics

Structure

Generally, there are two approaches for the structure of the sensor: One approach is to design the sensor in a way that the receiver is in the same optical path as the transmitter. The other is to place the receiver besides the transmitter's optical path.

Having receiver and transmitter united at one optical path has the advantage of allowing a single detector at a fixed position to receive the reflected light for any measuring distance. As long as the measured surface diffusely reflects light in the incident direction, which is required for the detectability of a material at a wide range of measurement angles, the receiver will always be well aligned. In contrast, a spatial offset of the receiver necessarily entails a distance dependent angular displacement of the reflected light to the receiver.

However, the implementation of a common optical path is challenging. A common approach would be to use a beam splitter as depicted in Fig. 5.13. The use of a beam splitter has the disadvantage of an inevitable power loss of at least 50% for both the transmitter and the receiver. Furthermore, any pollution of the beam splitter's surface might cause a direct redirection of the transmitted light into the receiver.

Another solution would be the use of a parabolic or flat mirror with a comparably small hole in the middle through which the transmitted light passes. As illustrated

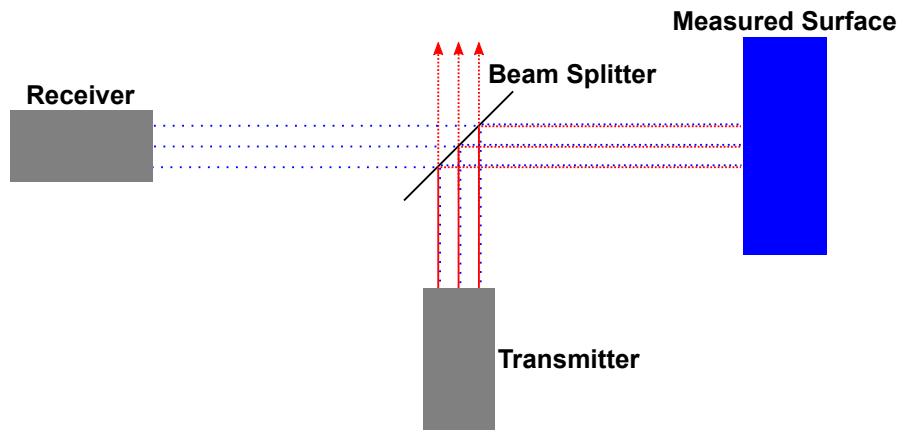


Figure 5.13: Optical paths united by a beam splitter.

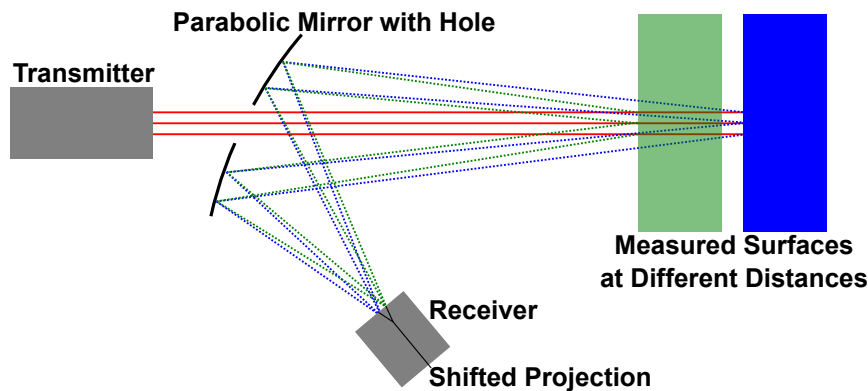


Figure 5.14: Optical paths aligned using a parabolic mirror. Distance dependent projections are illustrated.

in Fig. 5.14, the receiver would measure the incident light being redirected by the mirror. This design avoids high power losses at the disadvantage of not providing a common optical path in a strict manner. Instead, the optical path of the transmitter is encapsulated at the center of the receiver's optical path, which is aligned in parallel. As a consequence, the projection of the reflected light onto the receiver would be distance depending, eliminating the advantage of being able to measure at a fixed spot.

Both approaches share a severe problem that comes with the use of protective screens, which are usually part of the enclosure of optical sensors. Protective screens

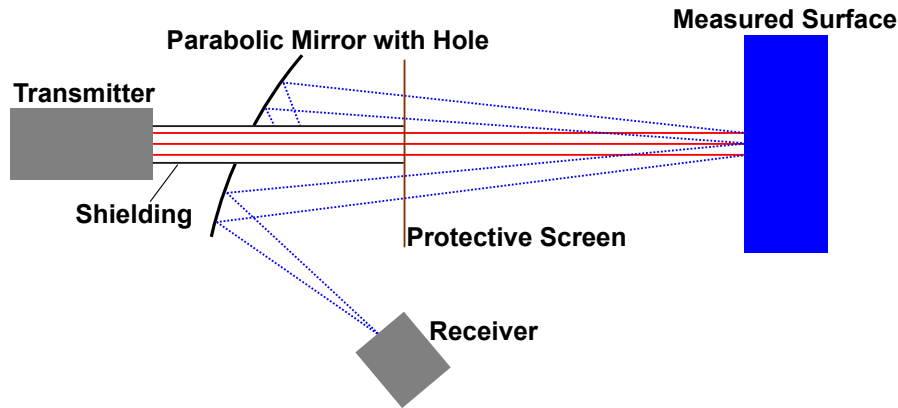


Figure 5.15: Optical paths aligned using a parabolic mirror. Obstruction by additional shielding is illustrated.

may easily become polluted at the outside, producing direct redirection from the transmitter to the receiver at short distances. This redirected light will interfere the measurements and, therefore, lower the reliability of operation. Besides pollution, even a coated protective screen will always reflect a small share of radiation. This general weakness of the design can be avoided by additional shielding as depicted in Fig. 5.15, at the expense of obstructing the optical path of a fraction of the redirected light by the shielding itself.

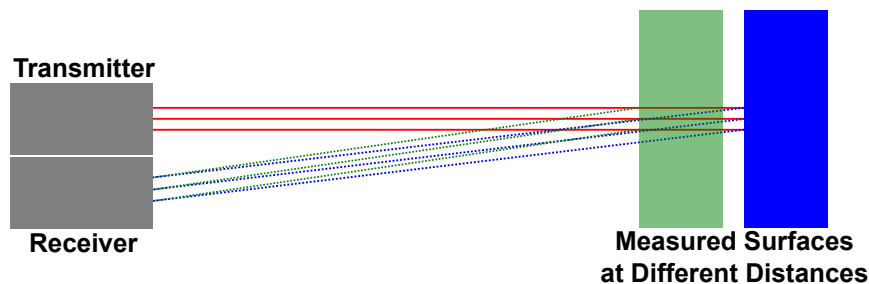


Figure 5.16: Optical paths aligned in parallel.

The second approach is to position receiver and transmitter side by side. As illustrated in Fig. 5.16, this straight forward design has the advantage that no further optical components are needed to redirect the light and, therefore, the loss of energy is minimal. On the other hand, the measurement angle of the receiver depends

on the distance from the center of the transmitter to the center of the receiver and on the measurement distance. Although this is no principle disadvantage of the measurement accuracy, as the angle of the surface to the sensors varies anyway, but it can be a limiting factor for the operable range of measurement distances. As with the use of a parabolic mirror, the receiver must be designed in a way that it is capable of receiving light from a range of incident angles to allow measurements in a corresponding distance range. To keep the setup of the sensor simple and compact, a side by side configuration was chosen for this work.

Distance estimation

The receiver's requirement of being able to receive light at different incident angles can be used to realize an additional feature: distance estimation by triangulation (if the receiver is able to measure the angle of incident light).

Additional value is provided by the ability to compensate the distance related reduction of light that is caught by the receiver. If approximating the scattering properties of human skin as a Lambertian scatterer, Lambert's cosine law can be used to calculate this relation [63]. Then, the reflected intensity perceived by the receiver r with an area of aperture A will exponentially decrease over the measurement distance d as a function of $r(d) = A/2\pi d^2$.

However, this function is not applicable for surfaces having a deviating scattering behavior. A mirror has the most divergent behavior with respect to a perfectly diffuse Lambertian scatterer. For a mirror, the amount of radiation being reflected into the receiver will not decrease as much as that reflected by a Lambertian scatterer over the same distance, as long as the half-angle between the optical paths of receiver and transmitter matches the orientation of the mirror to the sensor. Naturally, the measurement angle has a much greater effect for mirror-like surfaces than it has for

diffuse surfaces. Therefore, this type of amplitude correction cannot work accurately for mirror-like or shiny surfaces (see Sec. 7.2.3).

Beamforming

The beam emitted by the transmitter should be as near-collimated and homogeneous as possible. If the beam is diverging too much, the range of the AOMCPD will be limited by the distance at which the beam diameter \varnothing_b becomes larger than specified for safe operation. As discussed on page 71, an equal distribution of energy of all wavebands within the beam is very desirable to avoid artifacts if at least one object is intersecting the beam partially.

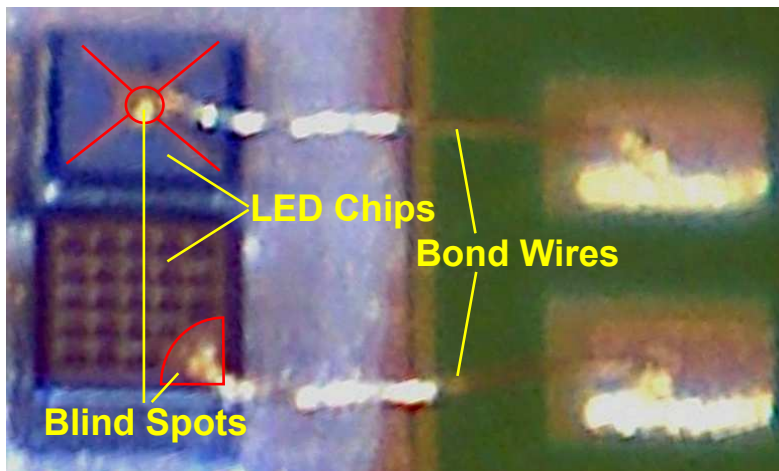


Figure 5.17: Image of two LED chips with bond wires.

In order to create a highly collimated beam, a point light source can be positioned at the focal point of a condenser lens. However, LED chips usually have a square footprint with an edge length from about 300 μm to 1000 μm with a topside emitting light in every direction. Generally, LEDs do not homogeneously emit light in every direction. For instance, a bond wire is necessarily connected to the LED's anode or cathode at the top side, which obstructs a part of the emitted light and produces a

blind spot at the connection port as shown in Fig. 5.17. Furthermore, the edges of LED chips also emit a considerable amount of the total radiant power [64]. Generally, the larger the lens in relation to the LED chip size, the more accurate becomes a simple approximation of the LED by a point light source. The relation is sometimes denoted as the lens-to-LED ratio [65].

The concept of an AOMCPD comprises a multispectral light source. To build an LED based multispectral light source, a two-dimensional array of multiple LED chips having individual wavebands is required, as the chips are not transparent and can therefore not be stacked on top of each other. According to information by Epigap-Optronic GmbH, a chip gap of at least $\leq 50 \mu\text{m}$ is required when installing multiple LED chips in a common housing. So, the footprint of an LED based multispectral light source having four distinct wavebands would optimally be positioned in a two by two pattern, which means that the edge length of the light source will be double the edge length of a single LED chip plus the chip gap, provided that all LED chips have an equal footprint. It is important to note that this multispectral light source emits the light of distinct wavebands from distinct LED chips or areas, which introduces the problem of forming a common optical path for all wavebands.

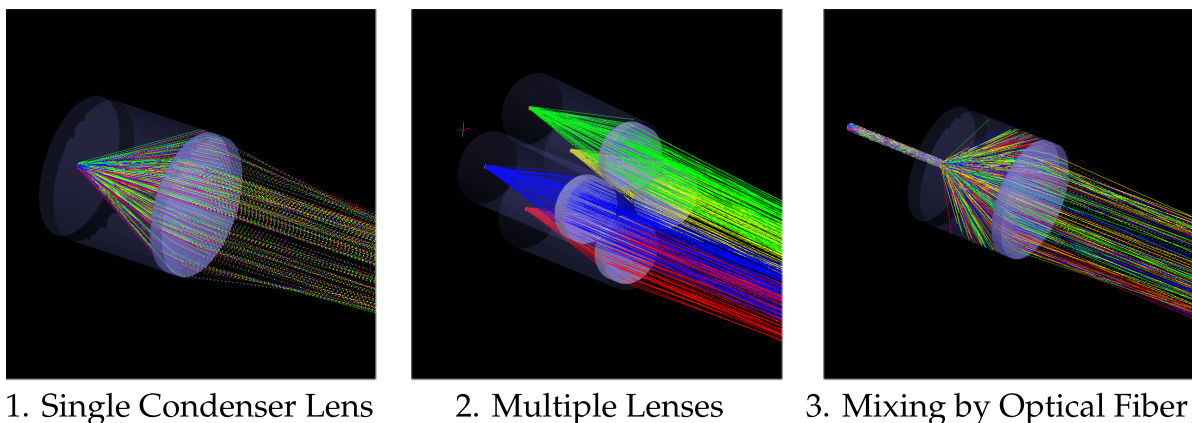


Figure 5.18: Overview of beamforming concepts.

Concepts on how to design the beamforming optics are listed below. A graphical overview of the first three concepts is depicted in Fig. 5.18.

1. The first concept comprises a single condenser lens and approximates the LEDs as a point light source.
2. The second concept installs one lens per LED. This way, each LED can be centered to the focal point of its lens. The focal point also depends on the used wavelengths. In this setup, each LED can easily be positioned in an optimal distance to the lens. This is a notable advantage of the concept, as it is difficult to position the LEDs at different heights within one common housing with the important secondary condition that the chip gaps should be minimal. Furthermore, the lenses can be rotated towards a common reference point. This way, the projected spot can be optimized for a specific distance of measurement, but it cannot be optimally homogeneous for all diverging distances. An advantage is the possibility of installing each LED chip within an optimized reflector to increase the optical output power.
3. Considering the first concept, the distribution of the light emitted by individual LEDs within the beam can be made more homogeneous if some kind of diffuser is used between the array of LED chips and the condenser lens. This can be implemented by coupling the light of the LEDs into a common optical fiber. Within this fiber, the light is mixed homogeneously as a result of multiple internal total reflections. The open end of the fiber is positioned at the focal point of a condenser lens. Ideally, the light emitted at the open end of the fiber would be mixed so well that the homogeneity of the beamforming is only limited by the dependency of the focal length to the wavelength. The fiber should preferably be bent to increase the number of internal reflections. Furthermore,

the optical fiber could become narrower towards the open end to come closer to the properties of a real point light source. Disadvantages of this concept are coupling loss and attenuation within the optical fibers [66]. According to information by Epigap-Optronic GmbH, the optical output power achievable with this design is below 25 % of the power achievable using individual lenses and optimized LED reflectors.

4. Further concepts on how to design optics for LED systems are presented in prior work and summarized in Sec. 3.1.4. Unfortunately, these approaches are practically not available for the realization of this work. Consequently, these approaches are excluded for further considerations, even though they could result in superior solutions.

These concepts have been compared using the optical engineering software FRED by Photon Engineering, LLC. To define comparable conditions, a lens with a focal length of $f'_1 = 23.25$ mm and a diameter of $\varnothing_1 = 22$ mm was chosen for models comprising a single lens. The multiple lens approach was modeled using lenses with a focal length of $f'_2 = 22$ mm and a diameter of $\varnothing_2 = 9$ mm to reduce the spatial shift between the individual sources. Both selected lenses are commercially available. Just as for the lenses, the modeled LED chips have the same peak-wavelengths and footprints as real parts available. All selected LED chips have an edge length of $360 \mu\text{m}$. They are arranged in a two by two array at a chip gap of $d_{gap} = 50 \mu\text{m}$. Using these settings, simultaneous projections of all four sources have been rendered as false color images at projection distances of 100 mm, 250 mm, 500 mm and 1 000 mm. The results of these simulations are depicted in Fig. 5.19.

Using a single condenser lens without additional optical elements will form a near-collimated beam of comparably poor homogeneity, rendering this concept to be

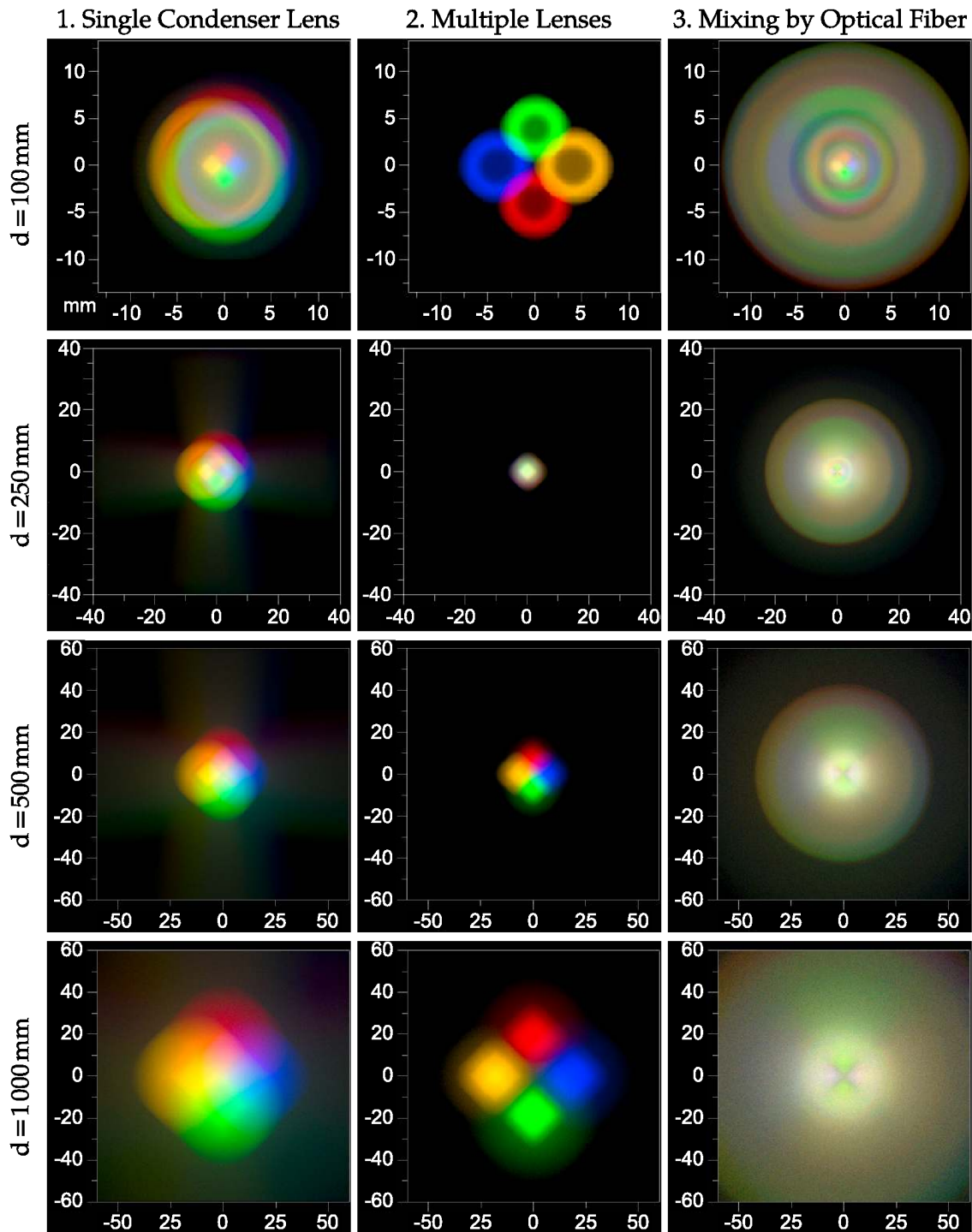


Figure 5.19: False color images of simulated projections from three concepts at four projection distances. All units in millimeter. Note that the scale changes with projection distance.

insufficient. Especially at $d = 100\text{ mm}$ it is clear that this is an imaging optic. The pattern of the LED array is sharply projected at the center of the beam.

The multiple lens setup was optimized on a reference spot at a distance of 250 mm, where all light is concentrated homogeneously within a diameter of only $\varnothing = 12\text{ mm}$. The downside of this approach is clearly the beam homogeneity, which worsens while moving away from the optimal point. Just as an auto focus of camera lenses, the optics can theoretically be readjusted to match every measurement distance. However, developing a mechanical actor to perform such an adjustment would be extremely challenging with respect to the application goals in terms of speed and robustness. Besides that, it would be necessary for the system to estimate its current measurement distance without being correctly adjusted beforehand. Facing these difficulties, an automated adjustment is disregarded.

The results show that the use of an optical fiber produces the best homogeneity over all distances. Nevertheless, the pattern of the LED array is visible at the center of the projection at $d = 100\text{ mm}$ even with this concept. So, this is not a true nonimaging optic, but it is a much better approximation of a nonimaging optic than the other simulated concepts. Despite this, the beam formed with the optical fiber yields large diameters, especially when compared to the concept comprising multiple lenses. Thus, this approach is chosen as the best available trade-off for this work.

Unfortunately, the beam widths of all projections at $d = 1000\text{ mm}$ are clearly larger than the desired $\varnothing_b = 21\text{ mm}$ for hand safety, as derived in Sec. 5.1.4. The beam formed by the chosen concept yields a beam width of $\varnothing_b = 6.6\text{ mm}$ at $d = 100\text{ mm}$ with an opening angle of $\alpha_b = 2.64^\circ$ [5]. Assuming an equal widening of the beam, the beam width reaches a diameter of $\varnothing_b = 21\text{ mm}$ at a distance of $d = 413\text{ mm}$. In consequence, the system would fulfill the requirements for hand safety for measurement distances of at most $d = 413\text{ mm}$, disregarding the safety margin required for sufficient reaction

speed as discussed in Sec. 5.1.3. Considering the requirements for finger safety, the **beam width** reaches a critical diameter of $\varnothing_b = 11$ mm at a distance of $d = 195$ mm (see Sec. 5.1.3). Considering these results as well as the results presented in prior work, the violation of the requirement for hand safety at distances of $d \geq 413$ mm is accepted for this work.

5.2.2 Electronics

Transmitter

Driving an **LED** to maintain a constant level of emitted radiance is not trivial. The radiance of **LEDs** is primarily related to the forward current, which varies as an exponential function of the forward voltage. Furthermore, the series resistance of an **LED** chip does not depend on the forward current or voltage alone, but also on its temperature and state of degradation [67]. To maintain a constant forward current, the forward voltage must be decreased linearly with the temperature. This cannot be achieved using a simple dropping resistor, as the total resistance of **LED** and dropping resistor will decrease with increasing temperature and the forward current will increase. A higher forward current additionally increases the self-heating of the **LED**, which then results in a furthermore reduction of its series resistance. Alternatively, a driving circuit can be used to actively control the forward current. For this purpose, convenient drivers with adjustable forward current are available¹.

The emitted radiance is decreasing as an exponential function of increasing temperature, if the current is held constant. To compensate this, the forward current can be readjusted as described by Bera et. al. [68]. Yet, the peak-wavelength of the **LED** will increase linearly with the temperature, even if the radiant power is controlled.

¹For instance, Infineon BCR450 or ILD4035.

According to a data sheet by Epitex Inc.¹, the peak-wavelength of an LED with a nominal peak-wavelength of 1550 nm varies from 1530 nm to 1590 nm within an ambient temperature range from 0 °C to 80 °C. This spectral shift could have a severe influence on the obtained spectral signature, which can result in false classifications. A way to take this spectral dependency into account is to regulate the temperature of the LED in the first place. This could simply be achieved by controlling an active heater element next to the LED. Employing such a heater, a target temperature of operation could be held as long as the ambient temperature does not exceed this target temperature with respect to the LED's self heating. A more sophisticated way to regulate the temperature is to use a Peltier effect based thermoelectric cooling. Cooling an LED instead of heating it up has the advantages of increasing the maximum optical output power as well as severely decreasing the LED's degradation rate and thus elongating its mean time to failure (MTTF) [67]. However, condense water may occur due to the cooling, which has to be considered for the system design.

Receiver

The receiver must be capable of performing a simultaneous measurement at all available photodiodes. To achieve this, a dedicated circuit to integrate the photocurrent can be supplied per photodiode. Integrating the photocurrent over the entire exposure time, which is given by the strobe pulse duration of the LEDs, instead of sampling at a single instant increases the signal-to-noise ratio (SNR). A single multiplexed analog-to-digital converter can then read all resulting voltages sequentially, if the integrating circuits are able to hold a sampled signal over a sufficiently long period of time.

¹<http://www.epitex.com/> (online 2012-12-22)

Self Testing Measures

First of all, self testing measures must be provided to monitor the correct behavior of the **microcontroller**. This can be done by using a single **microcontroller**, which is monitored by a watchdog¹. In this case, the **microcontroller**'s embedded software must set a number of flags at crucial waypoints within the main loop. At the end of the main loop, these flags must be checked using defined validity conditions. If these conditions are met, it can be assumed that the embedded software is in a valid state and, therefore, the watchdog can be reset. In the case of a failure, the watchdogs signal can trigger a warning to the user (e.g. flashing a warning light) or initiating an emergency stop of the machine in question.

Using a dedicated watchdog fits to the concept of a single-channel system with a test unit, as described in ISO 13849-1 and denoted as a *category two system*. Alternatively, a category three system would employ two **microcontrollers**, which must perform cross comparisons of their results or states. A category four system would have the same outline as a category three system, but with an average diagnostic coverage of $DC_{avg} \geq 99\%$, instead of $DC_{avg} \geq 60\%$ [46, Sec. 6.2].

Having a monitored **microcontroller**, tests for the other components of the sensor must be in place. For instance, the communication channel that is used to trigger a safety function must be tested periodically. This can be done by transmitting test messages, e.g. if a serial interface is used.

Besides these general diagnostic measures, which can be applied to a wide range of safety equipment, appropriate measures to monitor the components that are required for the operation of the sensor must be specified. For the discussed **AOMCPDs**, the transmitter can be tested by measuring the voltage drop across a shunt resistor, which

¹A watchdog monitors a periodic signal. If this signal is absent, the watchdog will periodically generate pulses itself. These pulses are usually used as a reset to the monitored **microcontroller**.

is in series to the LEDs. This way, it can be monitored that no current is flowing while the LEDs are deactivated as well as that the desired current is flowing through each LED during pulse time. However, this measure effectively tests the switches and current regulators, but is only able to detect the LED failure mode of an open circuit. As the LED is usually connected in series to its driver, only an open circuit will prevent that the desired pulse current can flow. To cover the failure modes of a short circuit or even a change of the series resistance of the LED beyond the tolerance limits, the voltage drops across each LED needs to be monitored.

The receiver can be tested indirectly, as each pulse of an LED should result in a positive change of the read signal. Exceptions might occur if the next surface facing the sensor is outside the range of operation or if the surface has an extremely high absorption rate. Furthermore, the projection of the reflected beam on the receiver should usually cover at least two detectors. This way, blind detectors could be identified by plausibility checks. A high diagnostic coverage can be reached by installing at least one additional LED which is directly pointing onto the photodiodes. Such an LED can be used to generate pulses of well-defined intensity and duration to check if all photodiodes are responding within predefined tolerances.

The function of the sensor might also be impaired by pollution of the protective screen, if the resulting signals are attenuated or distorted beyond acceptable limits. Such a scenario is a special case, as it is caused by external conditions instead of a failing component. Therefore, special measures for dust detection could be used. Experiments were carried out using an additional LED to illuminate the protective screen of the receiver at an angle of 30° as depicted in Fig. 5.20, which is similar to the operation principle of state-of-the-art dust sensors¹. If the protective screen is

¹E.g., dust sensor type GP2U06 by SHARP

polluted from the outside, the stains will be illuminated and eventually scatter light towards the detector array.

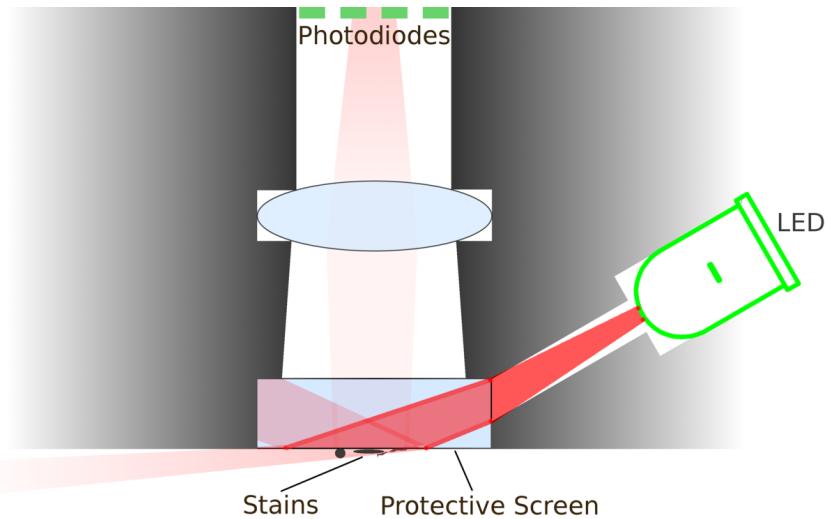


Figure 5.20: Detecting dust using an additional LED.

Fig. 5.21 illustrates a practical experiment, which was carried out using an earlier prototypical implementation [69]. Sawdust was applied to the protective screen to achieve different soil levels. The measurement results yielded a sufficient sensitivity of the sensor to the soil, as the scattered light coming from medium soil levels led to a significant increase of the measured signals.

In the next section, system specifications for a prototypical sensor implementation are derived with respect to the presented safety requirements and design concepts. These specifications should be chosen considering the requirements related to the targeted applications as well as to available technical solutions.

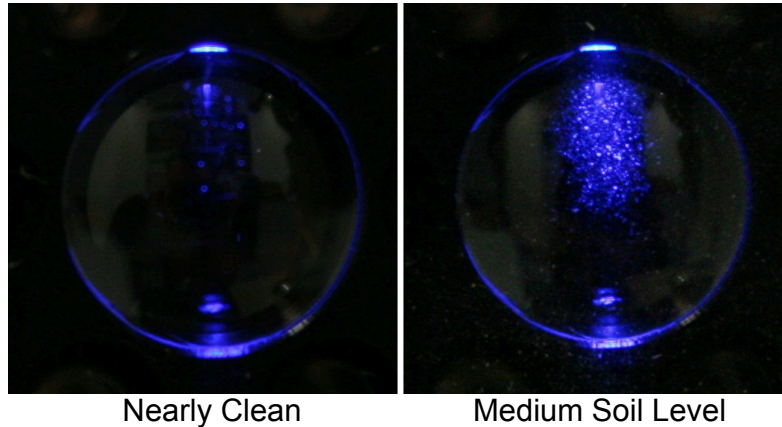


Figure 5.21: Sideways illuminated protective screen showing very low and medium soil level.

5.3 System Specifications

With the safety requirements and the sensor concept presented in the previous sections, it is now possible to define the system specifications for a prototypical implementation. The section is subdivided into functional and technical specifications.

5.3.1 Functional Specifications

Differentiable Materials

The targeted system is intended for *skin detection*. In consequence, it must be able to differentiate human skin from surface materials of common work pieces like wood, different types of plastics and metal.

Distance Range

The sensor must be capable to operate in a distance range from 0.1 m to 1 m, which should cover the requirements of many applications in the context of manually fed machines.

Beam Width (Detection Area)

Generally, the **beam width** should be as small as possible. The specified goal is a system which is finger safe for short distances of ≤ 0.2 m. As discussed in Sec. 5.2.1, the beamforming does not achieve the requirements for hand safety, as derived in Sec. 5.1.4, over the whole distance range. Therefore, a reduction of the distance range for safe hand detection must be accepted for this prototype.

Speed

A single measurement and signal processing must be performed within 2 ms to allow a measurement frequency of $f_{min} = 500$ Hz. For hand safety, the signal acquisition time must be at most $t_a \leq 1$ ms for a measurement frequency of $500 \text{ Hz} = \left(\frac{(21 \text{ mm} - 15 \text{ mm})}{K} - 1 \text{ ms} \right)^{-1}$ and a **beam width** of $\varnothing_b = 15$ mm (see Eq. 5.2 on page 58). According to simulations of the third transmitter design presented in Sec. 5.2.1, this **beam width** is reached at a distance of $d \approx 300$ mm. In conclusion, the minimum objective is to achieve true hand safety for measurement distances of $d_{min} \leq d \leq 300$ mm.

Permissible Temperature Range

The system must operate at a temperature range from 0°C to 50°C and a relative humidity of $\leq 95\%$, as defined in IEC 61496-1.

Ambient Light

The system must tolerate indirect sunlight and fluorescent room lighting, as these are the most relevant ambient lighting conditions. Ambient light compatibility tests for **AOPDs** as defined in IEC 61496-2 should be applied as far as applicable.

Modes of Operation

The system must operate in single-sided and two-sided configurations as in Fig. 5.6 on page 67 and 5.7 on page 68.

Eye Safety

The system must be compliant to LED class 1M as defined in IEC 60825-1.

Dimensions

Compact dimensions are important to allow a dense arrangement of sensors and to keep the housing of the sensors small enough to ensure that the feeding of workpieces to a machine is not obstructed. Anyways, the tolerable dimensions cannot be judged without knowing the actual setup of a machine and desired sensor positions. Therefore, no strict limits are defined for this work.

5.3.2 Technical Specifications

Wavebands

Due to the absorption bands of air, the spectral range from 1340 nm to 1450 nm must be avoided (see Fig. 5.3 on page 62). Besides this restriction, all wavebands should be chosen with respect to the spectral responsivity of InGaAs photodiodes if at least one waveband is located above 1100 nm (see Fig. 5.5 on page 66). In consistence with these restrictions and with the preexaminations presented in Sec. 4.3, LEDs with peak-wavelengths at $\hat{\lambda}_0 = 830\text{ nm}$, $\hat{\lambda}_1 = 1060\text{ nm}$, $\hat{\lambda}_2 = 1300\text{ nm}$ and $\hat{\lambda}_3 = 1550\text{ nm}$ are chosen.

Interface

The sensor must provide an interface to a control unit or computer. For instance, a 1 Mbit/s CAN-Bus interface could be used, as this type of interface was designed for industrial demands.

Self Testing Measures

The sensor must implement rudimentary self testing measures beyond the possibility of pure software-based tests such as a memory test. Particularly, the currents running through the LEDs must be readable by the embedded system for self-monitoring and the functionality of the receiver unit must be testable by running dynamic plausibility checks.

5.3.3 Delimitation of this System Specification

Some general requirements which are relevant for the certification of industrial products, such as electromagnetic compatibility, IP rating of the enclosure or shock resistance, are not considered within this work. It is very likely that all those requirements can be fulfilled and are not contradictory with the others, if enough effort is put into system design and testing.

5.4 Prototypical Implementation

An overview on the prototypical implementations of the concept is presented in this section. These prototypes aim for compliance with the presented system specifications and are used for an evaluation of the concept, which is presented in Chap. 7.

5.4.1 Implemented Concept

The prototypical implementation of the sensor system was designed to fulfill the specifications formulated in Sec. 5.3.

Optics

Body and optical components were designed in consultation with Epigap-Optronic GmbH, which manufactured and delivered a total of twelve bodies in two batches. Three different versions of the body were ordered for comparison, which are denoted as mark 1, 2 and 3. Mark 1 has a shorter optical fiber and mark 3 has a receiving lens of longer focal length as shown in Tab. 5.3.

Table 5.3: Modified parameters for *Skinner* mark 1, 2 and 3.

	Mark 1	Mark 2	Mark 3
Fiber Length	$l = 10 \text{ mm}$	$l = 20 \text{ mm}$	$l = 20 \text{ mm}$
Focal Length of Receiving Lens	$f' = 23.25 \text{ mm}$	$f' = 23.25 \text{ mm}$	$f' = 29.35 \text{ mm}$
LED Chip Gap	$d_{gap} = 100 \mu\text{m}$	$d_{gap} = 50 \mu\text{m}$	$d_{gap} = 50 \mu\text{m}$
LED Group Rotation	$r = 0^\circ$	$r = 45^\circ$	$r = 45^\circ$
Produced Amount	6	5	1

The mark 1 bodies were produced within the first batch. Mark 2 and 3 share the elongation of the optical fiber as well as the modifications to the LED placement, which are motivated by a relatively bad homogeneity of the beam created by mark 1 sensors for distances of $d < 150 \text{ mm}$ and artifacts discussed in Sec. 7.2.1. The unique characteristic of mark 3 is the longer focal length of the receiver's lens.

Having a longer focal length leads to a fuzzier projection of the beam's reflection onto the receiver line, as the aluminum body is unchanged and the photodiodes are positioned at the same distance to the lens. The advantage is that the projection covers more photodiodes and the incident energy to each photodiode changes less with respect to the measuring distance, resulting in an easier distance estimation and

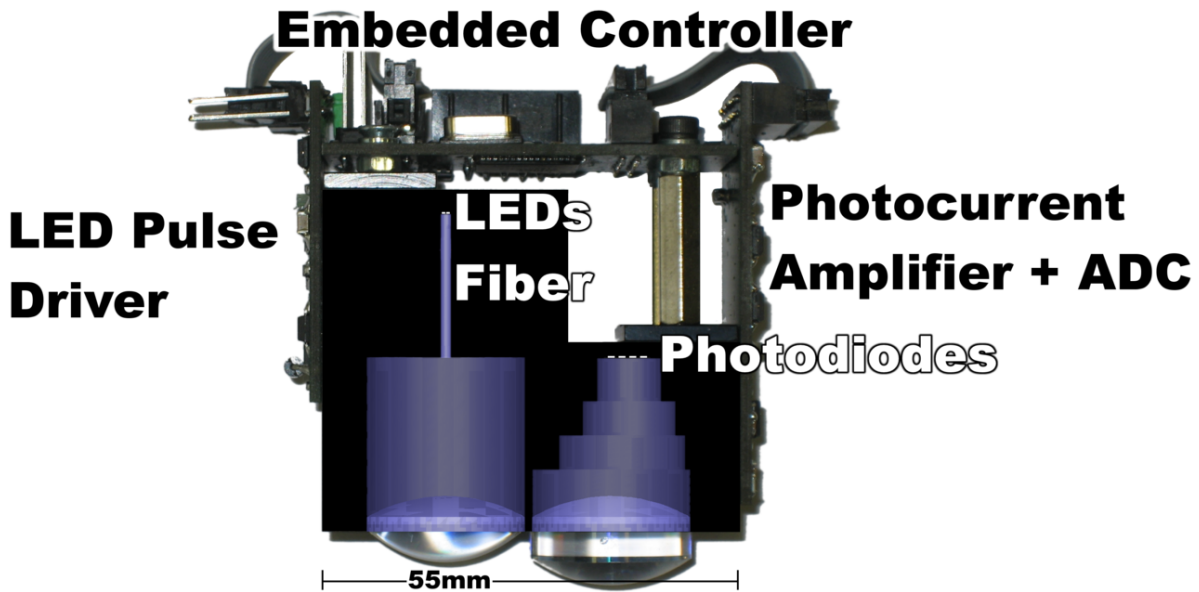


Figure 5.22: Virtually augmented photograph of the implemented sensor. Source: [5, Fig. 3].

data function as discussed in Sec. 7.1.2 and 7.1.3. The disadvantage is a significant loss of received optical energy per photodiode, as discussed in Sec. 7.1.3 as well. Fig. 5.22 illustrates the outline of a Skinner mark 3 sensor. All components are mounted onto the body, which is made of black anodized aluminum. Aluminum was used for its good machinability and shape stability. It was anodized to absorb internal stray light, which turned out to be a mistake as black anodized aluminum is highly reflective within the near infrared spectrum. In future work, black plastics should be used, which usually absorb the majority of radiation over the visual and near infrared spectrum.

Electronics

The structure of the sensor's complete circuitry is illustrated as a block diagram in Fig. 5.23. A primary microcontroller provides an external interface and controls the transmitter and receiver.

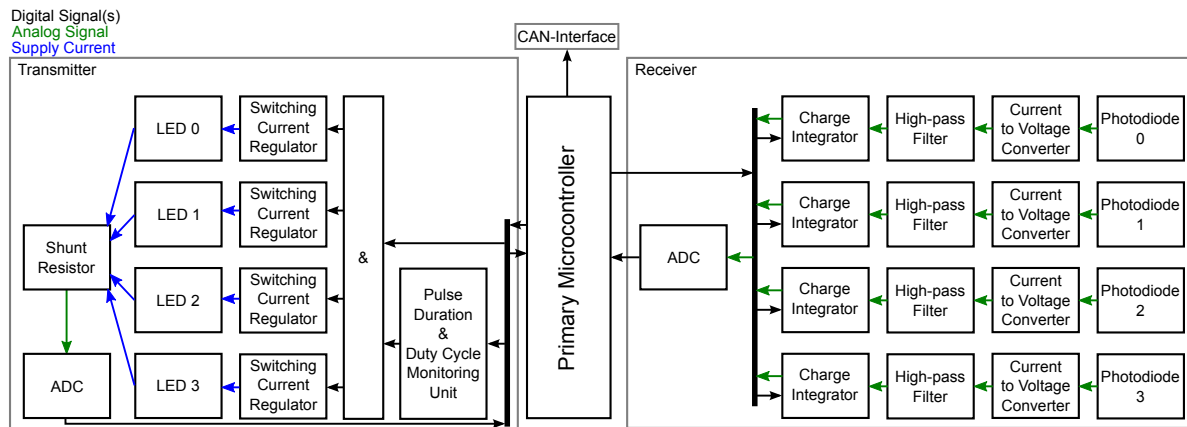


Figure 5.23: Block diagram of the Skinner sensor.

The transmitter comprises a monitoring unit to enforce a maximum pulse duration and duty cycle for each LED, to protect them from damage due to overuse. The signals of the primary microcontroller and the monitoring unit are combined by logic gates through a logic AND operation for each LED. Switching current regulators are used to activate the LEDs if requested through the corresponding AND conjunction. The supply currents of all LEDs are routed via a common shunt resistor. An analog-to-digital converter (ADC) is used to read the voltage across the shunt resistor to allow functional tests of the components.

The receiver comprises an ADC as well as four charge integrators, which are directly controlled by the primary microcontroller. Each charge integrator has two logical input signals to control the integration or perform a reset. The charge integrators are connected with the photodiodes through individual amplifying current-to-voltage converters and high-pass filters. This way, the primary microcontroller is able to control the entire acquisition process as described in Sec. 6.1. Further details on the actual implementation of the functional blocks are presented in this section.

As depicted in Fig. 5.24, the photodiodes and LEDs are mounted and directly bonded onto two small PCBs. These PCBs are designed to fit into notches at the back of the body, where they are fixed by two screw-locking brackets. Optionally, a Peltier

element can be installed at the back of the transmitter's PCB in order to regulate their temperature, which has not been tested by the time of this work.

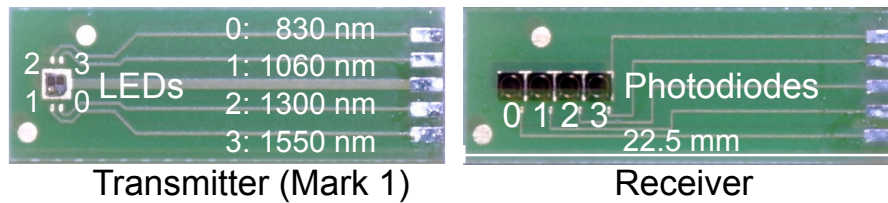


Figure 5.24: LEDs and photodiodes on their PCBs.

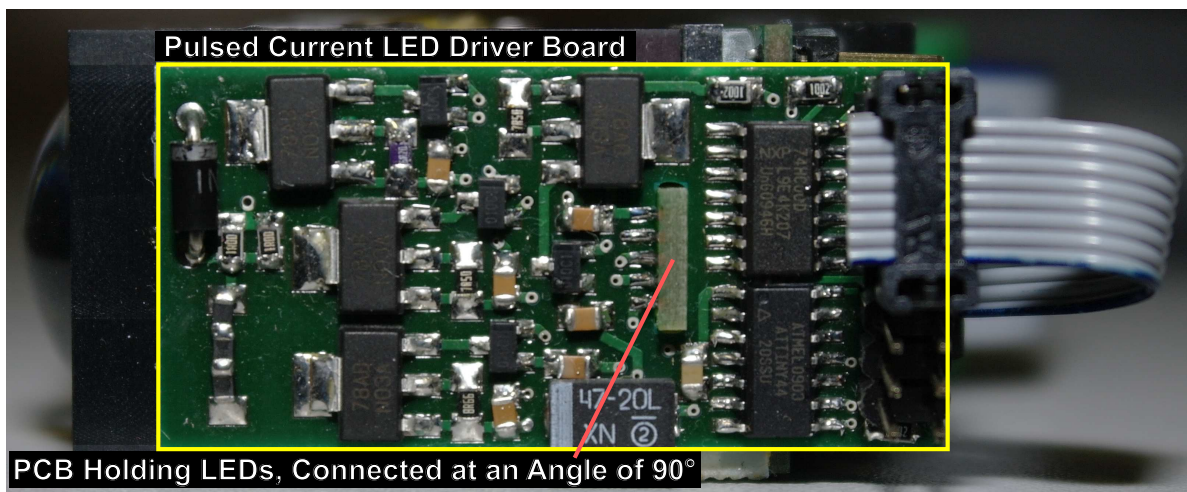


Figure 5.25: LED driver to generate pulses at controlled current.

The PCB holding the LEDs is soldered to the driver board at a right angle as shown in Fig. 5.25. The pulse current drivers are adjusted to currents of up to 200 mA, which is within the LED's rating if the pulse time is $t_p \leq 50 \mu\text{s}$ and the duty cycle is $\leq 50\%$. To prevent damage to the LEDs by violation of the allowable pulse time or duty cycle, this driver board features an ATtiny44 microcontroller which monitors the LED activation signals and is able to interrupt them. ATtiny microcontrollers are based on the proprietary AVR[®] 8-Bit, in-order execution, reduced instruction set computing (RISC) architecture by Atmel Corp., just as the better known ATmega and Xmega

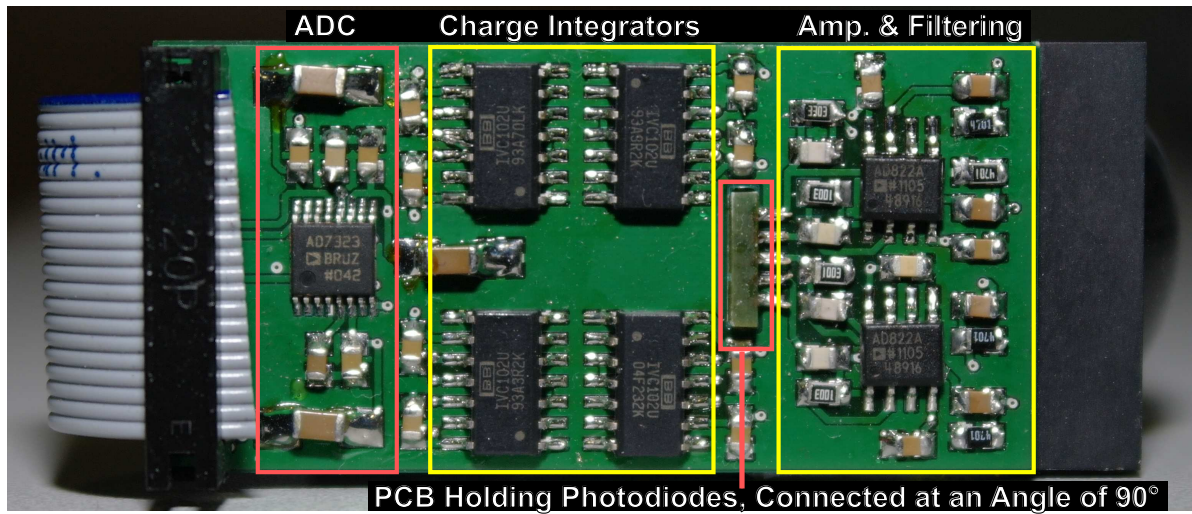


Figure 5.26: Photocurrent readout PCB.

microcontrollers. By default, all LED pulses have a duration of $t_p = 40 \mu s$, which leads to a duty cycle of 20% for measurement frequencies of $f_{min} = 500 Hz$.

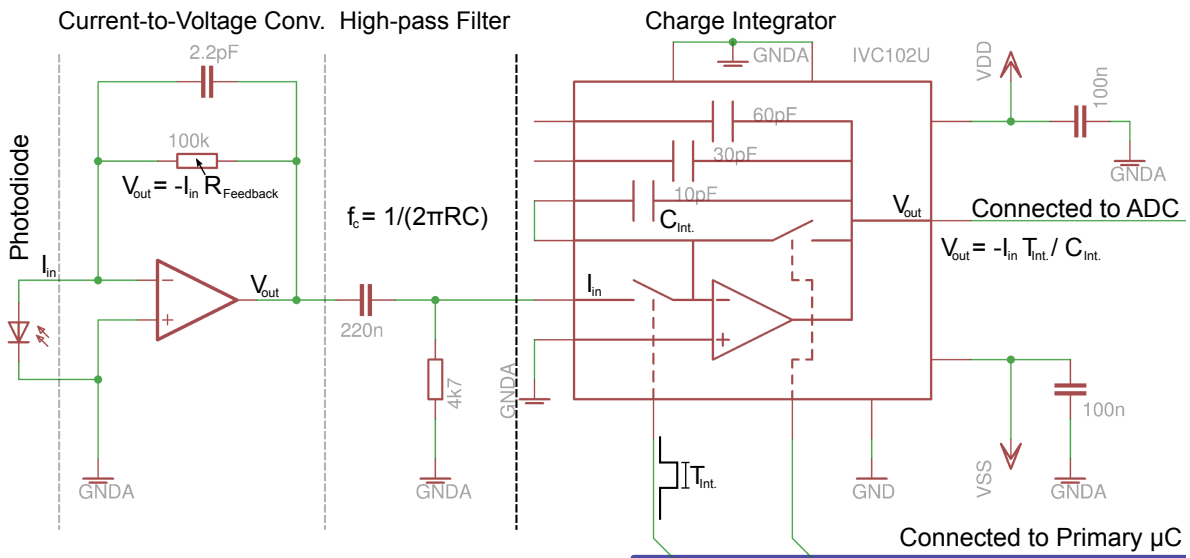


Figure 5.27: Schematic of the circuit for a single photodiode.

Similar to the LED driver board, the photocurrent readout board is soldered to the small PCB holding the actual photodiodes at a right angle. Fig. 5.26 illustrates the photocurrent readout board, which is basically structured in three function blocks.

A schematic of the first two blocks is presented in Fig. 5.27. The cathode of each photodiode is connected to an amplifying current-to-voltage converter followed by a passive high-pass filter of first order with a cutoff frequency of $f_c = 154\text{Hz}$. These components form the first block with respect to Fig. 5.26. Direct current and frequencies of $\leq 120\text{Hz}$, as typically caused by sunlight and artificial illumination, are (partially) rejected in the resulting signals. These signals are then connected to four charge integrators type IVC102U from Texas Instruments. It might be irritating that a current-to-voltage converter is set between the photodiode, which is a current source, and the charge integrator, which is an integrating current-to-voltage converter. The reason is that a continuous-time high-pass filtering can only be performed before the charge integrator discretizes the signal. However, the current produced by the photodiode is only in the magnitude of pA to μA , which is rather impractical as an input to a passive high-pass filter. In contrast, the current-to-voltage converter offers a signal within the magnitude of several mV and is capable of driving much higher output currents of up to 15mA ¹. Simulations and measurements have shown that the input current I_{in} to the charge integrator is proportional to the photocurrent and amplified by a factor of about -12. The computation of the actual amplification factor is complex, as it depends on many components including the high-pass filter's capacitor and resistor as well as the input characteristics of the ADC and the IVC102U's internal operational amplifier, which are permanently connected to the integrating capacitor. Therefore, the use of a simulation tool (e.g. B²Spice from Beige Bag Software Inc.) is appropriate to characterize the circuit's properties.

Each charge integrator is individually connected to the primary **microcontroller** by its *integrate* and *reset* control input. This way, a synchronous integration of the signal in parallel to each **LED** pulse can be performed by the **microcontroller**. When

¹Depending on the components specifications

the integration is completed, a stabilized output voltage is available at each charge integrator. These outputs are connected to the last function block comprising a multiplexed 13-Bit¹ ADC to sequentially convert these voltages to digital information, which is then transmitted to the primary microcontroller. After conversion of all four voltages, the charge integrators are reset by triggering their reset lines for a time period of 10 μ s.

5.4.2 Primary Microcontroller

An AT90CAN128 microcontroller by Atmel was chosen as primary controller. This controller features a 1 Mbit/s CAN interface and an integrated watchdog. The controller is running at a CPU clock of $f_{CPU} = 16$ MHz, which is the maximum rating for this type. As described in Sec. 7.1.5, the computational power of this microcontroller is too low to achieve a measurement frequency of $f_{min} = 500$ Hz. Therefore, a second version of the embedded system comprising a more powerful AT32UC3C0512C microcontroller, which is based on Atmel's 32-Bit AVR[®] architecture with a CPU clock of up to $f_{CPU} = 64$ MHz was developed. Similar to the AT90CAN128, the AT32UC3C0512C features a CAN interface and a watchdog. Additional features, such as a dedicated floating point unit (FPU) or higher clock rates are useful to improve the overall performance of the embedded software.

The CAN bus was selected as the primary interface to the sensor, as this bus was designed for rough environments and safety critical applications. Alternatively, a USB interface is available to establish a direct connection to a desktop computer or notebook.

¹12-Bit amplitude plus 1-Bit sign

5.4.3 Previous Prototypes

A total of three prototypical implementations of multispectral point sensors for skin detection were designed prior to the presented *Skinner* sensor, as described in Sec. 3.2. An article presenting the first prototype was published by Reinert et al. [35]. All of these earlier prototypes comprise transmitters with a separate lens for each LED instead of a common optical fiber, as described in Sec. 5.2.1. These transmitters are emitting at two to three different wavebands, instead of four as for the *Skinner* sensor. Furthermore, each receiver of the earlier prototypes comprises only one photodiode and thus does not feature an estimation of the measurement distance. Another unique feature of the *Skinner* sensor over its predecessors is the use of charge integrators to amplify the signals coming from the photodiodes.

In the next chapter, methods for signal acquisition and processing as well as material classification are proposed with respect to the *Skinner* sensor.

Chapter 6

Acquisition, Data Processing and Classification

The methods and algorithms used for signal acquisition and data processing are discussed in this chapter. Furthermore, calibration steps are required for some steps within the data processing chain, which are also discussed. As seen in Fig. 1.1 on page 2, the aim of the signal processing chain is to retrieve a spectral signature, which can then be used for material classification. The entire process from acquisition to material classification is also summarized as a flow chart in Fig. 6.1. Once a spectral signature is retrieved, it is classified using sophisticated state-of-the-art methods described in Sec. 2.3 and Sec. 6.4.

6.1 Data Acquisition

A well timed acquisition procedure is necessary to exploit the potential offered by the hardware. As described in Sec. 5.4.1, the photocurrent readout circuitry features a high-pass filter of first order with a cut-off frequency of $f_c = 154\text{Hz}$. This filter is

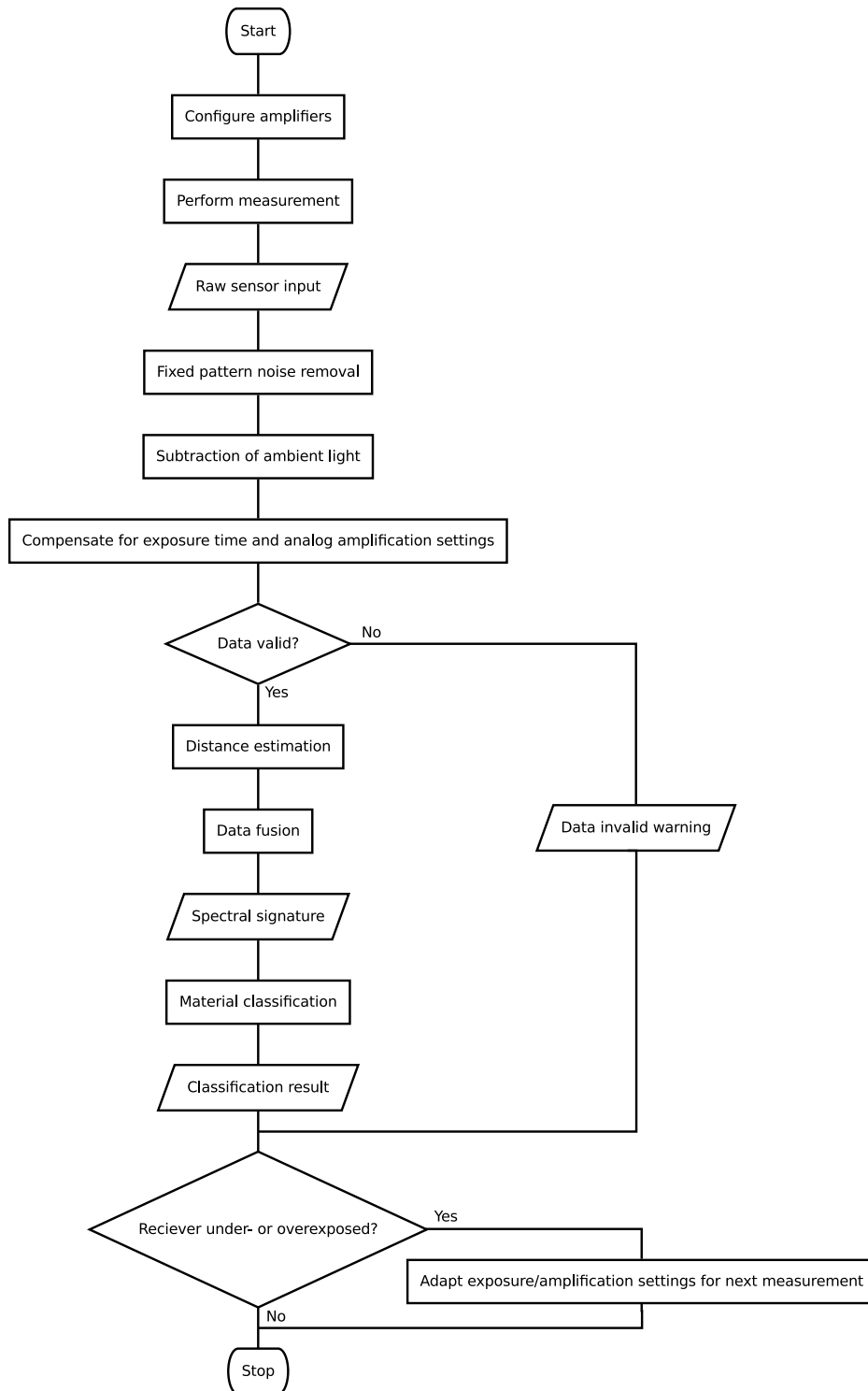


Figure 6.1: Flow diagram showing data acquisition and processing.

intended to reject ambient light caused by sunlight or electrical light sources emitting within the near-infrared spectrum, such as incandescent lamps. These lamps are oscillating with their supply voltage, which usually has a frequency of 50 Hz or 60 Hz. As the lamps light up at both positive and negative half-waves, the emitted light is oscillating at twice the frequency of the supply voltage. Fig. 6.2 illustrates how ambient light oscillating at frequencies from 100 Hz to 120 Hz will only be attenuated by less than half their original amplitude and constant ambient light will be suppressed strongly. In consequence, signals measured in presence of artificial lighting are much more problematic than sunlight, which can assumed to be relatively constant.

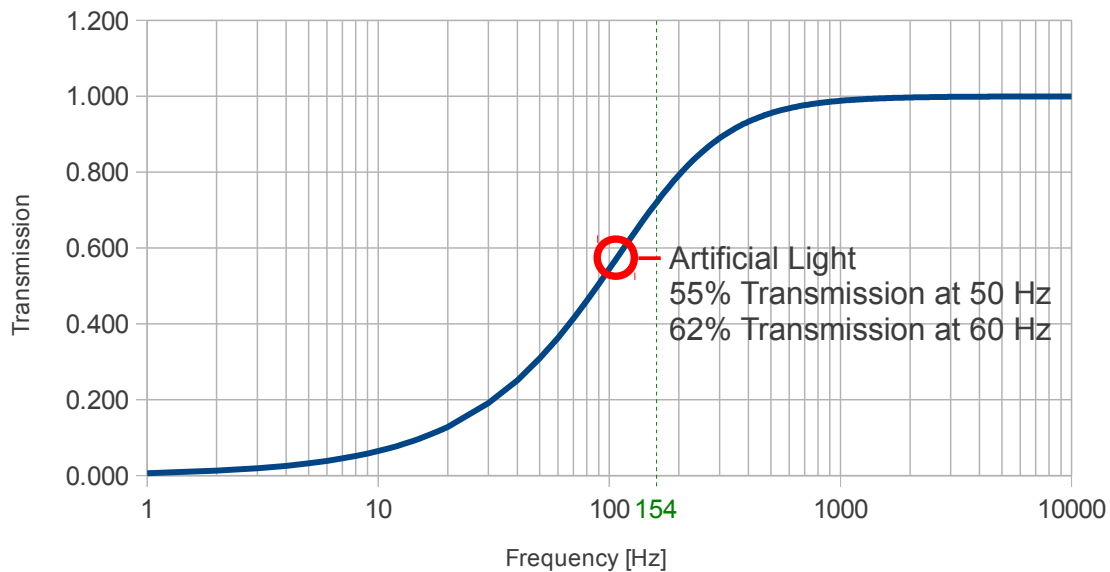


Figure 6.2: Transmission characteristic of the used $f_c = 154\text{Hz}$ high-pass filter of first order.

As the functional principle of the filter can be interpreted as a continuous adjustment of an offset signal to strive for an amplitude of $a \approx U_{ref} = 0\text{V}$, the effect can be algorithmically improved by sampling the signal just before transmitting a strobe pulse and using this signal as a reference rather than the static reference potential

$U_{ref} = 0V$. This can be understood as a form of correlated double sampling [70]. Using the AT90CAN128 microcontroller, it takes a total of $t = 150 \mu s$ from the beginning of the reference measurement to the end of the following strobe pulse. As illustrated in Fig. 6.3, this time period is subdivided into $t_i = 40 \mu s$ integration time of the reference signal, $t_h 10 \mu s$ pause to wait for the integrator's output voltage to settle, $t_{read} = 40 \mu s$ analog to digital conversion time for all four integrators, $t_r = 20 \mu s$ to discharge the integrator¹ and another $t_i = 40 \mu s$ to integrate over the pulse response.

$$\Delta a = 2 \sin\left(180r \frac{\pi}{180}\right) = 0.113$$

(6.1)

with $r = \frac{f_a = 120 \text{ Hz}}{f_t = 150 \mu s^{-1}} = 1.8 \times 10^{-2}$

The phase of a sinusoidal signal with a frequency of $f_a = 120 \text{ Hz}$ shifts by $360^\circ 120 \text{ Hz} / 150 \mu s^{-1} = 6.48^\circ$ within a time period of $f_t = 150 \mu s$. According to equation 6.1, the change of the ambient signal during the acquisition of a pulse response is at most 11.3% with respect to its peak-to-peak amplitude. As shown in Fig. 6.2, 62% of the original signal's peak-to-peak amplitude can pass the filter at 120 Hz. Using an additional reference measurement, the offset error drifts at most 11.3% of the remaining 62%, which is 7% of the signal's original amplitude. Furthermore, the maximum measurement error is less than these 7%, as this is the total drift from the beginning of the first integration to the end of the second integration. As the integrator averages the input signal, the magnitude of the measurement error can be assumed to be the signal's drift from the middle of the first to the middle of the second integration period. For an integration time of $t_i = 40 \mu s$, the time span can be reduced to $150 \mu s - 2 * 20 \mu s = 110 \mu s$, which results in a maximum drift of 5.1%.

Compared to the total offset error, which can be as high as 62% of the original

¹Including $t_p = 10 \mu s$ pause, as recommended in the datasheet of the IVC102 by Texas Instruments.

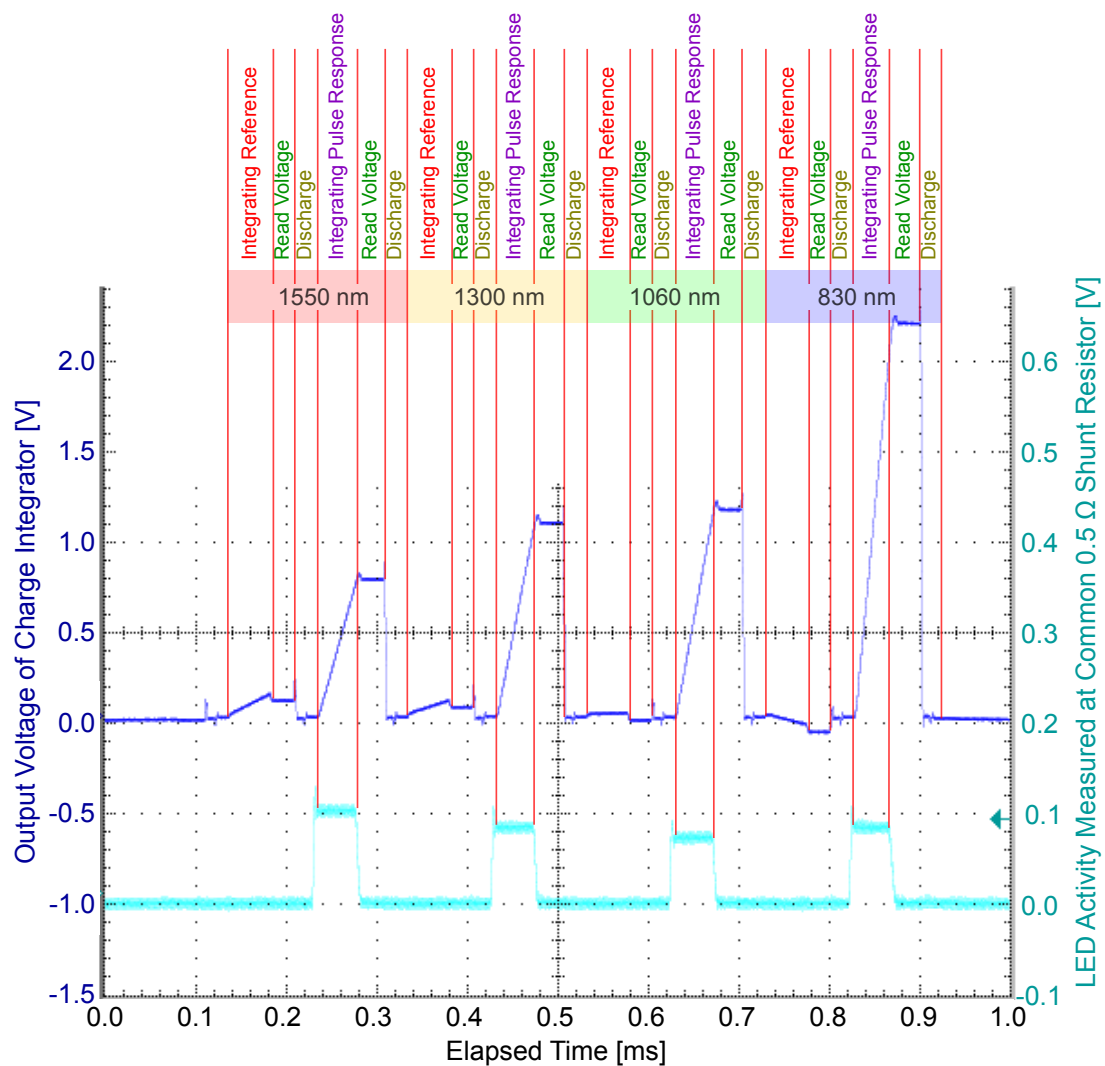


Figure 6.3: Output signal of a charge integrator during signal acquisition.

amplitude, this method reduces the maximum measurement error by a factor of twelve. Due to a faster communication with the [analog-to-digital converter](#) via the [serial peripheral interface \(SPI\)](#) when using the more powerful AT32UC3C0512C [microcontroller](#), the time required to read the voltages from all four integrators is reduced from $t_{read} = 40 \mu\text{s}$ to $t_{read} = 25 \mu\text{s}$. In consequence, the maximum measurement error is furthermore reduced to 4.4%. As discussed in [Sec. 7.3.1](#), an error of 4.4% is still severe in comparison to the potential 13-Bit resolution of the used analog-to-digital

converter. Note that the resulting signal will be cut off if the summed amplitudes of the attenuated 100 Hz or 120 Hz signal and the pulse response exceeds the rails of the analog output voltage of ± 15 V.

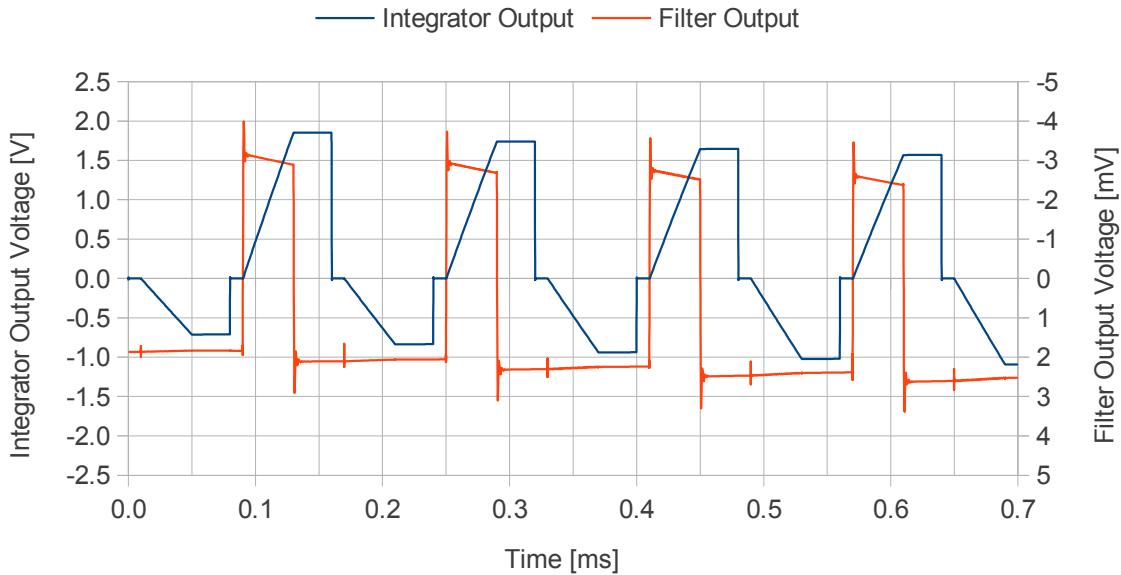


Figure 6.4: Simulation of high-pass filter and integrator output.

Fig. 6.3 illustrates the phases and timing for a complete signal acquisition of all four wavebands. Looking at the sampled reference voltages, a drift into the negative voltage range can be seen. This drift results from the high-pass filter as it reacts on the pulse responses, which have relatively high amplitudes. In consequence, the measurement itself induces a shift of the reference voltage. Fig. 6.4 is generated from a B²Spice¹ simulation and illustrates the behavior of the filter as well as the output of the integrator. It is clear to see that the pulse response signals are fading as the filter tries to readjust the offset. Fortunately, the attenuation of the filter depends on the frequency rather than the amplitude and thus the attenuation scales proportional to the input signal. However, the acquired spectral signature can still be distorted

¹A mixed-mode simulation software by Beige Bag Software Inc.

by the filter, as the filter will readjust its offset after every strobe pulse and the slope steepness depends on the amplitude of the offset error. The following measurement will be performed in parallel to the readjustment of this offset-error and, thus, a dependency to the previous strobe pulse (or pulses) is created. According to circuit simulations and measurements, this effect can cause distortions in the magnitude of several percent. However, this distortion is also related to the spectral signature of the respective surface material, which is generally good with respect to the differentiability of different materials. Anyways, the embedded software reduces this problem by generating strobe pulses in descending order from 1550 nm to 830 nm. Reminding the typical remission spectra of human skin, as shown in Fig. 2.1 on page 8, this order acquires small pulse responses first when measuring human skin. As a logical consequence, smaller offset errors are induced first to minimize distortion of the following measurements.

For an integration time of $t_i = 40 \mu\text{s}$, a complete signal acquisition of all four wavebands takes $t_a = 800 \mu\text{s}$ using the AT90CAN128 [microcontroller](#) (see Fig. 6.3 on page 109) and $t_a = 680 \mu\text{s}$ when using the faster AT32UC3C0512C [microcontroller](#). In conclusion, the required minimum measurement frequency of $f_{min} = 500 \text{ Hz}$, as defined in Sec. 5.3.1, can be achieved if the computation time required for data processing and material classification is below the remaining $2000 \mu\text{s} - t_a = 1200 \mu\text{s}$.

6.2 Low-Level Correction

It was observed that switching [LEDs](#) interferes with the integrator's output voltage. This effect is likely to be caused by electric or electromagnetic crosstalk. The [LEDs](#) are driven with currents in the range from 100 mA to 200 mA, while the photodiodes are generating much lower currents in the magnitude from pA to μA .

Measurements have shown that this crosstalk generates a fixed pattern noise corresponding to each pulse response measurement in the range from 15 mV to 30 mV, if a feedback resistor of 100 k Ω is used at the current-to-voltage converter circuit. When increasing the feedback resistor to 330 k Ω , as set for photodiode 0, the offset reaches up to 125 mV. As these offsets are fixed, they can be compensated by simply subtracting them from each measured value as the very first processing step.

The offsets are derived in a calibration process, which is done by performing measurements while the receiver is covered with an opaque cap. This way, no incident light reaches the photodiodes and therefore the unwanted offsets are isolated.

As a final low-level data correction, multipliers are applied to the resulting values that correspond to the reference voltages used by the ADC during acquisition time. The used AD7323 by Analog Devices can select between three different reference voltages: $V_{ref} = \pm 2.5\text{V}$, $V_{ref} = \pm 5.0\text{V}$ and $V_{ref} = \pm 10.0\text{V}$, whereby the voltage represented by the least significant bit V_{lsb} depends on the reference voltage as a function of $V_{lsb} = |V_{ref}|/2^{13}$. In consequence, the multipliers are defined as $V_{ref} = \pm 2.5\text{V} \mapsto 1$, $V_{ref} = \pm 5.0\text{V} \mapsto 2$ and $V_{ref} = \pm 10.0\text{V} \mapsto 4$. Therefore, a signal read at $V_{ref} = \pm 10.0\text{V}$ will be multiplied by four, which provides a virtual resolution of 14-Bit plus sign (1-Bit).

6.3 Data Processing Concept

This section introduces algorithms that are designed to extract a spectral signature out of raw sensor readings. Some of the presented results were also published in the IOP Journal of Measurement Science and Technology [4].

6.3.1 Distance Estimation

As described in Sec. 2.4, the input values of the sensor can be used to perform a distance estimation based on triangulation. Fig. 6.5 shows the relation between the input signal and the measurement distance. The input signal is denoted as a matrix $\mathbf{X}_{in} \in \mathbb{N}^{N \times B}$, as defined in Sec. 2.4.1, where $N \subset \mathbb{N}$ is the amount of available photodiodes or pixels and $B \subset \mathbb{N}$ is the amount of available wavebands.

Fig. 6.5 shows that the signal of each photodiode, with the exception of photodiode $n = 0$, can be approximated by a Gaussian function over the measurement distance. The signal at photodiode $n = 0$ is comparably asymmetric, as the internal shape of the receiver's housing (see Fig. 5.22 on page 98) occludes a portion of the incident light for shorter measurement distances of $d < 550$ mm. Furthermore, the overlap of the signals from neighboring photodiodes is relatively large. A large overlap is important to allow gapless operation over the whole distance range. Without a sufficient overlap, the quality of the acquired signals would be volatile over the specified distance range.

Considering an arbitrary object within the sensor's beam having an unknown surface material, the amount of light reflected towards the receiver depends on the surface material's diffuse reflectance coefficient. Furthermore, the amount of specular reflected light caught by the receiver depends on the surface material's specularity and the viewing angle. As all these parameters are (yet) unknown, a distance estimator cannot simply map the measured amplitudes to a distance. Fortunately, the ratios of the signals from neighboring photodiodes do not depend on absolute amplitudes, but are primarily depending on the spatial distribution of the reflected light on the detector array. As depicted in Fig. 6.6 on page 115, these ratios are steadily changing in between the peak positions of the corresponding pixels within a distance range from 130 mm to about 570 mm. In consequence, these ratios are a good basis to perform a

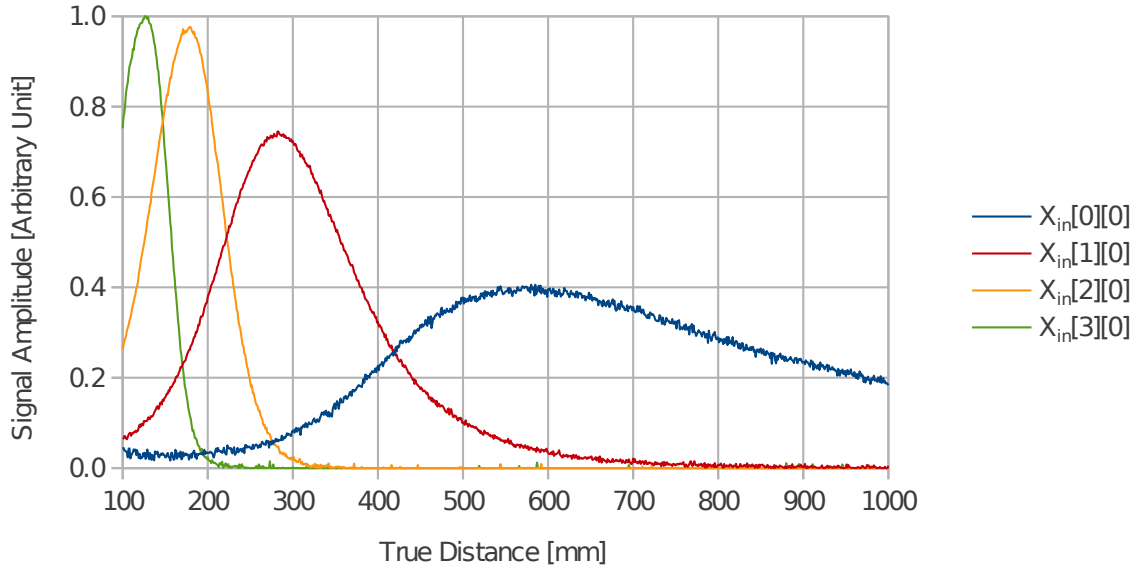


Figure 6.5: Sensor readings of all four photodiodes acquired at $\lambda_0 = 830$ nm ($\mathbf{X}_{in}[0][0]$ to $\mathbf{X}_{in}[3][0]$).

distance estimation over that range. However, the ratios are not developing steadily over the whole distance range. In fact, each slope has a point of inflection, which is a typical result when calculating the ratio of two Gaussian-like slopes [71].

Having points of inflection prevents a unique mapping of a certain distance to a certain value of a ratio. Therefore, a new method is introduced: the **quick binary tree mapping (QBTM)** (see [4]). This method aims to perform an accurate distance estimation using sensors with a small number of pixels or photodiodes, respectively. It starts with the determination of the index $\vec{v}_{max}[b] \in [0, N - 1] \subset \mathbb{N}$ which addresses the pixel with the strongest signal $\mathbf{X}_{in}[\vec{v}_{max}[b]][b]$ of all N pixels concerning waveband b . Furthermore, the index $\vec{v}_{max}[b]$ is a particular element of the B -dimensional vector \vec{v}_{max} with $b \in [0, B - 1]$, whereby each element holds the index of the strongest signal with respect to waveband b . Using this information, a binary decision tree $\mathfrak{T}_{n,b}$ is chosen with $n = \vec{v}_{max}[b] \in [0, N - 1] \subset \mathbb{N}, b \in [0, B - 1] \subset \mathbb{N}$,

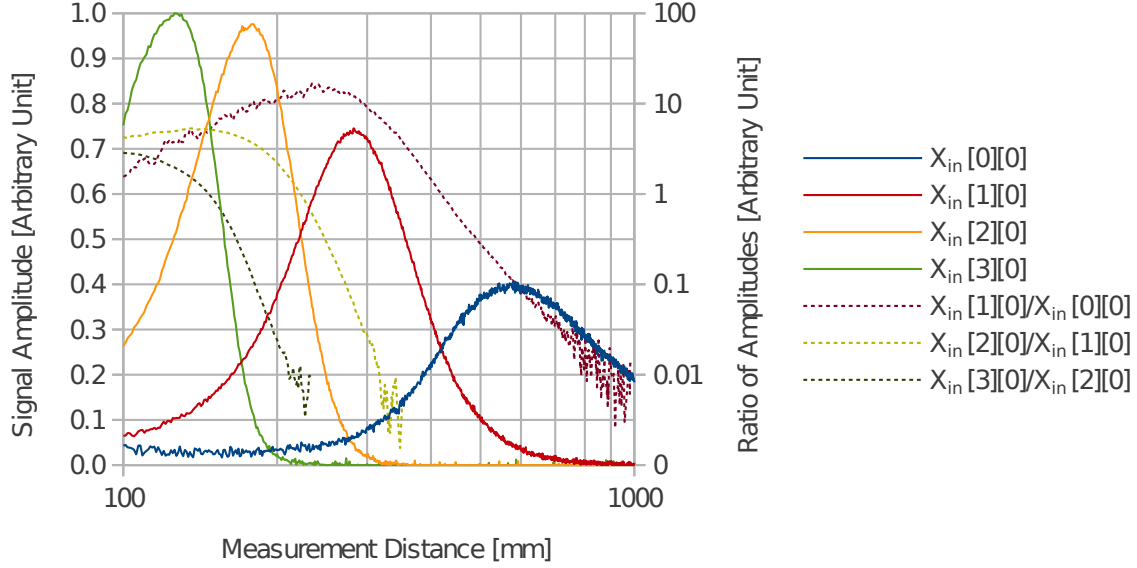


Figure 6.6: Sensor readings combined with ratios of signals from neighboring photo-diodes on a logarithmic scale.

whereby binary decision trees $\mathfrak{T}_{n,b}$ have been raised for every pixel $n \in [0, N - 1]$ in an offline process beforehand. The input signal \mathbf{X}_{in} is transformed in a preprocessing step before being used as input for the decision trees by computing ratios of amplitudes from neighboring pixels. This preprocessing step is defined as $f_Q(\mathbf{X}_{in}, b) = (\mathbf{X}_{in}[0][b]/\mathbf{X}_{in}[1][b], \mathbf{X}_{in}[1][b]/\mathbf{X}_{in}[2][b], \dots, \mathbf{X}_{in}[N - 2][b]/\mathbf{X}_{in}[N - 1][b])$. As explained above, computing these ratios is necessary to remove the material dependent signal gain and, therefore, to isolate the distance dependent information.

Once the ratios are computed, the distance mapping can be performed as $\hat{d}_{\text{QBTM}}(\hat{p}, b, \mathbf{X}_{in}) = \mathfrak{T}_{\hat{p}, b}(f_Q(\mathbf{X}_{in}, b))$ with $\hat{p} = \vec{v}_{\max}[b]$. Binary decision trees are used to evaluate the combined information given by all available ratios, as they are able to derive rules from multidimensional input data. This way, the symmetry of the slopes resulting from the computation of ratios is compensated by the comparison of mul-

multiple ratios, as each measurement distance is mappable to a unique combination of ratios. Therefore, a direct mapping $\mathfrak{T}_{\rho,b}(f_Q(\mathbf{X}_{in}, b)) \mapsto \hat{d}$ is performed.

To keep the depth of the trees as small as possible, individual trees are raised for each $\vec{v}_{max}[b] \in [0, N-1] \subset \mathbb{N}$. The maximum error by this forest is limited in comparison to one big tree, as each tree only learns distance values that are related to one $\vec{v}_{max}[b]$. That way, the whole algorithm only performs $N-1$ divisions and a small number of comparisons (given by the depth of the trees) for a complete estimation [4].

In this work, an extension to the QBTM is proposed to benefit from multispectral information. Generally, the spectral information in \mathbf{X}_{in} is redundant for the distance estimation, as the energy ratios at neighboring pixels do not depend much on the used waveband. However, if an individual QBTM is trained for each available waveband, the accuracy of the distance estimation might be improved by performing an individual distance estimation for all B wavebands and computing the median of all results. Analog to the multispectral quick binary tree mapping (MQBTM), the multispectral expanded generalized cross-correlation (MEGCC) and multispectral expanded average square difference function (MEASDF) can also be computed as the median result of individual estimators that are applied for each available waveband. Generally, similar implementations of multispectral extensions should be applicable to any distance estimation method. This approach is denoted as the MQBTM and evaluated in Chap. 7.

6.3.2 Data Fusion

In this section, the fusion of all available signals to a spectral signature is presented. Spectral signatures are represented as a vector \vec{s} which yields a remission amplitude value for each waveband b . The intention is that \vec{s} describes the remission spectrum

of a measured object's surface material. The influence of measurement conditions to the acquired spectral signature, such as the target's distance and angle to the sensor, should be as small as possible. Finally, spectral signatures are used as input for the material classifiers, which are described in the following section.

The presented data fusion approach is guided using the estimated distance \hat{d} to select a corresponding matrix of correction factors $\mathbf{C}_d \in C$ from a set C . Each matrix \mathbf{C}_d has the same dimension $N \times B$ as a matrix of raw sensor readings \mathbf{X}_{in} , whereby some elements $\mathbf{C}_d[n][b]$ yield non-zero factors which correct the corresponding sensor reading $\mathbf{X}_{in}[n][b]$ to a distance invariant value. The set C provides an individual matrix \mathbf{C}_d for every possible output value of the distance estimator $\hat{d} \in [d_{min}, d_{max}] \subset \mathbb{N}$. C is created in an offline process beforehand using Eq. 6.2, whereby $\vec{\mathbf{s}}_{ref}$ is a reference spectral signature, T is a set of measurements from the sensor which must be calibrated and τ_{max} is a manually chosen threshold that allows to avoid large correction factors, which may cause numerical inaccuracies. Analog to this, a lower threshold t_{min} is chosen for all input values, which should be higher than the system's noise level.

$$\mathbf{C}_d[n][b] = \begin{cases} \frac{\vec{\mathbf{s}}_{ref}[b]}{T_d[n][b]} & \text{if } \frac{\vec{\mathbf{s}}_{ref}[b]}{T_d[n][b]} \leq \tau_{max} \wedge T_d[n][b] > t_{min} \\ 0 & \text{else} \end{cases} \quad (6.2)$$

Spectroscopic reflectance measurements are taken from the surface of a reference object to acquire $\vec{\mathbf{s}}_{ref}$ as the desired output for the transformation of each $\mathbf{X}_{in} \in T$. The same reference object must be used to create the set T , which contains actual sensor readings over the whole range of measurement distances $d_{min} \leq d \leq d_{max}$ (compare Fig. 6.5 on page 114), whereby each element can be addressed uniquely by the ground truth measurement distance d as $T_d = \mathbf{X}_{in}^d$. For this work, T was created using a

step width of 1 mm, which results in 901 positions within a distance range from $d_{min} = 100$ mm to $d_{max} = 1000$ mm.

In a matrix of sensor readings \mathbf{X}_{in} , N readings from individual pixels or photodiodes are available for each waveband b . This information is corrected and combined using a weighted average function as defined in equation 6.3 [4].

$$\vec{s}[b] = \sum_{n \in V} \mathbf{X}_{in}[n][b] \mathbf{C}_d[n][b] \mathbf{W}[n][b] \quad (6.3)$$

In this equation, $\mathbf{W} \in \mathbb{N}^{N \times B}$ is introduced as a matrix of weights. Logically, a large correction factor $\mathbf{C}_d[n][b]$ is a result of a weak corresponding input signal $\mathbf{X}_{in}^d[n][b] \in T$. In general, smaller signals tend to have a weaker SNR, as some of the typical noise components in photocurrents, such as dark current and shot noise, do not scale proportional to the signal's amplitude [72]. Therefore, Eq. 6.4 computes each weight $\mathbf{W}[n][b]$ to be inversely proportional to the corresponding correction factor $\mathbf{C}_d[n][b]$ with respect to all other currently available correction factors within the same waveband b , which are given by the set V . Set V contains the indices of all pixels that satisfy mandatory conditions as defined in Eq. 6.5. Note that correction factors exceeding a manually chosen upper threshold τ_{max} will be set to 0, so that they are ignored for the fusion process. Furthermore, an important property of \mathbf{W} is $\sum_{v \in V} \mathbf{W}[v][b] = 1 \ \forall b \in [0, B - 1]$, which means that the results are always scaled with respect to V , as the weights for all related correction factors sum up to one.

$$\mathbf{W}[n][b] = \frac{\prod_{v \in V \setminus \{n\}} \mathbf{C}_d[v][b]}{\sum_{w \in V} \prod_{v \in V \setminus \{w\}} \mathbf{C}_d[v][b]} \quad (6.4)$$

$$V = \{n \in [0, N - 1] \mid \forall b \in [0, B - 1] : \mathbf{C}_d[n][b] \neq 0 \wedge \mathbf{X}_{in}[n][b] > t_{min}\} \quad (6.5)$$

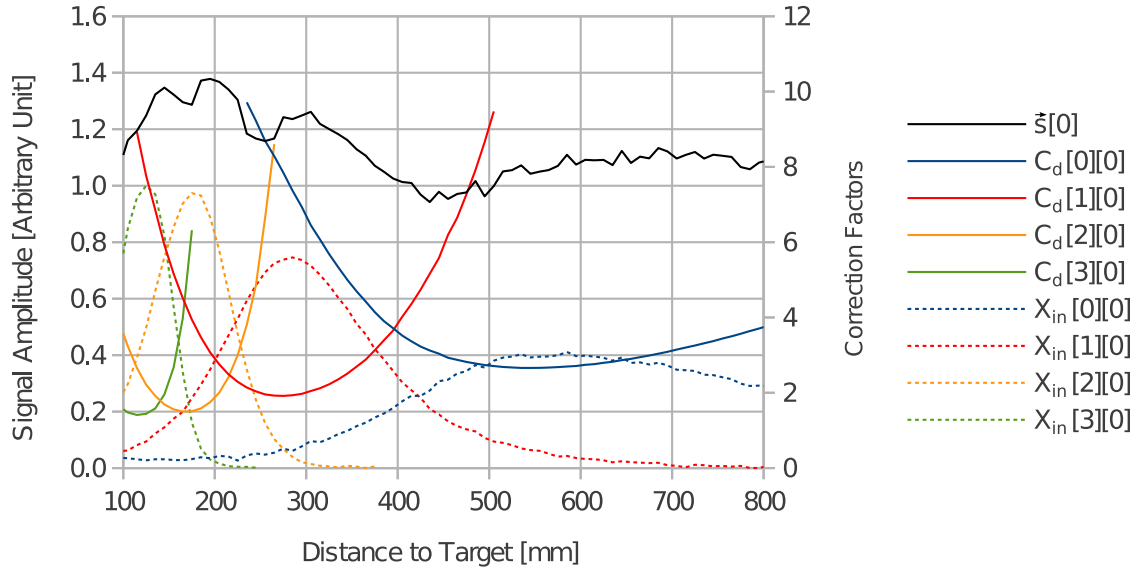


Figure 6.7: Exemplified data fusion $\mathbf{X}_{in} \rightarrow \vec{s}$.

For performance optimization when implementing the algorithm in an embedded software, the equations 6.3 and 6.4 can be converted to the much more compact, but mathematically identical Eq. 6.6:

$$\vec{s}[b] = \frac{\sum_{n \in V} \mathbf{X}_{in}[n][b]}{\sum_{n \in V} \mathbf{C}_d[n][b]^{-1}} \quad (6.6)$$

This conversion is possible, as all products $\mathbf{C}_d[n][b] \mathbf{W}[n][b]$ are equal for all n in an arbitrary set V and a distinct waveband b . Therefore, it is not actually necessary to compute the individual weights for every combination of $\mathbf{X}_{in}[n][b]$ and $\mathbf{C}_d[n][b]$. Instead, Eq. 6.6 sums up all available input values and (inverted) correction factors and scales the result implicitly by dividing them afterwards.

Fig. 6.7 illustrates a sample $\mathbf{X}_{in}[n][0] \forall n \in [0,3]$ which is fused to $\vec{s}[0]$ with the displayed correction factors $\mathbf{C}_d[n][0] \forall n \in [0,3]$. In this figure, the **relative standard deviation (RSD)** is 10% over a range of 700 mm [4]. This deviation to the ideal

output, which would be a straight line at a signal amplitude of about 1.1, is caused by imprecise results of the distance estimation as well as the sensor's noise. These effects are evaluated in Sec. 7.1.3. A precise distance estimation and data fusion are important factors for the quality of the retrieved spectral signature \vec{s} , which is the base for material classification.

6.4 Classification of Materials

The task of the material classification is to implement a mapping from a spectral signature to a class $m \in M$, whereby M will consist of at least two different classes (e.g. $M = \{\text{Legal}, \text{Illegal}\}$). Equation 6.7 formally describes the mapping, whereby \hat{m} is an estimated material class, $f_M(\vec{s})$ is an optional function for data preparation and A_M is the material classifier [4].

$$\hat{m} = A_M(f_M(\vec{s})) \quad (6.7)$$

For instance, it is recommended to scale all input values to be within -1.0 to 1.0 when training an SVM using LIBSVM. Without scaling, dimensions yielding large values would have a stronger influence on the algorithm than dimensions that contain smaller values [73]. This can be done by implementing a suitable function $f_{\text{LIBSVM}}(\vec{s})$. Training is then done by supplying a set E of tuples $(m, f_{\text{LIBSVM}}(\vec{s}))$, where $m \in M$ is a label denoting the actual class membership.

As said in Sec. 2.3.1, SVMs are capable of implicitly mapping a nonlinear classification problem to a linear solvable problem by transforming the input data into a feature space of higher dimensionality. The C4.5 tree learning algorithm, which is mentioned in Sec. 2.3.2, cannot perform such a mapping. Instead, a tree learning algorithm may raise a number of tree branches to describe a nonlinear class boundary, which increases the size of the resulting decision tree. However, the absolute

amplitudes within \vec{s} are influenced by the angle of measurement, while the ratios between wavebands remain stable, as mentioned in Sec. 4.4.1. In consequence, these ratios may deliver linear class boundaries even if the corresponding amplitudes are not linearly separable. Therefore, the preprocessing function presented in Eq. 6.8 computes ratios from all combinations of values within a spectral signature \vec{s} . This way, a characteristic ratio can be compared to a threshold within a single node of the tree, even if the corresponding amplitudes vary greatly among all samples of a targeted material class. However, these ratios are just offered as additional parameters to the tree learner. The original amplitudes are still supplied as $f_{\text{tree}}(\vec{s}, \vec{r})$ with \vec{r} being the additional vector of ratios. The vector \vec{r} is also used for the brute force search presented in 4.3.

$$f_r(\vec{s}) = (\vec{s}[0]/\vec{s}[1], \vec{s}[0]/\vec{s}[2], \vec{s}[0]/\vec{s}[3], \vec{s}[1]/\vec{s}[2], \vec{s}[1]/\vec{s}[3], \vec{s}[2]/\vec{s}[3]) = \vec{r} \quad (6.8)$$

In practice, it turned out that a simple threshold filter, which compares all values within \vec{s} and \vec{r} to skin-typical minimum and maximum values, is useful to reduce the chance of false positive skin classifications. This simple filter will classify a spectral signature as skin if all values are within the specified thresholds. If a spectral signature is classified as skin by this filter, a more sophisticated filter (e.g. a decision tree or SVM) is used for verification. The advantage of this method is in its very good performance on outliers, which are often misclassified by the more complex classifiers, if no similar samples were included in the set of training data. Methods such as SVMs try to separate the members of given classes with maximized margin, while the thresholds enclose the cluster of spectral signatures acquired from samples of human skin. This allows a rough decision whether a spectral signature is close to

122 CHAPTER 6. ACQUISITION, DATA PROCESSING AND CLASSIFICATION

that cluster or not. An evaluation of material classifiers based on thresholds, SVMs and decision trees is provided in the following chapter.

Chapter 7

Concept Validation

A quantitative evaluation of the presented sensor concept, prototypical implementation and data processing methods is provided in this chapter. The chapter is subdivided into four sections. Sec. 7.1 discusses the performance of the data processing methods. Sec. 7.2 discusses typical artifacts, that must be taken into account for the presented sensor concept. Experiments to investigate the impact of different environmental influences are presented in Sec. 7.3. The last section briefly discusses the achievable reliability of the system, if two or more of the discussed artifacts or environmental influences occur in parallel.

7.1 Data Processing Methods

This section presents an evaluation of the high-level methods for distance estimation, data fusion and material classification. As this is an evaluation of algorithms, both synthesized and real sensor data are used for evaluation. The synthesis of sensor data was done using a commercial software for optical engineering and ray tracing called

FRED as described in Sec. 7.1.1. This way, the results do not depend on the specific characteristics of the Skinner sensor prototypes alone.

7.1.1 Data Basis

A total of 17 different measurement configurations was chosen for test and training of different distance estimation methods. A white diffuse tile with a diameter of $\varnothing_t = 80\text{mm}$ was used as measurement target. Originally, this tile is meant to be used as a white-reference to calibrate spectrosopes. The tile was rotated and shifted about it's X- and Y-axis as depicted in Fig. 7.1. Tab. 7.1 defines 17 different configurations of the target. Configuration 1 to 15 define different rotations of the tile. Such rotations affect the light intensity distribution on the detector, as discussed in prior work [20]. As the light intensity distribution is used to perform the distance estimation, deviations caused by rotations should be suppressed to minimize the estimation error.

Table 7.1: Definition of the 17 orientations of the target tile (see [4, Tab. 1]).

Conf.	1	2	3	4	5	6	7	8
α	0°	-10°	10°	-20°	20°	-30°	30°	0°
β	0°	0°	0°	0°	0°	0°	0°	-10°
X	0 mm	0 mm	0 mm	0 mm	0 mm	0 mm	0 mm	0 mm

Conf.	9	10	11	12	13	14	15	16	17
α	0°	0°	0°	0°	0°	-20°	20°	0°	0°
β	10°	-20°	20°	-30°	30°	-20°	20°	0°	0°
X	0 mm	0 mm	0 mm	0 mm	0 mm	0 mm	0 mm	40 mm	-40 mm

The beam is centered on the tile if the axial shift is 0 mm. In configuration 16 and 17, the beam will be centered on the edge of the tile by a shift of $\pm 40\text{mm}$ on the X-axis. The rest of the beam disappears into open space, as no second object was located behind. As discussed in Sec. 5.1.3, measurements at a partial overlap of

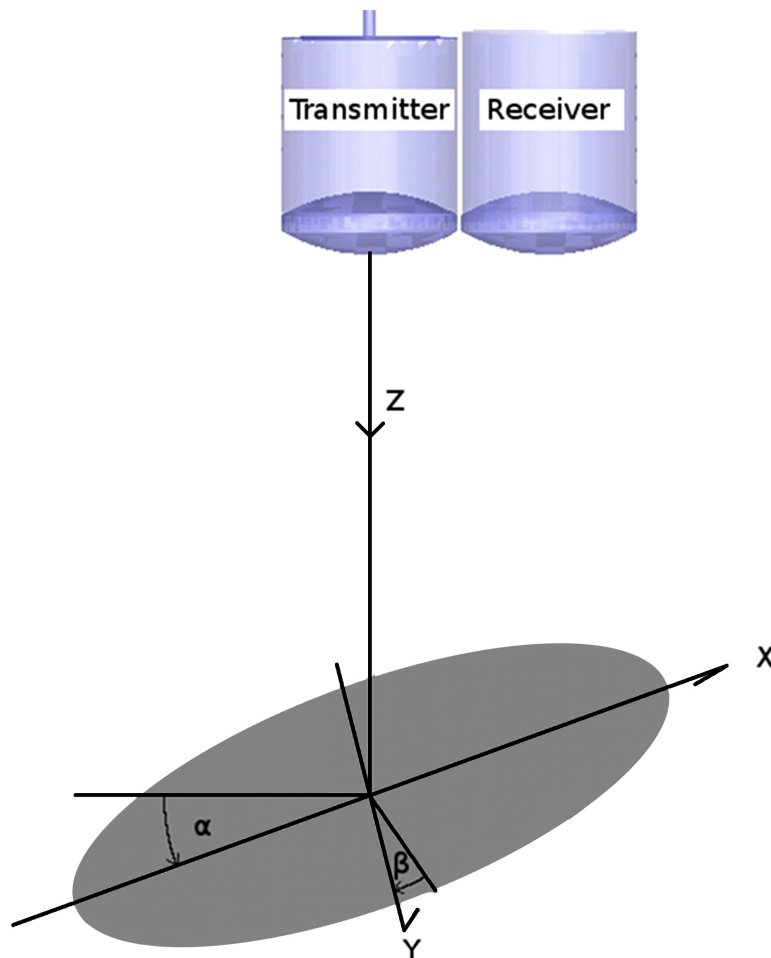


Figure 7.1: Rotation and shift of the reference tile (see [4, Fig. 8]).

the beam with an object will occur regularly while a new object is moved into the beam. In consequence, such measurement conditions must be included for a realistic evaluation.

A virtual model of the presented sensor was created to generate synthesized measurement data from simulations using a commercial software for optical engineering and ray tracing called **FRED**. The model was optimized iteratively to achieve synthesized data of sufficient quality at acceptable memory consumption and runtime of the simulation. Fig. 7.2 depicts a real and a synthesized measurement, showing that the shapes of the normalized curves are comparable for all corresponding pixels. How-

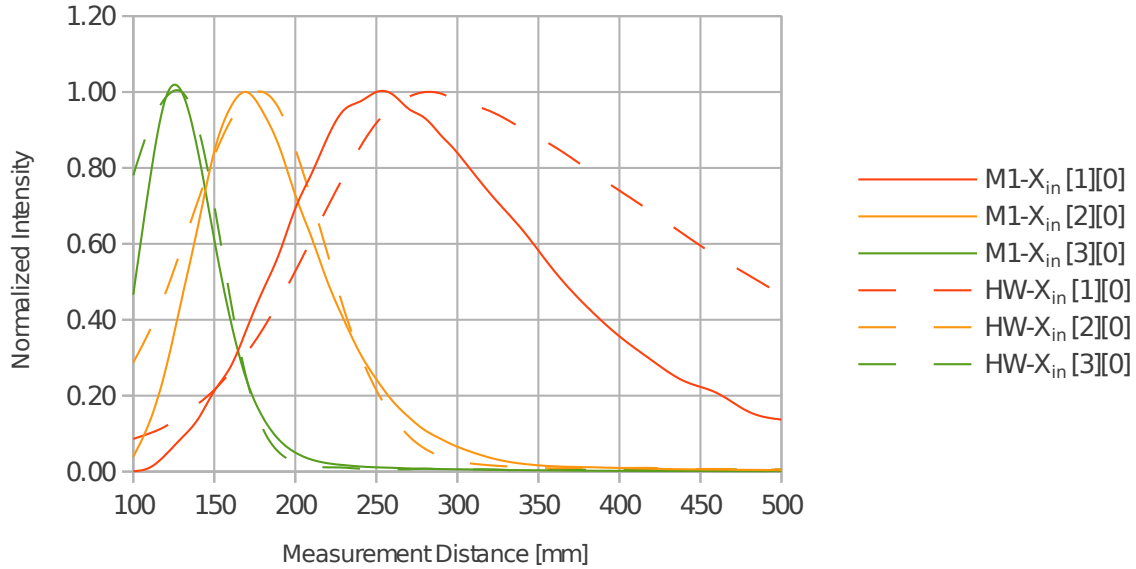


Figure 7.2: Comparison of real (HW) and synthesized (M1) data.

ever, the curves from the real sensor data (HW) are smoother than the synthesized curves (M1), which indicates that the real system's noise level is below the numerical inaccuracy of the simulation.

The model was modified to virtually create four alternative sensors. These alternative models were used to synthesize measurement data at all 17 target configurations to provide a wider data basis for evaluation, which does not depend on a specific implementation alone (see [4]). The first modification (M1) is an idealized housing of the detector, which absorbs all radiation. Therefore, no unwanted internal stray light can affect the sensor readings. Furthermore, the modified housing does not occlude portions of the incident light on the first detector, as described in Sec. 6.3.1. The second modification (M2) is an idealization of the transmitter. As discussed in Sec. 5.2.1, a point light source would be ideal to create a highly collimated beam. Therefore, the four LEDs were replaced by a single source of switchable waveband with a reduced edge length of 2×10^{-2} mm. For comparison, the actual LED-pattern

in Skinner mark 2 and 3 sensors has an edge length of 7.7×10^{-1} mm. The optical fiber was removed for this model and the idealized source is positioned directly at the focal point of the lens. This modification leads to an almost perfect match of the beams at different wavebands, as only the wavelength dependent refractive index of the glass lens causes a negligible mismatch. Furthermore, the beam width is reduced from $\varnothing_{b1} = 20$ mm to $\varnothing_{b2} = 7.5$ mm at a distance of $d = 500$ mm to the sensor.

The diameter of the beam \varnothing_b directly influences the length of the projection on the Z-axis l_z as a function of $l_z = \sqrt{(\varnothing_b / \sin(90 - \alpha))^2 - \varnothing_b^2}$, depending on the rotation angle α of the target. An example was published in [4] regarding configuration 5 with $\alpha = 20^\circ$ and beam diameters of $\varnothing_{b1} = 20$ mm and $\varnothing_{b2} = 7.5$ mm, whereby the resulting projection lengths are $l_{z1} = 7.3$ mm and $l_{z2} = 2.7$ mm. A projection length of $l_{z1} = 7.3$ mm will cause an ambiguous light intensity distribution, as the projection of the illuminated spot corresponds to a distance range rather than a distinct distance.

Two further modifications of the model (M3) and (M4) are based on the modifications M1 and M2 with eight instead of four photodiodes to achieve a higher spatial resolution. As the total length of the detector is unchanged, the round photodiodes with $\varnothing_p = 1$ mm are replaced by rectangular detectors with a footprint of $l_x = 0.62$ mm * $l_y = 1$ mm.

The evaluated distance estimators were trained and tested on input data of all configurations for all virtual and real sensors. For each configuration, measurement data were generated for a distance range from $d_{min} = 100$ mm to $d = 500$ mm. The data from a Skinner mark 2 sensor was gathered using a motorized linear driving stage, where 100 measurements were performed for each of 401 different sensor positions within a range from $d_{min} = 100$ mm to $d = 500$ mm to the target with an equidistant step width of 1 mm. As the variance over 100 samples per position and configuration is only 0.1 % to 3 %, a random selection of 10 samples was made for each position to

reduce the amount of data. Such a fine spatial sampling was not applicable for the data synthetization, as this would have consumed to much computation time.

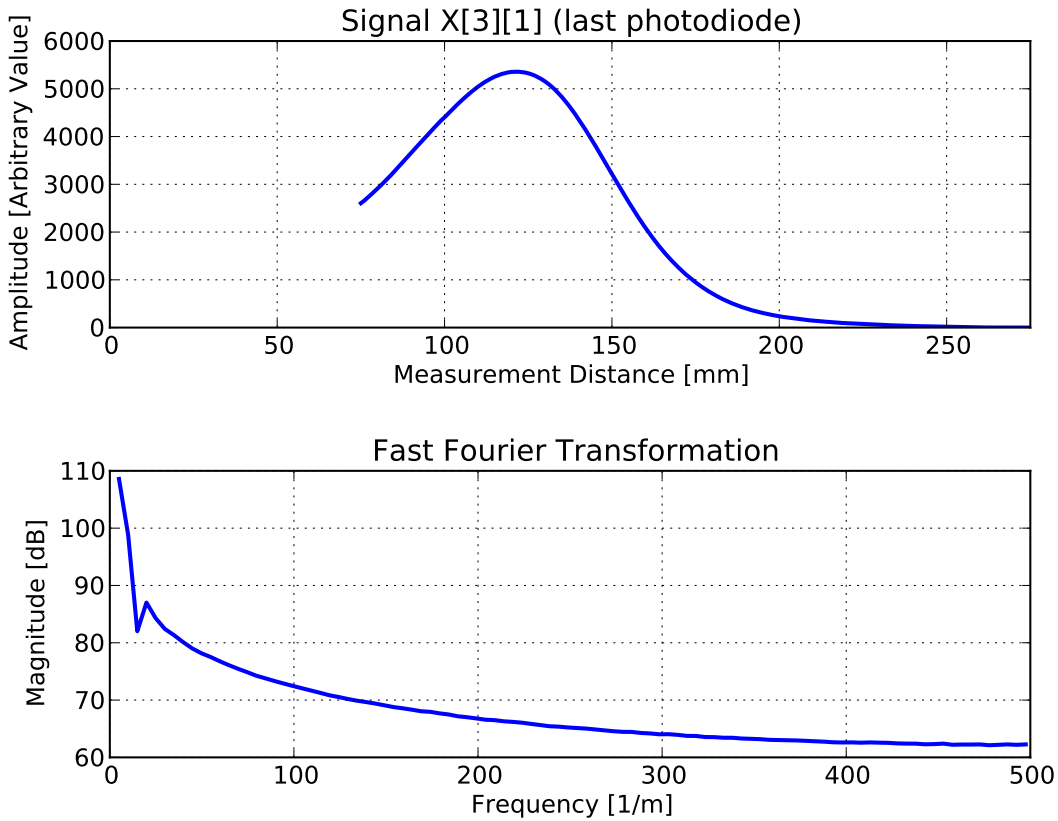


Figure 7.3: FFT of a signal from the last photodiode.

To find a sufficient sample frequency, a signal $X_{IN}[3][1]$ from the last photodiode, which generally shows the most rapid changes over the measurement distance, was converted into frequency domain by the [Fast Fourier Transformation \(FFT\)](#). Beforehand, the signal was averaged over 100 sample points per (discrete) measurement distance to reduce the dynamic noise components. The result shows that the highest frequencies are found at 500 m^{-1} , which is the natural limit from the original sampling steps of 1 mm. Furthermore, the magnitude is strongly increasing towards lower frequencies. The highest magnitude of about 109 dB is found at a frequency as low as

5 m^{-1} , which is about the expectable frequency if the part of the slope between the 120 mm and 220 mm mark would be mirrored and continuously repeated as a sinusoidal wave. From the results of the FFT it can be expected that the frequencies below 100 m^{-1} are most important to reconstruct the shape of the signal. According to the Nyquist-Shannon sampling theorem, the simulation was carried out with equidistant steps of $2 * 100 \text{ m}^{-1} = 5 \text{ mm}$ instead of 1 mm. This compromise accelerated the synthesization process by a factor of five, which was sufficient to perform all desired experiments in time. To achieve a full compatibility of the data, a step width of 1 mm was interpolated using cubic splines [74, p.40ff].

The data recorded by the Skinner mark 2 sensor yield a SNR of at least 21 dB, calculated from the random signal changes within a hundred measurements acquired at each of the 401 measurement distances per configuration. However, the SNR of the synthesized data cannot be determined easily, as the data is interpolated from synthesized sampling points. In Fig. 7.2 on page 126, a comparison of real and synthesized sensor data is showing that the real signals are smoother than the synthesized ones.

7.1.2 Distance Estimation

Common optical triangulation sensors often use red lasers to emit highly collimated beams with diameters of only about 1 mm. For the presented sensor concept, LEDs are preferred over lasers, as lasers of well suited wavelengths are more expensive. The receivers of common triangulation sensors consist of a lens system as well as a CCD or CMOS detector line with a comparably high spacial resolution of several hundred to several thousand pixels¹. Therefore, these sensors are much better preconditioned in terms of distance measurement than a Skinner sensor. On the other hand, fewer pixels of larger active area are useful to maximize the SNR and thus to acquire

¹E.g., see optoNCDT series by Micro-Epsilon Messtechnik GmbH & Co. KG.

spectral signatures \vec{s} of good quality. Maximizing the quality of spectral signatures is a primary design aim for the presented sensor concept, as the material classification is the most important feature. Therefore, optimizing the sensor design to maximize the accuracy of the distance estimation must be a secondary objective. Nevertheless, techniques presented in prior work for distance (or displacement) measurement such as the [EASDF](#) or [EGCC](#) (see Sec. 2.4) can be used as references to evaluate the new approaches of [QBTM](#) and [MQBTM](#) [4]. For this evaluation, the size of the search window for the [EASDF](#) and [EGCC](#) was always set to $M = 3$, as the best results were achieved with this value.

The [QBTM](#), [EGCC](#) and [EASDF](#) were compared in an experiment, where all configurations presented in the previous section were evaluated on all sensor designs. Tab. 7.2 shows the results of this experiment. The [EASDF](#) is outperformed by the [EGCC](#) and [QBTM](#) on the data from the [Skinner](#) sensor and the first modification (M1). The averaged results of the [QBTM](#) are significantly better than those of the other methods with the exception of the performance on the second virtual model (M2), where the [EASDF](#) has the best performance. The performance of the [QBTM](#) shown in this table differs from the evaluation presented in the related article [4], as the Orange tree induction algorithm (see [75]) was replaced by the C4.5 tree learning algorithm (see Sec. 2.3.2). The C4.5 implementation provided by the Weka data mining software was used with default parameters [76]. This algorithm was preferred as the resulting trees have about 80% less nodes than those raised using the Orange tree inducer. Furthermore, the Orange tree inducer was forced to produce trees with a maximum depth of 100 by a corresponding parameter, whereby this limit was reached for most trees. For comparison, none of the trees generated by the C4.5 algorithm is deeper than 15 layers. In consequence, the trees generated by the C4.5 algorithm require significantly less memory and are more computationally efficient

Table 7.2: Root mean square error (RMS) in millimeters of all configurations with all basic estimators. Measurements of a *Skinner* mark 2 sensor (HW) and virtual sensor configurations M1, M2, M3 and M4 are used as data sources (compare [4, Tab. 2]).

Configuration	1	2	3	4	5	6	7	8	9
QBTM (HW)	01.59	01.79	03.43	01.58	02.77	02.34	02.29	001.81	01.89
EGCC (HW)	05.74	06.48	05.48	06.32	05.48	06.56	06.00	005.57	06.00
EASDF (HW)	22.41	21.91	21.66	21.66	21.73	21.66	22.23	021.75	21.70
QBTM (M1)	02.81	07.06	05.07	06.74	06.27	07.60	18.55	005.49	06.16
EGCC (M1)	03.32	03.16	02.83	05.29	03.87	05.00	02.83	003.00	03.00
EASDF (M1)	21.59	15.33	19.67	16.37	12.88	29.24	27.91	018.11	16.46
QBTM (M2)	03.50	03.06	02.47	01.67	01.36	02.30	03.62	002.45	02.72
EGCC (M2)	02.65	02.24	02.24	02.65	02.65	03.32	02.83	003.00	02.24
EASDF (M2)	05.92	05.66	07.00	07.00	07.07	07.42	10.15	006.86	06.08
QBTM (M3)	00.28	00.25	00.36	00.64	03.11	00.21	00.23	000.63	00.34
EGCC (M3)	03.00	02.45	01.73	04.58	03.74	04.90	02.24	002.45	02.00
EASDF (M3)	06.48	05.66	02.83	05.57	05.20	11.22	04.69	002.45	05.00
QBTM (M4)	02.16	00.69	00.57	02.04	00.67	03.07	02.41	001.18	00.47
EGCC (M4)	02.24	02.00	02.24	02.24	02.00	02.24	02.00	002.00	02.00
EASDF (M4)	01.41	01.00	01.00	01.41	01.41	01.00	02.00	001.00	01.00

Configuration	10	11	12	13	14	15	16	17	Avg.
QBTM (HW)	01.06	01.05	01.19	01.25	05.06	01.76	18.99	019.43	04.07
EGCC (HW)	06.08	05.48	05.57	08.77	06.08	05.74	33.97	036.01	09.49
EASDF (HW)	21.61	21.66	22.00	22.05	22.25	22.34	29.03	044.75	23.67
QBTM (M1)	01.61	03.36	07.38	06.57	02.23	05.37	21.47	029.27	08.41
EGCC (M1)	02.83	03.00	03.16	02.83	03.74	03.61	53.27	088.06	11.34
EASDF (M1)	04.12	15.23	30.79	29.82	23.73	26.19	47.21	105.05	27.04
QBTM (M2)	03.19	02.37	02.08	02.32	01.00	03.22	10.49	020.93	04.04
EGCC (M2)	02.83	02.65	02.45	02.45	02.24	02.83	14.83	022.76	04.52
EASDF (M2)	01.00	01.41	01.41	01.41	01.00	01.41	14.35	025.44	03.45
QBTM (M3)	00.29	00.35	00.18	00.30	00.29	00.28	04.60	009.74	01.30
EGCC (M3)	02.00	02.00	03.00	02.00	03.61	03.16	57.93	070.63	10.08
EASDF (M3)	01.41	04.00	09.00	08.37	07.55	03.74	68.68	079.40	13.60
QBTM (M4)	01.29	05.71	01.39	00.50	01.29	02.14	08.34	017.41	03.02
EGCC (M4)	02.00	02.24	02.24	02.00	02.00	02.00	15.52	022.16	04.06
EASDF (M4)	01.00	01.41	01.41	01.41	01.00	01.41	14.35	025.44	03.45

for their shallow depths. When compared to the results achieved with the Orange tree inducer in [4, Tab. 2], the results of the **QBTM** presented in Tab. 7.2 are not as superior to the other methods as before. Especially the root mean square errors at configurations 16 and 17 are larger for the **QBTMs** using trees generated by the C4.5 algorithm. It can be assumed that the large trees generated by the Orange tree inducer delivered very specific rules to account for all training data, which does not guarantee a good performance on data that were not available for training. In literature, this problem is often denoted as overfitting. This was verified by removing these data from the training set. As a result, the performance of the **QBTM** was very close to that of the **EGCC** for configuration 16 and 17. In consequence, the tree learners used for the **QBTM** can derive special rules to account for special measurement situations like defined in those configurations. It is important to evaluate if these rules are a result of an overfitting to the training data or if those rules are generalized to improve the accuracy for a range of similar conditions.

Table 7.3: Results as averaged **RMS** in millimeters from additional configurations.

	Shift 30 mm	Shift -30 mm	Shift 50 mm	Shift -50 mm
EGCC (M1)	10.58	33.80	141.35	129.80
MEGCC (M1)	10.58	25.46	187.43	131.73
EASDF (M1)	32.12	63.68	150.04	147.56
MEASDF (M1)	32.93	50.69	136.20	149.48
QBTM (M1)	36.13	60.83	150.01	088.72
MQBTM (M1)	27.77	45.73	158.19	093.95

To evaluate this, an additional experiment was carried out on the virtual M1 model with shifts of ± 30 mm and ± 50 mm on the X-axis. The **MQBTM**, **MEGCC** and **MEASDF**, which are multispectral extensions to the basic methods as described in Sec. 6.3.1, were also applied to the data. The results displayed in Tab. 7.3 show that

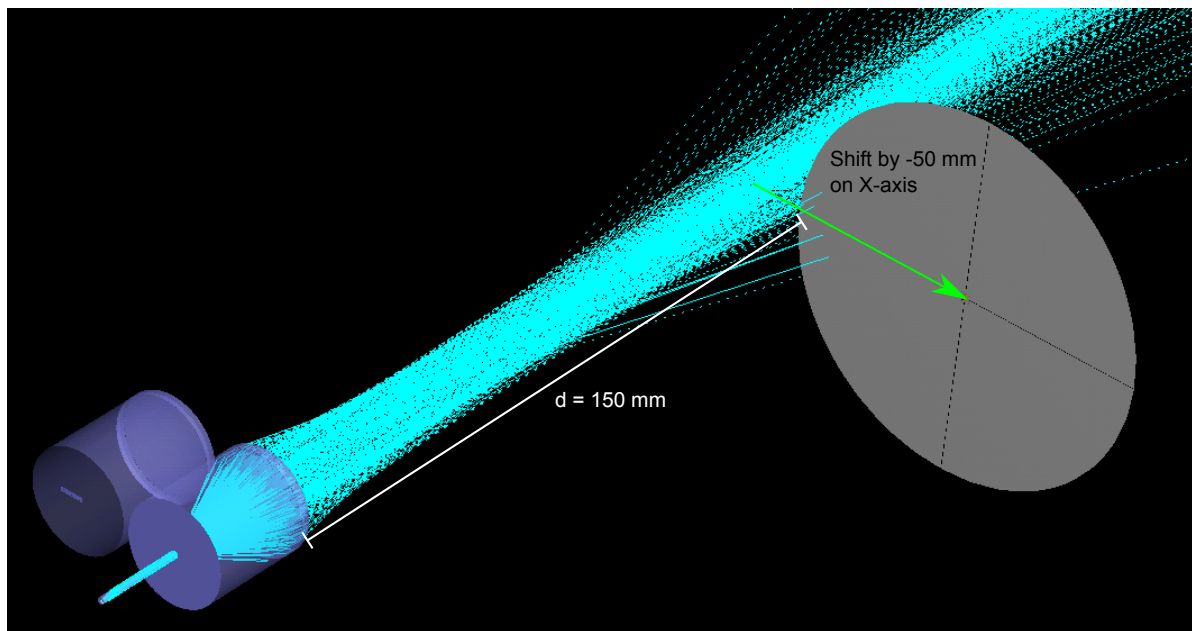


Figure 7.4: Simulation of sensor (M1) showing target shifted by -50 mm at $d = 150$ mm.

all methods perform very poor on the shifts by ± 50 mm, where the overlap of object and beam is minimal, especially for short measurement distances (see Fig. 7.4).

However, the [EGCC](#) and [MEGCC](#) clearly achieve the best results for shifts of ± 30 mm. Unfortunately, this shows that the good performance of the [QBTM](#) on configuration 16 and 17 is a result of a strong fitting to the training data. In consequence, the [QBTM](#) does not generally perform better at partial overlaps, but the performance could be optimized using big training sets which cover a wide range of measurement situations with the disadvantage of generating larger trees.

Tab. 7.4 extends Tab. 7.2 on page 131 by displaying results for the [MQBTM](#) and [MEGCC](#) on the original configurations. As in the experiment presented above, the results by the [MQBTM](#) improve more over the basic [QBTM](#) than the results of the [MEGCC](#) over those of the [EGCC](#). Especially the data provided by the modified model M2 improved much by the use of the redundancy within the sensor's data. Overall,

Table 7.4: Evaluation of multispectral extensions by the root mean square error (RMS) in millimeters of all configurations with all multispectral estimators. Measurements of a **Skinner** mark 2 sensor (HW) and virtual sensor configurations M1 and M2 are used as data sources.

Configuration	1	2	3	4	5	6	7	8	9
MQBTM (HW)	0.88	01.99	02.44	01.72	02.05	01.84	01.54	01.65	01.76
MEGCC (HW)	05.05	05.80	04.83	05.76	04.88	06.04	04.92	05.45	05.44
MQBTM (M1)	01.58	00.66	01.66	01.49	04.87	01.09	05.55	00.63	00.53
MEGCC (M1)	02.40	02.91	02.17	03.75	02.80	03.95	02.72	02.33	02.41
MQBTM (M2)	01.35	01.01	00.83	00.74	01.05	01.46	01.27	00.67	00.83
MEGCC (M2)	02.98	02.60	02.34	02.76	02.80	03.27	02.88	02.80	02.73

Configuration	10	11	12	13	14	15	16	17	Avg.
MQBTM (HW)	01.66	01.38	01.50	01.17	04.24	01.34	15.34	16.53	03.47
MEGCC (HW)	04.95	05.51	05.01	05.38	08.23	05.05	30.54	34.73	08.68
MQBTM (M1)	00.40	00.56	00.94	00.59	01.21	03.80	09.72	53.73	05.24
MEGCC (M1)	02.10	02.37	02.33	02.36	03.48	02.43	52.85	82.55	10.35
MQBTM (M2)	0.98	00.79	00.34	00.78	00.69	00.91	09.16	22.20	02.65
MEGCC (M2)	02.66	02.61	02.59	02.66	02.56	02.74	16.73	26.30	04.94

the **MQBTM** achieves the highest accuracy over the 17 test configurations of all tested methods.

In a further experiment, the ability of the estimators to process data which are very different from the training data is evaluated (see [4]). A total of 20 measurements from human hands, 15 measurements from wooden boards and seven samples from meat were measured using the same **Skinner** mark 2 sensor to provide further test data. The scattering properties of those samples are very different than that of the reference tile used for training. Tab. 7.5 summarizes the results. On the described data, the basic **QBTM** achieved the worst performance. This confirms the importance of appropriate training data for the **QBTM**. However, the **MQBTM** achieved comparable results to the **MEASDF**. In conclusion, the decision trees utilized by the **QBTM** often fail on previously unknown data, as one "wrong turn" in the decision tree may cause a severe error. This weakness of decision trees can partially be compensated by the

Table 7.5: Averaged **RMS** in millimeters on a selection of samples from hands, wooden boards and meat samples.

	Human Skin	Wooden Boards	Meat Samples
EGCC (HW)	8.93	7.04	24.18
MEGCC (HW)	10.72	6.88	22.23
EASDF (HW)	23.00	28.72	27.55
MEASDF (HW)	19.73	13.81	28.30
QBTM (HW)	40.62	46.67	51.22
MQBTM (HW)	18.52	17.06	24.34

MQBTM, as it chooses the median from four results. The used implementation of the median function computes the average of the second and third element in a sorted list of four elements. Nevertheless, the **EGCC** and **MEGCC** clearly achieved the best results in this experiment.

A true advantage of the **QBTM** and **MQBTM** over the **EGCC** and **EASDF** is their ability to estimate and differentiate distances if the focal point is on or even past the first or last photodiode. This is not possible for the **EGCC** or **EASDF**, as these methods estimate a subpixel position within a search window which is limited to reference data provided from available pixels (see Sec. 2.4). For the used **Skinner** mark 2 sensor, this limits the differentiable distance range for the **EGCC** and **EASDF** by 105 mm to 564 mm¹.

Fig. 7.5 shows a comparison of the results from an **EGCC** to a **QBTM** which was trained over a range from 75 mm to 800 mm. The plot reveals that the **QBTM** achieves a high accuracy within a distance range from 75 mm to 650 mm. The accuracy decreases drastically over ≈ 650 mm, as the available ratio approaches values of $X[1][b]/X[0][b] \leq 0.08$ (see Fig. 6.6 on page 115). However, the range is extended by $\approx 25\%$ over the **EGCC**.

Artificial, multiplicative noise was added to the data acquired with the **Skinner**

¹There are small differences from sensor to sensor that depend on the detector's alignment.

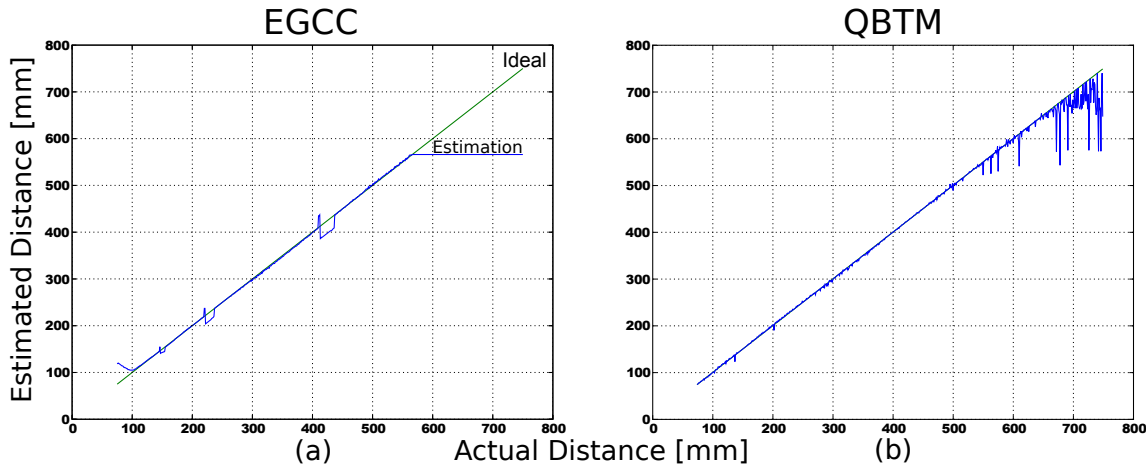


Figure 7.5: Distance estimation from 100 mm to 800 mm on actual sensor data using EGCC and QBTM (Compare [4, Fig. 10]).

sensor at configuration 1 to evaluate its influence on the accuracy of the distance estimation. The results of this experiment are plotted in Fig. 7.6. At a high SNR of 20 dB, the results primarily depend on the basic methods, namely the QBTM and the EGCC, regardless of the multispectral extension. For $\text{SNR} < 4\text{ dB}$, the results of the MQBTM and MEGCC as well as the QBTM and EGCC are very similar. So, both methods profit from their multispectral extensions on noisy data. Furthermore, the plot shows that the QBTM is not more susceptible to noise than the EGCC, as the estimation results of the QBTM do not get worse than those of the EGCC.

In conclusion, the multispectral extensions are generally useful for noisy and distorted sensor data. Furthermore, QBTM based distance estimators could achieve the highest accuracy from all evaluated methods. On the other hand, the EGCC based estimators have shown the best performance on variously distorted sensor readings, if they were not included in the training set. In conclusion, the EGCC and MEGCC are easy to train and yield a superior generalization, while the best accuracy can be achieved with the QBTM and especially the MQBTM, if an appropriate training set was used.

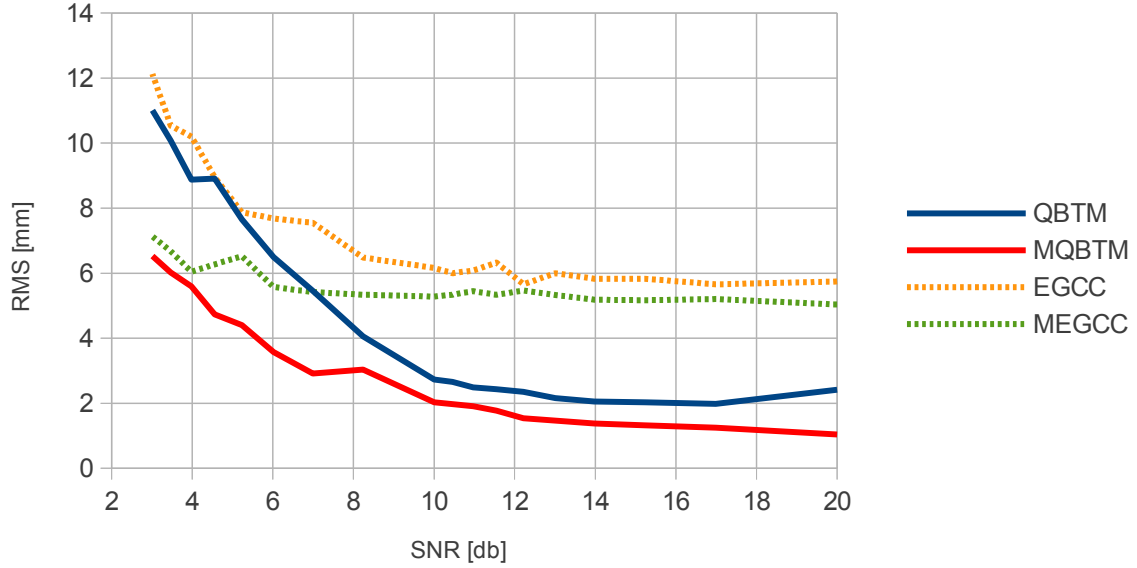


Figure 7.6: Influence of noise on the distance estimation.

7.1.3 Data Fusion

In this section, the transformation $\mathbf{X}_{in} \rightarrow \vec{s}$ as described in Sec. 6.3.2 is evaluated.

As no standard method for this specific problem could be found in literature, a comparison to the state of the art cannot be presented here. Instead, two alternative methods are introduced to evaluate the performance of the weighted average function defined in Eq. 6.3, 6.4 and 6.5 on page 118. The first alternative function is a simple average function defined in Eq. 7.1 (see [4]).

$$\vec{s}_{avg}[b] = |V|^{-1} \sum_{n \in V} \begin{cases} \mathbf{X}_{in}[n][b] \mathbf{C}_d[n][b] & \text{if } (\mathbf{C}_d[n][b] \neq 0) \wedge (\mathbf{X}_{in}[n][b] \geq t_{min} \forall b \in [0, B-1]) \\ 0 & \text{else} \end{cases} \quad (7.1)$$

The second alternative is defined in Eq. 7.2, where the first pixel which satisfies the condition $\mathbf{C}_d[n][b] \neq 0 \wedge \mathbf{X}_{in}[n][b] \geq t_{min} \forall b \in [n, B-1]$ is used as the only input. This simple approach tries to exploit the fact that the signals acquired at pixels with lower

indices have generally flatter slopes than those from pixels with higher indices (see Fig. 6.5 on page 114), which means that the same error of the distance estimation ρ will cause a smaller change to the corresponding signals (e.g., $d + \rho = \hat{d} = 308\text{mm} \mid d = 300\text{mm}, \rho = 8\text{mm}$).

$$\vec{s}_{heur}[b] = \mathbf{X}_{in}[\eta][b] \mathbf{C}_d[\eta][b] \quad (7.2)$$

with $\eta = \min_{n=0}^{N-1} \{n \mid \mathbf{C}_d[n][b] \neq 0 \wedge \mathbf{X}_{in}[n][b] \geq t_{min} \forall b \in [0, B-1]\}$

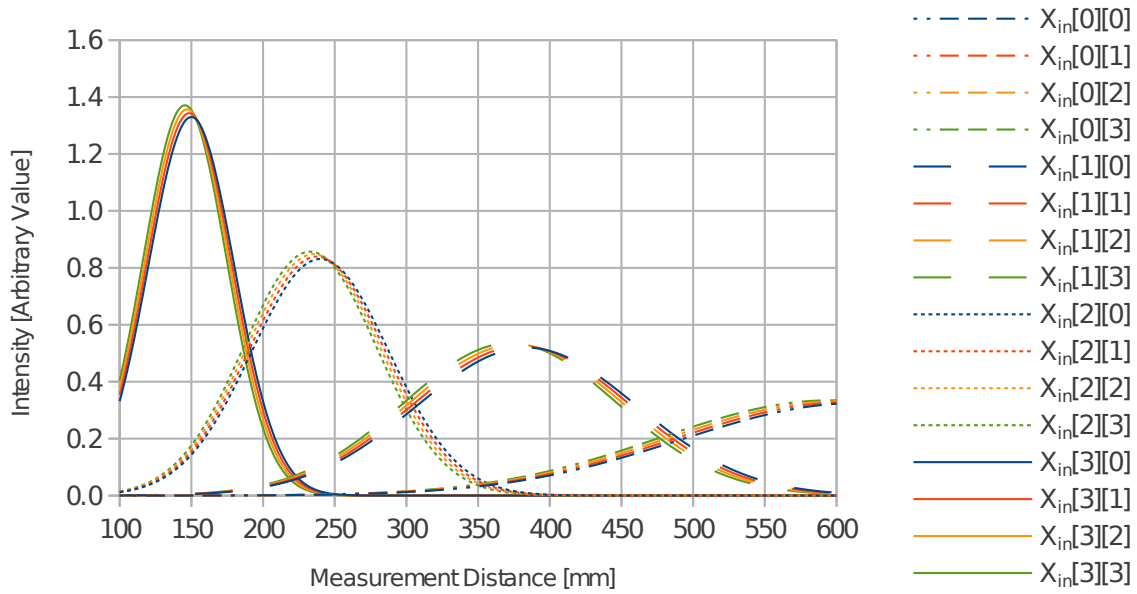
The data basis used for evaluation comprises four sets T_n of 501 samples acquired within a distance range from $d_{min} = 100\text{mm}$ to $d = 600\text{mm}$ from a flat surface made of CPflesh[®] silicon rubber. Each set was recorded with a different sensor, whereby the index of the set matches the mark of the used Skinner sensor. For instance, T_1 was recorded with a Skinner mark 1 sensor. The fourth set contains noise free, synthetic data, which are generated using Gaussian functions instead of the data presented in Sec. 7.1.1.

Real sensor data show different spatial peak positions for the signals of a distinct pixel at different wavebands. An analysis has shown that these differences are not significantly related to the corresponding wavebands with respect to the change of the refractive index of the lenses, yielding a focal length from $f'_{830\text{nm}} = 23.02\text{mm}$ to $f'_{1550\text{nm}} = 23.44\text{mm}$. Instead, the difference is related to the imperfect alignment of the beams corresponding to each waveband and thus depend on the LED-pattern within the transmitter.

Tab. 7.6 summarized the shifts measured with the different versions of the sensor. Obviously, the Skinner mark 1 sensor yields the largest shifts, which can be explained by the larger chip gap, the shorter fiber guide and orientation of the LED-pattern,

Table 7.6: Maximum distance between peak positions at all wavebands.

Skinner	Mark 1	Mark 2	Mark 3
$n = 0$	32 mm	17 mm	20 mm
$n = 1$	18 mm	5 mm	5 mm
$n = 2$	12 mm	3 mm	3 mm
$n = 3$	7 mm	2 mm	26 mm

Figure 7.7: Gaussian functions as noise free synthetic sensor data (T_4).

which is rotated about 45° for the other versions. This reduces the shift by $\sqrt{2}$ with respect to the X - or Y -axis. The suspiciously large shift for pixel $n = 3$ measured with the **Skinner** mark 3 sensor is a result of an unwanted internal reflection within the housing of the sensor. These shifts are causing distortions of the ratios in $f_r(\vec{s}) = \vec{r}$, if \vec{s} was fused using an estimated distance \hat{d} that differs from the true measurement distance d (see Eq. 6.8 on page 121). This was regarded in the synthesized data by increasing the mean of each Gaussian at waveband b by 1 % with respect to the mean of the Gaussian at waveband $b - 1$. All synthesized samples are displayed in Fig. 7.7.

Sets of correction factors C_n were built for each set T_n using the ground truth

measurement distance d . For T_1, T_2, T_3 , the reference was set to $\vec{s}_{ref} = (500, 500, 500, 500)$ with $t_{min} = 10$ and $\tau_{max} = 10.0$. Other values were chosen for T_4 , where the reference was set to $\vec{s}_{ref} = (0.1, 0.1, 0.1, 0.1)$ with $t_{min} = 0.01$ and $\tau_{max} = 10.0$, as the scale of the synthesized values is very different.

The concept of the following evaluation is to manipulate the ground truth measurement distance d by adding a static offset ρ and use the resulting false distance information $\hat{d} = d + \rho$ as input for the data fusion algorithms. As the error of the input information is constant, a comparison of the corresponding errors within the output \vec{s} can be made with respect to the presented data fusion methods. Furthermore, the reason to use a static offset ρ instead of the actual results generated with a particular distance estimation method, such as the QBTM, is to be independent of its particular characteristics. An analysis using different input errors within the range of $\rho \in [-32\text{mm}, 32\text{mm}] \subset \mathbb{Z}$ yielded that the output error is proportional to the offset error ρ . In consequence, the evaluation can be simplified by considering only one representative value for ρ , which was chosen to be $\rho = 8\text{mm}$ with respect to typical errors of the distance estimation presented in Tab. 7.2 on page 131.

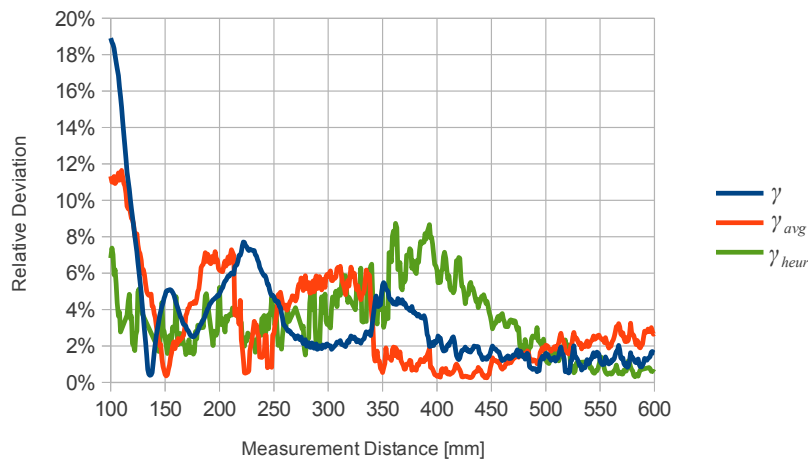


Figure 7.8: Relative deviations with $\rho = 8\text{mm}$ for the presented methods on set T_1 .

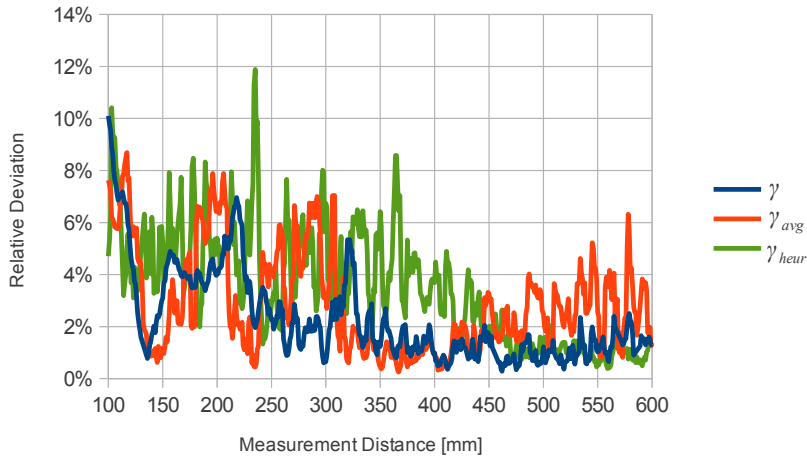


Figure 7.9: Relative deviations with $\rho = 8\text{mm}$ for the presented methods on set T_2 .

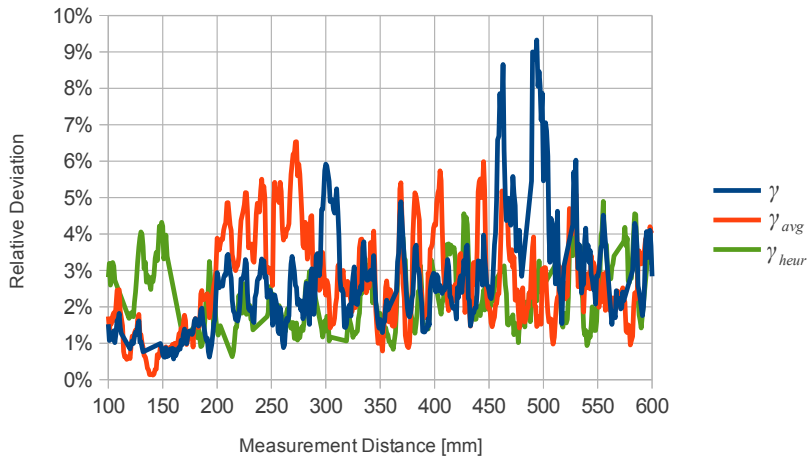


Figure 7.10: Relative deviations with $\rho = 8\text{mm}$ for the presented methods on set T_3 .

Figures 7.8 to 7.11 show the deviations $\gamma = \left| \frac{\vec{s}[0] - \vec{s}_{ref}[0]}{\vec{s}_{ref}[0]} \right|$, $\gamma_{avg} = \left| \frac{\vec{s}_{avg}[0] - \vec{s}_{ref}[0]}{\vec{s}_{ref}[0]} \right|$ and $\gamma_{heur} = \left| \frac{\vec{s}_{heur}[0] - \vec{s}_{ref}[0]}{\vec{s}_{ref}[0]} \right|$ that occurred for the presented methods. From the T_1 results displayed in Fig. 7.8 it is hard to judge which method performs best. Vector \vec{s} yields the highest deviation at d_{min} , but performs comparably good at $d > 250\text{mm}$. The pragmatic index priority approach of Eq. 7.2 on page 138 used to compute \vec{s}_{heur}

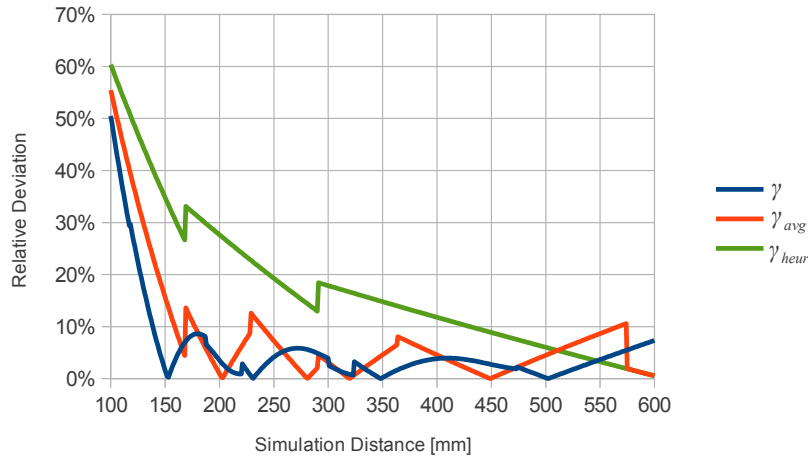


Figure 7.11: Relative deviations with $\rho = 8\text{mm}$ for the presented methods on set T_4 .

outperformed the averaging approaches for short distances of $d < 125\text{mm}$, as pixel $n = 3$ provides strong signals distributed over a short range of about 54mm with steep slopes. Therefore, relatively strong errors occur when multiplying the value from pixel $n = 3$ with a correction factor that was selected with respect to ρ .

Fig. 7.9 on page 141 displays the results for the Skinner mark 2 sensor, where \vec{s} yields the smallest deviations. Different from the results shown in Fig. 7.8 on page 140, all vectors yield comparable deviations for $d < 125\text{mm}$.

Unlike the deviations computed from T_1 and T_2 , the results from T_3 yield comparably small deviations for $d < 125\text{mm}$, which increase for $d > 200\text{mm}$ within \vec{s} and \vec{s}_{avg} (see Fig. 7.10 on page 141). The deviations of \vec{s}_{heur} to \vec{s}_{ref} are relatively constant over the whole distance range. Vector \vec{s} yields deviations of 9% at $d = 492\text{mm}$, which are almost two percent points higher than the largest deviation found with \vec{s}_{heur} . Therefore, the weighted averaging approach achieved the worst results on T_3 compared to the other approaches. However, the signals acquired by the Skinner mark 3 sensor are very different from the signals acquired by the other sources, as the unfocused receiver leads to comparably wide curves for all pixels. In Fig. 7.12 it can be seen that

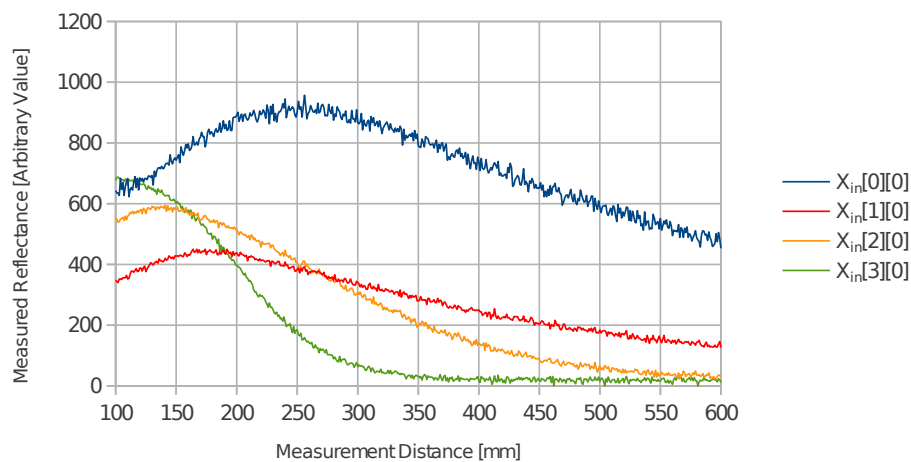


Figure 7.12: Raw signals within T_3 with $b = 0$.

the noise of the signals is comparably high. In conclusion, the deviations are more related to noise within the data than to the distance estimation error ρ .

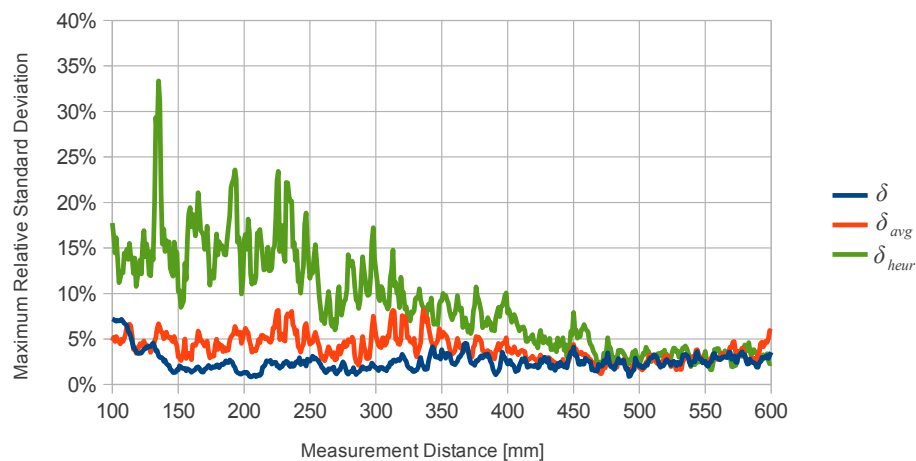


Figure 7.13: Maximum relative deviation δ computed from \vec{r} with $\rho = 8$ mm for the presented methods on set T_1 .

Compared to \vec{s}_{avg} and \vec{s}_{heur} , \vec{s} yields the lowest deviations on the last set T_4 . The results of the simple mean function \vec{s}_{avg} describe a zigzag-shaped curve, as smaller values at the steeply increasing parts of the signals have the same influence to the result

as the strong values around the peak positions of the signals. Here, the concept of the weighted averaging function performs well, as values from such steeply increasing parts are usually associated to smaller weights.

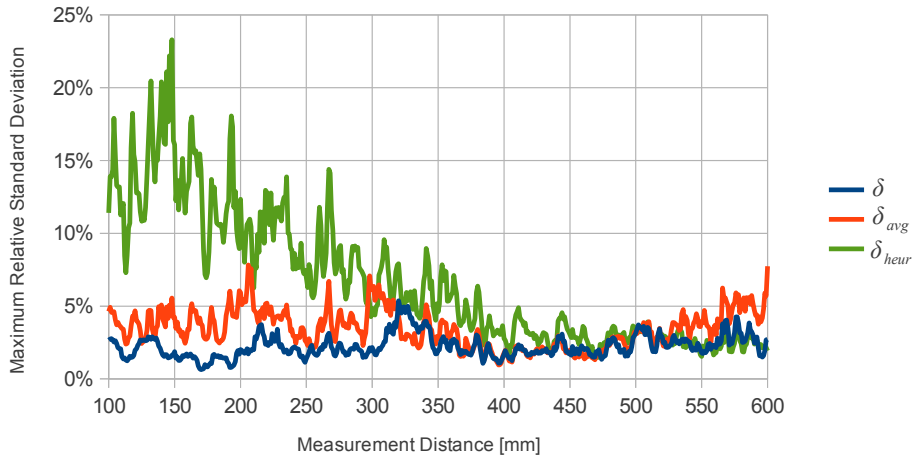


Figure 7.14: Maximum relative deviation δ computed from \vec{r} with $\rho = 8$ mm for the presented methods on set T_2 .

Finally, the methods are evaluated with respect to the vectors of ratios $f_r(\vec{s}) = \vec{r}$, $f_r(\vec{s}_{avg}) = \vec{r}_{avg}$ and $f_r(\vec{s}_{heur}) = \vec{r}_{heur}$. To evaluate the quality of each vector, the maximum relative deviation from the reference value over all six elements is computed using Eq. 7.3.

$$\delta = \max_{j=0}^5 \left| \frac{\vec{r}[j]_{ref} - \vec{r}[j]}{\vec{r}[j]_{ref}} \right| \quad (7.3)$$

All results are presented in figures 7.13 to 7.16. Fig. 7.13 and Fig. 7.14 show that the results of the weighted averaging function are overall better than those of the other methods, at least for measurement distances of $d < 300$ mm. The results of the index priority approach represented by δ_{heur} clearly yield the strongest deviations. This is also true for the analysis on data set T_3 , whereby δ and δ_{avg} are indifferent.

For Fig. 7.16, δ_{heur} yields the smallest deviations. Here, the assumption behind

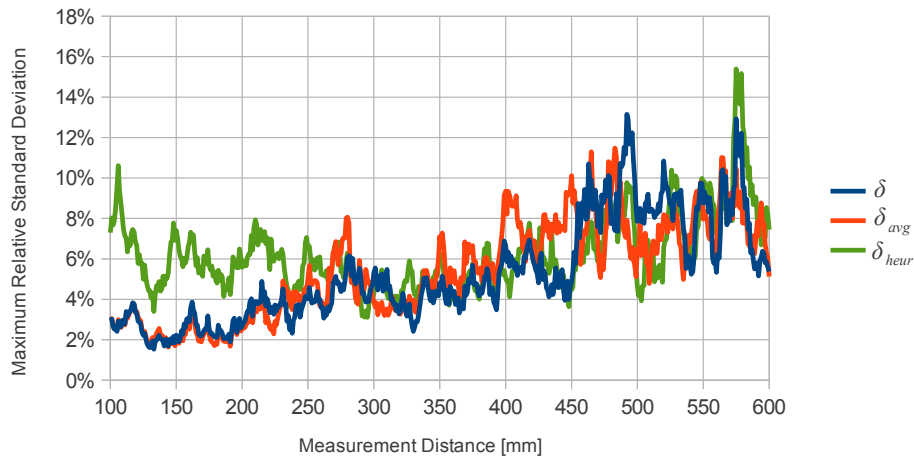


Figure 7.15: Maximum relative deviation δ computed from \vec{r} with $\rho = 8$ mm for the presented methods on set T_3 .

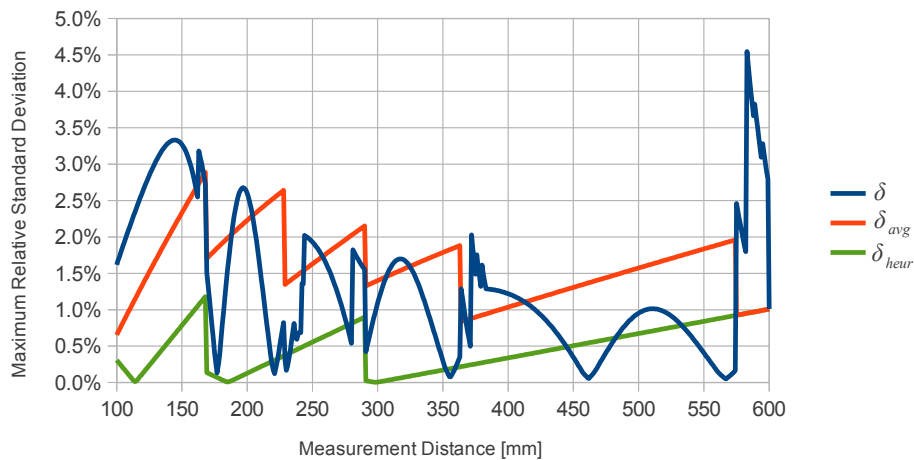


Figure 7.16: Maximum relative deviation δ computed from \vec{r} with $\rho = 8$ mm for the presented methods on set T_4 .

the weighted averaging function that larger values yield a stronger SNR is not true, as T_4 is free of noise. Therefore, the only advantage over the simple mean function is that values from step parts of the signals will potentially be associated to smaller weights. Nevertheless, δ_{avg} is smaller at some measurement distances. For instance, at about $d = 190$ mm, the signals from the pixels $n = 2$ and $n = 3$ are equally strong

and will thus be equally weighted. However, Fig. 7.7 on page 139 shows that this part of the signals from pixel $n = 3$ change much more rapidly over the measurement distance than the signals from pixel $n = 2$. Eq. 6.4 on page 118 does not account for such properties of the signals, although they can be derived from a test or training set T . For future work, the steepness of the signals could be taken into account by an extension to the presented method which defines a static bias for each weight at each distance in an offline process in parallel to the generation of C .

In conclusion, the weighted averaging function achieves the best quality with respect to \vec{r} on test data from real sensor systems. However, the stability of the amplitudes in \vec{s} is not generally better than that achieved with the simple reference methods. With the assumption that the quality of \vec{r} is more important to the material classification, the weighted averaging function is the best choice of the considered methods.

7.1.4 Material Classification

In this section, the material classification is evaluated on five scenarios: *Skin vs. Wood*, *Skin vs. Meat*, *Leather vs. Wood*, *Nitrile vs. Wood* and *Glove vs. Meat*. Test sets of measurements for each scenario were acquired from a number of samples within the full specified distance range from $d_{min} = 100$ mm to $d_{max} = 1000$ mm with a step width of 1 mm using a [Skinner](#) mark 2 sensor. This results in 901 measurement distances for each sample. The test sets comprise skin measurements from 10 individuals as well as measurements from 13 pieces of wood, 16 different gloves (i.e. latex, leather, nitrile and vinyl) and 10 pieces of meat (i.e. pork, beef, turkey and chicken). 20 spectral signatures were acquired at each measurement distance at samples of human skin and 100 spectral signatures were acquired at each measurement distance for all other types of samples. As wet and greasy meat samples often have a shiny appearance,

some meat samples were measured at random angles to achieve a realistic variance of the corresponding set. All measurements of human skin were taken from the palm and back of the hand. For three individuals, all measurements were repeated at an angle of 45° to the sensor. The measurement spots on the meat samples were selected with respect to the dominant tissue type, such as fat, bone or flesh. Different tree types such as birch, oak, spruce, beech, pine and plastic-coated wood are included within the wood samples. Two samples (birch and spruce) were measured at moisture levels of about $\sim 10\%$ to $\sim 100\%$ ¹. The test set for gloves comprised samples of nitrile, latex and vinyl gloves. In particular, three disposable nitrile gloves in blue and yellow, an impregnated nitrile glove in blue, disposable latex gloves in red, green, blue and yellow as well as two vinyl gloves in green and yellow. The same data basis was previously used for an evaluation published in an IOP article [4]. All spectral signatures used for the first part of this evaluation were computed using a basic QBTM distance estimator and a weighted averaging function for data fusion (see previous sections). As described in Sec. 6.4, the C4.5 tree learning algorithm as well as SVMs were used to implement material classifiers.

Table 7.7: Results for material classification using decision trees.

Scenario	ACC	TPR	FPR	PREC
<i>Skin vs. Wood</i>	1.0000	1.0000	0.0000	1.0000
<i>Skin vs. Meat</i>	0.9834	1.0000	0.0255	0.9834
<i>Leather vs. Wood</i>	0.9475	0.5689	0.0114	0.9890
<i>Nitrile vs. Wood</i>	0.9242	0.9247	0.0043	0.9956
<i>Glove vs. Meat</i>	1.0000	1.0000	0.0000	1.0000

Tab. 7.7 presents the results of binary decision trees for all scenarios. The results were determined through a ten-fold cross-validation. As described in Sec. 2.3.3,

¹100% wood moisture is reached if the weight of the contained water equals the bone-dry weight of the sample.

the accuracy (ACC), true positive rate (TPR), false positive rate (FPR) and precision (PREC) are used as quantitative measures. The differentiability is perfect for *Skin vs. Wood* as well as *Glove vs. Meat*, which confirms the performance of the sensor concept.

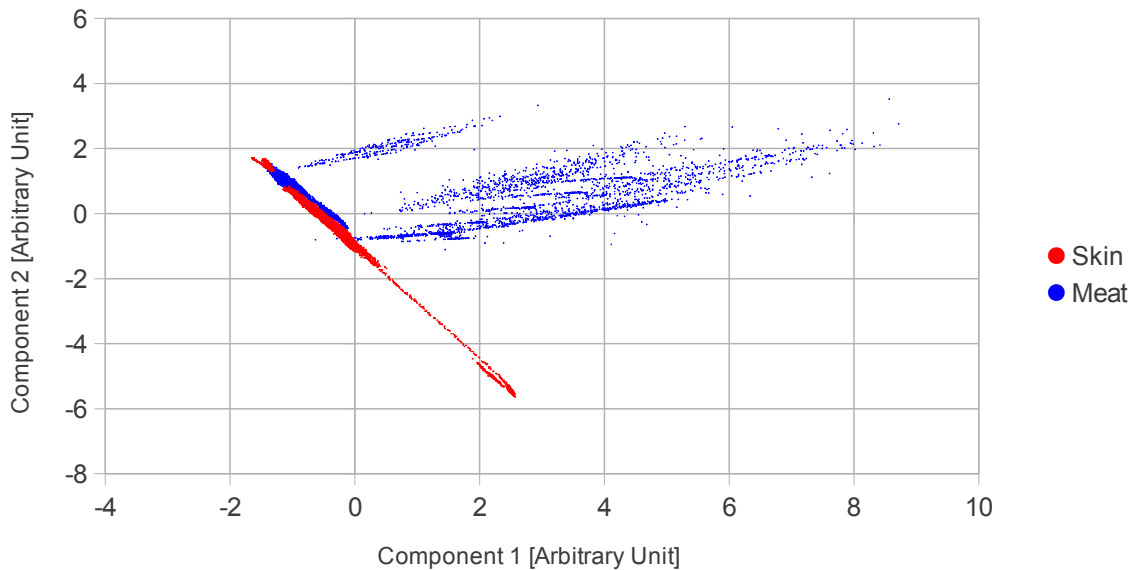


Figure 7.17: PCA of spectral signatures acquired from all samples of human skin and meat (compare [4, Fig. 12]).

The results of *Skin vs. Meat* are relatively good when considering the similarities of the tissues. A PCA was performed on a set of all available spectral signatures from human skin and meat samples, which is shown in Fig. 7.17. Besides a good clustering of meat samples in two or three groups, there is a group of meat samples that is located right within the skin cluster. Fig. 7.18 shows a selection of reflectance spectra acquired from pork at regions of fat or bone marrow in comparison to a selection of reflectance spectra from human skin. This shows that the presented sensor concept is not optimally suited for the differentiation of human skin from animal tissue, as both have very similar (optical) characteristics.

The scenarios *Leather vs. Wood* and *Nitrile vs. Wood* were chosen with respect to

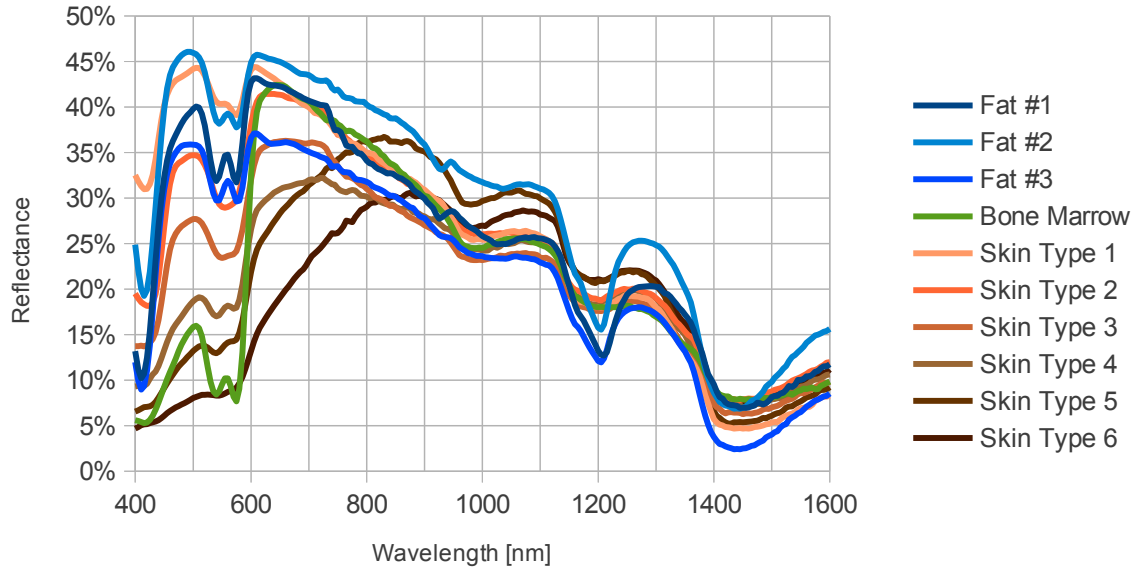


Figure 7.18: Similar spectra from human skin and pork samples.

the application of circular bench saws at construction sites, which is discussed in the next chapter. Unfortunately, both scenarios do not reach a perfect separation, which makes a practical use in the context of functional safety unlikely. As mentioned in Sec. 8.3, the reflectance spectra of these gloves are not very distinctive in comparison to typical workpieces. In conclusion, gloves with spectral markers would be required to realize such an application.

For comparison, C-SVMs were also used to solve the same scenarios. As shown in Tab. 7.8, optimized learning parameters were selected for each scenario by a grid search algorithm, where a 10-fold cross validation is performed for a total of 110 different combinations of the parameters $C = \{2^{-5}, 2^{-3}, 2^{-1}, \dots, 2^{15}\}$ and $\gamma = \{2^{-15}, 2^{-13}, 2^{-11}, \dots, 2^3\}$ (see [77]). For explanation, γ is a LIBSVM specific parameter within the radial basis function (RBF) kernel $K(x, y) = e^{-\gamma \|x-y\|^2}$ and C is a C-SVM specific parameter to influence the trade-off between margin maximization and training error minimization [73, 12].

Table 7.8: Results for material classification using C-SVMs (compare [4, Tab. 4]).

Scenario	C	γ	ACC	TPR	FPR	PREC
<i>Skin vs. Wood</i>	8	0.5	1.0000	1.0000	0.0000	1.0000
<i>Skin vs. Meat</i>	512	8	0.9980	1.0000	0.0047	0.9965
<i>Leather vs. Wood</i>	128	8	0.9648	0.9808	0.0045	0.9956
<i>Nitrile vs. Wood</i>	32	8	0.9995	1.0000	0.0000	1.0000
<i>Glove vs. Meat</i>	0.5	0.5	1.0000	1.0000	0.0000	1.0000

When comparing the results in the tables 7.7 and 7.8, the performance achieved by the SVMs is generally better than that of the decision trees. However, the use of SVMs could only achieve perfect separations in the scenarios *Skin vs. Wood* and *Glove vs. Meat*. In consequence, SVMs do not enable further applications.

In a final experiment, the robustness of the classifiers against artificially increased variance was tested. The variance was added as artificial multiplicative white noise to each component of every sensor reading X_{in} . The data sets of the scenario *Skin vs. Wood* was used, as this is one of the two sets that achieved a perfect separation. This test was performed with and without an optional threshold-based classifier, as described in Sec. 6.4. Furthermore, the analysis was performed using an EGCC and a QBTM distance estimator, whereby the QBTM estimator was trained on all available original data over the full distance range from $d_{min} = 100$ mm to $d_{max} = 1000$ mm. Tab. 7.9 shows all results of this experiment. Overall, the SVMs perform better than the decision trees. Furthermore, the simple threshold filter achieved a false positive rate of 0.0 and a precision of 1.0 at the expense of a lowered true positive rate for all configurations. This means that the risk of false positives and therefore false alarms is drastically reduced. In consequence, the availability of a production machine would be maximized in trade for a lowered safety level. The results are almost indifferent with respect to the chosen method of distance estimation.

Table 7.9: Analysis of the scenario *Skin vs. Wood* with artificially added white noise.

Noise	Dist. Est.	Mat. Class.	Thresholds	ACC	TPR	FPR	PREC
10 %	EGCC	C4.5	false	0.9973	1.0000	0.0038	0.9906
20 %	EGCC	C4.5	false	0.9894	1.0000	0.0149	0.9643
30 %	EGCC	C4.5	false	0.9871	0.9992	0.0178	0.9578
40 %	EGCC	C4.5	false	0.9871	0.9950	0.0161	0.9613
10 %	EGCC	C4.5	true	1.0000	1.0000	0.0000	1.0000
20 %	EGCC	C4.5	true	0.9997	0.9989	0.0000	1.0000
30 %	EGCC	C4.5	true	0.9944	0.9804	0.0000	1.0000
40 %	EGCC	C4.5	true	0.9762	0.9171	0.0000	1.0000
10 %	EGCC	C-SVM	false	1.0000	1.0000	0.0000	1.0000
20 %	EGCC	C-SVM	false	1.0000	1.0000	0.0000	1.0000
30 %	EGCC	C-SVM	false	0.9999	1.0000	0.0002	0.9995
40 %	EGCC	C-SVM	false	0.9988	0.9999	0.0016	0.9959
10 %	EGCC	C-SVM	true	1.0000	0.9999	0.0000	1.0000
20 %	EGCC	C-SVM	true	0.9984	0.9945	0.0000	1.0000
30 %	EGCC	C-SVM	true	0.9828	0.9400	0.0000	1.0000
40 %	EGCC	C-SVM	true	0.9546	0.8419	0.0000	1.0000
10 %	QBTM	C4.5	false	0.9970	1.0000	0.0042	0.9898
20 %	QBTM	C4.5	false	0.9884	1.0000	0.0163	0.9610
30 %	QBTM	C4.5	false	0.9877	0.9993	0.0170	0.9595
40 %	QBTM	C4.5	false	0.9892	0.9954	0.0132	0.9681
10 %	QBTM	C4.5	true	1.0000	1.0000	0.0000	1.0000
20 %	QBTM	C4.5	true	0.9997	0.9991	0.0000	1.0000
30 %	QBTM	C4.5	true	0.9954	0.9839	0.0000	1.0000
40 %	QBTM	C4.5	true	0.9788	0.9262	0.0000	1.0000
10 %	QBTM	C-SVM	false	1.0000	1.0000	0.0000	1.0000
20 %	QBTM	C-SVM	false	0.9999	0.9999	0.0000	1.0000
30 %	QBTM	C-SVM	false	0.9998	1.0000	0.0003	0.9992
40 %	QBTM	C-SVM	false	0.9993	1.0000	0.0010	0.9974
10 %	QBTM	C-SVM	true	1.0000	1.0000	0.0000	1.0000
20 %	QBTM	C-SVM	true	0.9988	0.9959	0.0000	1.0000
30 %	QBTM	C-SVM	true	0.9853	0.9487	0.0000	1.0000
40 %	QBTM	C-SVM	true	0.9582	0.8543	0.0000	1.0000

At this point, it is required to derive requirements with respect to applicable safety standards. As discussed in Chap. 5.1.1, the international standard IEC 61508-1 can be used to derive requirements for the **true positive rate**. This standard defines the safety integrity levels (SIL) 1 to 4, which are defining a range for the average **probability of a dangerous failure on demand (PFD)** from 10^{-5} to 10^{-1} . Generally, every single

classification result can be a *demand* in terms of the standard, if there is a worst case scenario where only one measurement can be performed before an accident becomes inevitable. For instance, if a little finger, moving at maximum foreseeable velocity, passes the beam so that only one measurement at full intersection of beam and finger will be performed before the finger leaves the beam towards the danger zone. In this worst case scenario, a dangerous failure on demand occurs if the measurement at full beam intersection would be misclassified. In consequence, the *TPR* must satisfy the condition $TPR > 1 - PFD$. The safety requirements for a safeguarding system at a manually fed machine can be expected to be *SIL*=2 for many cases, which corresponds to $PFD < 0.01$ or $TPR > 0.99$, respectively [47, Tab. 2]. However, Tab. 7.9 yields results satisfying this condition for all tested magnitudes of multiplicative noise, whenever no additional thresholds are used. A *true positive rate* of at least 0.9999 was achieved using *SVMs* without thresholds, which complies with the requirements for the highest *safety integrity level* (*SIL*=4).

In conclusion, both evaluated methods to implement material classifiers perform very robustly with respect to the chosen scenario. The *SVMs* generally achieve better results than the decision trees raised using the C4.5 tree learning algorithm. On the expense of a lowered *true positive rate*, the risk of false positive classifications can be reduced to 0.0000, although the data is highly distorted. This is especially important for the practical acceptance of this new technology, as sensors which often produce false alarms would not be accepted for most of the targeted applications. Furthermore, a perfect *true positive rate* of 1.0000 was achieved at four of five test scenarios, although the wavebands acquired by the sensor were exclusively chosen with respect to the first scenario of *Skin vs. Wood*.

7.1.5 Computational Performance

The aimed measurement rate of $f_{min} = 500\text{Hz}$ can only be achieved if the data processing is done sufficiently fast on the used **microcontroller**. A series of measurements was performed to evaluate the actual computing time of the presented methods on an AT90CAN128 **microcontroller** clocked at $f_{CPU} = 16\text{MHz}$ and an AT32UC3C0512C **microcontroller** clocked at $f_{CPU} = 64\text{MHz}$ [78]. The embedded software was written in C and compiled using the **GNU Compiler Collection** at the highest optimization level (O3).

Table 7.10: Maximum measured computational time.

Microcontroller	Floating Point	EGCC	Data Fusion	Decision Tree	C-SVM	Overhead	Total ¹
AT90CAN128	in software	660 μs	1030 μs	30 μs	7060 μs	680 μs	2400 μs
AT32UC3C0512C	in software	66 μs	68 μs	7 μs	1080 μs	74 μs	215 μs
AT32UC3C0512C	FPU	44 μs	11 μs	7 μs	792 μs	20 μs	82 μs

¹ Total = EGCC + Data Fusion + Decision Tree + Overhead (Without C-SVM)

Unfortunately, the measurements only comprise a selection of the presented methods: An **EGCC** distance estimator, the weighted averaging function for data fusion, a binary decision tree for material classification with a maximum depth of 5 as well as a **C-SVM** with 26 support vectors. Tab. 7.10 displays the results of these measurements, which show that the targeted measurement frequency of $f_{min} = 500\text{Hz}$ can only be achieved with the stronger AT32UC3C0512C **microcontroller**. When using the binary decision tree for material classification, the total computation time is only $t_p = 82\ \mu\text{s}$ for the 32-Bit AT32UC3C0512C with enabled **FPU**. With this configuration, the measurement frequency can even be increased to more than $f = 1000\text{Hz}$, as $t_a + t_p < 1\text{ms}$. Even the **C-SVM** based material classifier can be evaluated in time with this **microcontroller** ($t_a + t_p < 2\text{ms}$). The 8-Bit AT90CAN128 does not feature an **FPU** and needs a total of $t_p = 2.4\text{ms}$ to compute all steps, if the decision tree is used for material classification.

7.2 Typical Artifacts

Measurement artifacts due to imperfections of the beamforming have shown to be a major problem in the context of the presented sensor concept. Especially a misalignment of the individual beams formed at certain wavebands to each other can lead to serious deviations in specific situations. These situations comprise measurements at partial overlap of the multispectral beam to an object and at shiny surfaces. Another type of artifact occurs if several objects intersect the multispectral beam at once. The spectral signatures acquired at such situations are influenced by the reflectance spectra of all intersecting objects and are therefore denoted as *mixed signatures*.

7.2.1 Measuring on Edges

Partial intersections of the beam and moving objects are expected to occur regularly during standard operation of an AOMCPD. Therefore, it is discussed in Sec. 5.1.3 that it is not necessary to correctly classify a safety critical material (such as skin) at such conditions. However, a false positive classification may occur if a spectral signature acquired from a work piece at a partial beam overlap coincidentally shows the expected characteristics of human skin. To avoid such false positives, the artifacts that occur at such measuring conditions must be investigated. Three relevant factors were identified: target movement during acquisition, the shape of the target's projection on the detector array and inhomogeneity of the multispectral beam.

The acquisition speed is critical if the target passes a great fraction of the beam's diameter \varnothing_b during the measurement process. For instance, when the first waveband would be acquired at an overlap of 10% to 20% and the last waveband would be acquired at 60% to 70% overlap. As a result, the share of reflectance acquired at the last waveband would be disproportionally large compared to that at the first

waveband. Therefore, a heavy distortion of the spectral signature would occur with respect to the actual properties of the object's surface. However, such conditions can be ignored relatively easily, e.g. by requiring two consecutive positive classifications before triggering protective measures. Such a filter function over two or more measurements would reduce the reaction speed of the system, which will result in higher temporal requirements.

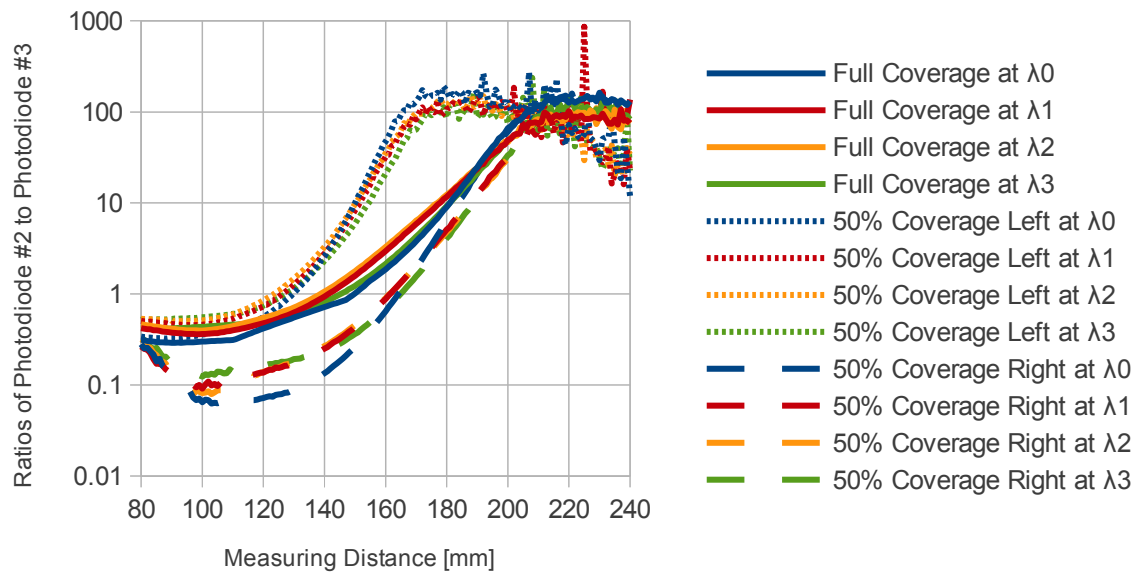


Figure 7.19: Signal ratio of neighboring photodiodes. Measured at full and partial beam coverage using a [Skinner](#) mark 1 sensor.

For this evaluation, a target was shifted on the X-axis to a 50% overlap with the beam and then measured within a distance range from $d = 80$ mm to $d = 1000$ mm. This is important, as the receiver is also shifted to the transmitter on the X-axis. A partial overlap at the X-axis leads to an altered projection of the target's remission onto the detector, as the reflecting area is reduced to the overlap. This causes a change of the obtained energy distribution over neighboring pixels as illustrated in Fig. 7.19. As discussed in Sec. 7.1.2, such changes may result in large errors of the estimated

distance, which reduces the performance of the data fusion. However, it is shown in Tab. 7.2 on page 131 that the QBTM is able to derive rules to compensate for such conditions, if adequate training data is available.

Furthermore, as a fraction of the emitted radiance misses the surface, the amplitudes found in the spectral signature will be lowered. Having lowered amplitudes is not problematic as long as the material classes in question are differentiable by the ratios of multispectral amplitudes (see vector \vec{r} in Sec. 6.4) and the spectral signature is not distorted beyond the contrast between those classes. However, if the emitted beam is not homogeneously composed over all available wavebands, the resulting ratios will be distorted for measurements at partial overlaps. The problem is illustrated in Fig. 5.19 on page 86, where projections of exit beams from different transmitter designs are presented. These projections show clearly how a partial overlap of a surface and an inhomogeneously composed beam will result in over- or under-representations of certain wavebands. This was evaluated in a practical experiment involving a Skinner mark 1 and mark 2 sensor. Skinner mark 1 sensors have fiber guides with a length of $l_1 = 10\text{mm}$, which is half the length of the fiber guides within Skinner mark 2 sensors. Shorter fiber guides lead to less attenuation of the emitted radiance at the expense of a less homogeneous beam composition, as fewer internal reflections will occur in the fiber [5].

A series of measurements at full and partial overlap with a wooden board have been acquired using both sensors over the full distance range. The wooden board was shifted left and right on the X-axis to achieve a 50% beam coverage. This way, two complementary overlaps of the beam and the object were achieved, just as in configuration 16 and 17 in Tab. 7.1 on page 124. Spectral signatures were derived from the acquired data, whereby the ground truth distance information was used as input to the data fusion to prevent a dependency to a specific estimator. For

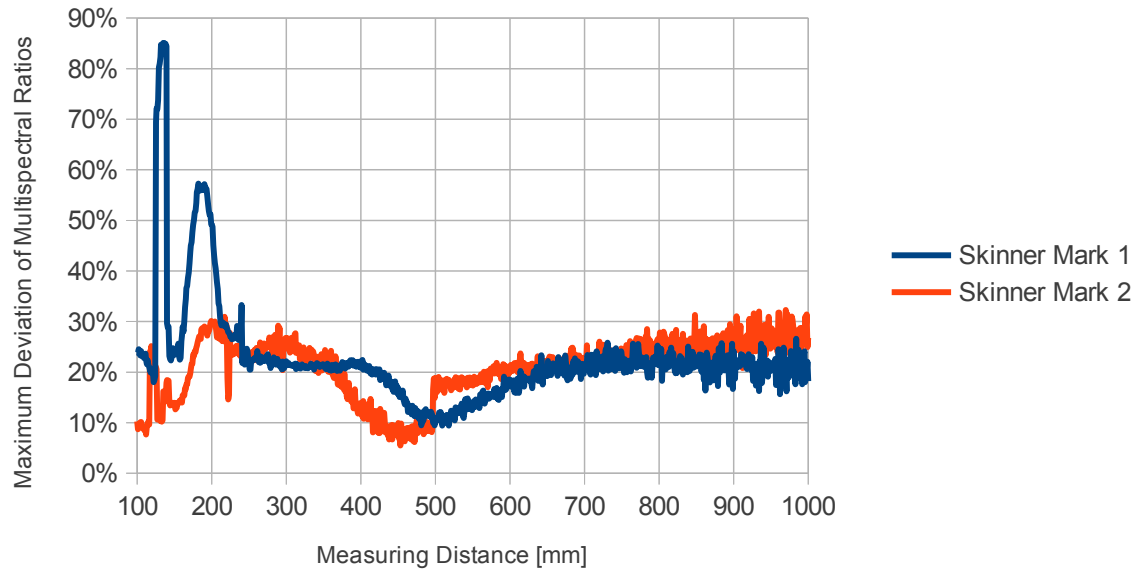


Figure 7.20: Maximum deviation of ratios within spectral signatures acquired at partial beam coverage to a wooden board using Skinner mark 1 and mark 2 sensors.

evaluation, the vector \vec{r} was computed from all spectral signatures \vec{s}_i , to determine if any waveband was over- or underrepresented. The maximum deviations within the vectors \vec{r} acquired at partial beam overlap with respect to those acquired at full overlap are illustrated in Fig. 7.20, where significant differences between the sensors are shown for shorter measuring distances of $d \leq 250$ mm. Still, with maximum deviations of about 30 % for the Skinner mark 2 sensor, the combination of a partial beam overlap and an inhomogeneous beam composition is responsible for severe measuring artifacts - even if the target is not moving. In conclusion, optimizing the beam homogeneity must be a main objective for the optical design.

7.2.2 Measuring Multiple Objects Simultaneously

As considered in Sec. 5.1.3 and Sec. 5.1.4, the possibility of acquiring a mixed spectral signature from several surfaces at once occurs if there is a partial overlap of the beam

with an object or several objects. Furthermore, it was discussed that it is not necessary that a sensor is able to classify one of the two surfaces correctly at such situations. Instead, the system must be designed in a way that a total coverage of a critical object (e.g. a finger) and the beam must occur before an accident becomes inevitable. This requires the beam to be smaller than the shortest edge of the smallest object which must be detectable. For finger detection, this is $\varnothing_f = 11 \text{ mm}$ for a smaller than average female little finger, as stated in DIN 33402-2 [51, Tab. 39]. Eq. 5.2 on page 58 shows that the beam must be even smaller with respect to the maximum velocity of the objects to detect and the data acquisition speed of the sensor.

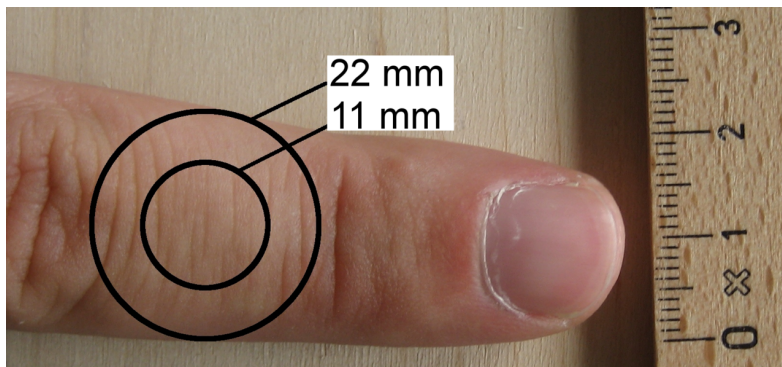


Figure 7.21: A forefinger on a wooden board as measurement target.

However, these requirements are not fulfilled by the *Skinner* sensor for the whole distance range. Therefore, a practical experiment on finger detection was carried out using a *Skinner* mark 2 sensor: As shown in Fig. 7.21, a male forefinger, with a diameter of $\varnothing_f = 22 \text{ mm}$ in the middle, was positioned on a wooden board. A linear positioning stage was used to gather measurements at a distance range from 100 mm to 1000 mm. This measurement was repeated with a modified sensor having an external field stop to crop the exit beam's initial diameter to $\varnothing_b = 7 \text{ mm}$. A simulation of this modification yielded that the *beam width* at $d_{max} = 1000 \text{ mm}$ would be reduced

from $\varnothing_b = 48\text{ mm}$ to $\varnothing_b = 38\text{ mm}$. The results of this experiment were also published in the OSA Journal of Applied Optics [5].

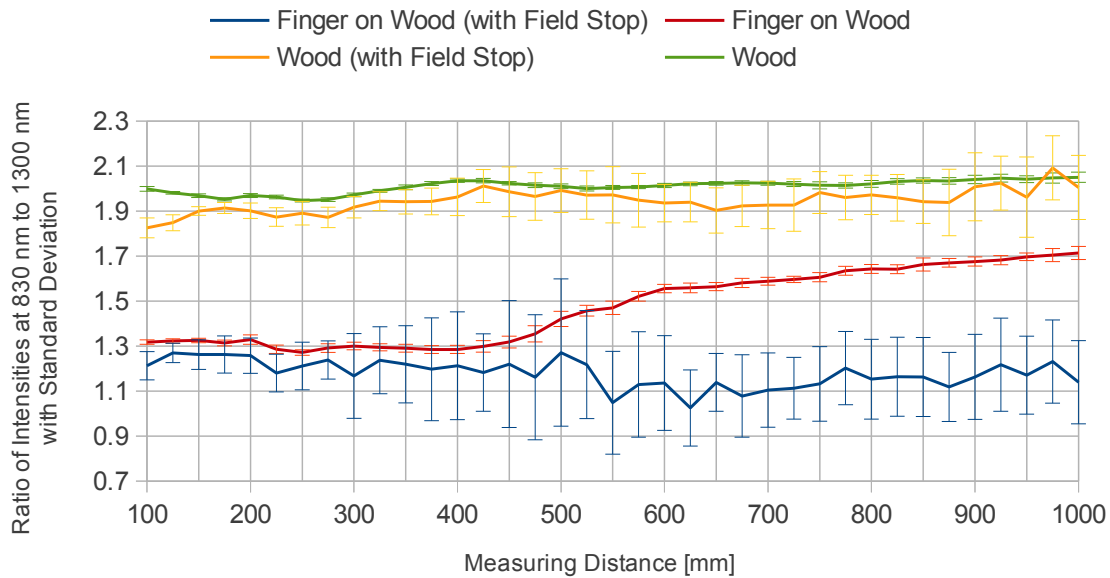


Figure 7.22: Evaluation of the experiment using the ratio of $\vec{s}[0]/\vec{s}[2]$ (see [5, Fig. 6]).

Fig. 7.22 illustrates the results of the experiment on the example of the ratio $\vec{s}[0]/\vec{s}[2]$, which is usually about $\vec{s}[0]/\vec{s}[2] = 1.3$ for skin and $\vec{s}[0]/\vec{s}[2] = 2.0$ for the used wooden board. The ratios acquired with the original sensor setup start to drift from a distance of $d \geq 450\text{ mm}$, while the modified setup with the field stop delivers relatively constant ratios over the whole distance range. However, the standard deviation is significantly worse for the modified version, as a lot of optical energy is absorbed by the field stop. This loss of illumination strength results in a reduction of the SNR by about 10 dB, as illustrated in Fig. 7.23. In fact, ratio $\vec{s}[1]/\vec{s}[3]$ yields typical values for skin of about $\vec{s}[1]/\vec{s}[3] = 7.0$, while it is only about $\vec{s}[1]/\vec{s}[3] = 1.0$ for the used wooden board. Nevertheless, this ratio could not be used to generate Fig. 7.22, as the SNR of values acquired at $\hat{\lambda}_3 = 1550\text{ nm}$ with the modified sensor are as low as 3 dB for the

finger measurement, which results in a very noisy plot. For comparison, the SNR of values acquired with the original sensor are not below 14 dB for all measurements and wavebands. In conclusion, the use of a field stop changes the maximum measurement distance for which the ratio of $\vec{s}[0]/\vec{s}[2]$ is not influenced by the wooden board from about $d = 450$ mm to the maximum specified measuring distance d_{max} . However, the SNR of the acquired signals was reduced to an insufficient level. For future sensor designs, a field stop could be used if its inner diameter is chosen as a tradeoff with respect to a required SNR.

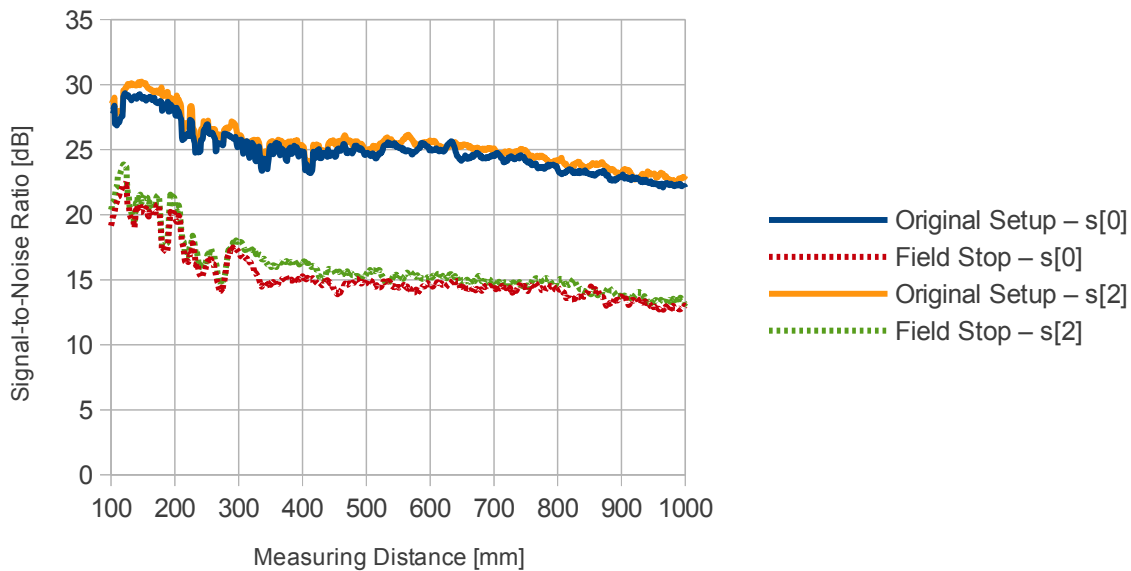


Figure 7.23: Signal-to-noise ratios of $\vec{s}[0]$ and $\vec{s}[2]$ from measurements of the wooden board. Acquired with and without field stop.

7.2.3 Measuring Shiny Surfaces

A simple experiment was carried out to evaluate the range of spectral signatures that occur when measuring shiny surfaces: A *Skinner* mark 2 sensor was continuously

probing a flat surface of brushed aluminum at a measuring distance of 1 m. Meanwhile, the surface was panned back and forth between -45° to 45° to the sensor's beam with three repetitions. As a result, the amplitudes at all wavebands vary from zero to maximum level. There are even a few outliers showing values close to maximum level for three wavebands and a very little response for one arbitrary channel. In consequence, all ratios in \vec{r} are varying between extreme values of $0.001 < \vec{s}[x]/\vec{s}[y] < 200$.

Nevertheless, the spectral signatures of 8 % of all samples are yielding skin typical amplitudes within three of four bands, but not a single sample is within the typical amplitude range within all four wavebands. Considering the ratios mentioned above, no sample has skin typical values at more than three of the six computed values within \vec{r} . In consequence, the danger of a false positive classification is negligible.

To validate that those sensor readings are not a result of oscillations within the analog circuits of the receiver, a Harvey-Shack scatterer was used in the optical engineering software **FRED** to simulate a shiny surface. Measurements with a virtual model of the **Skinner** mark 2 sensor have been made with a setup as depicted in Fig. 7.1 on page 125 and at a measurement distance of $d = 800$ mm. The orientation of the targeted tile was altered using $\alpha \in \{-1.0^\circ, -0.5^\circ, 0.0^\circ, 0.5^\circ, 1.0^\circ\}$ and $\beta \in \{-10^\circ, -9^\circ, \dots, 10^\circ\}$. The results of this simulation are very comparable to the data recorded with the real sensor by showing extreme variations within all values. Even a comparable, unequal development for different wavebands at small changes of the target's orientation (e.g., by 0.5°) could be observed within the data from both experiments. Therefore, it can be assumed that the deviations are primarily a deterministic function of α and β with respect to (minor) inhomogeneities of the multispectral beam composition.

7.3 Environmental Influences

In this section, the influence of common ambient parameters is discussed on the basis of experimental data. This is the practical counterpart to the theoretical discussions presented in the previous chapters.

7.3.1 Ambient Light

An experiment was carried out with a *Skinner* mark 2 sensor, which was equipped with an AT90CAN128 microcontroller. The sensor was aimed at a target of diffusely scattering CPflesh^{®1} silicon rubber, which was positioned at a distance of 1 m. With these fixed measuring conditions, the ambient lighting was altered using a 50 W halogen lamp with a reflector and a color temperature of about 3000 K. The lamp was supplied by an alternating current at a nominal frequency of 50 Hz. Note that this lamp satisfies the requirements for a white quartz lamp as cited in Sec. 5.1.8, in terms of color temperature, frequency and the use of a parabolic reflector.

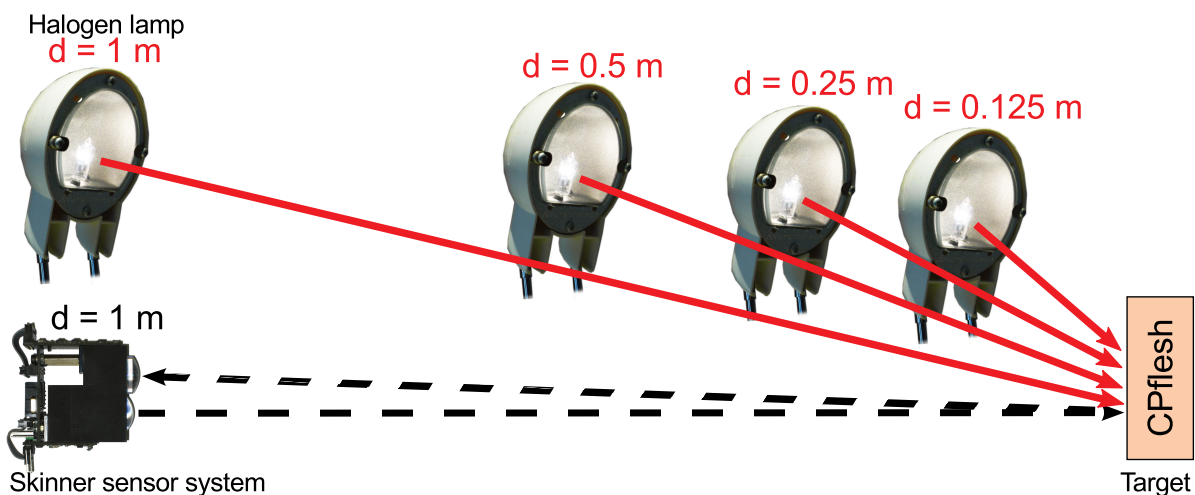


Figure 7.24: Positions of ambient light source.

¹See <http://www.cpflesh.de/> (online 2012-12-22)

The lamp was placed at four different positions as depicted in Fig. 7.24. A thousand measurements were taken for each position of the halogen lamp. Furthermore, a thousand measurements were taken with the lamp turned off as reference.

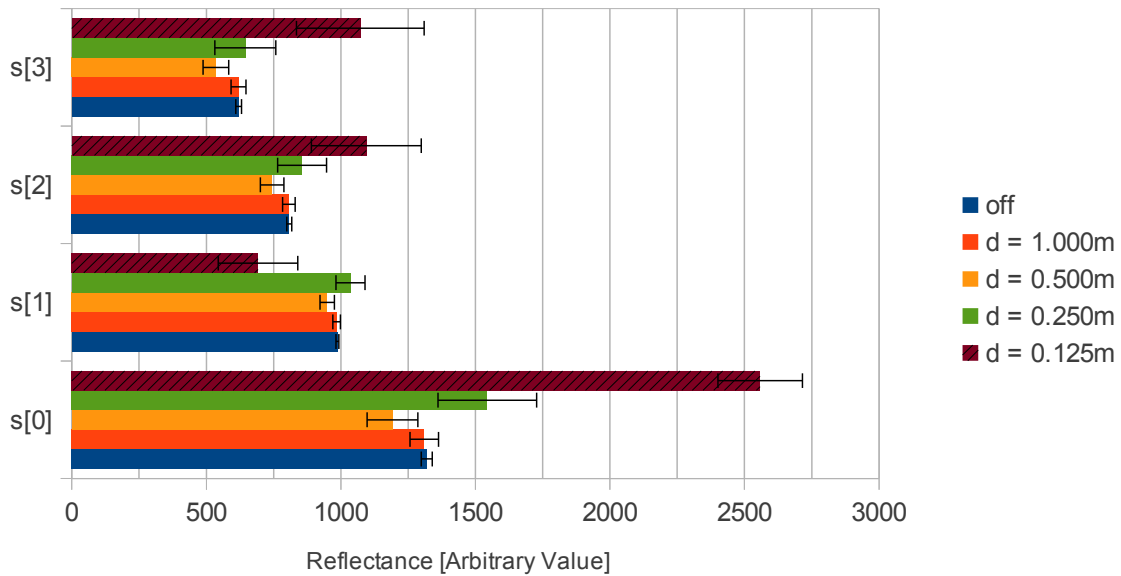


Figure 7.25: Averaged spectral signatures with standard deviation acquired at different positions of an AC powered 50 W lamp.

The results of this experiment are illustrated in Fig. 7.25, where the average of the acquired spectral signatures is shown along with the standard deviation. It is clear to see that the standard deviation is increasing with decreasing distance of the lamp to the target. Tab. 7.11 lists the relative standard deviation for each ambient lighting condition, averaged over all wavebands.

Table 7.11: Development of the relative standard deviation in relation to the position of an AC powered 50 W lamp, averaged over $s[0]$ to $s[3]$.

	Off	$d = 1.000\text{m}$	$d = 0.500\text{m}$	$d = 0.250\text{m}$	$d = 0.125\text{m}$
RSD	2.50%	6.43%	12.78%	22.64%	34.14%

Although the distortion of the spectral signatures is extreme for $d = 0.125\text{m}$, all

acquired spectral signatures are correctly classified as *not skin* by a decision tree based classifier for skin detection. An additional experiment, in which the silicon rubber target was replaced by a hand, has shown that the same classifier could reliably detect human skin for all conditions except for $d = 0.125\text{ m}$, where the influence of the ambient light is too dominant. Therefore, having the lamp at a distance of $d = 0.25\text{ m}$ to the target is defining the limit for the sensor's operation.

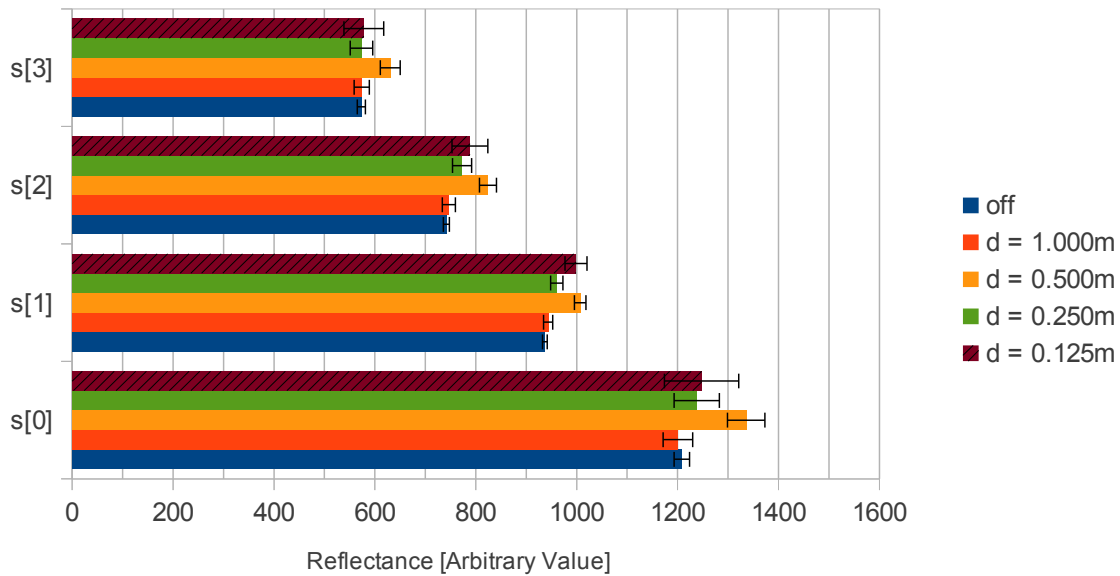


Figure 7.26: Averaged spectral signatures with standard deviation acquired at different positions of a DC powered 50 W lamp.

Table 7.12: Development of the relative standard deviation in relation to the position of a DC powered 50 W lamp, averaged over $\vec{s}[0]$ to $\vec{s}[3]$.

	Off	$d = 1.000\text{ m}$	$d = 0.500\text{ m}$	$d = 0.250\text{ m}$	$d = 0.125\text{ m}$
RSD	1.98%	3.87%	4.53%	5.61%	9.72%

The experiment was repeated with a DC power supply connected to the lamp, which was adjusted to a voltage of 12 V. This matches the effective voltage of the AC power supply used for the previous experiment, resulting in the same wattage

and color temperature as before. Fig. 7.26 and Tab. 7.12 are showing the results of this experiment, which yields much lower distortions to the acquired spectral signatures. Compared to the previous experiment, the **relative standard deviation** for $d = 0.125\text{m}$ is lower than that for $d = 0.500\text{m}$ when using an AC power supply. Therefore, a constant ambient light has a much smaller influence on the acquired spectral signatures than an oscillating ambient light (compare Sec. 6.1).

In conclusion, these rather simple experiments have confirmed the effectiveness of the implemented analog and digital filters, which are discussed in Sec. 6.1. However, it is unclear if the presented Skinner sensors fulfill all requirements for conventional AOPDs as defined in IEC 61496-2 [49, Sec. 5.4.6.2]. Nevertheless, there is still a lot of potential to optimize the presented readout circuitry, e.g. by implementing filters of higher order.

7.3.2 Atmospheric Humidity

Fig. 7.27 illustrates the atmospheric attenuation in relation to the absolute air humidity per waveband. The measurements were carried out in a climate chamber within 20°C to 50°C , which allows a wide range of absolute humidity. Within the climate chamber, a target of diffuse white plastic was measured at a fixed distance of 0.25m . An adjustment of the values was necessary, as the ambient temperature affects the sensor's performance (see Sec. 7.3.3). Furthermore, an averaging over ten measurements was done to reduce variance.

The results show an attenuation of up to about 11 % with respect to the reference measurement at an absolute air humidity of 1.91g/m^3 . From the reference measurement to the measurement with the second highest humidity of 62.44g/m^3 , the wavebands $\hat{\lambda}_0 = 830\text{nm}$ and $\hat{\lambda}_1 = 1060\text{nm}$ are attenuated less than the wavebands $\hat{\lambda}_2 = 1300\text{nm}$ and $\hat{\lambda}_3 = 1550\text{nm}$ with a difference of up to 0.89 percentage points.

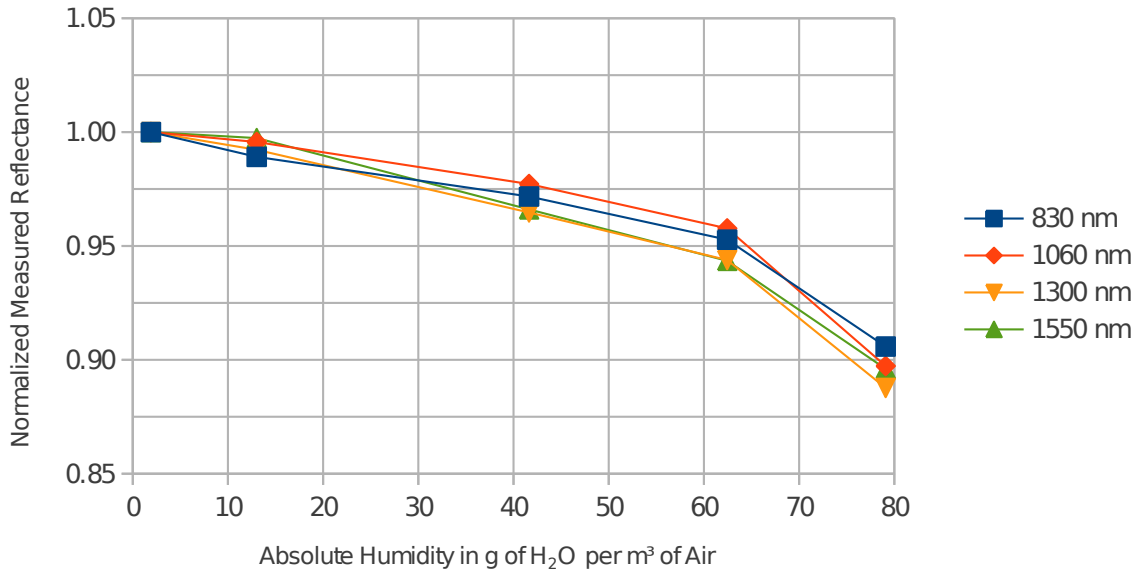


Figure 7.27: Atmospheric attenuation measured using a Skinner mark 2 sensor.

A comparably large attenuation at $\hat{\lambda}_2 = 1300\text{nm}$ can be explained by the neighboring absorption band, which is centered around 1365nm as discussed in Sec. 5.1.5. The used LED¹ for this waveband, has a nominal FWHM of 85nm . Therefore, 50% of the LED's peak intensity is radiated at $1300\text{nm} + 42.5\text{nm} = 1342.5\text{nm}$, which is already within an H₂O absorption band. However, the absorption bands shown in Fig. 5.1 on page 60 have only little overlap with the emission spectrum of the waveband $\hat{\lambda}_3 = 1550\text{nm}$, which has a nominal FWHM of 130nm ². Furthermore, the measurement at the highest humidity of 79.1g/m^3 yields a surprising development, as the attenuations for $\hat{\lambda}_1 = 1060\text{nm}$ and $\hat{\lambda}_2 = 1300\text{nm}$ increase disproportional to each other. This measurement was performed twice at 50°C at a relative humidity of 95%. A possible reason might be that the peak-wavelengths of the LEDs are shifted towards longer wavelengths due to the increased ambient temperature, as discussed

¹1300 nm LED chip type Epigap EOLC-1300-17-1

²1300 nm LED chip type Epigap EOLC-1550-17-1

in Sec. 5.2.2. According to the datasheet of a 1550 nm LED type L1550-03 from Epitex¹, the peak-wavelength increases by 21 nm for a temperature change of 30 °C. This could result in a larger overlap of the shifted emission spectra of these LEDs to the absorption bands, which are centered at about 1130 nm and 1365 nm. Therefore, the atmospheric attenuation will naturally increase with the overlap of the emission spectra and the absorption bands. The adjustment of the data compensates for the lowered sensitivity of the photodetectors as well as the lowered emission intensity of the LEDs, which is related to the increased ambient temperature. However, the shift of the peak-wavelengths could not be taken into account, as the emission spectra were not measured during the experiment. Another factor can be unequal self-heating of the LEDs, as discussed in the following subsection.

The relative attenuation, measured at an absolute humidity of 79.1 g/m³, is within a magnitude of 9.4 % to 11.2 % for all available wavebands. As the absolute reflectance intensities also depend on further parameters (e.g. the angle of measurement), they are not as reliable as the ratios between available wavebands anyways. However, these ratios remain stable, if the attenuation is uniform. In conclusion, the experiment confirmed that the Skinner sensors are sufficiently robust against varying atmospheric humidity. Furthermore, it can be expected that the attenuation on all wavebands can be harmonized by controlling the temperature of the LED chips as suggested in Sec. 5.2.2, as this would stabilize the emission spectrum and optical output power for each LED.

7.3.3 Ambient Temperature

The influence of the ambient temperature was also tested in a climate chamber. Again, a target of diffuse white plastic was measured at a fixed distance of 0.25 m and with

¹Source: www.epitex.com/products/led_plastic_mold/pdfs/L1550-03.pdf (online 2012-12-22)

ambient temperatures ranging from 0 °C to 50 °C. All measurements presented here were performed at minimal relative humidity, which was about 10 % to 15 % for the used climate chamber.

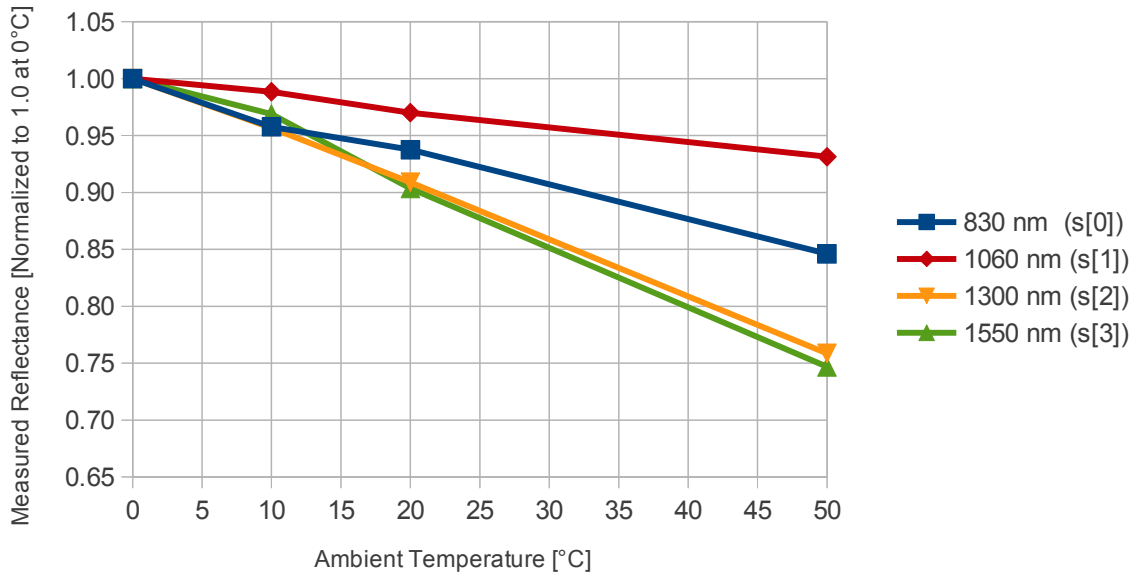


Figure 7.28: Spectral signatures acquired from 0 °C to 50 °C using a *Skinner* mark 2 sensor.

Fig. 7.28 illustrates the spectral signatures, averaged from ten measurements per temperature. As expected, the amplitudes decrease with increasing temperature, because the temperature affects the efficiency of the *LEDs* and photodiodes (see Sec. 5.2.2). However, the amplitudes at $\hat{\lambda}_0 = 830\text{ nm}$ and $\hat{\lambda}_1 = 1060\text{ nm}$ decrease significantly less than the amplitudes at $\hat{\lambda}_2 = 1300\text{ nm}$ and $\hat{\lambda}_3 = 1550\text{ nm}$.

Table 7.13: Pulse current settings for the used *Skinner* sensor.

830 nm	1060 nm	1300 nm	1550 nm
167 mA	144 mA	167 mA	202 mA

As listed in Tab. 7.13, the 1060 nm *LED* is operated at the lowest current and the 1550 nm *LED* is driven at the highest current. The currents of the *LEDs* emitting at

1060 nm, 1300 nm and 1550 nm were set with respect to their forward voltages to achieve equal levels of power dissipation. To compensate the lower sensitivity of the detector at 830 nm, the current for the corresponding LED was set to result in a higher power dissipation.

A possible explanation for the unequal signal regression over the temperature is that the forward voltages and thus the power dissipation of the LEDs is changing differently with the ambient temperature. Furthermore, the LED emitting at 830 nm has the highest power dissipation and therefore the strongest self heating, which could result in a reduced dependence on the ambient temperature. Nevertheless, the temperature of the transmitter should be supervised by the embedded system to allow an algorithmic compensation to minimize the distortion of the spectral signatures.

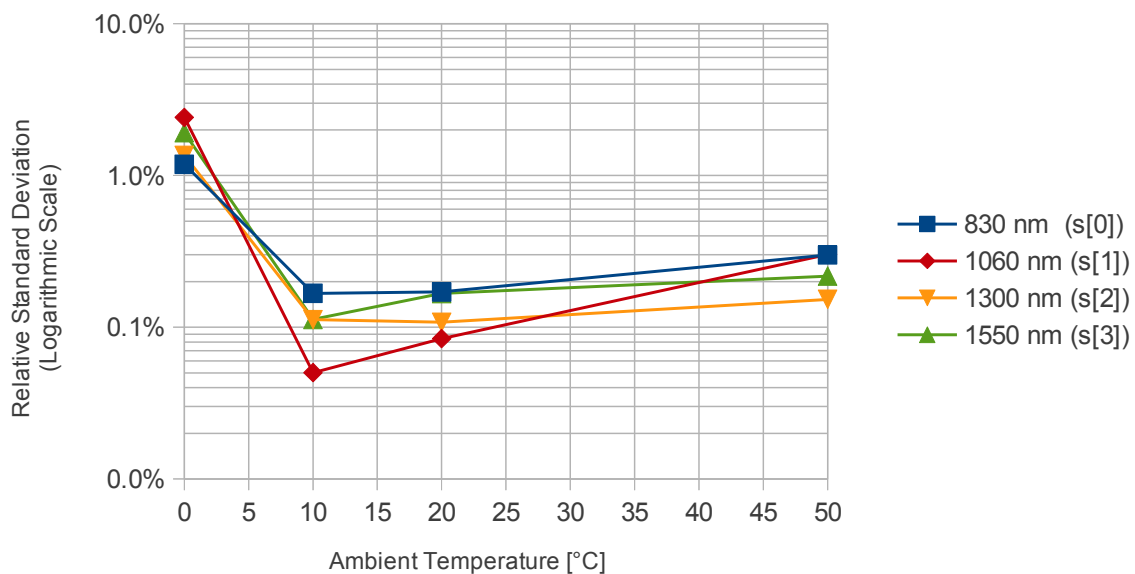


Figure 7.29: Relative standard deviation of spectral signatures acquired over a temperature range from 0 °C to 50 °C.

Fig. 7.29 shows the RSD measured at different ambient temperatures. The minimum is at 10 °C with an average RSD of 0.11 %, which increases to 0.24 % at 50 °C.

However, the maximum **RSD** of 1.72 % on average was measured at 0 °C. Usually, the electrical characteristics of analog components are better at low temperatures, but the component¹ which is used to control the pulse current of the **LEDs** has an exponentially increasing drop-out voltage with decreasing temperature. Furthermore, it is the only component which is not specified to operate at temperatures below 0 °C. Therefore, the measurement was performed at the component's specified limit. As a consequence, this component should be replaced by one which is rated for an extended temperature range for future designs (such as Infineon BCR321U).

7.4 Cross Relations of Interference Factors

The last sections provided an evaluation of the presented methods as well as the significance of typical artifacts and environmental influences to **Skinner** sensors. In practice, different artifacts or external interference factors might occur at once. For instance, measurements at partial beam overlap will occur if a new object is moved into the beam while being illuminated by a strong incandescent lamp, which is oscillating at 100 Hz. In this situation, a systematic deviation of the spectral signature would be combined with an increased variance (Sec. 7.3.1+7.2.1). In consequence, the additional variance may cause false classifications that would not occur with one of the two distorting factors alone, if the acquired spectral signatures would be distorted towards the characteristics of another material class. Naturally, this scenario can be extended by more factors, such as a high ambient temperature.

In summary, it is not possible to investigate all combinations of several interference factors and their extents, but it is possible to categorize the mode of interference of the discussed factors. Such a categorization is attempted in Tab. 7.14.

¹Adjustable regulator type LM1117-ADJ

Table 7.14: Overview of interference factors and their impact.

Factor	Distortion Type	Effect on \hat{d}	Effect on \vec{s}	Effect on \vec{r}
Partial Beam Overlap	systematic	medium ¹	high	high ²
Multiple Objects	systematic	medium ³	high	high
Shiny Objects	systematic ⁴	low	extreme	extreme
Ambient Light	increases variance ⁵	low	medium	medium
Air Humidity	attenuating	very low	medium	low
Amb. Temperature	attenuating/variance ⁶	very low	medium	low

¹ Depending on estimator

² Depending on beam homogeneity

³ Leads to ambiguous data

⁴ Random values may occur if object is moving and/or beam is not homogeneous

⁵ Saturation of receiver possible (depending on distances, radiation power and frequency)

⁶ Depending on (opto-)electronics (if not temperature compensated)

This table can only be seen as a point of orientation, as the actual significance and mode of the distortion is depending on various factors. For instance, ambient light can be constant or oscillating at different frequencies and within a wide range of tolerable intensities. Besides these obvious limitations, the table shows that optical measurement artifacts are the most problematic group of interference factors. Furthermore, the extent of those artifacts is depending on the optical design, especially the beamforming. The evaluation presented in this chapter shows which measures are appropriate to reduce some of these artifacts. However, there is still room for improvement with respect to several applications. This is discussed in the following chapters, which are concluding this thesis.

Chapter 8

Examples of Applications

Within Chap. 5, different assumptions were made to characterize typical requirements for an AOMCPD. In this chapter, three examples of possible applications for such sensors are presented. Each example bares unique requirements to an AOMCPD, as shown in the following sections.

8.1 Woodwork Shops

At woodwork shops, large sliding table saws are widely used. According to technical information on the F45 ELMO IV sliding table saw by Altendorf, saw blades with diameters \varnothing_{blade} of 250 mm to 550 mm can be used. The saw blade can be adjusted in height and tilted to an angle of up to 45° . Both settings and the blade's diameter \varnothing_{blade} effect the position of the blade's cutting edge on the worktop and thus the definition of the danger zone. Furthermore, a second saw blade can be installed in front of the primary saw blade, which is denoted as the scoring blade. This blade is significantly smaller with diameters of about $\varnothing_{scoring} \approx 80$ mm and it protrudes only a couple of millimeters over the worktop. Having such a variable danger zone, the

AOMCPD(s) cannot be installed at a fixed position(s), if a constant distance to the actual danger zone is desired. Simultaneously, the top safety hood of the saw should always be adjusted to the thickness of the workpiece to prevent that the user's hands can get underneath [79, p.129]. The top safety hood is designed to encompass the largest specified saw blades at the highest possible position together with the optional scoring blade (see Fig.8.1). So, if the top safety hood would always be adjusted to the height of the workpiece, the user could hardly ever reach the saw blade and the risk of injury would be minimized. According to information provided by the [Institute for Occupational Safety and Health of the German Social Accident Insurance \(IFA\)](#), this safety rule is often flouted, which is most likely a reason for the high amount of accidents at such machines (see Chap. 1).

In consequence, an effective attempt is to ensure a minimal height of the safety hood in every situation by an automatic adjustment. Fig. 8.1 depicts the concept, where only one spot directly in front of the safety hood is observed by an AOMCPD. The AOMCPD measures the height of approaching workpieces and controls a motorized height adjustment, which lifts the safety hood a couple of millimeters above the workpiece's surface. Furthermore, the AOMCPD recognizes skin and will not adjust the height of the safety hood for an approaching hand, so that the saw blade(s) can hardly be reached.

Technically, such an automatic height adjustment is relatively simple to implement, as only the narrow front side of the safety hood must be observed and extremely fast brakes for the saw blades are not required. Braking the saw blades within some tens of milliseconds is especially problematic for sliding table saws, because large and heavy saw blades are used which rotate at up to 5000 rpm. This concept was successfully investigated in the first part of the SMART.HOOVER¹ project.

¹Funded by the Berufsgenossenschaft Holz und Metall (BGHM).

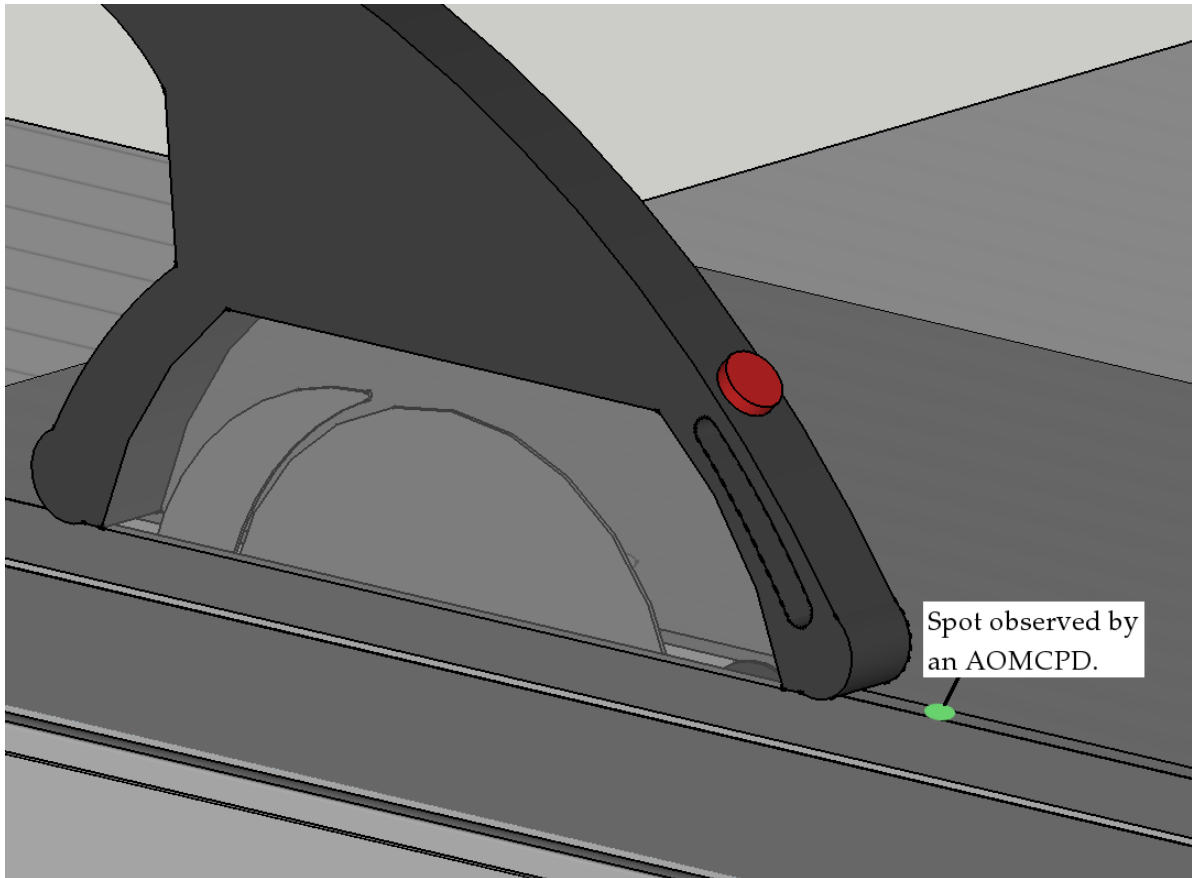


Figure 8.1: Concept image depicting an observed spot. (Source: SMART.HOOVER project)

For a simplified cost estimation, the costs for the required optoelectronic components can be used, as they are among the most expensive parts of the sensor. According to a reseller of optoelectronic components¹, the costs for a set of four LEDs at the desired wavebands are about EUR 22 by the time of this work. At the same reseller, an InGaAs photodiode costs about EUR 15. In consequence, the total costs for the required optoelectronic components for a single sensor with four photodiodes are about $\text{EUR } 22 + 4 * \text{EUR } 15 \approx \text{EUR } 80$. Naturally, the costs for the components would scale down for a mass production. For this estimation, it is assumed that this saving will compensate the additional direct costs and common expenses. As only

¹Roithner Lasertechnik GmbH, Austria.

the front side of the safety hood must be observed, a small amount of one to three sensors can be expected to be sufficient. For three sensors, the costs would be about $\text{EUR } 80 \cdot 3 = \text{EUR } 240$. According to Altendorf, a sliding table saw type F45 ELMO IV costs between EUR 31 800 to EUR 50 000, depending on the options. In consequence, the sensor system would cost less than 1 % of the machine's total costs with respect to the basic version of the saw.

Furthermore, the functional requirements related to this application example are good-natured: The sensors would operate at relatively close distances, as the top safety hood cannot be moved much higher than the maximum cut depth of the saw, which is at most 200 mm for an F45 ELMO IV. Usually, only dry wood is processed at woodwork shops, which is easier to differentiate from skin than wet wood. As such machines are installed indoors, lighting and temperature are usually controlled as well. Furthermore, it is disregarded to work with gloves at such machines. In consequence, the [AOMCPD](#) must differentiate skin from different types of wood, including plastic laminated finishes. Saw dust is removed by suction underneath the worktop and within the top safety hood. Therefore, pollution of the sensors can be prevented.

8.2 Meat Processing

In this section, the example of a bone band saw is chosen to discuss the applicability of an [AOMCPD](#). Bone band saws are operated indoors at low temperatures. They are frequently cleaned using hot water from high-pressure cleaners. In consequence, a sensor being a part of such a machine must withstand water at high pressures and changing ambient temperatures. Fortunately, the environment is very clean and

the user's gloves or skin will be covered at most by a thin layer of grease from the processed meat.

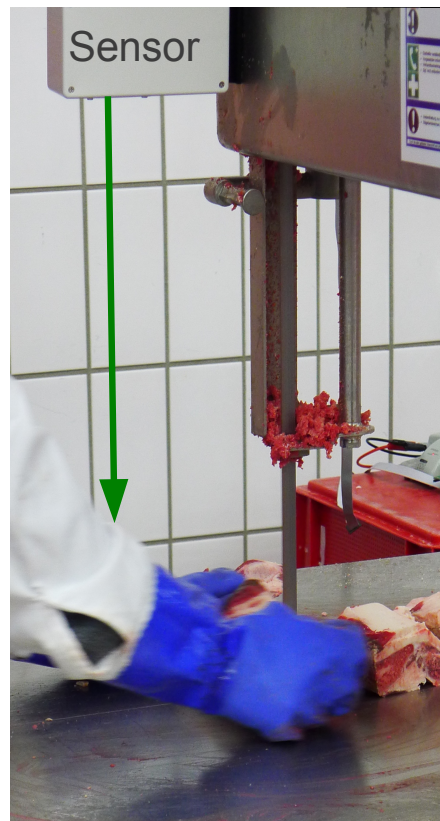


Figure 8.2: Practical test of a [Skinner](#) mark 2 sensor at a bone band saw.

As shown in Fig. 8.2, a practical test was carried out using such a machine as part of the [LBIS](#) project. A single [Skinner](#) mark 2 sensor was mounted at the machine with the detecting beam in parallel to the band saw at a distance of about 180 mm. Two tests were performed with this setup. First, the sensor was measuring at maximum frequency with two visible [LEDs](#) attached, to signalize if human skin or gloves were detected. Afterward, a total of 95432 measurements were recorded at a frequency of 60 Hz in a second run. As a result of the tests, the user's gloves could be perfectly differentiated from the processed meat and bones, while meat was often misclassified as human skin. In consequence, the recorded data were analyzed to see if the classifier

for human skin could be improved to avoid false positive classifications. Using the original classifier, about 15000 recorded measurements were misclassified as human skin. A new SVM was trained on a combination of the laboratory measurements and recorded data. Using the resulting classifier, only 44 false positive classifications occur on the recorded data. However, having 44 false positives in less than 27 minutes is clearly too much, as it would lead to an unacceptable rate of false alarms. As only a differentiation of gloves and meat could be done reliably, the users need to wear gloves in order to be protected by such a sensor system.

Furthermore, it was shown that the distance of the sensor to the band saw was too large. The test user's opinion was that it should be as close as 40 mm to the band saw. Assuming that a distance of 40 mm would be sufficient to stop the band saw in time, such a machine could be monitored using a small amount of about one to four sensors.

In the previous section, the costs for one sensor were predicted to be EUR 80. Therefore, with one to four sensors the costs for the whole system would be in the range from EUR 80 to EUR 320, which is about 2.5 % to 10 % of the price for a high-end bone band saw such as the SO2400 INOX from Sirman SpA. This bone band saw was offered for EUR 3100 by the gi management GmbH (a reseller for gastronomic equipment) in December 2012.

8.3 Construction Sites

For construction sites, circular table saws are selected as an example for a dangerous manually fed machine. Such machines are used outdoors at construction sites. In consequence, they are unprotected from rain, direct sunlight and a wide temperature

range. Therefore, the AOMCPD must be designed to withstand water, strong ambient illumination and must be able to operate from $-20\text{ }^{\circ}\text{C}$ to $50\text{ }^{\circ}\text{C}$.



Supporting timber



Used nitrile glove

Figure 8.3: Soiled supporting timber and glove from a construction site.

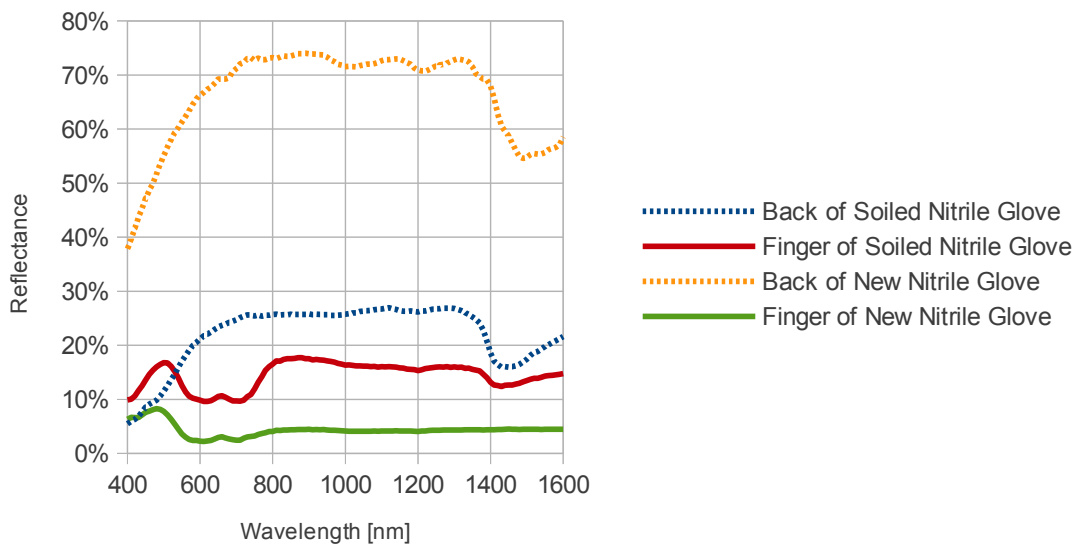


Figure 8.4: Reflectance spectra of new and soiled nitrile gloves.

These saws are used to cut supporting timber, plastic pipes and other materials. The users may wear nitrile gloves to protect their hands from splinters. As shown in Fig. 8.3, gloves and workpieces can be soiled, wet and worn out. Fig. 8.4 shows reflectance spectra from a new and a used and soiled nitrile glove. The back of the gloves is not covered with nitrile, so the uncoated cloth is visible. The fingers are fully covered by nitrile. All presented spectra were measured at a construction site as part of the preliminary study presented in Chap. 4. Comparing the spectra of the gloves, it can be seen that the overall reflectance differs strongly between the new and the used glove.

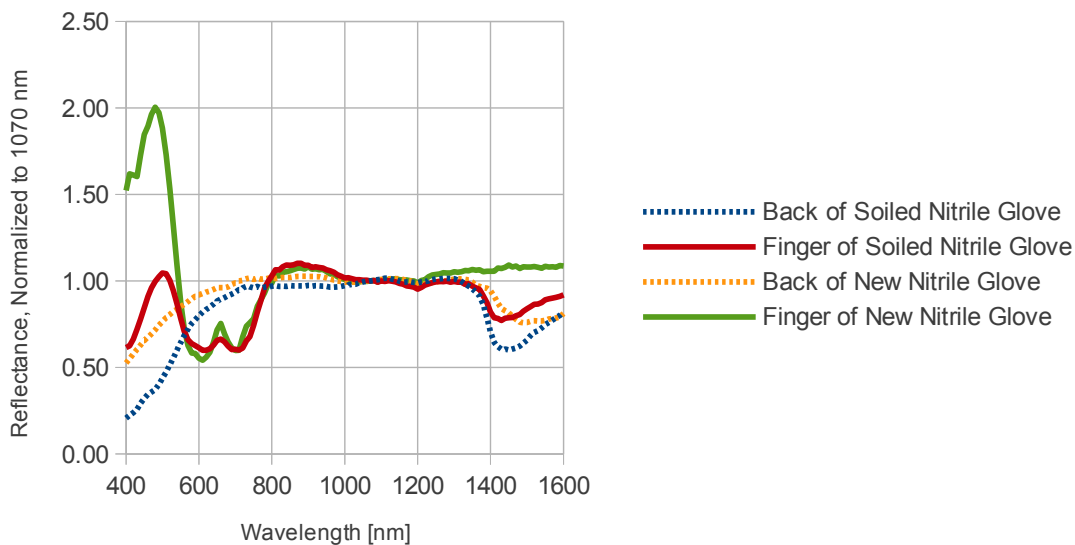


Figure 8.5: Reflectance spectra of new and soiled nitrile gloves, normalized to the reflectance at 1070 nm.

However, the shape of the spectra is quite stable within the range from 800 nm to 1350 nm, as illustrated in the normalized plot in Fig. 8.5. As the *Skinner* sensors possess three wavebands within this range, these gloves can be detected relatively good. However, the shape of the spectra is not very distinctive, as it basically provides

a steady reflectance level. As shown in Fig. 8.6, other artificial materials such as polyvinyl chloride (PVC) or hard polystyrene foams yield similar reflectance spectra. Unfortunately, these materials are often used for tube spacers and thermal insulation, which can be cut using circular table saws. In consequence, distinctive spectral markers (such as fluorescent dyes) should be added to the gloves to increase their differentiability from typical workpieces.

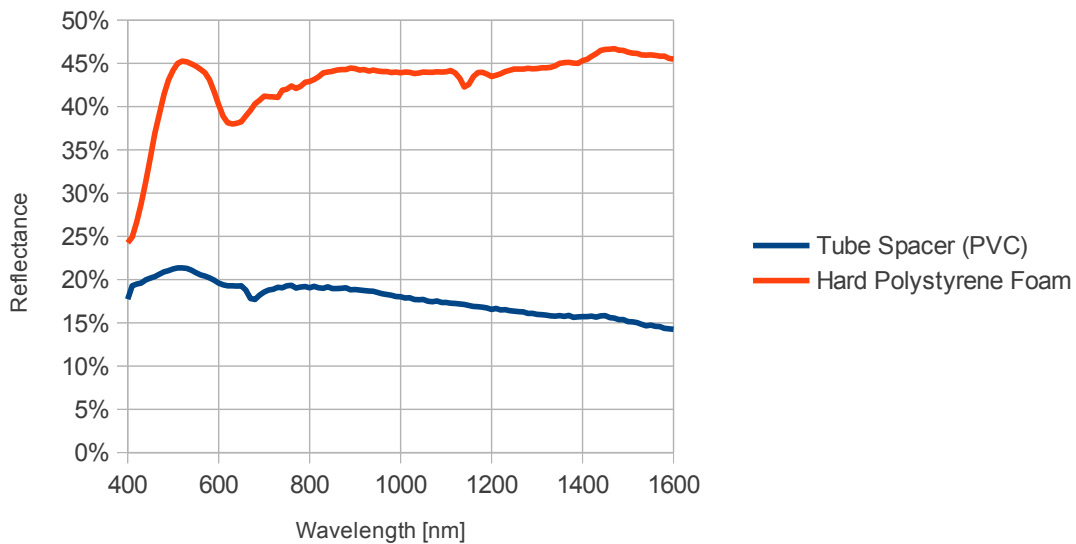


Figure 8.6: Reflectance spectra of common workpieces at construction sites.

Unlike sliding table saws, modern circular table saws for construction sites feature self-adjusting safety hoods (e.g., see AVOLA ZBV-10). Therefore, the sides of the saw blade are usually shielded and only the area in front of the saw blade must be protected by additional sensors. Assuming that one sensor is enough to protect this area, the costs estimated in the last sections would be EUR 80, which is about 3 % of a high-end circular table saw for construction sites as the AVOLA ZBV 500. Such a saw was offered for about EUR 2580 without further equipment options by Escher Schalungszubehör GmbH in December 2012.

In summary, the presented sensor concept is applicable to many different applications, but each application's specific requirements and characteristics must be taken into account.

Chapter 9

Summary and Outlook

9.1 Summary

In this thesis, the concept for a multispectral sensor for safety applications is presented in detail, which introduces the class of active optoelectronic material classifying protective devices (AOMCPD). This concept makes use of the distinctive characteristics of human skin within the near-infrared spectrum as a basis for the differentiation of skin against a wide range of other materials [9]. To classify the surface material of an object in question, its spectral key properties are acquired contact-free by a sequential reflectance measurement at several wavebands. To achieve this, LEDs are used to generate strobe pulses at distinct wavebands. If these strobe pulses illuminate a surface, the incident energy will partially be absorbed and reflected in a characteristic ratio. This ratio varies from waveband to waveband, creating a *spectral signature* for each material. A selection of appropriate wavebands, which represents spectral key properties with respect to the application field of skin detection at manually fed machines, has been determined through an analysis of reflectance spectra gathered from several hundred people and workpieces.

Besides a well-suited selection of wavebands, a good optical design is crucial to acquire precise measurements from a sharply defined spot. This work presents a design concept, which comprises beamforming optics to generate a narrow and homogeneous multispectral beam and a receiver unit to measure the reflected radiation. Furthermore, a concept to implement the electronics and self testing measures is described. As a result, system specifications for a prototypical implementation are derived. This prototype is denoted as the *Skinner* sensor system. Introducing a set of profound methods for signal processing, the prototype's raw sensor readings are converted into the desired spectral signature, which is then used for material classification. The material classification either results in the detection of an uncritical material representing an arbitrary workpiece or a critical material, such as human skin. If a critical material is detected, the sensor would trigger protective means in order to prevent a potential accident. Additionally, the sensor's distance to the targeted surface is determined.

Both, the *Skinner* sensor system and the presented methods are evaluated with respect to their susceptibility to measurement artifacts and external influences. Synthesized data from optical simulations of idealized sensor models are used to evaluate the distance estimation methods individually. This way, the comparison of the methods depends less on the specific characteristics of the built hardware [4]. Furthermore, a multispectral extension was proposed and evaluated for all respected methods, which yields an improved accuracy on noisy and distorted data. The data fusion method is validated using idealized input values and intentionally added errors to allow for a validation apart of the distance estimator's accuracy. As the last step of signal processing, the classification reliability was evaluated for several application scenarios. The results show that the *Skinner* sensor system is capable of perfectly discriminating human skin from typical workpieces, such as wood and plastics.

Furthermore, the performance of two state-of-the-art methods for the implementation of material classifiers is evaluated in several experiments. The evaluation of the presented methods is concluded by a measurement of the computational time using an AT32UC3C [microcontroller](#) by Atmel, yielding that the entire data acquisition and processing can be done in about $t = 0.9$ ms. Furthermore, the results of several experiments on external influences such as ambient light, temperature, air humidity and artifacts arising when measuring at partial overlap of the beam with a surface are presented. The results are yielding that unfavorable geometrical measurement conditions, such as a partial overlap of the beam with a surface, are causing the most severe distortions.

Active optoelectronic material classifying protective devices ([AOMCPDs](#)) define a new type of safety equipment, which is not yet covered by international safety standards. Therefore, current safety standards are used as a basis to derive common safety requirements for the presented sensor concept. Especially the IEC 61496-2 is important among these standard, which defines requirements and tests for common optoelectronic protective devices ([AOPD](#)), i.e. light curtains and light barriers [49]. Some of these requirements can directly be applied to [AOMCPDs](#), while requirements on optical properties are generally harder to adopt. Therefore, the current limits are discussed and new safety requirements and test procedures are proposed as a primary contribution.

9.2 Outlook

The validation of the system has shown that the beamforming could be optimized furthermore to reduce artifacts when measuring at partial overlap of the beam to a surface and to allow the detection of single fingers at larger measurement distances. Therefore, alternative beamforming design methods should be investigated. Furthermore, an algorithm could be developed to detect a partial overlap of an object with the beam, which could be done by analyzing the light intensity distribution over the photodetectors. A snapshot of the light intensity distribution is captured with each strobe pulse for each waveband. An algorithmic comparison of these light intensity distributions per waveband could allow to detect shiny surfaces or a quick movement of an object's edge within the beam.

The evaluation has shown that the data fusion method could be improved by taking the shape of the individual signals into account. The electronics for the suppression of ambient light might be optimized as well. Additionally, a temperature control or at least an algorithmic temperature compensation should be implemented.

Another important task is the actual industrialization of the sensor concept. This requires optimized designs in terms of costs and performance with respect to the targeted applications. Furthermore, the existing international safety standards on [AOPDs](#) are not covering all relevant aspects for this new type of sensors. In conclusion, requirements and test procedures for [AOMCPDs](#) should be included into future versions of the corresponding standards to ensure legal certainty for manufacturers and operators of [AOMCPDs](#). This work is meant to be a starting point for such normative processes as well as product developments.

Bibliography

- [1] Holz BG, "Holzinfo", Tech. Rep. 122, Holz-Berufsgenossenschaft, Holz BG, Am Knie 8, 81241 Munich, Germany, 2006.
- [2] N. Marcy, G. Rutherford and A. Mills, "Hazard screening report, power tools and workshop equipment", Tech. rep., U.S. Consumer Product Safety Commission, 4330 East West Highway, Bethesda, MD 20814, USA, 2003.
- [3] Fachausschuss Persönliche Schutzausrüstungen der BGZ, "Berufsgenossenschaftliche Regeln für Sicherheit und Gesundheit bei der Arbeit - Einsatz von Schutzhandschuhen", Tech. Rep. 195, German Social Accident Insurance (DGUV), Mittelstraße 51, 10117 Berlin, Germany, 2004.
- [4] O. Schwaneberg, U. Köckemann, H. Steiner, S. Sporrer, A. Kolb and N. Jung, "Material classification through distance aware multispectral data fusion", *Meas. Sci. Technol.*, **vol. 24** (2013), no. 4, p. 045 001.
- [5] O. Schwaneberg, H. Steiner, P. Haring Bolívar and N. Jung, "Design of an LED-based sensor system to distinguish human skin from workpieces in safety applications", *Appl. Opt.*, **vol. 51** (2012), no. 12, pp. 1865–1871.

- [6] O. Schwaneberg, U. Köckemann, H. Steiner and N. Jung, "A near-infrared LED-based material classification sensor system", in *Proc. OSA Int. Conf. Optical Sensors*, p. SMD4, Optical Society of America, 2011.
- [7] G. ElKoura and K. Singh, "Handrix: animating the human hand", in *Proc. Int. Symp. Computer Animation*, SCA, pp. 110–119, Eurographics Association, Aire-la-Ville, Switzerland, Switzerland, 2003.
- [8] H. Nazarudin, Internet Blog "two girls in the jungle", 2011.
URL http://www.twogirlsinthejungle.com/wp-content/uploads/2011/03/fitzpatrick_landing_faces.png
- [9] J. Jacquez, J. Huss, W. McKeehan, J. Dimitroff and H. Kuppenheim, "Spectral reflectance of human skin in the region 0.7-2.6 μm ", *Appl. Physiol.*, **vol. 8** (1955), no. 3, p. 297.
- [10] T. Fitzpatrick, "The validity and practicality of sun-reactive skin types i through vi", *Arch. Dermatol.*, **vol. 124** (1988), no. 6, p. 869.
- [11] F. Rosenblatt, "The perceptron: A probabilistic model for information storage and organization in the brain", *Psychol. Rev.*, **vol. 65** (1958), no. 6, pp. 386–408.
- [12] B. Scholkopf and A. J. Smola, *Learning with Kernels: Support Vector Machines, Regularization, Optimization, and Beyond*, The MIT Press, 2001.
- [13] V. Vapnik and A. Chervonenkis, *Theory of Pattern Recognition [in Russian]*, Nauka, Moscow, 1974.
- [14] C. Cortes and V. Vapnik, "Support-vector networks", *Mach. Learn.*, **vol. 20** (1995), pp. 273–297.

- [15] C.-C. Chang and C.-J. Lin, "LIBSVM: A library for support vector machines", *ACM Trans. Intelligent Systems and Technology*, **vol. 2** (2011), pp. 1–27.
- [16] J. R. Quinlan, *C4.5: programs for machine learning*, Morgan Kaufmann Publishers Inc., San Francisco, CA, USA, 1993.
- [17] J. R. Quinlan, "Induction of decision trees", *Mach. Learn.*, **vol. 1** (1986), pp. 81–106.
- [18] T. Fawcett, "ROC graphs: Notes and practical considerations for researchers", Tech. rep., HP Laboratories, 2004.
URL <http://www.hpl.hp.com/techreports/2003/HPL-2003-4.pdf>
- [19] J. Davis and M. Goadrich, "The relationship between precision-recall and ROC curves", in *Proc. Int. Conf. Machine Learning (ICML)*, 23, pp. 233–240, ACM, New York, NY, USA, 2006.
- [20] K.-C. Kim, J. A. Kim, S. Kim and Y. K. Kwak, "A robust signal processing algorithm for linear displacement measuring optical transmission sensors", *Rev. of Sci. Instrum.*, **vol. 71** (2000), no. 8, p. 3220.
- [21] K.-C. Kim, S. B. Oh, S. H. Kim and Y. K. Kwak, "Design of a signal processing algorithm for error-minimized optical triangulation displacement sensors", *Meas. Sci. Technol.*, **vol. 12** (2001), no. 10, p. 1683.
- [22] G. Jacovitti and G. Scarano, "Discrete time techniques for time delay estimation", in *IEEE Trans. Signal Processing*, vol. 41, p. 525, 1993.
- [23] C. Knapp and G. Carter, "The generalized correlation method for estimation of time delay", in *IEEE Trans. Acoustics, Speech and Signal Processing*, vol. 24, pp. 320 – 327, 1976.
- [24] T. M. Mitchell, *Machine Learning*, McGraw-Hill Science/Engineering/Math, 1997.

- [25] I. Pavlidis, P. Symosek, B. Fritz and N. Papanikolopoulos, "A near-infrared fusion scheme for automatic detection of vehicle passengers", in *Proc. IEEE Conf. Comp. Vis. Beyond the Vis. Spec.; Workshop Methods and Applications (CVBVS)*, pp. 41–48, 1999.
- [26] J. Dowdall, I. Pavlidis and G. Bebis, "Face detection in the near-ir spectrum", *Image Vision Comput.*, **vol. 21** (2003), no. 7, pp. 565–578.
- [27] H. Iwasaki, K. Miyazawa and S. Nakauchi, "Visualization of the human face skin moisturizing ability by spectroscopic imaging using two near-infrared bands", in *Proc. Int. Symp. Multispectral Color Science*, vol. 6062, pp. 606 203–606 203–8, SPIE, 2006.
- [28] H. Steiner, O. Schwaneberg and N. Jung, "Advances in active near-infrared sensor systems for material classification", in *Proc. OSA Int. Conf. Imaging Systems and Applications*, p. ITu2C.2, Optical Society of America, 2012.
- [29] Hacskeylo, "Automatic human body detector", US patent 4,500,784, 1985.
- [30] G. Determan and D. Wunderlin, "Encoded binary liveness detector", US patent 2008/0203307 A1, 2008.
- [31] A. Cvetkovic, O. Dross, J. Chaves, P. Benitez, J. C. Miñano and R. Mohedano, "Etendue-preserving mixing and projection optics for high-luminance LEDs, applied to automotive headlamps", *Opt. Express*, **vol. 14** (2006), no. 26, pp. 13 014–13 020.
- [32] C.-C. Sun, I. Moreno, Y.-C. Lo, B.-C. Chiu and W.-T. Chien, "Collimating lamp with well color mixing of red/green/blue leds", *Opt. Express*, **vol. 20** (2012), no. S1, pp. A75–A84.

- [33] G. Wang, L. Wang, F. Li and G. Zhang, "Collimating lens for light-emitting-diode light source based on non-imaging optics", *Appl. Opt.*, **vol. 51** (2012), no. 11, pp. 1654–1659.
- [34] J.-J. Chen, T.-Y. Wang, K.-L. Huang, T.-S. Liu, M.-D. Tsai and C.-T. Lin, "Freeform lens design for LED collimating illumination", *Opt. Express*, **vol. 20** (2012), no. 10, pp. 10 984–10 995.
- [35] D. Reinert, O. Schwaneberg, N. Jung, S. Ullmann, W. Olbert, K. D. and R. Kohler, "Finger and hand protection on circular table and panel saws", *Safety Sci.*, **vol. 47** (2009), no. 8, pp. 1175 – 1184.
- [36] O. Schwaneberg, *Differenzierung von Haut und Werkstoffen durch einen optischen Sensor und geeignete Auswertungsalgorithmen in einem sicherheitsbezogenen Umfeld*, Master's thesis, Bonn-Rhine-Sieg University of Applied Sciences, 2006.
- [37] D. Reinert, N. Jung and O. Schwaneberg, "A manually fed machine for working on materials, objects and the like, and protective means for such a machine", 2009, patent EP2054193 / EP2193878 / US 8,171,831 B2.
- [38] O. Schwaneberg, N. Jung and D. Reinert, "Apparatus for authenticating a person on the basis of at least one biometric parameter", 2008, WIPO Patent Application WO/2008/125491.
- [39] O. Schwaneberg, H. Steiner, N. Jung and D. Reinert, "Push-buttons with material classification based on spectral signatures", in *Proc. Int. Conf. Safety of Industrial Automated Systems (SIAS)*, 6, pp. P:1–5, Finnish Society of Automation, Tampere/Finland, 2010.

- [40] T. Troy and S. Thennadil, "Optical properties of human skin in the near infrared wavelength range of 1000 to 2200 nm", *Biomed. Opt.*, **vol. 6** (2001), no. 2, pp. 167–176.
- [41] I. V. Meglinski and S. J. Matcher, "Quantitative assessment of skin layers absorption and skin reflectance spectra simulation in the visible and near-infrared spectral regions", *Physiol. Meas.*, **vol. 23** (2002), no. 4, p. 741.
- [42] S. Pfeifer, *Concept and development of a system for measuring angle dependent spectral remission to distinguish material surfaces for safety applications*, Bachelor's thesis, Bonn-Rhein-Sieg University of Applied Sciences, 2011.
- [43] L. Wolff, "Polarization-based material classification from specular reflection", in *IEEE Trans. Pattern Analysis and Machine Intelligence*, vol. 12, pp. 1059–1071, 1990.
- [44] R. Anderson and J. Parrish, "The optics of human skin", *Invest. Dermatol.*, **vol. 77** (1981), no. 1, pp. 13–19.
- [45] IEC, "Safety of machinery - Electro-sensitive protective equipment - Part 3: Particular requirements for equipment using active opto-electronic protective devices responsive to diffuse reflection (AOPDDR) (IEC 61496-3)", 2009, pre-standard.
- [46] ISO, "Safety of machinery - Safety-related parts of control systems - Part 1: General principles for design (ISO 13849-1:2006)", 2007.
- [47] IEC, "Functional safety of electrical/electronic/programmable electronic safety-related systems (IEC 61508)", 1997.

- [48] IEC, "Safety of machinery - Electro-sensitive protective equipment - Part 1: General requirements and tests (IEC 61496-1 : 2004 + A1 : 2007 + Corrigendum : 2008)", 2009.
- [49] IEC, "Safety of machinery - Electro-sensitive protective equipment - Part 2: Particular requirements for equipment using active opto-electronic protective devices (AOPDs) (IEC 61496-2)", 2008, prestandard.
- [50] ISO, "Safety of machinery - Positioning of safeguards with respect to the approach speeds of parts of the human body (ISO 13855:2010)", 2010.
- [51] DIN, "Ergonomics - Human body dimensions - Part 2: Values (DIN 33402-2)", 2005.
- [52] IEC, "Safety of machinery - Part 1: Equipment classification, requirements and user's guide (IEC 60825-1)", 2001.
- [53] A. Hüning, W. Link, F. Pfaffinger, C. Preusse and D. Schilling, "Maschinen der Zerspannung", Tech. rep., 2008.
URL <http://publikationen.dguv.de/dguv/pdf/10002/bgi5003.pdf>
- [54] R. Rohde, Global Warming Art Project, 2007.
URL http://www.globalwarmingart.com/wiki/File:Solar_Spectrum_png
- [55] T. Elder and J. Strong, "The infrared transmission of atmospheric windows", *J. Franklin Inst.*, vol. 255 (1953), no. 3, pp. 189 – 208.
- [56] IEC, "Classification of environmental conditions - Part 1 : Environmental parameters and their severities (IEC 721-1 : 1990 + A1 : 1992 + A2 : 1995)", 1997.

- [57] R. Hardy, "ITS-90 formulations for vapor pressure, frost point temperature, dew point temperature, and enhancement factors in the range -100 to $+100$ C", in *Proc. Int. Symp. Humidity and Moisture*, vol. 1, pp. 214–222, 1998.
- [58] Beer, "Bestimmung der Absorption des rothen Lichts in farbigen Flüssigkeiten", *Ann. Phys.*, vol. 162 (1852), no. 5, pp. 78–88.
- [59] IEC, "Degrees of Protection Provided by Enclosures (IP Code) (IEC 60529:1989 + A1:1999)", 2001.
- [60] EPIGAP Optoelektronik GmbH, 12555 Berlin, Köpenicker Str. 325b, Haus 201, Germany, *Photodiode-Chip EPC-1300-1.0-1*, 2009.
URL http://www.epigap-optronic.de/tl_files/frontend/epigap/Datenblaetter/PD%20Chips/EOPC-1300-1.0.pdf
- [61] Authorless, "Lamp spectra and irradiance", Tech. rep., LOT-Oriel Group Europe, 2012.
URL http://www.lot-oriel.com/files/downloads/lightsources/eu/LQ_Lamp_spectra_and_irradiance_eu.pdf
- [62] E. Sutter, *Schutz vor optischer Strahlung: Laserstrahlung, inkohärente Strahlung, Sonnenstrahlung ; Normenreihe DIN EN 60825 (VDE 0837)*, VDE-Schriftenreihe Normen verständlich, VDE-Verlag, 2002.
- [63] W. J. Smith, *Modern optical engineering*, McGraw-Hill New York, 2000.
- [64] I. Moreno, "LED intensity distribution", in *Proc. Int. Conf. Optical Design*, 8, p. TuD6, Optical Society of America, 2006.

- [65] T. Kari, J. Gadegaard, T. Søndergaard, T. G. Pedersen and K. Pedersen, "Reliability of point source approximations in compact LED lens designs", *Opt. Express*, **vol. 19** (2011), no. S6, pp. A1190–A1195.
- [66] K. H. Yang and J. D. Kingsley, "Calculation of coupling losses between light emitting diodes and low-loss optical fibers", *Appl. Opt.*, **vol. 14** (1975), no. 2, pp. 288–293.
- [67] M. Fukuda, "Laser and LED reliability update", *Lightw. Technol.*, **vol. 6** (1988), no. 10, pp. 1488–1495.
- [68] S. Bera, R. Singh and V. Garg, "Temperature behavior and compensation of light-emitting diode", *IEEE Photon. Technol. Lett.*, **vol. 17** (2005), no. 11, pp. 2286 – 2288.
- [69] N. Jung, O. Schwaneberg and P. Adam, "Field study results of a skin detecting safety sensor on circular saws", in *Proc. Int. Conf. Safety of Industrial Automated Systems (SIAS)*, 6, Finnish Society of Automation, Tampere/Finland, 2010.
- [70] J. R. Janesick, *Scientific charge - coupled devices*, SPIE Press Monograph, Vol. PM83, SPIE, 2001.
- [71] G. Marsaglia, "Ratios of normal variables", *Stat. Softw.*, **vol. 16** (2006), no. 4, pp. 1–10.
- [72] H. Tian, B. Fowler and A. Gamal, "Analysis of temporal noise in cmos photodiode active pixel sensor", *IEEE J. Solid-State Circuits*, **vol. 36** (2001), no. 1, pp. 92–101.
- [73] C. Chang and C. Lin, "LIBSVM: A library for support vector machines", *ACM Trans. Intell. Syst. Technol.*, **vol. 2** (2011), pp. 1–27.

- [74] C. De Boor, *A Practical Guide to Splines*, no. Bd. 27 in Appl. Math. Sci., Springer, 2001.
- [75] T. Curk, J. Demšar, Q. Xu, G. Leban, U. Petrovič, I. Bratko, G. Shaulsky and B. Zupan, "Microarray data mining with visual programming", *Bioinformatics*, **vol. 21** (2005), pp. 396–398.
- [76] M. Hall, E. Frank, G. Holmes, B. Pfahringer, P. Reutemann and I. H. Witten, "The weka data mining software: an update", *SIGKDD Explor. Newsl.*, **vol. 11** (2009), pp. 10–18.
- [77] C.-W. Hsu, C.-C. Chang and C.-J. Lin, "A practical guide to support vector classification", Tech. rep., National Taiwan University, Department of Computer Science, Taipei 106, Taiwan, 2003.
- [78] T. Scheer, *Portierung und Erweiterung der Embedded-Software eines Hauterkennungssensors*, Bachelor's thesis, Bonn-Rhein-Sieg University of Applied Sciences, 2012.
- [79] "Arbeitssicherheit und Gesundheitsschutz Schreinereien/Tischlereien", Tech. rep., 2005.
URL <http://publikationen.dguv.de/dguv/pdf/10002/bgi725.pdf>
- [80] K. Pearson, "On lines and planes of closest fit to systems of points in space", *Philos. Mag.*, **vol. 2** (1901), no. 11, pp. 559–572.
- [81] S. Wold, K. Esbensen and P. Geladi, "Principal component analysis", *Chemometr. Intell. Lab.*, **vol. 2** (1987), no. 1–3, pp. 37 – 52.

Abbreviations

AC	alternating-current xx, xxii, 163–165
ACC	accuracy 17, 147, 148, 150, 151
ADC	analog-to-digital converter 99, 102, 103, 109, 112
AOMCPD	active optoelectronic material classifying protective device xxi, 53, 55, 56, 63, 65–69, 71, 72, 74, 77, 78, 82, 83, 90, 154, 173, 174, 176, 179, 183, 185, 186
AOPD	active optoelectronic protective device 53, 54, 61, 63–68, 72, 94, 165, 185, 186
AOPDDR	active optoelectronic protective devices responsive to diffuse reflection 53
ASDF	average square difference function 18, 20
BRSU	Bonn-Rhein-Sieg University of Applied Sciences 35
DC	direct-current xx, xxii, 164
DIN	German Institute for Standardization e.V. 55

EASDF	expanded average square difference function 20, 21, 130–132, 135
EGCC	expanded generalized cross-correlation 20, 21, 130–133, 135, 136, 150, 151, 153
FN	false negative 17, 41, 56
FP	false positive 17
FPR	false positive rate 17, 147, 148, 150, 151
FPU	floating point unit 103, 153
GCC	generalized cross-correlation 18, 20
IEC	International Electrotechnical Commission 55
IFA	Institute for Occupational Safety and Health of the German Social Accident Insurance 35, 174
InGaAs	indium gallium arsenic xvii, 27, 29, 66, 67, 95, 175
LED	light emitting diode xv, xvii, xviii, 2, 25, 29, 31–35, 41, 42, 44, 45, 78, 82–85, 87–89, 91, 92, 95–97, 99–102, 104, 111, 126, 129, 138, 166– 170, 175, 177, 183

MEASDF	multispectral expanded average square difference function 116, 132, 134, 135
MEGCC	multispectral expanded generalized cross-correlation 116, 132–136
MQBTM	multispectral quick binary tree mapping 116, 130, 132–136
MTTF	mean time to failure 89
PCB	printed circuit board xviii, 99–101
PFD	probability of a dangerous failure on demand 56, 57, 76, 151, 152
PFH	probability of a dangerous failure per hour 76, 77
pl	performance level 54, 76, 77
PMD	Photonic Mixing Device 6
PMMA	Polymethylmethacrylate 56
PREC	precision 17, 147, 148, 150, 151
QBTM	quick binary tree mapping 114, 116, 130–136, 140, 147, 150, 151
RH	relative humidity xvii, 60–63
RISC	reduced instruction set computing 100
RMS	root mean square error xxi, xxii, 132, 135
RSD	relative standard deviation 119, 163–165, 169, 170

SIL	safety integrity level 54, 56, 57, 76, 151, 152
SMD	surface mounted device 33
SNR	signal-to-noise ratio 89, 118, 129, 136, 145, 159, 160
SPI	serial peripheral interface 109
TN	true negative 17
TP	true positive 16, 17
TPR	true positive rate 17, 57, 147, 148, 150–152

Glossary

- beam width The *beam width* denotes the diameter of a beam defined as its full width at half-peak intensity (3dB below maximum intensity). 58, 59, 71, 72, 87, 88, 94, 127, 158
- BSRDF The Bi-directional Spectral Reflectance Distribution Function is an extension of the BRDF to regard for spectral information. 46
- CAN The *Controller Area Network* is an industrial standard bus system, which was originally developed for the automotive industry. It is specified as an international standard in ISO 11898. 96, 103
- FFT An efficient algorithm to compute the discrete Fourier transformation (DFT). It is used to convert discretely recorded time or spatial data into the frequency domain or the other way around. 128, 129

- FRED is a commercial software for optical engineering and simulation by raytracing. FRED is developed by Photon Engineering, LLC. See <http://www.photonengr.com/software/> . 85, 124, 125, 161
- FWHM The *full-width at half-maximum* denotes the width of an emission spectrum, measured from peak intensity to the wavelengths having the half of the peak intensity. 28, 45, 166
- GCC The GNU Compiler Collection (GCC) is an open source project which comprises compilers for various programming languages and platforms. It was founded by Richard Stallman and is available at <http://gcc.gnu.org/>. 153
- irSys 1.7 A near-infrared spectrometer manufactured by TQ-Systems GmbH. The device acquires 120 bands in a spectral range of 660 to 1 730 nm, which equals a spectral resolution of 9 nm. xvi, 37, 38, 44–46, 49, 51, 61

- LBIS** A research project to investigate an adaptive, contactless near-infrared-sensor-systems for protective devices at saws. The projects name "LBIS" is an abbreviation of the German title. Project sponsor is the German statutory accident insurance DGUV. Project reference is FFFP0289. [37](#), [177](#)
- Microcontroller** A microcontroller is an integrated circuit comprising all basic components of a computer. Namely, a processing unit, programmable input/output peripherals as well as memory. Usually, microcontrollers can execute software without the use of external components. [15](#), [90](#), [98–103](#), [108](#), [109](#), [111](#), [153](#), [162](#), [185](#)
- NIRS** The near-infrared spectrum denotes electromagnetic radiation with a wavelength of about 800 nm to 2 500 nm. This wavelength range is directly adjacent to the visual spectrum (VIS). [7](#), [25](#), [40](#), [46](#), [59](#)

- PCA The principle component analysis (PCA) is commonly used as a tool to explore high-dimensional data (see [80, 81]). It creates q linear combinations over all p original dimensions of a data set, whereby $q \leq p$. These linear combinations capture the essential patterns of the original data in q dimensions. [xix](#), [43](#), [148](#)
- Skinner The sensor is named after the fictional character Seymour Skinner from the TV show "The Simpsons" (1989-today), whose name can be understood as a word play for "see more skin(ner)". [xviii–xxii](#), [36](#), [43](#), [44](#), [48](#), [50](#), [52](#), [54](#), [66](#), [97–99](#), [104](#), [124](#), [127](#), [129–131](#), [134](#), [135](#), [138](#), [139](#), [142](#), [146](#), [155–158](#), [160–162](#), [165–168](#), [170](#), [177](#), [180](#), [184](#)
- Spectral signature A vector of multispectral remission intensity values, which can be used for classification of an object's surface material. [8](#)

- spectrocam A hand-held spectrometer, originally manufactured by Avantes BV. The device acquires 75 bands in a spectral range of 380 to 750 nm, which equals a spectral resolution of 5 nm. The device possess a pulsed Xenon gas discharge tube as an illumination source for reflectance spectroscopy. 37
- SVM A support vector machine is a classifier technique which classifies sets of objects in a way that the margin between the classes is maximized. A detailed description can be found in chapter 2.3.1. xxii, 9, 10, 13, 14, 42, 120–122, 147, 149–153, 178
- VIS The visual spectrum denotes electromagnetic radiation that can be detected by the human eye, which is roughly within a wavelength range from 380 nm to 780 nm. 37, 203

